Controlling, storing and manipulating light using on-chip Brillouin scattering

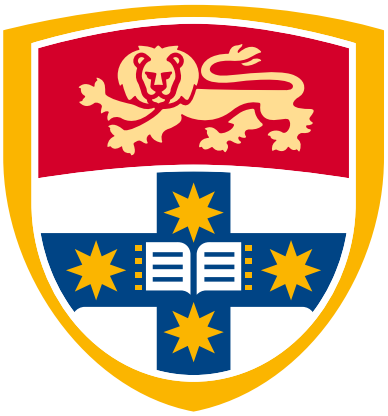

Moritz Merklein

School of Physics, Faculty of Science
The University of Sydney

A thesis submitted in fulfilment of the requirements for the degree of
Doctor of Philosophy

April 2018

Declaration

I, Moritz Merklein, declare that this thesis titled, "Controlling, storing and manipulating light using on-chip Brillouin scattering" and the work presented in it are my own. To the best of my knowledge, this thesis contains no copy or paraphrase of work published by another person, except where duly acknowledged in the text. This thesis contains no material that has been previously presented for a degree at the University of Sydney or any other university.

Moritz Merklein
April 2018

Acknowledgements

First of all, I would like to thank my supervisor Prof. Ben Eggleton for giving me the opportunity to conduct my Ph.D. studies in his group, for his guidance and mentorship and all the opportunities he presented me. Ben, I will be forever grateful for this experience. Furthermore, I would like to thank my co-supervisors Dr. Irina Kabakova and Dr. Birgit Stiller for all the time you spend with me in the lab, reading carefully through the thesis and all the advise you gave me over the last years. It was a pleasure working with you and I am very proud that the time working with both of you was crowned by getting our work published in Nature Communications. Furthermore, I would like to thank Dr. Radan Slavík. Radan, it was a pleasure working with you. Also thanks to your team at ORC Southampton that made my stay there an absolutely delightful experience.

I would also like to thank all the CUDOS Ph.D. students and postdocs I was overlapping with during my time here in Sydney. We had a blast - I will always remember the great times we had together and all the insightful discussions. It is impossible to list all the people that had a positive influence on my journey over the last few years, but I would like to thank Thomas Buettner by name for all the great times we had in and out of the lab.

Finally, I would like to thank my family for all their support over the years. I love you all to the bits! And of course, I would like to thank my lovely partner Silke who came with me all the way to Australia.

Abstract

The importance of optical signal processing techniques is growing rapidly in recent years due to the exponentially increasing demand for bandwidth, capacity and power efficiency in communications and computing. In particular, on-chip implementations that can complement state-of-the-art electronic micro-chip architectures are highly desired. Due to their bosonic nature, however, photons do not interact with each other, unless there is a nonlinear medium present mediating the interaction.

The desire to switch and process data all-optically led to the field of *integrated nonlinear optics*. One of the strongest and most tailorable nonlinear effects is the interaction of light waves, photons, with sound waves, acoustic phonons, which is known as stimulated Brillouin scattering (SBS). In the SBS process, an optical pump wave interacts with a traveling acoustic wave, generating a backscattered optical Stokes wave that is frequency-shifted by the frequency of the acoustic wave. The beating between the two optical waves reinforces the acoustic wave. Hence it is referred to as a *stimulated* scattering process.

In a recent paradigm shift, it was shown that these resonant interactions of light and sound waves could be harnessed in a chip scale platform. The pristine properties of this coherent interaction allow for applications, hard to achieve in purely photonic processing schemes.

This thesis experimentally investigates on-chip SBS. The fundamental coupling strength between the light and sound waves is studied, and it is shown that the interaction strength can be tailored by using one-dimensional photonic bandgap structures. By altering the waveguides' density of states (DOS) an enhancement of the SBS interaction is observed, and a 15-line Brillouin frequency comb (BFC) could be generated. Importantly it is shown that the generated frequency comb is phase-locked, a key requirement for any application. But it is also shown that one can fully inhibit the SBS interaction by exploiting the low DOS inside the photonic bandgap. This is an important finding as it allows to mediate SBS in cases where it is considered a nuisance, such as in many telecommunication applications or high-power lasers and amplifiers.

While in the previously described case optical feedback is used to enhance SBS and generate a frequency comb or pulsed laser source, the possibility of employing radio frequency (RF) feedback is also explored. In this configuration, very stable RF oscillations were generated

via beating an optical pump and the - via SBS generated - first-order Stokes wave on a photo-detector.
Besides allowing for the generation of unique on-chip sources, such as the above described pulsed laser or microwave synthesizer, SBS also enables the storage of light signals, one of the holy grails of all-optical signal processing. Storing and delaying light signals is of key importance in optical networks to enable synchronization, buffering, rerouting and further signal processing operations on the data.
Ideally, this is achieved in a small footprint integrated platform. On-chip SBS offers great potential as optical memory because it enables a resonant coherent transfer of information from an optical data pulse to an acoustic wave and back. The acoustic wave travels five orders of magnitude slower than the optical wave, quasi-stopping the flow of information encoded in an optical data-stream in the waveguide. It is shown in this thesis that a Brillouin-based memory (BBM) technique allows storing not only the amplitude but also the phase of optical data pulses, which significantly increases the amount of data that can be stored and promises full compatibility with modern complex encoding schemes.
Furthermore, the unique phase-matching condition between the optical and traveling acoustic waves allows for multi-wavelength operation with minimum crosstalk and allows advanced signal processing operations such as uni-directional light storage. Cascading the transfer between optical and acoustic waves paves the way towards a distributed optical memory, where information can be stored everywhere in a photonic circuit, just by tailoring the control pulses from one external laser source. It is also shown that the limitation in storage time of the acoustic lifetime could potentially be overcome by operating the memory in an inverse frequency regime, the Stokes instead of the anti-Stokes regime. In this regime, the acoustic wave does not get depleted by the control pulses but is replenished.

The body of work of this thesis presents an advance in on-chip optical signal processing by using coherent sound waves. It is shown that the SBS interaction can be fully tailored by periodically patterning a photonic waveguide, from strongly enhancing to fully suppressing the build-up of a Stokes wave. Furthermore, it is shown that operating SBS in a hybrid RF cavity allows to synthesize ultrastable RF signals. Finally, it is shown that coupling optical signals to coherent traveling acoustic waves can be harnessed for storing and delaying optical signals in an integrated circuit with high fidelity, preserving key parameters of optical data streams such as amplitude, phase, and wavelength, while operating at a high bandwidth.

Publication List

This thesis by publication is based on the following five articles that appeared in peer reviewed journals and five postdeadline papers that were reviewed and presented at international conferences.

Journal papers

M. Merklein, B. Stiller, K. Vu, S. J. Madden, and B. J. Eggleton, "A chip-integrated coherent photonic-phononic memory," Nature Communications **8**, no. 1, 574 (2017).

M. Merklein, B. Stiller, I. V. Kabakova, U. S. Mutugala, K. Vu, S. J. Madden, B. J. Eggleton, and R. Slavík, "Widely tunable, low phase noise microwave source based on a photonic chip," Optics Letters **41**, no. 20, 4633 (2016).

M. Merklein, A. Casas-Bedoya, D. Marpaung, T. F. S. Büttner, M. Pagani, B. Morrison, I. V. Kabakova, and B. J. Eggleton, "Stimulated Brillouin scattering in photonic integrated circuits: novel applications and devices," IEEE Journal of Selected Topics in Quantum Electronics **22** no. 2, 336 (2016).

M. Merklein, I. V. Kabakova, T. F. S. Büttner, D.-Y. Choi, B. Luther-Davies, S. J. Madden, and B. J. Eggleton, "Enhancing and inhibiting stimulated Brillouin scattering in photonic integrated circuits," Nature Communications **6**, 6396 (2015).

T. F. S. Büttner, M. Merklein, I. V. Kabakova, D. D. Hudson, D.-Y. Choi, B. Luther-Davies, S. J. Madden, and B. J. Eggleton, "Phase-locked, chip-based, cascaded stimulated Brillouin scattering," Optica **1**, no. 5, 311 (2014).

Postdeadline papers

K. Jaksch, M. Merklein, K. Vu, P. Ma, S. J. Madden, B. J. Eggleton, and B. Stiller, "Brillouin-based Light Storage of 200ps-long Pulses for 70 Pulse Widths," Frontiers in Optics (FIO) 2017, FTh4A.5

B. Stiller, M. Merklein, K. Vu, P. Ma, S. J. Madden, and B. J. Eggleton, " Simultaneous opto-acoustic light storage at multiple frequency channels," CLEO-PR, OECC and PGC 2017, 10-s2906.

M. Merklein, B. Stiller K. Vu, P. Ma, S. J. Madden, and B. J. Eggleton, "On-chip non-reciprocal light storage," CLEO/Europe-EQEC 2017, 2191 PD-2.4.

B. Stiller, M. Merklein, K. Vu, S. J. Madden, and B. J. Eggleton, "A coherent on-chip optical memory: storing amplitude and phase as acoustic phonons," Nonlinear Photonics (NP) 2016, JW6A.1

M. Merklein, B. Stiller, K. Vu, S. J. Madden, and B. J. Eggleton, "Storing Light as Sound in a Photonic Integrated Circuit," Frontiers in Optics (FIO) 2015, FW6C.6

Table of contents

Nomenclature

μm micrometer.

4WM four-wave mixing.

AlGaAs Aluminium gallium arsenide.

ALN Aluminium nitride.

As_2S_3 Arsenic trisulfide.

As_2Se_3 Arsenic triselenide.

BBM Brillouin-based memory.

BDG-DS Brillouin dynamic grating distributed sensing.

BEDS Brillouin echo distributed sensing.

BFC Brillouin frequency comb.

BFS Brillouin frequency shift.

BOCDA Brillouin optical correlation domain analysis.

BOFDA Brillouin optical frequency domain analysis.

BOTDA Brillouin optical time domain analysis.

BOTDR Brillouin optical time-domain reflectometry.

CaF_2 Calcium fluoride.

CHF_3 Fluoroform.

cm centimeter.

CMOS complementary metal–oxide–semiconductor.

CO_2 Carbon dioxide.

CROW coupled-resonator optical waveguides.

CW continuous wave.

dB decibels.

dBc signal-to-carrier power ratio in dB.

dBm decibel-milliwatts.

DC direct current.

DFB distributed feedback.

DOS density of states.

e.g. for example.

EDFA erbium doped fiber amplifier.

EIT electromagnetically induced transparency.

et al. and others.

etc. and the rest.

FEM finite element method.

FG function generator.

fig. figure.

FSR free spectral range.

FWHM full width at half maximum.

GaAs Gallium arsenide.

GAWBS guided acoustic-wave Brillouin scattering.

Ge Germanium.

GHz gigahertz.

Hz hertz.

i.e. that is.

IM intensity modulator.

kHz kilohertz.

km kilometer.

kW kilowatt.

LC-circuit resonant conductor-inductor circuit.

$LiNbO_3$ Lithium niobate.

LN EDFA low-noise erbium doped fiber amplifier.

LO local oscillator.

m meter.

MHz megahertz.

mm millimeter.

MOD modulator.

mW milliwatt.

MWP microwave photonics.

NA numerical aperture.

nm nanometer.

ns nanosecond.

NSR noise-to-signal ratio.

OEO optoelectronic oscillator.

OMIT optomechanically induced transparency.

OSA optical spectrum analyzer.

PBG photonic-bandgap.

PC polarization controller.

PCF photonic crystal fiber.

PD photodetector.

PG pulse generator.

PM power meter.

pm picometer.

PPT photon-phonon translator.

ps picoseconds.

PTFE Polytetrafluoroethylene.

Q-factor quality factor.

RBW resolution bandwidth.

RF radio frequency.

RIN relative intensity noise.

SBS stimulated Brillouin scattering.

SEM scanning electron microscope.

SiO_2 Silicon dioxide/ silica.

SMF standard single mode fiber.

SPM self-phase modulation.

SSB single-sideband.

TE transverse electric.

Te Tellurite.

THz terahertz.

TM transverse magnetic.

TPA two-photon absorption.

UV ultraviolet.

VCO voltage controlled oscillator.

VNA vector network analyzer.

W watt.

Chapter 1

Introduction

This thesis investigates the interaction of photons with coherent hypersound waves in integrated waveguides. This resonant interaction between traveling sound and light waves is canonically referred to as stimulated Brillouin scattering (SBS). In this process, an optical pump wave interacts resonantly with an acoustic wave which generates a frequency downshifted Stokes wave. The process is stimulated when the beat-note between the pump and the Stokes wave is reinforcing the acoustic wave, leading to an exponential build-up of the generated Stokes wave.
SBS is an effect which was observed in optical fibers for many decades, but even though it has many applications, such as narrow-linewidth lasers or temperature and strain sensors, research often focused on mediating SBS in optical communication systems where it is known to be a nuisance. In a recent paradigm shift, the field of SBS research moved from long lengths of optical fibers towards sub-micrometer to nanometer size waveguides, enhancing the opto-acoustic interaction strength by orders of magnitude, enabling many on-chip applications and greatly expelling the capabilities of integrated nonlinear optics.
Harnessing SBS on a chip was enabled by a better understanding of what is required to guide optical and acoustic waves simultaneously in a waveguide, a prerequisite for strong opto-acoustic interaction. A waveguide made out of a soft glass like chalcogenide sandwiched between rigid silica glass turns out to fulfill this condition, enabling ultra-high Brillouin gain. Being one of the strongest and most tailorable nonlinear interactions renders SBS a candidate for a wide variety of applications in integrated photonic circuits. This thesis investigates SBS in on-chip waveguides from a fundamental physics point of view of tailoring the SBS interaction strength to proof-of-principle demonstrations that lay a foundation for many potential future applications, ranging from on-chip multi-wavelength or pulsed laser sources, the generation of stable widely tunable microwave signals and the ability to stop and storing optical signals. Developing an all-optical light storage technique is key for buffering, rerout-

ing and processing of optical signals on a chip.

The first step for efficiently harnessing SBS is to form a deeper understanding of how to control, and if required alter, the SBS interaction in an integrated platform. In this thesis, a method that allows tailoring the nonlinear Brillouin interaction strength by periodically patterning the waveguide, forming a one-dimensional photonic bandgap structure, a Bragg grating. The grating alters the dispersion of the waveguide and hence alters the propagation of optical waves in the structure. Close to the band-edge, the group velocity of light is decreased, and a buildup of the optical field energy can be observed. This effect is used to enhance the SBS interaction.
The enhancement of the SBS interaction strength is used to generate a cascade of several Stokes lines, a Brillouin frequency comb (BFC). The individual Stokes lines are spaced by the SBS frequency shift of around 10 GHz. Time-domain measurements of the cascaded Stokes waves show a stable pulse train, which means that the spectral lines of the BFC are phase-locked ensuring the constant line spacing. The origin of the phase-locking is identified as a complex interplay between Kerr four-wave mixing (4WM) and SBS within a highly nonlinear chalcogenide waveguide with optical feedback. Frequency combs with precise comb line spacing have several important applications from spectroscopy to metrology.
Whereas the group velocity of light is reduced at the band edges of the one-dimensional photonic bandgap, the propagation of optical waves is forbidden within the frequency range of the stopband. In this thesis, it is shown that the build-up of the Stokes wave is fully inhibited in the stopband. This is an important finding given that SBS is considered a nuisance in many applications. As SBS is one of the strongest nonlinear effects, a method to effectively suppress SBS is required for linear photonic circuits, high power applications, such as lasers and amplifiers and for on-chip signal processing schemes that exploit other nonlinear optical effects, such as, e.g., 4WM or second harmonic generation.
A framework that describes both the effects, enhancement and inhibition, is the description of the optical density of states (DOS). Inside the stopband the DOS is low; hence the Stokes scattering efficiency is quenched while at the band edges the DOS is high; hence the Stokes scattering is enhanced.
This demonstration of tailoring the DOS of a waveguide shows that the generation of the Stokes wave can be altered solely by means of tuning the pump laser frequency relative to the bandgap. It greatly increases the control over the strength of light-sound interaction, allowing for advanced SBS signal processing schemes at reduced power levels, but also allows to completely suppress SBS for the cases when it is considered a nuisance. Furthermore, it should be pointed out that this technique of selectively suppressing nonlinear interactions

via a photonic bandgap can also be extended to other nonlinear effects and hence has many potential future applications in classical optical as well as quantum signal processing.

As the spacing of the BFC is in in the 10 GHz range it is predestined for microwave processing. In this thesis, it is shown that it is in particular suitable for GHz frequency microwave synthesizing. A chip-scale microwave source has many important applications ranging from wireless communication to radar. Beside the compactness and low power-consumption, key requirements for such a microwave source are stability and tunability. The stable microwave signals are generated by feeding the microwave signal that is generated by beating an optical carrier wave with a Stokes wave at a photodetector back to a modulator that seeds the on-chip SBS interaction. This hybrid electronic-optical cavity configuration is known as an optoelectronic oscillator (OEO). We show that the strong SBS interaction in our waveguides enables the realization of a compact optoelectronic oscillator (OEO) with ultra-wide tunability and low phase noise.

Besides enabling unique on-chip sources, in the optical as well as microwave regime, SBS also allows performing manipulation and processing of optical waves, in particular the ability to store information that is carried by optical pulses. Coherently transferring optical data pulses to acoustic waves and vice versa can delay optical signals due to the five orders of magnitude difference in the velocity of light and sound waves. Achieving large delays in a compact footprint is particularly challenging, given that light travels about a foot in one nanosecond in air. Therefore, optical delay and storage techniques are crucial for next-generation microchips that harness photonics to achieve higher speeds, larger bandwidth and overall better energy efficiency. Many different approaches for an on-chip optical buffer have been pursued in the past, such as slow-light implementations based on structural and material resonances. However, a buffer that has a large bandwidth is able to achieve a large fractional delay and is compatible with complex telecommunication encoding techniques, such as amplitude and phase encoding plus multi-wavelength channel operation, is still elusive.

In this thesis a Brillouin-based memory (BBM) that stores optical information as acoustic waves on a chip is shown. Optical data pulses with multiple amplitude levels could successfully be stored and retrieved. Moreover, the coherence of this process is demonstrated by encoding different phase levels. The ultra-large Brillouin gain in chalcogenide waveguides allows large operational bandwidths that are exceeding a GHz and enable large fractional delays of tens of pulse widths. Multi-wavelength operation of the BBM is experimentally demonstrated, whereas the phase-matching condition between traveling acoustic waves and

optical waves ensures that there is no observable mixing between the individual wavelength channels. This phase-matching condition, furthermore, breaks the symmetry between forward and backward traveling optical data streams, enabling advanced signal processing such as non-reciprocal light storage.

The rest of this thesis is organized as follows:

Chapter 2 provides the reader with the state-of-the-art in SBS research necessary to contextualize the work presented in this thesis. It starts with a historic perspective from the first demonstrations of SBS towards recent on-chip implementations. Furthermore, a first introduction to the fundamental physics of SBS is provided, and an overview of applications of SBS is given, with the focus on new opportunities arising from on-chip SBS.

Chapter 3 gives the mathematical description of SBS, i. e. the interaction between optical waves and sound waves. It starts with a description of optical wave propagation to guided optical waves followed by a description of propagating sound waves and acoustic waveguides. In the final steps, these two types of waves are coupled together in a photonic-phononic waveguide.

Chapter 4 provides the theoretical background of Bragg gratings and slow-light propagation. It is shown how Bragg gratings alter the dispersion relation in a waveguide leading to the formation of a bandgap, which as shown in chapter 5 can be used to either enhance or suppress SBS.

Chapter 5 shows how tailoring the optical DOS by periodically patterning a waveguide enables pristine control of the SBS interaction strength. Enhancement, which enabled the generation of a cascade of Stokes waves, as well as fully suppression of the nonlinear effect that enabled depletion-free transmission, are demonstrated.

In chapter 6, SBS is applied in a microwave cavity can be used to generate microwave signals. The distinctive frequency tunability and low phase-noise of this Brillouin microwave oscillator are shown.

Chapter 7 shows the storage of optical signals as coherent traveling acoustic waves in a highly nonlinear waveguide. The many distinguished features of the Brillouin memory technique are shown, such as high bandwidth, coherence, large fractional delay and multi-wavelength

operation.

The final chapter 8 gives a summary of the presented work in this thesis and provides an outlook on future research directions of on-chip phonon-photon interactions.

Chapter 2

Historical background, fundamentals and state-of-the-art

This chapter discusses the foundations of SBS, starting with a historical perspective followed by a high-level description of the fundamental physics of SBS. In the final section of the chapter, the most common applications of SBS are reviewed with a special focus on on-chip applications and the new possibilities the ultra-strong SBS interaction in photonic-phononic waveguides has enabled.

2.1 Light sound interactions - a historical perspective

Here the evolution of Brillouin scattering research from the beginning of the 20th century to today's on-chip nano-structures, which are carefully designed and tailored to show efficient *stimulated* Brillouin scattering, is provided. The chapter follows the development of SBS research by means of selected experimental and theoretical breakthroughs in the field.
The second part of the chapter discusses the development of Brillouin scattering from a device point of view, starting from the first observation of SBS in a waveguide, an optical fiber, to modern chip-scale SBS platforms with strongly enhanced opto-acoustic coupling.

2.1.1 Initial theoretical predictions and pioneering experiments

The first theoretical description of Brillouin scattering was published in 1922 by Leon Brillouin [1]. In parallel there were similar studies conducted by Mandelstam in Russia published in 1926 [2], hence the effect is sometimes referred to as "Brillouin-Mandelstam scattering" in the literature. For the rest of this thesis, however, we refer to the effect as

"Brillouin scattering" or "stimulated Brillouin scattering (SBS)" depending on whether the scattering process occurs spontaneously or is stimulated, respectively. Brillouin scattering describes, in the broadest sense, the scattering of an optical wave from an acoustic wave, that is a pressure or density wave inside a material, but can also be an acoustic surface wave. The field of Brillouin research has seen several paradigm shifts:

- Phase 1: starts from the first theoretical predictions in the 1920s and experimental investigations of *spontaneous* scattering processes.
- Phase 2: starts with the invention of the laser in the 1960s that allowed for the first time to study *stimulated* scattering processes.
- Phase 3: starts from the development of low loss optical waveguides in the 1970s. SBS in optical fiber was studied to develop applications but even more so to mediate it and minimize its detrimental effects in optical data transmission systems.
- Phase 4: starts from around 2000 and shows major research efforts on controlling and harnessing SBS in micro-structured waveguides and integrated chip-scale platforms.

The first period of Brillouin scattering research ranges from the initial description of inelastic light interactions with acoustic vibrations to the invention of the laser in 1960 [3]. In this period due to a lack of coherent light sources the main focus was on investigating the *spontaneous* scattering of optical waves from acoustic waves. Shortly after Brillouin's and Mandelstam's predictions, the first experimental demonstrations of light scattering from vibrations were reported [4–6].
These initial investigations, pioneered by Raman, dealt with the inelastic scattering of light, although the nature of the vibrations involved in these studies is can be distinguished from the acoustic vibrations considered in Brillouin's theoretical study. Even though both cases are dealing with the scattering of light from matter, in Raman's initial experiments the light scatters from molecular vibrations instead of the density waves in the case of Brillouin scattering [7–9]; or in other words, Raman scattering deals with the scattering from optical phonons, whereas Brillouin scattering involves acoustic phonons. The first experimental observation of Brillouin scattering was by Gross in 1930 [7], where he observed a change in the wavelength of light due to the scattering of heat waves in a liquid.
Hence today one distinguishes between Raman and Brillouin scattering depending on the dynamic of the scattering process, or in other words the type of "phonon" involved in the scattering process. The term phonon was introduced by Tamm in the 1930s [10] and describes the fundamental quanta of a lattice vibration, in an analogy of the term photon for optical excitations. The density or pressure waves which function as scatterer in the case of Brillouin

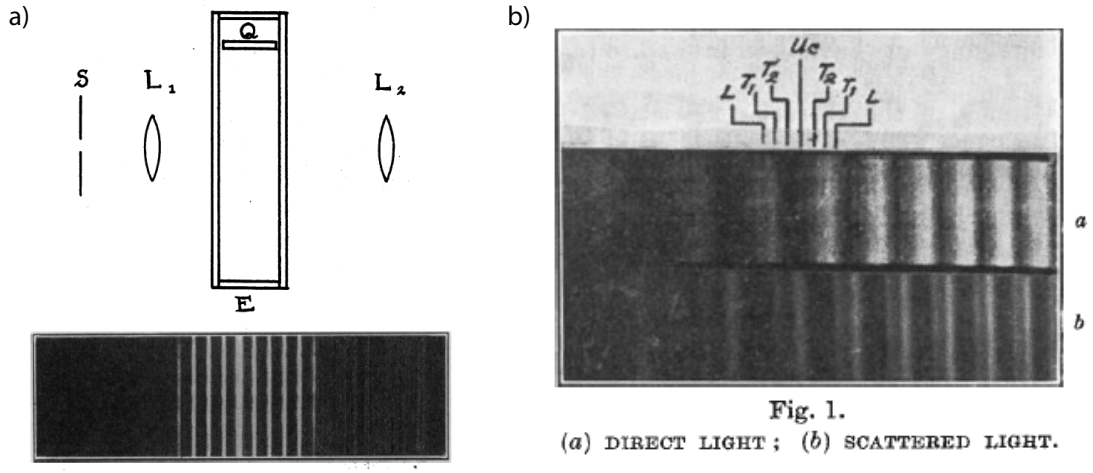

Fig. 2.1 Experimental demonstrations of light scattering from sound waves. a) Experimental setup and observed scattered light in a liquid from a monochromatic light source [8]. b) Observation of light scattered from acoustic waves in a crystal [11].

scattering are termed *acoustic* phonons and show a linear dispersion relation in bulk (Note that this linear relationship can be altered in waveguides; the dispersion relation will be explained in more detail in section 2.2). On the other hand, the molecular vibrations studied in Raman scattering have a flat dispersion and are known as *optical* phonons. Besides the dispersion relation the two scattering processes, Brillouin and Raman, show quite different frequency shifts and bandwidths of the inelastic scattered Stokes waves. Raman scattering usually shows a relatively large frequency shift in the THz range while Brillouin scattering is observed in the GHz range with a narrow spectral width of the Stokes wave in the MHz range.

Results from two pioneering Brillouin scattering experiments in liquids are shown in figure 2.1. Figure 2.1 a) shows a measurement of Brillouin scattering in liquid performed by Debye and Sears in 1932 [8] that followed shortly after the first report of Brillouin scattering in liquids by Gross [7] and showed for the first time a measured spectrum of the scattered light waves from the liquid. The first measurement of SBS in a crystal by Raman in 1938 is shown in figure 2.1 b).

These early experiments rely on a monochromatic light source and an interferometric measurement technique, where additional spectral lines next to the light source were observed. As the frequency shift of these additional spectral components depends on the elastic properties of the material, one of the first applications of Brillouin scattering was the characterization of crystals [12].

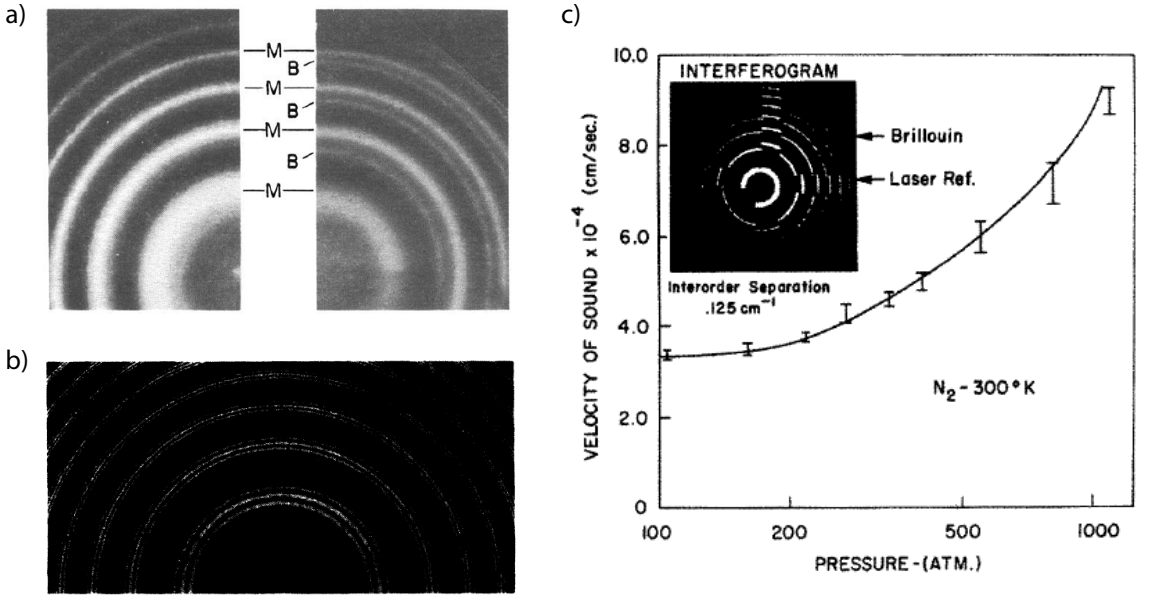

Fig. 2.2 Experimental demonstrations of *stimulated* light scattering from sound waves. a) *Stimulated* Brillouin scattering in a crystal [14], b) in liquids [16] and c) in gases [18].

A new paradigm in the field of Brillouin scattering, as in many other fields, started with the development of the laser at the beginning of the 1960s [3]. The pristine coherence properties and the high power levels of the laser enabled to reach, for the first time, the regime of *stimulated* Brillouin scattering. The first nonlinear effects using a laser, however, were not related to SBS, but reported the first demonstration of second harmonic generation [13]. Many papers on further nonlinear effects followed. The first demonstration of SBS was reported in 1964 in Quartz and Sapphire crystals [14], shortly followed by demonstrations of SBS in liquids [15–17] and in gases [18].

A theoretical description based on a classical model of electrostriction and photoelasticity was presented by Kroll shortly after these first pioneering experimental demonstrations [19]. The theory was further developed taking into account nonlinear relations between the coupled waves, such as saturation, and expressions for the strength of the coherent acoustic wave were derived [20]. The nature of the acoustic wave involved the Brillouin process was further investigated and the first theoretical and experimental study of the phonon lifetime was presented [21].

Experimental results of these first demonstrations of SBS are shown in figure 2.2. As in the case of the first *spontaneous* Brillouin scattering measurements an interferometric measurement technique was used to detect the additional spectral features generated, however the incoherent light source from early experiments was now replaced by a coherent maser or laser source, respectively.

2.1.2 Brillouin scattering in optical fiber

At the same time as the invention of the laser, and the initialization of the field of nonlinear optics, another revolutionary development took place: the deployment of low loss optical waveguides pioneered by 2009 Nobel prize laureate Charles Kao [22]. These developments ultimately led to optical fibers that can guide light for several kilometers with losses as low as 0.2 dB/ km. Optical fibers provided a completely new platform to study nonlinear optics as the interaction length is now increased from the short focal length of a focused laser to many meters and kilometers.
Following this development, the first demonstration of SBS in optical fiber was published by Ippen and Stolen [23] in the beginnings of the 70s. The experimental results from this first demonstration are shown in figure 2.3 a). Compared to the previous demonstrations on spontaneous Brillouin scattering, in this experiment, an oscilloscope is used to measure the effect of SBS directly on a propagating light pulse instead of an interferometric detection technique (compare figure 2.1 and 2.2). One can clearly identify the distortion on the forward traveling pulse (left graph in figure 2.3 a) and the generated backscattered Stokes signal (right graph in figure 2.3 a). Interestingly already in this first demonstration the authors pointed out the limitations SBS will impose on communication systems by limiting the maximum power that can be transmitted:

"From these experiments, it is clear that SBS can indeed occur at low power levels in optical fibers. In particular, SBS limits the amount of narrow-band power which one can transmit through a fiber."

This early realization of SBS being a potential hindrance turned out to be a major challenge in communication systems with major research efforts undertaken to mediate or suppress SBS[24–34]. Different approaches were pursued by scientists and are ranging from the development of specialty fiber to applying heat and stress gradients along fiber spools. Other techniques are based on purposely jittering of the pump or periodically interrupting the fibers with isolators to avoid the build-up of the Stokes wave (these different approaches are explained in detail in section 2.3 "SBS as a nuisance").

Besides being regarded as a nuisance for transmitting signals via optical fibers, the ability to exploit SBS in optical fiber, also enabled useful applications, such as the first demonstrations of a Brillouin laser [35]. Brillouin lasing was achieved by forming a fiber loop, which acts as a laser cavity (figure 2.3 b). Measurements of the laser threshold are shown in figure 2.3 c). Without the feedback loop closed the transmitted pump power increases linearly with

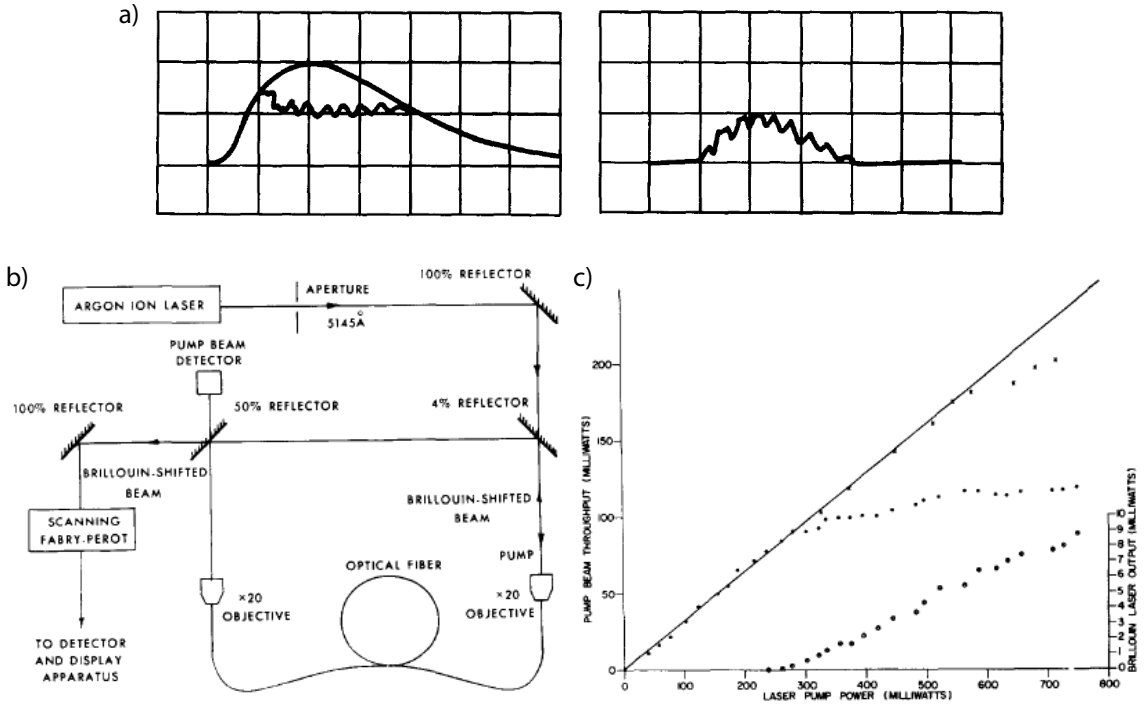

Fig. 2.3 Experimental demonstrations of SBS in an optical fiber. a) Left graph: forward traveling pulse. Right graph: detected backscattered signal generated via SBS [23]. b) Experimental setup of a fiber loop Brillouin laser [35]. c) Power measurement of an open and closed laser cavity. The lasing threshold for the Stokes signal can clearly be identified [35].

input power. With a closed feedback loop, however, the pump starts to deviate from this linear behavior due to pump depletion. At the same time, the Stokes lasing signal builds up. One can clearly identify the threshold for the Stokes lasing, one of the requirements for determining lasing behavior.
The first cascaded Brillouin laser was demonstrated shortly after the initial Brillouin laser [36]. The possibility of mode-locking cascaded Stokes orders to generate short pulses was investigated in several theoretical and experimental papers over the following years [37–39]. All these initial Brillouin laser demonstrations were utilizing a cavity that relies on both, an optical fiber spool and free-space components. The first all-fiber setup was presented a few years after this initial studies and having the advantage of lower overall cavity loss that led to a sub-milliwatt threshold [40].

Another class of light-sound interactions in optical fiber was discovered by Shelby et al. in 1985 [41] in which transverse acoustic waves, traveling between the fiber core and the fiber cladding, interact with the light guided in the fiber core. The observed acoustic frequen-

cies are much lower (MHz to hundreds of MHz) than its longitudinal counterparts (around 10 GHz) and can be observed in the forward direction. A spectrum of these transverse modes of a fiber is shown in figure 2.4 a). This class of Brillouin interactions is known as guided acoustic-wave Brillouin scattering (GAWBS).

In the mid-90s a new class of optical fibers was developed termed photonic crystal fiber (PCF) [42, 43]. The light is guided in a glass core surrounded by holes forming a photonic crystal in the transverse direction.
The small core, however, also enhances the interaction between light and sound waves by trapping the acoustic mode in the core [44]. Scattering of light from transverse acoustic modes was reported and termed Raman-like scattering, due to the resemblance of the underlying dynamics of Raman scattering. The dispersion band of the acoustic modes that are observed in the photonic crystal fiber (PCF) is rather flat, similar to the case of optical phonons in Raman scattering. The scattering direction is forward, and there is only a small change in the momentum of the light due to the mainly transverse direction of the acoustic mode. In that sense it is similar to the previously described GAWBS, however, here the acoustic mode is trapped in the very small core of the PCF and hence a larger frequency shift is observed compared to GAWBS in standard silica single-mode fiber. GAWBS in PCF and small core waveguides were subject to extensive experimental and theoretical studies [45–49].
A measurement of forward Raman-like scattering processes for two different PCFs is shown in figure 2.4 b). It illustrates the strong dependence of the observed acoustic modes on the structure of the fiber core.
Besides light scattering in the forward direction, backward SBS was also demonstrated in small core PCFs [50]. In contrast to standard single mode fiber several Brillouin peaks at around 10 GHz could be observed (see figure 2.4 c). These peaks can be attributed to different acoustic mode families in the small silica core of the PCF. It shows the dependence of the Brillouin interaction of the core-structure and shows how SBS can be tailored through micro-structuring the waveguide. The dependence of SBS on the structure of the fiber core was later measured in a distributed system, giving the opportunity of characterizing the microstructure along the PCF [51, 52].

In this section, it was shown how a PCF with a small core effects the light-sound interaction and hence shows that micro-structure waveguides enable to alter and control these interactions. In the next section an overview of SBS chip-scale platforms is presented, from micro- and

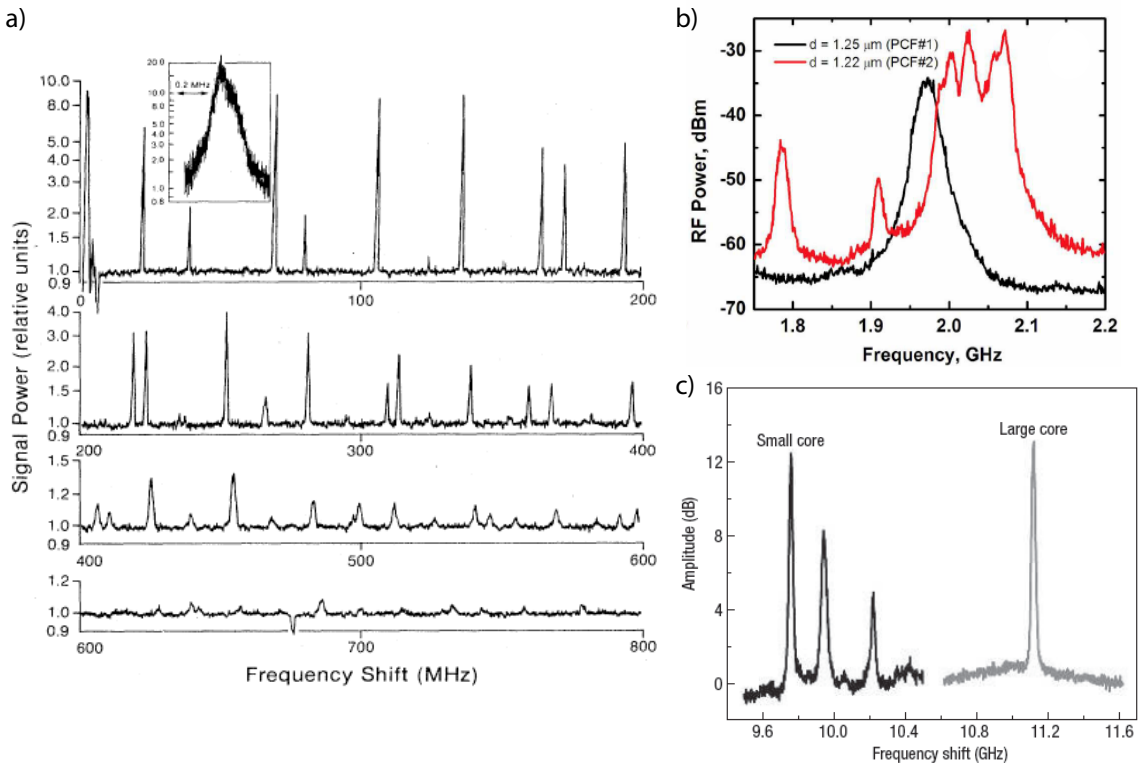

Fig. 2.4 a) Transverse acoustic modes in a 125 μm diameter fiber [41]. b) Forward Raman-like scattering in a PCF. The two measurements were performed for different PCFs and demonstrated the strong spectral dependency of the scattering process on the fiber core structure [44]. c) Backward SBS in a PCF [50].

sub-micro-meter sized waveguides, wires and suspended membrane structures to high quality factor (Q-factor) resonators.

2.1.3 Entering the chip-scale - novel SBS platforms

In the recent decade, there is another paradigm shift in SBS research occurring, from the long lengths of optical fiber towards micro- and nano-structures with high Brillouin gain coefficients. This shift was enabled by great progress in fabrication methods and techniques of photonic devices, allowing the fabrication of low-loss waveguides on chips and high Q-factor resonators with meticulous control over the dimensions. This precise control in the fabrication allowed SBS research to explore new device structures and starting to enter the nanoscale.

This section gives an overview of novel SBS platforms, focusing on the design requirements to achieve strong Brillouin interactions. An overview of applications based on these new platforms is given in section 2.3. The realization of the ability to harness SBS on a chip along with the ability to tailor the SBS interactions in micron- to sub-micron waveguides greatly excelled the field of SBS research, making SBS today one of the strongest nonlinear effects that is versatile and highly tailorable. This recent progress in SBS research allows for new functionalities in integrated photonic circuits, otherwise hard to achieve (see section 2.3))

Besides new functionalities, light-sound interaction in micro- to nano-scale structures opens a plethora of possibilities to study fundamental science questions [53–66]. It gives access to study the influence of different optical forces such as bulk electrostriction and boundary radiation pressure forces [67, 68]. For the first time it allows to tailor these two kind of optical forces and study their interplay [34]. Radiation pressure forces allowed for example (e.g.) to cool a mechanical resonator into its quantum ground state [57]. This seminal demonstration shows that studying the interactions between optical waves and mechanical motion can give access to fundamental science questions such as the observation of quantum effects of macroscopic systems.
First investigations of waveguide size effects on the Brillouin interactions date back to the 70s [69–74]. For example, it was realized by Sandercock that the Brillouin spectrum would exhibit discrete spectral lines within the Brillouin linewidth in thin films due to the discrete nature of the phonon wave vectors [69]. Further experiments investigated the effects of Brillouin scattering from acoustic surface phonons [72]. A scheme of a basic experiment investigating these type of scattering interactions is shown in figure 2.5 a). Prisms are used to couple light into the TE_0 waveguide mode. The light that was scattered by a 90° angle and is now in the TM_0 mode was collected by a second prism.

SBS in chalcogenide waveguides

Following these early considerations of SBS in thin films, the first observation of SBS in a planar rib waveguide on a chip was realized in 2011 [75]. Here the longitudinal acoustic wave is guided in the chalcogenide glass that is sandwiched between a silica substrate and cladding. As the speed of sound is higher in silica surrounding compared to chalcogenide core, the acoustic wave is well trapped in the waveguide. This acoustic guidance mechanism can be seen in analogy to optical waveguides where the optical mode is guided in the material with the higher refractive index n and hence the lower velocity of the optical mode c / n.
A basic scheme of the chalcogenide rib waveguide used in this demonstration is shown in figure 2.5 b) with a scanning electron microscope (SEM) image shown in the inset. The Brillouin gain in chalcogenide waveguides is around two orders of magnitude larger than in standard single mode fiber. As described in section 2.2 about the fundamental physics of SBS, this increased gain originates from the large refractive index of chalcogenide glass, as well as the small mode area of the rib waveguides and the large overlap between the optical and the acoustic wave in the waveguide core.
The Brillouin gain spectrum of the rib waveguides is shown in the left panel of figure 2.5 c). It shows a Lorentzian shape and a width of around 34 MHz. The exponential amplification of a small Stokes seed is shown in the right panel of figure 2.5 c). SBS was also investigated in directly laser written chalcogenide waveguides [76], however, in this case, the acoustic mode is not well guided, and hence the observed Brillouin gain is lower and the linewidth of the observed Stokes spectrum, which is inversely proportional to the lifetime of the acoustic mode, is broadened.
This new SBS platform enabled a manifold of applications in a small footprint photonic circuit, such as on-chip SBS slow and fast light [77], narrowband filtering [78], dynamic gratings [79] and Brillouin laser [80]. In particular harnessing SBS for microwave filtering, and SBS-based microwave photonic signal processing [81], generated a significant amount of interest [82].

SBS in high-Q resonators

In parallel to the development of SBS in planar integrated waveguides, SBS was investigated in high-Q resonators. Following the first demonstration of SBS in a Calcium fluoride (CaF_2) resonator in 2009 [83], the field quickly expanded to different resonator types and materials such as, e.g., silica [84, 85]. An overview of the different resonators used to investigate Brillouin interactions is shown in figure 2.6 a) - c).

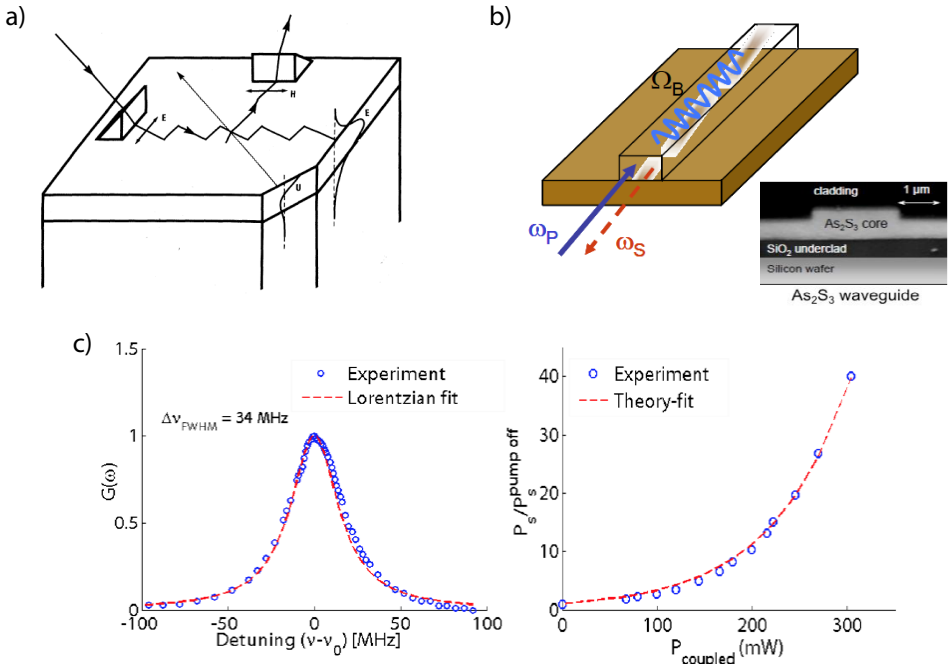

Fig. 2.5 a) Basic scheme of the experiment to observe Brillouin scattering from surface phonons [72]. Prisms were used to couple in and out of the waveguide modes. b) Basic scheme and SEM image of the rib waveguides used in the first SBS on-chip demonstration [75]. c) Lorentzian Brillouin gain spectrum (left) and exponential build-up of the backscattered Stokes wave (right) [75].

Figure 2.6 a) shows a high-Q CaF_2 resonator that supports whispering gallery modes, while 2.6 b) and c) show a silica sphere resonator fabricated using a CO_2 laser and a re-flow method and a lithographically fabricated silica wedge-resonator on a silicon chip, respectively. Note that the sound-light interactions in resonators considered in this section are Brillouin type interactions, in the sense that they rely on traveling acoustic waves. The interaction, therefore, underlies the known Brillouin scattering phase matching conditions and show a Brillouin frequency shift in the GHz range, given by the resonator material properties (compare section 2.2 on the fundamentals of SBS). Hence this Brillouin sound-light interaction can be distinguished from canonical opto-mechanical interactions in micro-resonators, which are usually dealing with transverse or breathing type acoustic modes with much lower mechanical frequencies (kHz - MHz) alongside much higher acoustic quality factors [53, 86]. Both cases rely on optical forces causing mechanical deformation and hence rely on the same underlying physics. In particular, with the recent studies of SBS in nano-scale waveguides where radiation pressure forces at the boundaries need to be considered in addition to the electrostrictive bulk forces that underly the Brillouin process in optical fiber or bulk. Moreover, it was shown that nano-mechanical rresonators can reach frequencies of multiple GHz [87].

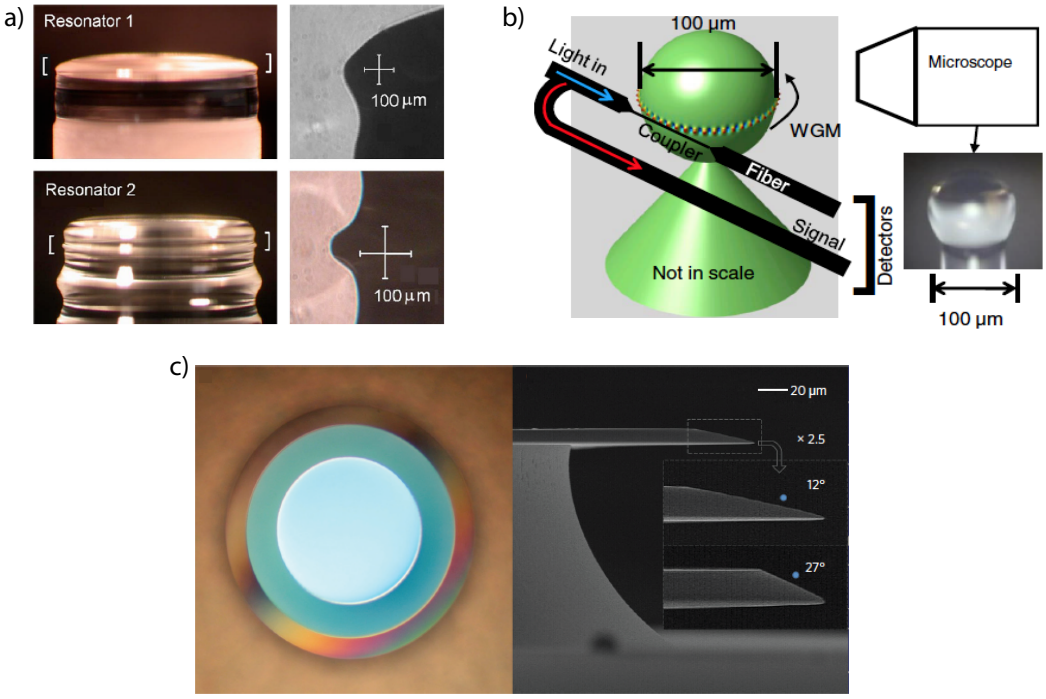

Fig. 2.6 a) Two CaF_2 resonators. The brackets mark the location of the whispering gallery modes [83]. b) The basic setup of a silica fiber-tip resonator experiment. The inset shows a photograph of a silica resonator [84]. c) Micro-graph from the top of a silica wedge resonator with around 1 mm diameter (left). SEM image of the wedge resonator from the side with different wedge angles (right) [85].

Chemically etched ultra-high Q-factor resonators on a silicon chip with the free spectral range (FSR) matching the Brillouin frequency shift [85] propelled the field of resonator based SBS further, allowing for ultra-stable Brillouin lasing [88, 89] and pure microwave generation [90, 91]. These resonators show record Q-factor values approaching one billion. The ultra-high Q-factor greatly lowers the power requirements for exciting the Stokes wave, however, also impose stringent requirements on the fabrication, as the FSR has to match the Brillouin frequency shift exactly [85].
Besides the aforementioned Brillouin lasers and microwave sources, SBS in high-Q resonators was shown to have applications as gyroscopes, greatly exceeding the performance of previous gyroscopes based on micro-optical techniques [92].

Brillouin interactions have also been observed in a different type of resonators made out of silica spheres. These spheres are made by heating a fiber-tip and can show high Q-factors. The main difference to the previously described resonators, however, is their size. These fiber-tip resonators are just about 100 µm in diameter (see inset figure 2.6 b)), compared to the

relatively large (mm-size) diameter silica wedge resonators described previously (compare figure 2.6 c). Due to the smaller size, the FSR of these resonators is not matched to the Brillouin frequency shift. However, by coupling to different mode families, phase-matching can be achieved, and Brillouin interactions can be observed [84, 93]. Demonstrations of microwave oscillations [84], Brillouin cooling [94], Brillouin induced transparency and non-reciprocal transmission [95, 96] have been shown in these resonators.

SBS in silicon

The field of on-chip Brillouin scattering received a further boost when Rakich and co-workers predicted giant SBS enhancement in silicon nano-waveguides [67]. A scheme of the theoretically proposed structure is displayed in figure 2.7 a). It was shown that moving boundary effects in these small waveguides enhance the opto-acoustic interaction in the Brillouin process that is generally purely induced via bulk electrostriction effects. Furthermore, the much smaller effective mode area in these silicon waveguides leads to an additional increase of the strength of the nonlinear scattering process.
The structure considered in the theoretical study was a silicon nanowire surrounded by air, to avoid leakage of the phonons into the substrate that is usually made out of silica for most silicon photonic circuits. Note that the situation for silicon-on-silica waveguides is the inverse regime to the chalcogenide-on-silica waveguides described previously. Whereas in the latter case the acoustic mode is guided in the chalcogenide waveguide, in the silicon case the acoustic wave leaks out of the silicon waveguide into the silica substrate. Due to this acoustic leakage, the overlap between the optical and acoustic waves is small, and hence the SBS gain is quenched. In fact mediating the phonon leakage was (and partially still is) one of the main challenges of SBS in silicon research.

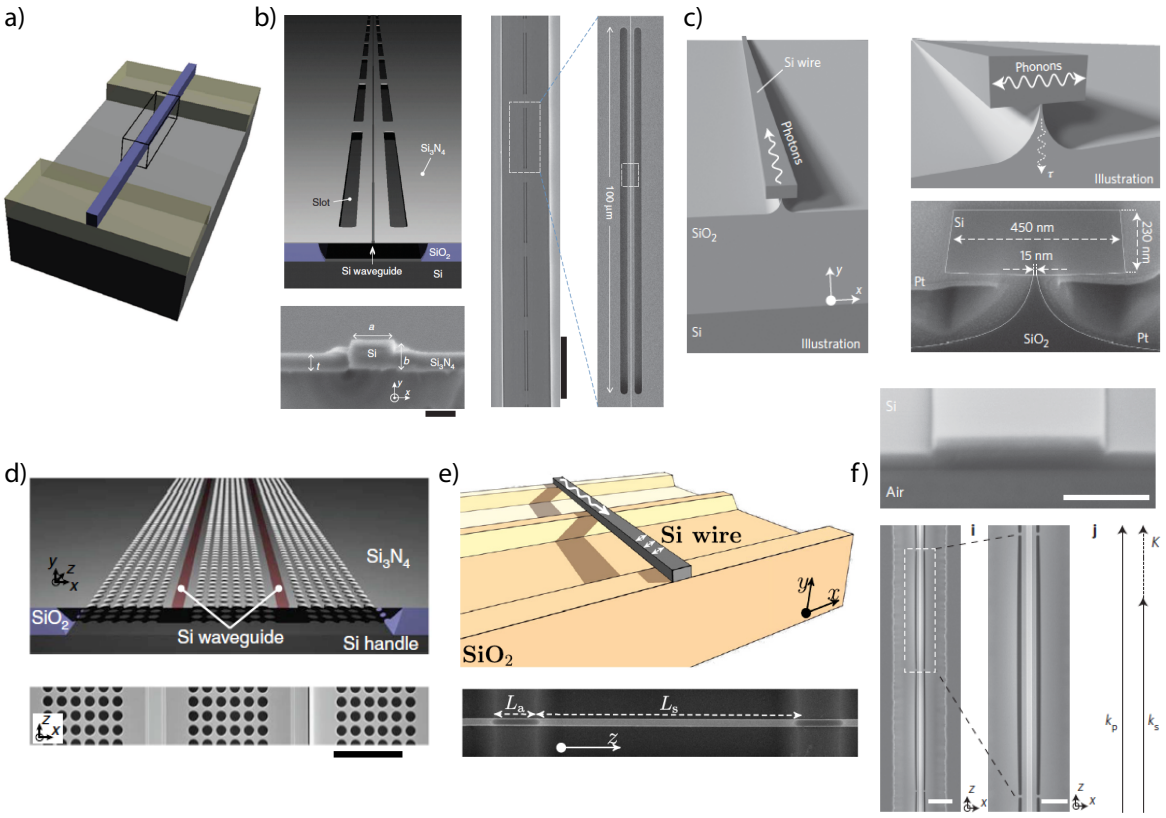

Fig. 2.7 a) Structure considered for the theoretical prediction of SBS in silicon [67]. b) Under-etched silicon waveguide with silicon-nitride wings. The optical mode is guided in the silicon waveguide whereas the wings serve the purpose of guiding the acoustic vibrations [97]. c) Silicon nanowire supported by a small nano-pillar running along the waveguide [98]. d) Two silicon waveguides in the vicinity of each other surrounded by a silicon-nitride phononic crystal. The phononic crystal wings guide the acoustic mode via Bragg reflection, but also allows the two waveguides to "communicate" via phonons [99]. e) Fully suspended silicon nanowire [100] that resembles most closely the theoretically proposed structure shown in (a). f) All-silicon suspended waveguide with wings [101].

However, due to its technological importance silicon is still a promising platform for SBS research and applications, due to the tremendous infrastructure capabilities provided by the complementary metal–oxide–semiconductor (CMOS) industry. Hence further research efforts to achieve Brillouin amplification in silicon, despite the acoustic leakage, are still actively pursued.

Several different silicon structures were designed to overcome the challenge of acoustic leakage and forward Brillouin interactions in silicon could be shown [97–99, 101–103], while backward SBS is still elusive in silicon. Theoretical studies suggest that the reason

behind the weak backward SBS interaction in silicon originates from the counteraction of the electrostrictive and radiation pressure forces in silicon. It was shown in silica tapers that these two contributions, electrostriction and radiation pressure, to the overall optical force can completely cancel each other [34].

The initial demonstration of Brillouin scattering in silicon was shown in a hybrid structure made out of a suspended silicon waveguide that guides the optical mode, with silicon-nitride wings attached to the side to guide the acoustic mode [97] (figure 2.7 b). A demonstration of Brillouin scattering in partially suspended nanowires made purely out of silicon followed shortly after [98] (figure 2.7 c). The nanowires were supported by a several nm wide pillar along the length of the waveguide and it could be shown that the acoustic leakage depends critically on the size of that pillar. Another major challenge Brillouin scattering in silicon is facing are nonlinear losses when operated at telecommunication wavelength of 1550 nm. Two-photon absorption TPA, and more severely free-carrier absorption hinder high coupled power levels and restrict the achieved Brillouin gain so far to a couple of dB [104].

In the following these initial platforms were further developed; for example, the silicon-nitride wings from the initial experiment [97] were patterned to form a phononic crystal [99] (figure 2.7 d) to guide the acoustic mode via Bragg reflections. By putting two silicon waveguides next to each other this configuration allowed to send information via phonons from one waveguide to the other. An all-silicon solution (without the silicon-nitride wings) was presented in the following [101], that achieved for the first time significant net gain of more than 5 dB in silicon (figure 2.7 f). The waveguide cross-section in this demonstration was much larger than previous implementations to avoid the prohibitively large nonlinear losses.
Even though being a major step forward, this demonstration was not the first to achieve a net gain in silicon but followed a demonstration of SBS in fully suspended silicon nanowires [100] (figure 2.7 e). These nanowires assembled most closely the initial theoretical proposal [67], and showed for the first time that the Brillouin gain in silicon can overcome the linear losses of the waveguides.

Further advancements in the field of on-chip SBS in silicon showed recently multi-mode Brillouin interactions in all-silicon membranes with large waveguide core [103]. Another interesting theoretical proposal investigates Brillouin scattering in thin silicon slot waveguides on silica with a height-to-width aspect ratio of around 3:1 [105]. This geometry reduces the velocity of the mechanical modes in the GHz frequency below that in the silica substrate,

and hence leakage of the mechanical to the substrate is prevented. It is theoretically shown that these waveguides can have large Brillouin gain coefficients for forward and interestingly also for backward Brillouin scattering.

2.2 Introduction to the fundamental physics of SBS

In this section, a phenomenological introduction to SBS is provided, with a deeper mathematical description following in section 3. It elaborates on the underlying physics and important concepts to gain intuition for the complex interaction between optical and acoustic waves. Requirements like the phase-matching condition and energy conservation will be discussed as well as the important SBS gain coefficient, and the Brillouin spectrum will be introduced. Parts of the following section are based on the review article by Merklein et al. [81].

Brillouin scattering - spontaneous light-sound interactions

The scattering of a photon from a thermally excited acoustic phonon is known as *spontaneous* Brillouin scattering. The term *spontaneous* scattering means that the presence of the optical field does not alter the response of the material in contrast to the case of *stimulated* Brillouin scattering where the optical field induces and reinforces the acoustic wave.
There are other types of spontaneous scattering processes, such as Raman or (elastic) Rayleigh scattering, however in the following we focus solely on Brillouin interactions. A schematic description of these interactions is shown in figure 2.8.

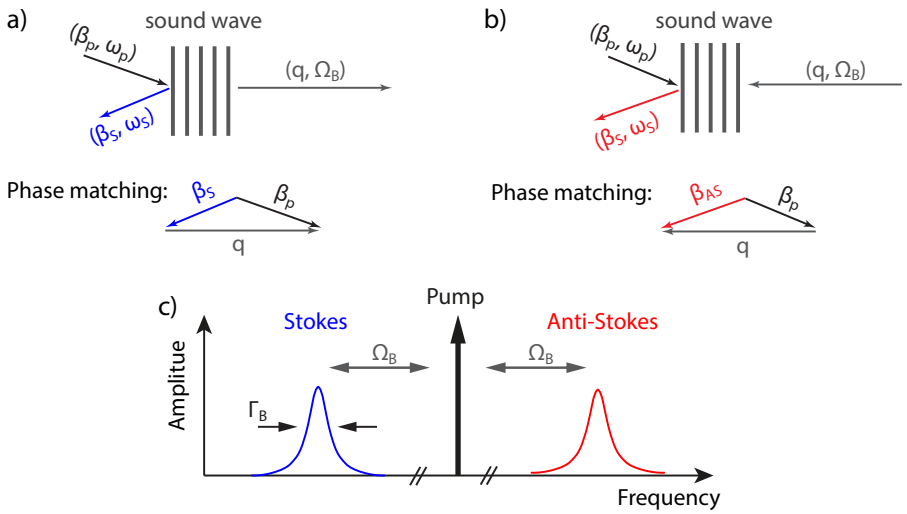

Fig. 2.8 a) Incoming plane wave scattering of a density / pressure wave, generating a backscattered Stokes signal. Due to the Doppler shift the Stokes signal is at lower frequency. Inset: Phase matching condition for Stokes scattering process. b) Same as a) but for the case of anti-Stokes Brillouin scattering. The anti-Stokes wave has the higher frequency relative to the pump wave. c) Scheme of a typical spectrum of spontaneous Brillouin scattering in backreflection.

Without loss of generality we consider plane optical and acoustic waves $\mathbf{E}(\mathbf{r},t), \mathbf{A}(\mathbf{r},t)$ to derive simple relations for the scattering frequencies and momenta from the diagrams shown in figure 2.8. These plane waves can be written in the following form, and are mainly dependent on the wave vectors $\boldsymbol{\beta}\,/\,\mathbf{q}$ and the frequencies $\omega_i\,/\,\Omega$ for the optical and acoustic wave, respectively:

$$\mathbf{E}(\mathbf{r},t) = \mathbf{E}_0 \cdot \exp\left[i\left(\boldsymbol{\beta}\cdot\mathbf{r} - \omega\cdot t\right)\right] \tag{2.1}$$

$$\mathbf{A}(\mathbf{r},t) = \mathbf{A}_0 \cdot \exp\left[i\left(\mathbf{q}\cdot\mathbf{r} - \Omega\cdot t\right)\right] \tag{2.2}$$

with $\mathbf{E}_0\,/\,\mathbf{A}_0$ being the respective amplitude vectors and $\mathbf{r}\,/\,t$ being the spatial / temporal coordinates, respectively.

There are two types of secondary optical waves generated in the Brillouin process: the Stokes and the anti-Stokes wave. The Stokes wave has a lower frequency relative to the optical pump wave while the anti-Stokes wave is up-shifted in frequency (see figure 2.8). This frequency shift can be associated with the Doppler shift of a wave that scatters of a moving object, which is, in this case, the propagating acoustic density wave.

Both of the scattering processes have to fulfill stringent phase matching and energy conservation conditions. So does energy conservation require the frequency difference of the optical pump wave ω_p and the Stokes wave ω_S (anti-Stokes wave ω_aS) to be equal to the frequency of the acoustic wave Ω_B:

$$\omega_{\mathrm{S/aS}} = \omega_\mathrm{p} \mp \Omega_\mathrm{B} \tag{2.3}$$

Furthermore the wave vectors of the optical waves $\boldsymbol{\beta}_{\mathrm{p,S,aS}}$ and the acoustic wave $\mathbf{q}$ have to add up to zero (see figure 2.8 a) and b)):

$$\boldsymbol{\beta}_{\mathrm{S/aS}} = \boldsymbol{\beta}_\mathrm{p} \mp \mathbf{q} \tag{2.4}$$

Here the momenta of the different waves are vectorial properties and hence have to be added and subtracted vectorially. In waveguides, however, the scattering angle is restrained; hence only forward or backward traveling optical modes are supported. In this case the angle between the momenta vectors becomes either 0° or 180°, simplifying the addition or subtraction of the momenta.

If we assume a relative large waveguide cross-section relative to the wavelength in the material (i.e. valid assumption for all waveguides used in this thesis) the dispersion relation for acoustic phonons, that is the dependence of the frequency on the wavenumber, can be assumed to be linear and is given by:

$$|\mathbf{q}| = \frac{\Omega_\mathrm{B}}{v_\mathrm{l}} \tag{2.5}$$

with the longitudinal sound velocity in the material v_l. The optical dispersion relation on the other hand is given by the following expression:

$$|\boldsymbol{\beta}| = \frac{n\,\omega}{c} \tag{2.6}$$

where c is the speed of light in vacuum and n is the refractive index.
Let us consider for now a waveguide geometry that limits the propagation direction of optical waves to one spatial axis. As the frequency difference Ω_B between the optical pump ω_p and Stokes / anti-Stokes waves $\omega_\mathrm{S/aS}$ is very small ($\frac{\Omega_\mathrm{B}}{\omega_\mathrm{p}} \approx 20 \cdot 10^{-6}$), the momentum of the acoustic wave $|\mathbf{q}|$ is approximately given by $|\mathbf{q}| \approx 2|\boldsymbol{\beta}_\mathrm{p}|$ for the case of backward Brillouin scattering. Hence the momentum transfer $|\mathbf{q}|$ is quite large in this case which is in stark contrast to the case of forward Brillouin scattering.
With these considerations the Brillouin frequency shift in a waveguide is given by:

$$\Omega_\mathrm{B} = \frac{2\,n_\mathrm{eff}\,v_l}{\lambda} \tag{2.7}$$

with the refractive index n replaced by the effective index of the waveguide n_eff and the (optical) wavelength λ.

Stimulated Brillouin scattering - electrostriction and photoelasticity

In contrast to the *spontaneous* Brillouin scattering process described so far, *stimulated* Brillouin scattering is a two-way process [106, 107]: the optical wave changes the density of the material, enforcing the acoustic wave via an effect called electrostriction, whereas the change in density modifies the permittivity of the material, that is known as the photoelastic effect. This change in permittivity on the other hand causes a back-action on the optical wave [108]. This two-way-interaction is schematically shown in figure 2.9.
An optical pump wave is coupled into a waveguide (figure 2.9 a). A small optical seed wave is counter-propagating (the origin of this seed wave is not important for now and will be discussed in more detail later in this chapter, section 2.2). The pump wave and the seed wave form an interference or beat-pattern (figure 2.9 b). This interference pattern is traveling with the speed of sound, instead of the speed of light, through the waveguide and therefore is able to resonantly excite a density wave that also travels with the acoustic velocity (figure 2.9 c). The frequency difference between the two optical waves is given by the Brillouin frequency shift Ω_B and hence momentum and energy conservation is obeyed.

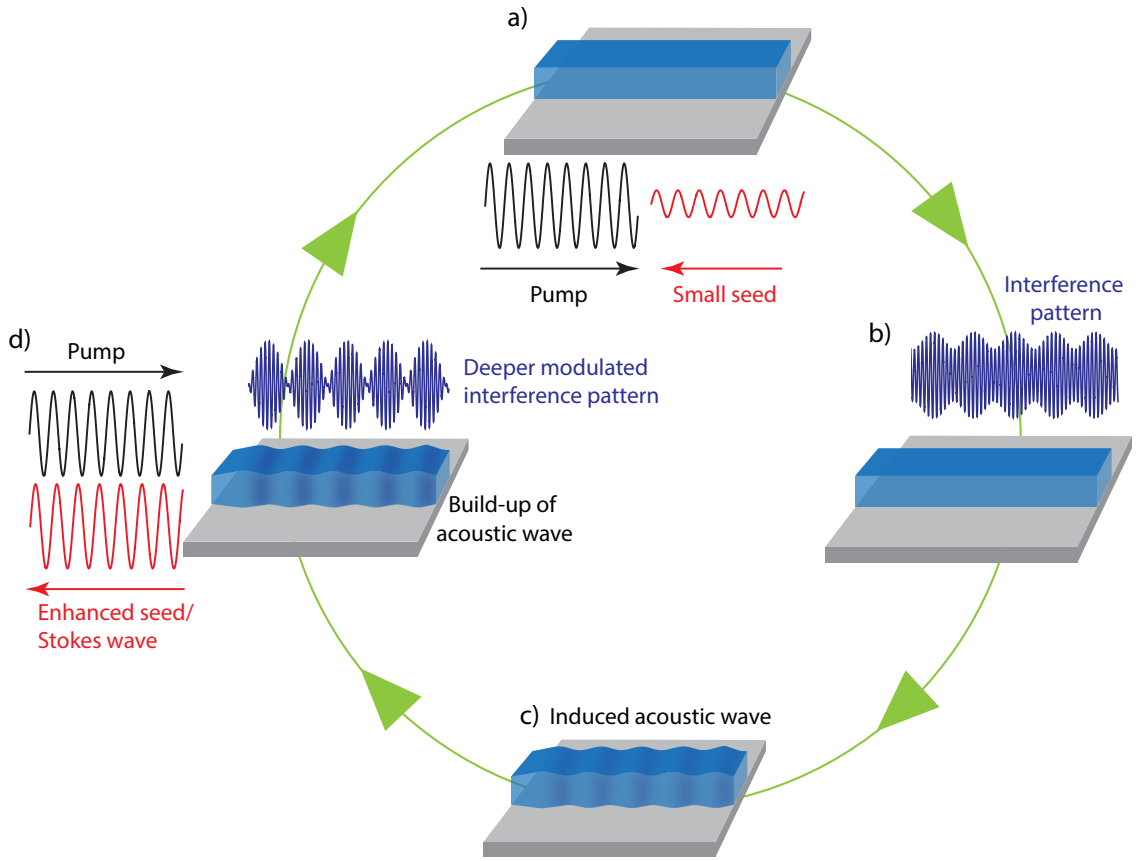

Fig. 2.9 a) An optical pump wave coupled into a waveguide with a counter-propagating optical seed wave. b) The two counter-propagating waves form a interference / beat-pattern with high and low intensities. c) If the beat-pattern from b) is strong enough and travels with the speed of sound it excites resonantly an acoustic wave. d) The acoustic wave backscatters the pump at the same frequency as the optical seed (Stokes) wave, which subsequently builds up and hence forms a deeper interference pattern.

The intensity of the interference pattern has to be high enough to alter the density of the material. Therefore, in contrast to the spontaneous light scattering described previously, *stimulated* Brillouin scattering depends on the optical input power of the pump laser and hence is a truly nonlinear optical effect. The build-up of the acoustic wave will lead to Bragg reflections of the strong optical pump wave, but as the density wave is moving the backscattered pump light is shifted in frequency. In fact, it is shifted by exactly the Brillouin frequency shift Ω_B. Hence energy is transferred from the pump to the optical (Stokes) seed wave, which starts building up. The build-up of the Stokes wave leads to a deeper modulated interference pattern, and the acoustic wave further strengthens (figure 2.9 d). The Stokes wave is exponentially growing with increasing pump power, however, reaches a maximum

when its power approximately equals the power of pump wave, which leads to depletion of the later. Traditionally, this was an effect only seen in long lengths of fiber [23] as the exponential build-up of the Stokes wave is not only proportional to the optical power of the pump laser but equally depends on the length over which the Stokes wave can build-up.

A closer look at the two processes described above - i.e., electrostriction and photoelasticity - will help to understand the main requirements a structure has to fulfill to serve as a platform for SBS. Electrostriction describes how strong a material compresses under optical radiation. To illustrate this effect, let us consider a material made out of electric dipoles. An incoming electro-magnetic wave will cause the dipoles to oscillate, and the electro-magnetic wave passes through the material with the speed of light, reduced by the optical refractive index (figure 2.10 a). However, if two interfering optical waves form a beat-pattern in the material, there will be regions of high and low intensity. In this case, electrostriction will generate a force towards the high-intensity region (figure 2.10 b). This force will lead to a periodic compression of the material, and a density wave is formed. On the other hand, a compression of the material density is also accompanied by a change in the refractive index, that is the photoelastic effect. The density wave hence generates a periodic change of the refractive index, which is nothing else than a moving Bragg grating (figure 2.10 c). Hence the pump is reflected due to the Bragg condition. However, as the periodic index modulation is moving the reflected signal is shifted in frequency.
For this back-action to be effective, the structure needs to guide the acoustic wave as well as the optical wave [109]. If there is no guidance, the acoustic mode leaks away and there is no back-action or scattering of the pump wave ω_p from the acoustic vibration Ω_B. This puts stringent requirements on the design of SBS devices. Hence a photonic-phononic waveguide needs to exhibit a contrast in the refractive index as well as a difference in the speed of sound in the core and the cladding of the waveguide [109] that ensures a mismatch in the acoustic impedance (the sound velocity contrast can be treated as an acoustic analogue to the refractive index contrast of an optical waveguide and will be discussed in more detail in chapter 3).

As a note: Electrostriction is commonly known as a bulk effect, however, it was shown that in small sub-micron structures the radiation pressure of the light at the interfaces of the waveguide can also contribute to the generation of an acoustic mode [67]. It was theoretically predicted that in a silicon nanowire the combination of the small mode area and the effect of radiation pressure on the waveguide boundaries can lead to an enhancement of the Brillouin interaction [67]. Whereas in the case of bulk electrostriction the photoelastic effect causes

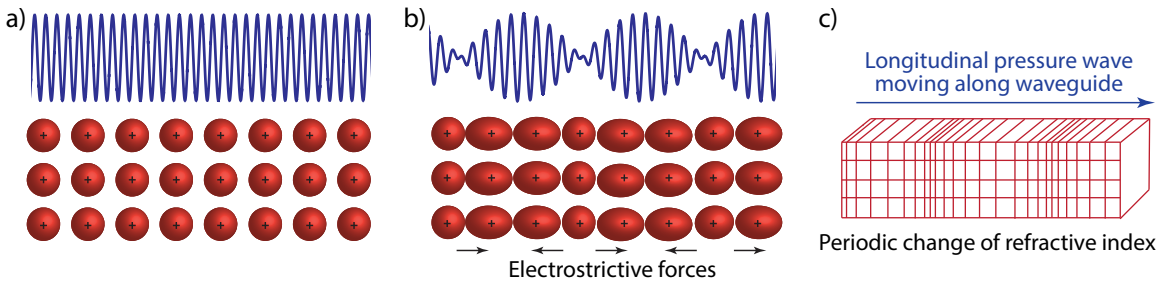

Fig. 2.10 a) Material made of dipoles (positive charge ('+') surrounded by negative charge (red circle)) and an optical wave. b) The material gets compressed via electrostriction induced by an optical interference pattern. c) The electrostrictive forces induce a density wave that leads to a periodic modulation of the refractive index.

a back-action of acoustic mode on the optical mode, in the case of radiation pressure the back-action is caused by the moving boundaries of the waveguide.

SBS generation and amplification

So far, the origin of the small optical seed wave counter-propagating the pump was neglected; however, there are three different SBS configurations that can be distinguished by the initial optical waves, as shown in figure 2.11.
The first one is called SBS generator (figure 2.11 a). The SBS process starts from spontaneous scattering of the optical pump from thermal phonons in the material. In this case, only an optical pump wave is coupled in the waveguide as opposed to the SBS amplifier configuration shown in figure 2.11 b). Here, a small Stokes seed is injected in the waveguide which is then amplified via SBS. The third configuration is a Brillouin laser (figure 2.11 c), where a cavity provides optical feedback to the Stokes wave. The Stokes wave starts oscillating above a certain threshold, allowing for linewidth narrowing of the pump laser. The threshold behavior and the narrow linewidth of the Stokes output, qualifies this configuration to be termed "laser".

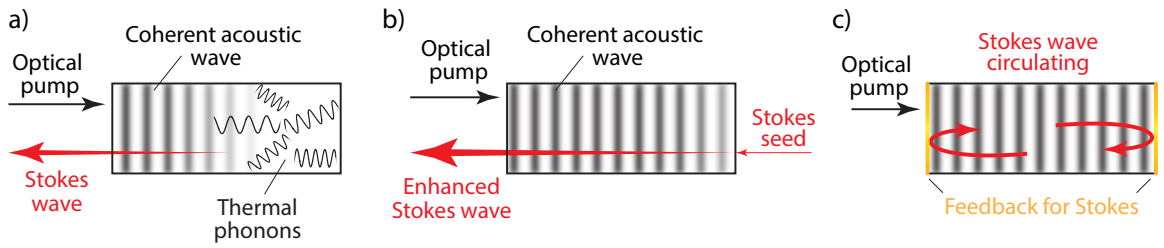

Fig. 2.11 Different Brillouin configurations. a) Brillouin generator. b) Brillouin amplifier. c) Brillouin laser.

A common metric to describe the efficiency of SBS and therefore characterize different material platforms and waveguide architectures is the Brillouin gain G. It connects the power of a Stokes seed $P_0(0)$ at the waveguide input with the Brillouin amplified Stokes wave at the waveguide output $P_S(L)$ via $P_S(L) = P_0(0) \cdot e^G$, with the Brillouin gain G given by [108]:

$$G = \frac{g_{B,wg}\, P\, L_{eff}}{A_{eff}} \tag{2.8}$$

With P being the power of the optical pump wave, A_{eff} the effective mode area and L_{eff} the effective interaction length, defined as $L_{eff} = (1/\alpha) \cdot (1 - e^{\alpha L})$ with the linear attenuation coefficient of the material α and the physical length L. The Brillouin gain coefficient in a waveguide $g_{B,wg}$ is given by [107, 75]:

$$g_{B,wg} = \frac{4\,\pi\, n^8\, p_{12}^2}{\lambda_p^3\, c\, \rho_0\, \Omega_B\, \Gamma_B} \cdot \eta \tag{2.9}$$

and depends on the material refractive index n, the elastooptic coefficient p_{12}, the pump wavelength λ_p, the speed of light c, the material density ρ_0, the Brillouin shift Ω_B , the Brillouin gain linewidth Γ_B and the acousto-optic overlap η.

SBS is a resonance effect and hence goes along with a strong amplitude and phase response [108] (see figure 2.12). The Lorentzian amplitude response $M(\omega)$ is given by the following equation [110]:

$$M(\omega) = \exp\left\{ G \cdot \frac{\Gamma_B^2}{4 \cdot (\omega_p - \Omega_B - \omega)^2 + \Gamma_B} \right\} \tag{2.10}$$

The width of the Lorentzian SBS gain bandwidth is in the order of several tens of MHz and is inversely proportional to the lifetime of the acoustic wave. This narrow-band amplitude response is utilized in many applications, from on-chip narrow linewidth filters to amplifiers and lasers (see section 2.3).

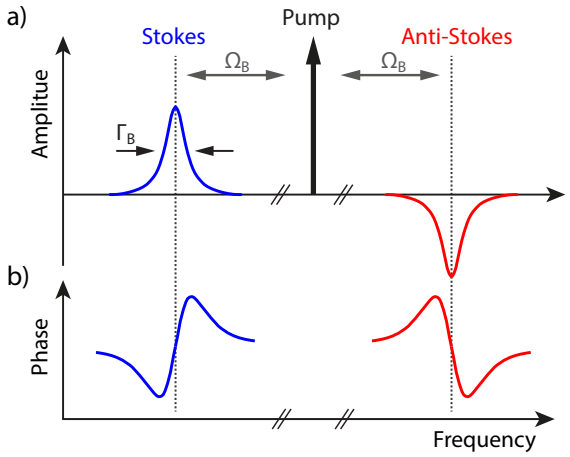

Fig. 2.12 a) Amplitude response of SBS. b) The according phase response of SBS.

The strong and narrowband amplitude response is accompanied by an equally narrow phase response $\Phi(\omega)$ (see figure 2.12 b). This phase response is given by [110]:

$$\Phi(\omega) = -G \cdot \Gamma_B \cdot \frac{\omega_p - \Omega_B - \omega}{4 \cdot (\omega_p - \Omega_B - \omega)^2 + \Gamma_B^2} \tag{2.11}$$

The fact that the phase response occurs over a narrow frequency range can be harnessed as selective RF phase shifter [111, 110, 112]. As the amplitude and phase response of SBS only depend very little on the wavelength of the pump, SBS enables devices with ultra-wide frequency tunability (see section 2.3).

Different types of Brillouin scattering

The final section of this chapter is dedicated to the different modes of Brillouin scattering. So far we only described the effect of a backscattered Stokes wave, which is the type of interaction most relevant to this thesis. However, other types of Brillouin scattering, such as forward Brillouin scattering and intermodal Brillouin scattering, are interesting interactions to study and play an important role in the field of Brillouin research. The most obvious way to distinguish these three types of Brillouin interactions is by means of the respective dispersion diagrams (figure 2.13).

The case of backward Brillouin scattering is shown in figure 2.13 a). The optical pump and Stokes wave are counter-propagating, and the difference in momentum and energy is provided by the acoustic wave. Importantly the dispersion relation of this acoustic wave is linear and starts at the origin.

The situation is quite different in the case of forward Brillouin scattering (figure 2.13 b).

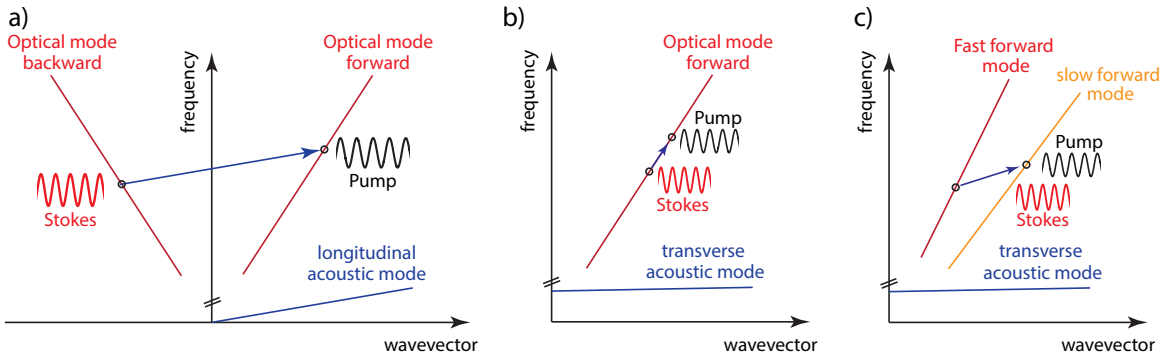

Fig. 2.13 a) Dispersion curve for backward SBS. b) Dispersion curve for forward Brillouin scattering. c) Dispersion curve for intermode Brillouin scattering.

Here, the dispersion of the acoustic wave is almost flat, resembling the optical phonons involved in Raman scattering. The flat dispersion band also indicates that the acoustic mode is only slowly moving in the direction of the optical pump and there is only a minimum momentum difference between the pump and the Stokes wave. Hence forward Brillouin scattering mainly involves transverse acoustic modes. Due to the flat dispersion band, the scattering process starts cascading for higher power levels [113]. Furthermore, in the case of forward Brillouin scattering there is no exponential energy transfer from the pump to the Stokes wave but the acoustic wave has rather the effect of phase modulating the pump, generating two sidebands. Hence the dynamics of forward Brillouin scattering exhibit many similarities to Raman scattering.
The last case considered here is intermodal Brillouin scattering (figure 2.13 c). This scattering process can occur in waveguides that support several different optical modes. In the dispersion diagram shown in figure 2.13 c) the simple case of a birefringent waveguide with a slow and fast axis is considered. Here Brillouin interactions can drive transitions between the two different optical dispersion branches.

In this section, the underlying physical concepts and properties of SBS were introduced. In the next section, we see how these properties, such as, e.g., the narrowband SBS gain and phase response, can be harnessed in a manifold of applications.

2.3 Applications of SBS

This chapter gives an overview of the applications of SBS with the main focus on applications of on-chip SBS. Many applications were initially developed in optical fiber and were just recently transferred to chip-scale devices. On-chip SBS not only provides an overall smaller footprint and lower energy consumptions but, due to the higher local gain, also enables applications not feasible in an optical fiber.
The applications of on-chip SBS are spanning over a wide field ranging from optical signal processing, laser sources, microwave photonics and sensing. The last section of this chapter gives an overview of techniques to suppress or mediate SBS; here SBS is not an application in itself but a problem that has to be addressed and solved. In this sense, SBS indirectly played a major role for many applications of photonics, such as telecommunications, as the success of many demonstrations critically depends on the ability to mediate distortions or power limitations caused by SBS.
As with the previous chapter, main parts of the following sections are based on review paper [81], however, more recent applications are added, broadening the scope to include Brillouin lasers, sensors, and signal processors.

Brillouin CW laser sources

Researchers recognized early that SBS could be used to generate narrow linewidth lasers [35]. A Brillouin laser consists of a feedback loop for the generated Stokes wave which leads to stable oscillations inside this cavity. This type of oscillator is termed Brillouin laser as it resembles many features of a conventional laser, such as: 1.) The oscillating Stokes wave shows a clear threshold behavior as it is common for a laser. 2.) It narrows the linewidth of the pump laser producing an output with higher coherence than the pump. There are, however, also subtle differences to a conventional laser as there is, for example, no population inversion.
The Brillouin laser is a powerful concept due to several advantages; it can be realized in a fiber loop or more recently in a chip architecture without the requirement of an additional gain medium (such as, e.g., doping of the medium) as it feeds purely from the intrinsic Brillouin gain. The linewidth narrowing effect - that results from an interplay between cavity feedback and the acoustic mode that generates the Stokes wave - can be exploited to purify a lower quality pump laser signal and generate a highly coherent output [114–117]. This effect makes this laser concept not only interesting for telecommunication applications at 1.55 µm, where higly coherent lasers are required, but also for wavelength regions where highly coherent laser sources are not readily available. Here the Brillouin laser is not restricted to

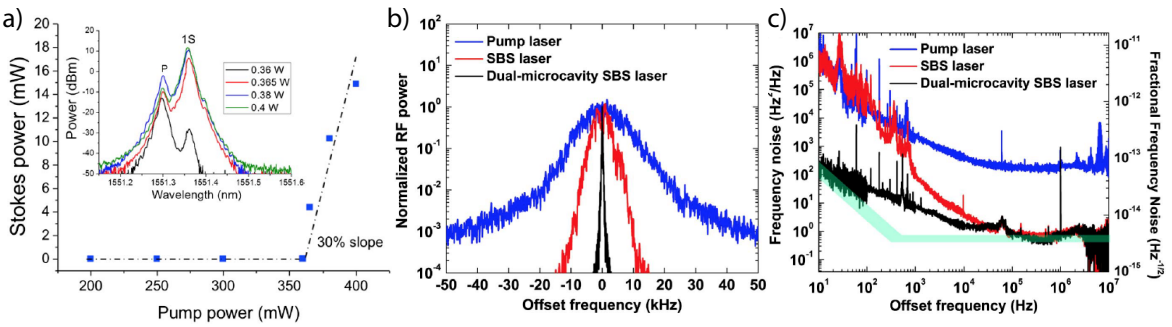

Fig. 2.14 a) Brillouin laser threshold and 30% slope efficiency. The inset shows the laser pump and Stokes spectrum [80]. b) Brillouin laser linewidth narrowing of the Brillouin laser (red curve) of the pump laser (blue curve). Further narrowing is achieved when the laser gets locked to a second microcavity (black curve) [89]. c) Phase noise of pump laser, Brillouin laser and stabilized Brillouin laser [89].

the availability of energy levels of possible dopants in a material. Of particular interest are longer wavelengths, such as, e.g., 2 µm and beyond, where it is notoriously challenging to generate highly pure signals [118]. Here, the Brillouin laser approach has the potential to have a large impact performing spectral purification.

The concept of the Brillouin laser was demonstrated on chip-scale platforms such as planar chalcogenide waveguides [119] and high-Q resonators [120, 89, 121, 88]. In the former, an optical fiber feedback loop that includes a high Brillouin gain waveguide is used to achieve Brillouin lasing. The power threshold and the slope efficiency of this approach are shown in figure 2.14 a). Furthermore, linewidth narrowing below the intrinsic Brillouin linewidth could be observed.

The second platform to realize on-chip Brillouin lasing is based on high-Q resonators, where the FSR matches the Brillouin frequency shift. The high-Q value allows very narrow linewidth Brillouin lasing as it can be seen in figure 2.14 b). Here the architecture of the laser not only relies on a Brillouin active resonator but also includes a second resonator for further stabilization. The effect of this second resonator on the reported linewidth narrowing becomes more clear when looking directly at the phase noise properties of the Brillouin laser (figure 2.14 c). As one can see, a laser with the Brillouin active resonator only effectively suppresses high-frequency noise due to the slow response of the acoustic wave that transfers the energy from the optical pump to the optical Stokes wave. However, the low-frequency noise is still present (figure 2.14 c). Here, locking the laser to a second resonator can suppress the low-frequency noise, therefore, stabilizing the Brillouin laser output.

Recently a different class of on-chip "Brillouin lasing" was investigated [122, 123]. In contrast to the previous demonstrations the optical linewidth of the resonator is not narrower

than the acoustic Brillouin linewidth - or in other words, the photon lifetime in the resonator is shorter than the phonon lifetime. Hence there is no narrowing of the optical Stokes wave but a narrowing of the acoustic mode. This behavior resembles the phonon laser regime that has been shown in a resonator previously [124], however, can be distinguished from this earlier demonstration as here the coherent phonon does not make a full round trip in the resonator and hence does not start oscillating.
At the last note two further laser sources will be mentioned briefly, even though both have not yet been shown on a chip - a Brillouin distributed feedback (DFB) laser [125, 126] and random Brillouin laser [127–129]. The Brillouin DFB laser relies on the interplay of a Bragg grating that provides feedback and Brillouin gain. The used Bragg grating is usually a π-phase-shift grating to achieve a sharp resonance. The pump is aligned in a way that the Stokes wave falls into this resonance, and the output is a stable single frequency laser mode. The possibility of an on-chip Brillouin DFB laser was theoretically investigated for highly nonlinear chalcogenide chips [130], however, the influence of other nonlinear effects (e.g., 4WM) in the waveguide and thermal effects due to the high power build-up in the resonance structure turned out to be a nuisance and inhibiting factor so far.
A random Brillouin laser, compared to all the previously described Brillouin lasers, does not rely on an external cavity to provide feedback but relies on a random feedback mechanism through scattering events and multi-path interference in the scattering medium. No alignment to a cavity is required and laser speckles are not observed in random lasers making it a robust source for imaging [131]. So far this kind of Brillouin laser has not yet been shown on a chip.

Brillouin based pulsed laser sources

In the previous section SBS based continuous wave (CW) lasers were introduced. However, SBS can also be utilized to generate pulsed laser sources, which we want to describe in this section. These laser pulses are generated via cascading the Stokes wave generation, forming a BFC [132–134]. Chip-based BFCs are discussed in more depth in chapter 5, so this section serves as a first introduction and provides an overview.
Compact integrated frequency comb sources are highly desirable for many applications ranging from arbitrary waveform generation [135], spectroscopy [136] to advanced telecommunication schemes [137]. Cascading SBS enables the generation of highly coherent frequency combs with GHz repetition rate [133, 134].
Cascaded SBS occurs when the power of the first Stokes wave exceeds the SBS threshold P_{SBS} generating a second order Stokes wave shifted by 2Ω away from the pump ω_{p}. A further increase in pump power P_{p} can then lead to the generation of even higher order Stokes

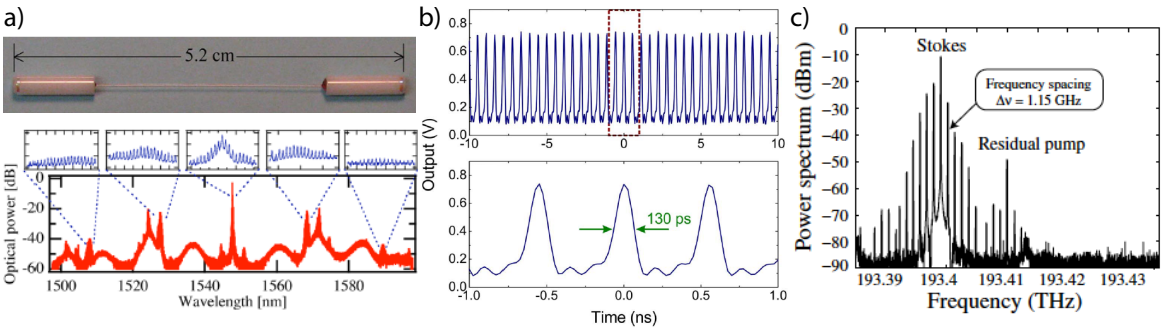

Fig. 2.15 a) Highly nonlinear fiber cavity (top). Generated BFC [134]. b) Pulse train generated using forward scattering in PCF [139]. c) Frequency comb generated via acoustic modulation instability in PCF [140].

waves [138]. However, as the generation of the first Stokes wave in a chip scale device is already challenging (as the SBS gain G is proportional to the interaction length L), cascading SBS requires a further enhancement of the intrinsic SBS gain.

One approach is to use resonators, which significantly lowers the power requirements for the cascading process [84, 138, 88]. It has been shown that a frequency comb could be generated in a 5 cm highly nonlinear fiber Fabry-Perot cavity [134]. The fiber cavity and the generated frequency comb is shown in figure 2.15 a).

The frequency comb generated in figure 2.15 a) is based on cascaded backward scattering. On the other hand, there are also approaches based on forward Brillouin scattering [141, 139, 140]. As described in section 2.2 forward Brillouin scattering is more prone to cascading due to the flat dispersion relation [113]. These Brillouin comb demonstrations rely on fiber ring cavities including a PCFs, which allow for strong Brillouin interactions. In this configuration forward Brillouin scattering from transverse acoustic modes is generating several sidebands. A pulse train generated by Brillouin interactions in a PCF is shown in figure 2.15 b). The effect of acoustic modulation in a PCF inducing a Brillouin laser with 1.15 GHz line spacing is shown in figure 2.15 c).

In chapter 5 it will be shown that integrating a Bragg grating into a highly nonlinear chalcogenide waveguide can significantly increase the cascading process [33]. A frequency comb with up to 15 comb lines was generated through cascaded SBS by harnessing the enhancement effect of a multi-stopband grating in a 6.8 cm chalcogenide chip. These on-chip BFCs were further characterized in the time domain, showing that the comb modes are equally spaced with a stable phase-relationship [132, 133].

Coherent on-chip frequency combs are of great interest because of their line spacing in the GHz range and the fact that they are phase locked [133]. Furthermore, it is known that SBS can suppress the pump phase and amplitude noise [114]. Reducing the noise with

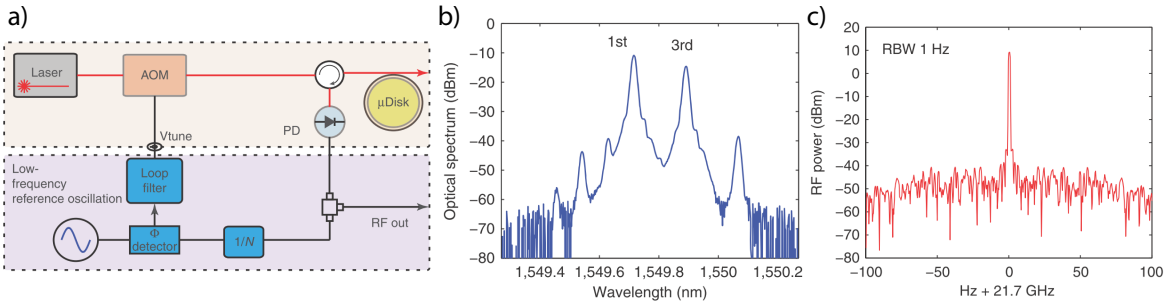

Fig. 2.16 a) Principle of an SBS based microwave source harnessing a high-Q resonator [90]. b) Generated Brillouin spectrum showing the first and second order Stokes waves [90]. c) Narrow linewidth microwave output generated by beating the first and third order Stokes wave on a photodetector (resolution bandwidth (RBW) of 1Hz) [90].

every cascaded Stokes wave is expected to lead to a low-noise BFC with high stability and great spectral purity. These are desirable properties for low noise on-chip optical-to-digital synthesizers and chip-scale microwave generators.

Brillouin based microwave sources

Brillouin scattering did not only find applications as laser sources but was also used to build microwave sources. As in the case of laser sources, SBS can lead to very pure oscillations in the microwave domain, leading to low phase noise sources. A manifold of microwave sources harnessing SBS in fiber has been demonstrated, ranging from beating the generated Stokes wave with the pump wave [142], using SBS to select certain spectral lines of a frequency comb [143] to OEO configurations [144]. In this section, however, we will limit our considerations to chip-based approaches.

As emphasized in the previous section, cascaded SBS leads to several spectral lines with a characteristic line spacing of several GHz. Beating these spectral components on a photodetector, therefore, leads to a microwave signal, making SBS a predestine candidate for microwave synthesizing [84, 90, 91]. The backbone of these three demonstrations are ultra-high-Q microresonators. The Q-factor of on-chip silica resonators exceeds several hundred millions [85]. These high-Q microresonators led to the first demonstration of a chip-based microwave source with record low white phase noise (-160 dBc Hz^{-1}) [90]. A basic scheme of such a microwave synthesizer is shown in figure 2.16 a).

The microresonator used in this demonstration has a diameter of around 6 mm, matching the FSR and the Brillouin shift of 10.8 GHz in silica [90]. The generated first and third order Stokes wave (figure 2.16 b)) were beat on a photodetector to generate the microwave signal [90]. The upper box in figure 2.16 a) can be seen as the photonic analog of an electrical

voltage controlled oscillator (VCO). By using f/N frequency dividers microwaves with almost any frequency smaller than the 21.7 GHz (the frequency difference between the first and third Stokes wave) can be generated. Measurements of the RF spectrum of the microwave synthesizer in closed feedback loop operation reveal a very narrow linewidth [90] (figure 2.16 c)). A photonic microwave synthesizer has the great advantage over electronics that the phase noise performance does not degrade with increasing frequency.
It was shown that the performance of the microresonator SBS based microwave source can be further improved by using frequency division [91]. Here, two very stable Brillouin lasers generate a high frequency signal that is divided down to RF frequencies. Hence the phase noise of the signal is divided as well, leading to record low noise RF signals.
In chapter 6 in this thesis an approach of harnessing on-chip SBS in an OEO configuration is presented. The advantage of this approach is the ultra-wide frequency tunability while still maintaining low phase noise [145].

SBS in microwave photonics

SBS has not only great potential as microwave sources but also many different applications in the field of microwave photonics (MWP) in general. It allows microwave signal processing with unprecedented performance. In particular the wide bandwidth photonics is able to provide leads to widely tunable devices at high RF frequencies, something hard to achieve in electronics. Also the ability to generate SBS in chip-scale devices boosted the field even further as it promises compact light-weight devices with increased power efficiency.
This section provides an overview of on-chip SBS applications in this field with particular focus on microwave filtering - i.e. manipulating the amplitude of a given RF signal - and microwave phase-shifting, i.e. controlling and manipulating the phase of a given RF signal.

The narrow linewidth of SBS is particularly well-suited for the implementation of narrowband MWP filters. The low wavelength dependence of the SBS process ensures that the filter shape is not changing when the frequency is tuned over a wide RF frequency range [82].
The most straightforward approach of an SBS based microwave filter is to exploit the narrowband SBS gain or loss resonance to manipulate the amplitude of an optical sideband that is generated via a modulator and carries the RF signal in the optical domain (see figure 2.17 a) bottom) [78, 146]. Even though achieving MHz reofsolution, the disadvantage of this direct approach is that it requires high power to achieve a high suppression, as it can be seen from figure 2.17 b).
A more recent architecture uses a dual-parallel Mach-Zehnder modulator to shape the modulation sidebands in a way that they are in anti-phase with unequal amplitudes [82]. An SBS

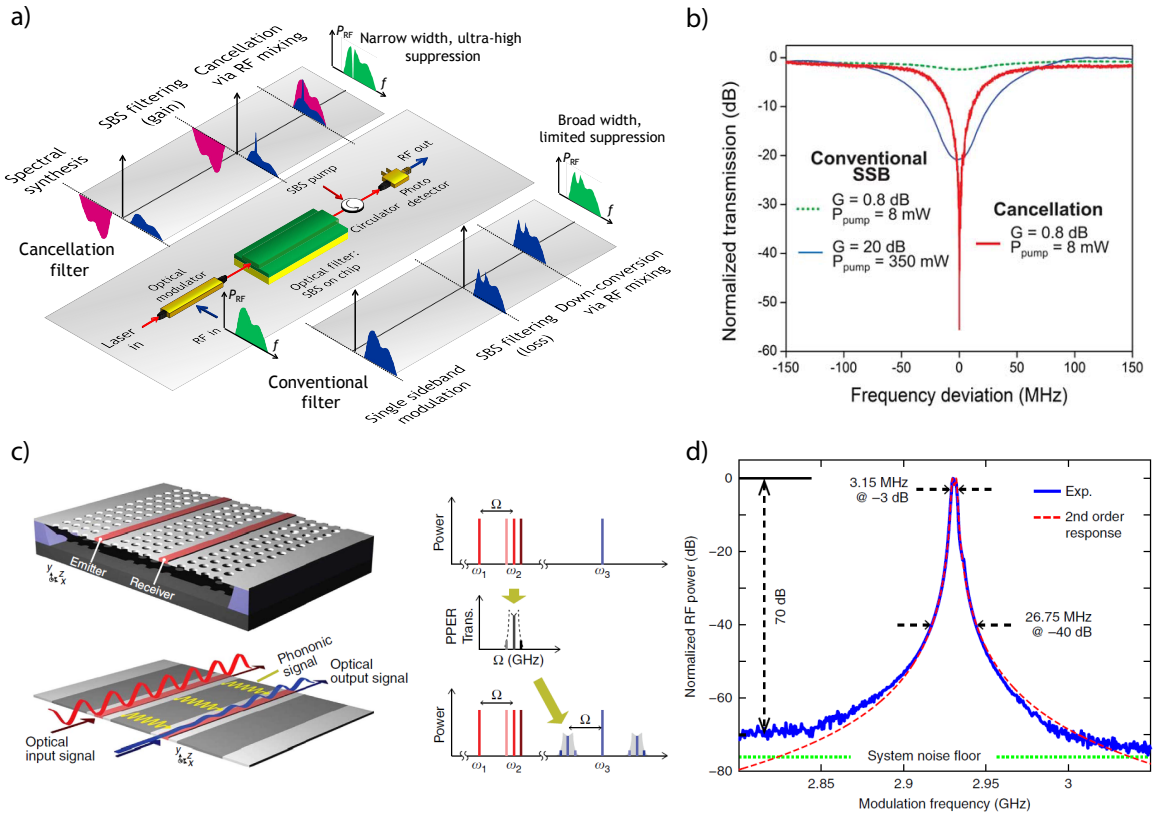

Fig. 2.17 a) Basic principle of a microwave photonic link (middle), a conventional SBS microwave filter (bottom) and a cancellation based technique (top) [82]. b) Comparison of extinction ratio and power consumption of the techniques shown in (a) [82]. c) Two waveguides transversely connected via a phononic crystal structure that allows sending phonons from one waveguide to the other [99]. d) Resulting bandpass filter shape from the structure presented in (c) [99].

resonance is then used to equalize the amplitudes (figure 2.17 a) top) such that, after photodetection, destructive interference results in an ultra-high suppression notch (>50 dB)(figure 2.17 b)). The main advantage of this technique is that even very low levels of SBS gain ($\leq$ 1 dB) can be exploited to achieve ultra-high suppression notch filter. It makes this approach well suited for on-chip implementation, where it was demonstrated first in chalcogenide rib waveguides [82] and, more recently, in suspended silicon nanowires [147].

The biggest advantage of MWPs over conventional electronics is the wide frequency tunability of optics. Frequency tuning over 30 GHz while maintaining a suppression of more than 50 dB and frequency selectivity of tens of MHz has been shown [82]. The frequency tunability was achieved by simply tuning the frequency of the SBS pump laser relative to the optical carrier frequency and is in principle only limited by the bandwidth of the modulator and the photodetector.

However, on-chip SBS microwave filters are not limited to narrow bandwidth notch filters, and broadband microwave filter with a bandwidth much wider than the intrinsic Brillouin gain linewidth could be demonstrated [148, 149]. In these demonstrations the optical pump spectrum is broadened to achieve a broadband Brillouin response [148, 149]. As the pump wave is spectrally broadened much more pump power or Brillouin gain is required to achieve the same performance. Here, chalcogenide chips have an advantage over fiber implementations as they can provide Brillouin gains of over 50 dB in about 20 cm long waveguides [149].
A different approach to generate an MWP filter was demonstrated in 2015 showing a bandpass filter in a silicon/ silicon-nitride hybrid structure [99]. A scheme of the structure and the basic operation principle is shown in figure 2.17 c). Here two waveguides in close proximity act as a photonic-phononic emitter-receiver structure. Phonons travel from the "emitter" optical waveguide to the "receiver" waveguide and are imposing sidebands on an optical carrier wave. The phononic response is then used to generate a narrow bandpass filter with a linewidth of only 3.15 MHz and an impressive suppression of over 70 dB [99] (figure 2.17 d)).

We have seen in the previous section that the SBS gain can be used to achieve MWP filters. However, as SBS is a resonant process, there is not only an amplitude response but also a change in the phase [108] (compare previous chapter 2.2 on the fundamentals of SBS). This phase response was harnessed to demonstrate an SBS based on-chip phase shifter [111]. Due to the narrow linewidth of the SBS resonance, only the phase of the carrier is changed without effecting the sidebands. Phase shifters are important building blocks of RF communication schemes and phased-array antennas. Most applications require the phase shifter to fulfill certain properties, i.e., ideally a fully tunable $0^\circ - 360^\circ$ phase shift that can be applied over a frequency range of several GHz and importantly has a flat amplitude response. The latter is extremely challenging to achieve in on-chip architectures, which are usually based on ring resonators [150, 151] or Bragg grating resonances [152]. By utilizing the SBS gain and loss response simultaneously, a flat amplitude response can be achieved [111]. This concept was first introduced by Loayssa and Lahoz in long lengths of optical fiber [112]. Applying this concept in a chalcogenide chip, therefore, reduces the footprint significantly and makes it accessible for further integrated on-chip operations [111].
The concept of the SBS on-chip phase shifter is illustrated in figure 2.18 a). Two optical pumps are used to induce an SBS gain (Stokes) resonance and an SBS loss (anti-Stokes) resonance. It can be seen from the illustration that this leads to the cancellation of the amplitude response while the phase response adds up [111, 110, 112]. Figure 2.18 b) shows the continuous tunability of the phase shift over 240° over a wide frequency range with a flat

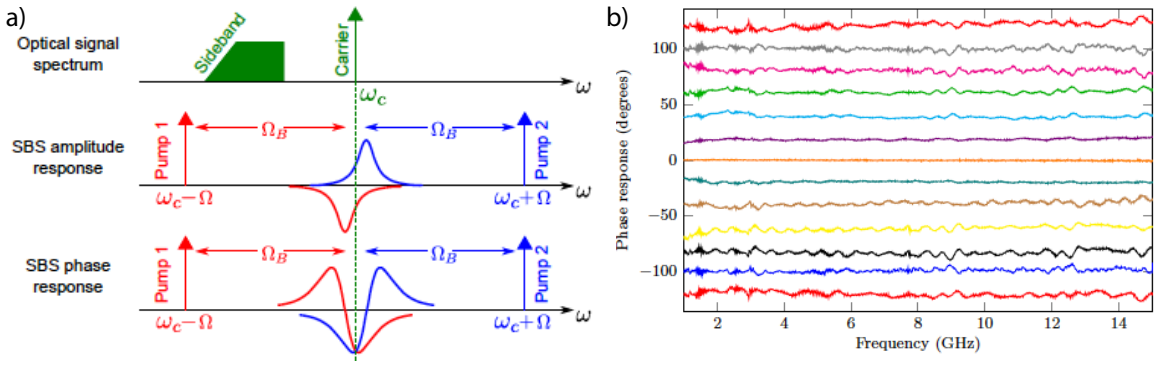

Fig. 2.18 a) Basic principle of a microwave phase shifter based on SBS. The amplitude response cancels while the phase response adds up [111]. b) Frequency tunability of an SBS phase shifter [111].

amplitude response [111].

One advantage of using SBS as a phase-shifter is that the dispersive response can be fully controlled by the external pump and probe laser. Hence one does not rely on, e.g., a fixed structural resonance. So it could be shown that by broadening the pump an SBS phase shifter over a broad bandwidth could also be achieved [153].

SBS for sensing

The commercially most advanced technology relying on SBS today is sensing. As the Brillouin shift Ω_B is sensitive to both, strain and temperature, different techniques to exploit this dependency for sensing were developed. The Brillouin shift Ω_B is given by equation 2.7 depending on the effective refractive index n_{eff}, the acoustic sound velocity v_a and the optical wavelength of the pump laser λ. In particular, relying on fiber and telecommunications components only enabled a swift transition from the lab to field applications. Importantly, it allows sensing temperature and strain variations in a distributed fashion, meaning it can be used for structural health monitoring in long pipelines, bridges, buildings, airplane wings, etc. Over the years different techniques were developed to increase the spatial resolution of this sensing technology. These techniques can be categorized in time domain measurement or frequency domain measurements and are known as Brillouin optical time-domain reflectometry (BOTDR) [154, 155], Brillouin optical time domain analysis (BOTDA) [156–160], Brillouin echo distributed sensing (BEDS)) [161–165], Brillouin dynamic grating distributed sensing (BDG-DS) [166–168], Brillouin optical frequency domain analysis (BOFDA) [169, 170] and Brillouin optical correlation domain analysis (BOCDA) [171–173].

Recently a BOCDA based sensing technique was brought to chip-scale devices [174, 175]. Figure 2.19 shows a measurement of a silica and a chalcogenide spiral waveguide, respec-

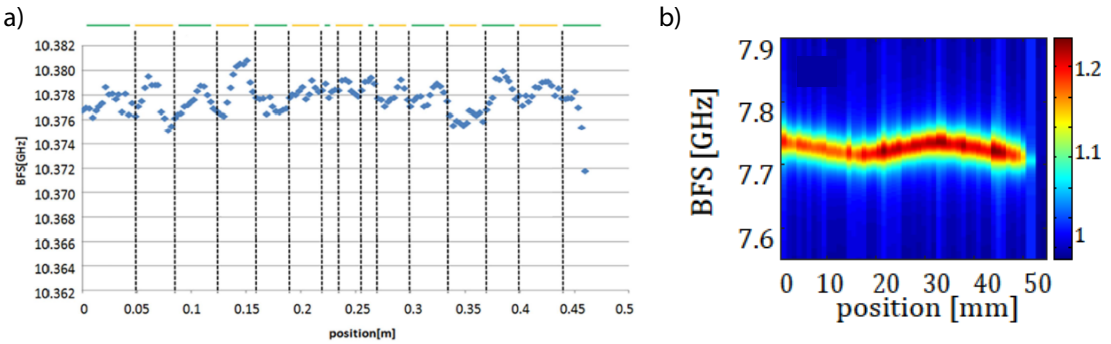

Fig. 2.19 a) BOCDA measurement of a 46.8 cm long silica spiral waveguide [174]. b) Scan along 4 cm spiral chalcogenide waveguide. Variation of the Brillouin frequency shift (BFS) can be assigned to effective refractive index variations in the chalcogenide waveguide [175].

tively. This transition from several meters to kilometers long fibers to chip scale waveguides was enabled by improvements in spatial resolution with the record resolution for a Brillouin sensor recently shown in a chalcogenide waveguide. To achieve resolutions of mm and below a correlation domain measurement technique was used. The technique is based on frequency or phase modulating a pump and probe signal in a way that only a very localized correlation peak in the sample forms from where the Brillouin amplification is measured. The resolution in this technique depends crucially on the modulation bandwidth of the pump and probe signal to form the spatially most localized correlation peak. A variation of this technique was proposed and demonstrated in optical fiber based on a broadband random source [173] instead of modulating a narrowband laser. The broad white noise source is split into two paths - pump and probe - and due to its random nature, a localized correlation peak is formed where the time-of-flight between pump and probe arm coincide. This point can then be scanned through the device under test via an optical delay line in one of the arms. This approach enabled the first sub-mm resolution of a Brillouin sensor, fully mapping the fabrication uniformity of an integrated chalcogenide waveguide (figure 2.19 b) [175].

Bringing Brillouin sensing techniques on a chip has a manifold of applications. Not only does it allow to locally measure the interaction strength between acoustic and optical waves, but can also function as a powerful characterization tool for integrated circuits in general. Fabrication uniformities of the waveguides but also local hotspots or temperature gradients can be revealed.

Optical signal processing based on SBS

SBS also has a variety in optical signal processing. The most prominent are Brillouin based amplifier and filter [176]. Here the large amplification over a narrow bandwidth turns out to

be advantageous with many studies conducted to understand and quantify induced noise in the amplification process from spontaneous Brillouin scattering [177]. Recently the ability to act as a filter and amplifier at once - an active filter - was harnessed in a telecommunication to purify a frequency comb source [178]. Most of these applications were so far fiber based but have great potential to be implemented in chip scale structures.
Another SBS application that caused great interest are SBS based delay lines [179, 180]. The group velocity of a laser pulse is slowed down in the vicinity of the SBS gain resonance as a consequence of the Kramers-Kronig relationship (details of the underlying physics will be given in chapter 4.2). SBS slow-light is particularly interesting as it operates at room temperature, is fully realized in standard communication components and gives control over the delay by adjusting the external pump power. Even though sparking lots of research interest the fractional delay, i.e., how many pulse widths a signal can be delayed, could not significantly overcome the deadlock of a few pulse widths [181]. A technique to overcome this limit is presented in chapter 7. A more detailed foundation of slow-light and its different flavors (structural slow-light, SBS slow-light) will be given in chapter 4.2. Also, the ability of slow-light to not only slow-down light signals but to enhance nonlinearities will be discussed in chapter 5.

SBS as a nuisance

As a final remark in this section, an overview is given of the importance of mediating SBS in telecommunications and the efforts undergone to mediate the effect. The detrimental effects SBS has on fiber communication was already pointed out in the first SBS in fiber paper [23]. As the SBS threshold in long lengths of optical fiber can be as low as a couple of mW it becomes a limiting factor on the power and therefore the distance one can send data [182, 24].
Different techniques were developed to mediate the effects of SBS and to increase the threshold. One powerful method is to frequency modulate or dither the pump wavelength [24]. The broadened spectrum of the pump increases the Brillouin threshold significantly. A measurement of a transmission link with and without SBS suppression using pump dithering is shown in figure 2.20 a). Furthermore fibers were developed with a non-uniform core diameter [25] or non-uniform doping concentration [26] which also increases the Brillouin threshold. The effect of these two approaches on the Brillouin threshold are shown in figure 2.20 b) and c), respectively. Also combinations of the previous described techniques were investigated, e.g. applying a temperature gradient to a fiber with a non-uniform core [32].
Another way to get around limitations through SBS is by using very short data pulses, hence the spectrum of the pulses exceeds the Brillouin linewidth and an increase in threshold can

be observed. Other approaches were relying on dividing the fiber in segments and including isolators to avoid a build-up of the Stokes wave, applying non-uniform heat or strain to fiber-spools. The non-uniform strain or temperature profile will cause a shift in the Brillouin frequency along the fiber (see equation 2.7) and therefore circumvents the build-up of a strong Stokes wave [31, 30]. The effect of applying strain to the fiber on the Brillouin threshold is shown in figure 2.20 d) with the inset showing the broadening of the Brillouin gain spectrum by the applied strain. Lastly it was theoretically predicted that Bragg gratings along a fiber are able to fully suppress SBS if the Stokes wave falls inside the stopband [29]. This approach was recently experimentally demonstrated in integrated waveguides (see chapter 5 and reference [33]). Besides being well known as a nuisance in telecommunication SBS also plays a crucial role for high-power lasers and amplifiers [28, 27]. Here similar techniques can be applied as described above.

Recently, it was shown that in waveguides with small cross-section the bulk elasto-optic effect and the moving boundary effect can completely cancel each other and hence suppress the SBS [34].

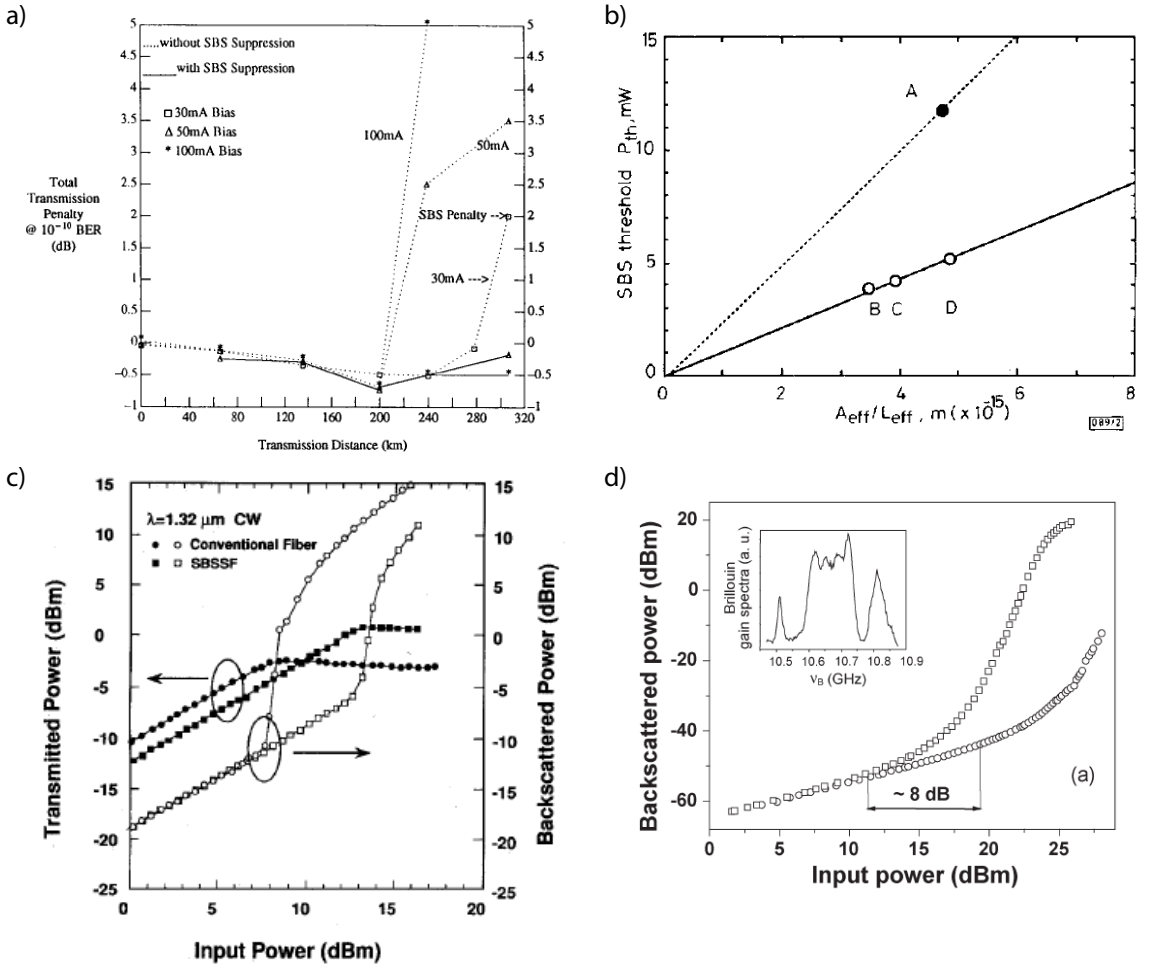

Fig. 2.20 a) Degradation of signal in transmission link due to SBS (dotted lines) compared to the case with SBS suppression using pump dithering [24]. b) Increased SBS threshold for fiber with non-uniform core radius (A). Point (B), (C) and (D) show a dispersion shifted fiber, pure silica core and non-dispersion shifted fiber, respectively [25]. c) Typical SBS threshold measurements for normal fiber and fiber with non-uniform doping concentration and increased SBS threshold [26]. d) Backscattered Stokes power for an unstrained fiber and a fiber with a linear strain. The by the strain broadened Brillouin gain spectrum is shown in the inset [30].

Chapter 3

Light interacting with acoustic waves - Stimulated Brillouin scattering

This chapter describes and derives the fundamental equations underlying the interaction between optical and acoustic waves. The chapter is divided into three parts: The first part starts with a description of propagating optical waves and optical waveguides and gives a short introduction into nonlinear optics. The second part describes acoustic waves and acoustic waveguides. The analogies to optics are emphasized whenever possible. The final part of the chapter couples optical and acoustic waves, providing the underlying equations for SBS.

3.1 Propagating optical fields

First, the propagation of optical waves is described. Therefore we start from Maxwell's equations and derive the optical wave equation. The here presented derivation is kept fairly compact, and the reader is referred to standard optics textbooks, such as [108, 183, 184], for a more detailed derivation.
The Maxwell equations describing electric and magnetic field vectors **E** and **H**, respectively, have the following form:

$$\nabla \cdot \mathbf{D} = \rho \tag{3.1}$$

$$\nabla \cdot \mathbf{B} = 0 \tag{3.2}$$

$$\nabla \times \mathbf{E} = -\frac{\partial \mathbf{B}}{\partial t} \tag{3.3}$$

$$\nabla \times \mathbf{H} = \frac{\partial \mathbf{D}}{\partial t} + \mathbf{J} \tag{3.4}$$

With the electric field vector **E** being connected with the electric displacement field **D** via the relation $\mathbf{D} = \varepsilon_0\mathbf{E} + \mathbf{P}$, where **P** is the polarization vector and ε_0 the vacuum permittivity. The magnetic auxiliary field vector **H** is connected with the magnetic field **B**, in the case of a nonmagnetic material, via $\mathbf{B} = \mu_0\mathbf{H}$, where μ_0 is the vacuum permeability. Furthermore the free charge density ρ and the free current density **J** were introduced in equation 3.1 and 3.4, respectively.
In all the relevant cases considered in this thesis we can assume the absence of any free charges and free currents, and hence $\mathbf{J} = 0$ and $\rho = 0$. To attain the first intuition for the propagation of optical waves, and optical waveguiding in general, we will also neglect the polarization vector **P** for now. However, we will see later that **P** plays a crucial role in the nonlinear optical response of a medium and the coupling between optical and acoustic waves.
The wave equation can be derived in a straightforward way from Maxwell's equations by taking the curl of equation 3.3 and inserting it in 3.4. After using the definitions given in the previous paragraph, the assumption of a uniform material so that $\nabla\mathbf{D} = 0$ implies that also $\nabla\mathbf{E} = 0$, and some basic calculus, one receives the wave equation for optical waves in free space:

$$-\nabla^2\mathbf{E} + \frac{1}{c^2}\frac{\partial^2\mathbf{E}}{\partial t^2} = 0 \tag{3.5}$$

with the speed of light c that is given by $c = (\varepsilon_0\mu_0)^{-1/2}$. Equation 3.5 describes the propagation of optical waves in free-space. A common solution to the wave equation are plane waves.

$$\mathbf{E}(x_\mathrm{i}, t) = \mathbf{E}_{0,\mathrm{j}} \cdot \exp\{i(k_\mathrm{i}x_\mathrm{i} + \omega t)\} \tag{3.6}$$

with the three space coordinates x_i, the amplitude vector $\mathbf{E}_{0,\mathrm{j}}$ with the different polarizations j, the wave-vector **k** (often simply referred to as "k-vector") and the frequency ω. After we know now how to describe the propagation of light, we will have a closer look at structures that guide light, i.e., optical waveguides.

3.1.1 Guided optical waves - an introduction to waveguides

Guiding light in waveguides can be seen as one of the biggest technological breakthroughs in the 20$^{\text{th}}$ century, today underpinning the Internet and any long-haul communication around the globe. Besides using optical fibers to send information over long distances, routing, controlling and manipulating light in integrated photonic circuits on chips is increasing steadily in importance.
In this section, the fundamentals of guiding optical waves is presented. The biggest difference to free-space propagating is that in a waveguide the optical waves are restrained in transverse

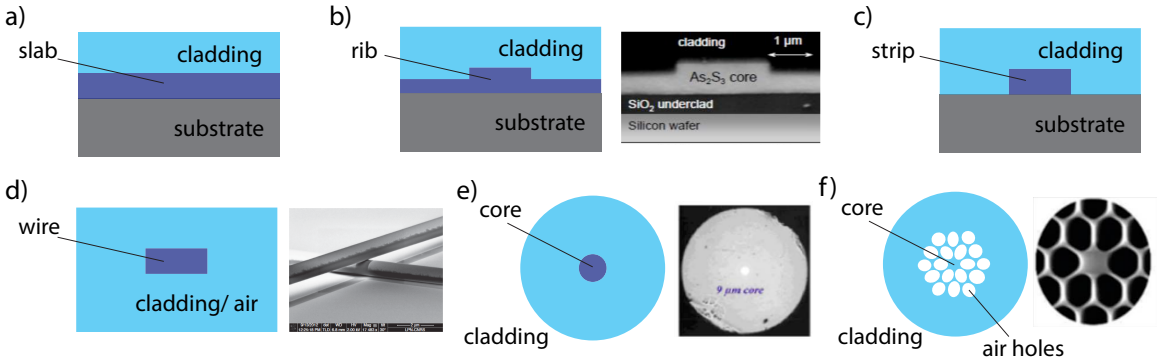

Fig. 3.1 a) Slab waveguide where the optical mode is confined in a plane of high index material. b) Rib waveguide with the optical mode confined in the high index material rib [75]. c) A strip waveguide. d) An optical wire that can be embedded or suspended in air [185]. e) An optical fiber most commonly made out of silica glass. The guidance is achieved by doping the fiber core to achieve a larger index (with the most common used dopant being Germanium). f) PCF, where the waveguide core is surrounded by air holes [50].

direction by the boundary conditions imposed by the waveguide geometry. These boundary conditions led to the concept of optical modes. A mode is defined by its transverse profile and a polarization direction and does not change along the waveguide (assuming there is no perturbation that induces coupling between separate modes). A few examples of common waveguides are shown in figure 3.1, a slab waveguide, a rib or ridge waveguide, a strip waveguide, an optical wire, the optical fiber (that is the most ubiquitous waveguide) and a PCF.

The waveguides shown in figure 3.1 are dielectric waveguides where guidance relies on total internal reflection. For a general dielectric waveguide the core is made out of a material with a higher refractive index than the cladding material. In the case of the optical fiber, which is the by far most common waveguide structure, this index contrast is achieved by doping the fiber core with germanium.

To introduce a few of the key terms, relations and definitions of guided wave optics it is convenient to look at the most simplistic case first, that is two reflecting plates in the xz-plane that confine an optical wave in the y-direction (see figure 3.2 a)). The intention of this section is to provide an intuition to waveguides and to provide the necessary nomenclature and background to understand SBS in waveguides. For a more detailed description of guided optics the reader is referred to standard textbooks such as e.g [183].

Let us start with considering an optical plane wave traveling between the two reflecting plates in the xz-plane shown in figure 3.2 a). From here one obtains in a straight forward manner the self-consistency condition given by the confinement of the optical wave in

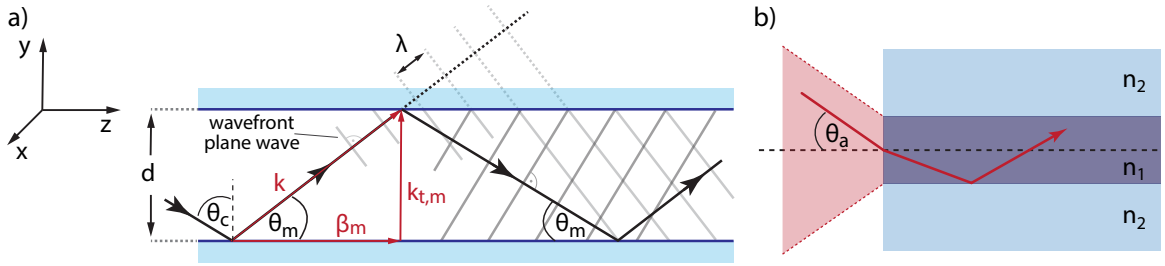

Fig. 3.2 a) Schematic of two reflecting plates in the xz-plane. b) Visualization of the NA and hence the acceptance angle when coupling into a waveguide.

y-direction [183]:

$$\sin\Theta_{\mathrm{m}} = m\frac{\lambda}{2d} \tag{3.7}$$

with the optical wavelength λ, the distance between the two reflecting plates d and the reflection angle Θ_{m} (compare figure 3.2 a)). The distinct modes are numbered using the integer m in equation 3.7. The name "self-consistency condition" arises from the fact that it ensures constructive interference between the incoming wave and the reflected wave in the guiding structure (including all phase shifts occurring on reflection).

Furthermore we see from figure 3.2 that the k-vector of the electro-magnetic plane wave can be separated in two components, the transverse vector $\mathbf{k}_{\mathrm{t,m}}$ and the propagation vector $\boldsymbol{\beta}_{\mathrm{m}}$, that points in z-direction (see figure 3.2a). The two quantities have the following form:

$$|\mathbf{k}_{\mathrm{t,m}}| = m\frac{\pi}{d} \tag{3.8}$$

$$|\boldsymbol{\beta}_{\mathrm{m}}|^2 = |\mathbf{k}|^2 - \frac{m^2\pi^2}{d^2} \tag{3.9}$$

In the case described so far, the optical wave is traveling in z-direction, confined in y-direction and with the electric field pointing in the x-direction; the optical waveguide mode is therefore referred to as a transverse electric (TE) mode. A very similar treatment applies for the case with the magnetic field in x-direction, which is commonly referred to as transverse magnetic (TM) mode.

The two reflecting plates approach gives a good intuition for optical waveguiding, however in reality optical waves are almost always guided in dielectric waveguides. Here a waveguide core is formed by a high index material and the optical wave is guided via total internal reflection at the interface between the high index material waveguide core and the lower index material cladding. The formalism to describe dielectric waveguides is quite analogue to the description given in the previous paragraphs. The guiding is still based on reflection, with the main difference being that the reflected wave not necessarily experiences a π phase

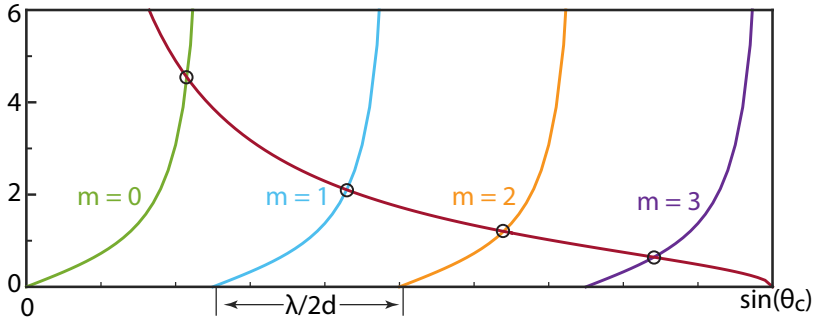

Fig. 3.3 Right- and left-hand-side of self-consistency condition for a dielectric waveguide. The waveguide modes are given by the intersection points.

shift but a phase shift φ that depends on the angle and polarization of the electro-magnetic wave. As a consequence the self-consistency condition 3.7 is modified (here given for a TE mode) [183]:

$$\tan\left(\pi\frac{d}{\lambda}\sin\Theta - m\frac{\pi}{2}\right) = \left(\frac{\sin^2\Theta_c}{\sin^2\Theta} - 1\right)^{1/2} \tag{3.10}$$

where Θ_c is the critical angle. A plot of equation 3.10 is shown in figure 3.3 assuming a wavelength λ of 1.55 µm and a waveguide height d of 3 µm. As one can see in figure 3.3 several optical modes fulfill the self-consistency condition 3.10 (intersection points in the graph). In this case the waveguide is considered a multi-mode waveguide for the considered wavelength.

After describing the guiding mechanism one has also to consider how to couple light into the guiding structure. There is a maximum acceptance angle Θ_a under which light is coupled into the waveguide (see figure 3.2 b)). The sinus of this angle is known as the numerical aperture (NA). From straightforward geometric considerations, one finds that the numerical aperture (NA) can be simply written as the difference in terms of the refractive index of the waveguide core n_1 and the cladding n_2. The relationship has the following form:

$$\sin\Theta_a = NA = \sqrt{n_1^2 - n_2^2} \tag{3.11}$$

When coupling light into a waveguide one has not only to consider the maximum acceptance angle Θ_a but also ensure that all external fields match the field of the guided mode at all boundaries. This requirement is termed ”mode matching”. Hence a description of the transverse mode field in the waveguide is required. To describe the propagation of optical fields in a waveguide we start from the wave-equation 3.5. As an ansatz to solve said equation we separate the variables of the optical field in a transverse electric field components **E**(x,y)

and a propagating plane wave in z-direction:

$$\mathbf{E}(x,y,z,t) = \mathbf{E}(x,y) \cdot \exp\{i(\beta_{\mathrm{m}} z + \omega t)\} \tag{3.12}$$

Here β_{m} is the z-component of the propagation vector $\boldsymbol{\beta}_{\mathrm{m}}$ we introduced earlier. Inserting the ansatz 3.12 into the wave equation 3.5 leads to the following equation, which is known as the Helmholtz equation:

$$\left(\nabla^2 - \beta_{\mathrm{m}}^2 + n_2^2 \frac{\omega^2}{c^2}\right)\mathbf{E}(x,y) = 0 \Rightarrow \left(\nabla^2 - \gamma_{\mathrm{m}}^2\right)\mathbf{E}(x,y) = 0 \tag{3.13}$$

Here we introduced:

$$\gamma_{\mathrm{m}}^2 = \beta_{\mathrm{m}}^2 - n_2^2 \frac{\omega^2}{c^2} = \beta_{\mathrm{m}}^2 - n_2^2 k_0^2 \tag{3.14}$$

For guided modes we find: $\beta_{\mathrm{m}} > n_2 k_0$ and hence $\gamma_{\mathrm{m}}^2 > 0$. Consequentially, this solution of equation 3.13 is proportional to an exponential decay $\propto \exp(-\gamma_{\mathrm{m}}(x+y))$ in the cladding region. In other words, the optical mode is guided inside the waveguide core with exponentially decaying evanescent components in the cladding.

3.1.2 Nonlinear optics

So far we have not considered the response of the waveguide medium to the electric field, which we will now introduce and include in our description. The key parameter to consider is the polarization vector **P** that is related to the electric field **E** and the displacemt field **D** via $\mathbf{P} = \mathbf{D} - \varepsilon_0 \mathbf{E}$.
For large intensities this polarization vector starts to depend in a nonlinear way on the electric field vector **E**. It is often convenient to separate **P** in a linear and a nonlinear part:

$$\mathbf{P} = \mathbf{P}^{\mathrm{L}} + \mathbf{P}^{\mathrm{NL}} \tag{3.15}$$

with $\mathbf{P}^{\mathrm{L}}$ depending linearly on the electric field and $\mathbf{P}^{\mathrm{NL}}$ describing the nonlinear response of the medium. Taking into account the polarization **P** we can derive the wave equation in an analogue way to the previous derivation and receive:

$$-\nabla^2 \mathbf{E} + \frac{1}{c^2}\frac{\partial^2 \mathbf{E}}{\partial t^2} = -\frac{1}{\varepsilon_0 c^2}\frac{\partial^2 \mathbf{P}}{\partial t^2} \tag{3.16}$$

This version of the wave equation has an additional term on the right hand side, that includes the polarization **P**. This term can be identified as a driving term. This driving term becomes

important later when we introduce coupling between optical and acoustic waves. Before describing this coupling in more detail we will have a closer look at the polarization term **P** in general as it is the crucial quantity to describe nonlinear optical effects.
The induced polarization **P** is connected to the electric field **E** via the following relation:

$$\mathbf{P}(t) = \varepsilon_0 \chi^{(1)} \mathbf{E}(t) \tag{3.17}$$

where $\chi^{(1)}$ is the (linear) susceptibility. However, this model can be extended to also capture the *nonlinear* response of the material. Therefore one can express the polarization term in a power series of the electric **E**:

$$\mathbf{P}(t) = \varepsilon_0 (\chi^{(1)} \mathbf{E}(t) + \chi^{(2)} \mathbf{E}^2(t) + \chi^{(3)} \mathbf{E}^3(t) + ...) \tag{3.18}$$

Here we introduced the second and third order susceptibilities $\chi^{(2)}$ and $\chi^{(3)}$, respectively. Nonlinear effects are usually categorized by the order of the proportionality of the electric field or susceptibility. Typical second order or $\chi^{(2)}$ nonlinear effects are second harmonic, sum- and difference frequency generation. Due to the symmetry of the underlying potential, second order nonlinearities only occur in non-centro symmetric materials (e.g. Lithium niobate ($LiNbO_3$)) and are not present in amorphous waveguides as e.g. silica or chalcogenide. Typical third order nonlinear effects are third harmonic generation, 4WM, Kerr lensing and stimulated Raman and stimulated Brillouin scattering.

3.2 Propagating acoustic waves

This section introduces acoustic waves and waveguides (in analogy to the in the previous chapter described description for optical waves). However, first we need to introduce a few key terms to describe mechanical waves in a continuum description. Again the purpose of this chapter is to provide enough background to the reader to understand the underlying physics of SBS. For a more detailed description of acoustic waves the reader is referred to the standard textbooks, such as e.g. [186, 187].

3.2.1 Stress, strain and Hooke's law

In this section we introduce some of the fundamental terms used to describe mechanical interactions in a medium using a continuum dynamic description. The two key properties that are introduced are the stress σ and the strain η. Both quantities are usually a tensor and are connected via the elasticity of the medium. This linear relationship is known as

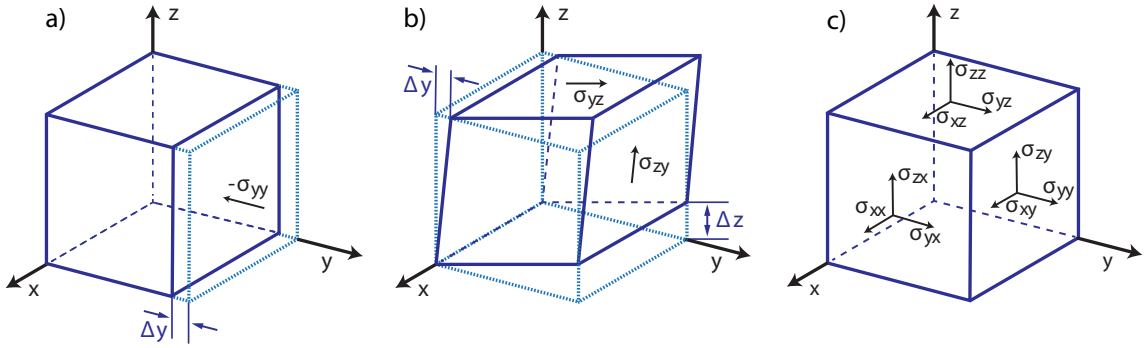

Fig. 3.4 a) Stress acting in y-direction inducing stress/compression of the medium [188]. b) Stress acting in yz- and zy-direction causing a shear deformation of the medium [188]. c) Schematic of the different components of the stress tensor depicted on the surface of the body [188].

the generalized Hooke's law as it resembles the 1-dimensional Hooke's law where a force (action) is connected to a displacement (reaction). The stress σ is the force acting on an area of a solid body. A schematic visualization of the stress tensor σ_{ik} is shown in figure 3.4. The indices of the stress tensor indicate the direction of the force and the plane in the body it acts upon.

The induced stress on a body leads to a deformation of the later which is described by the strain tensor. To get an intuitive understanding of the strain tensor, let us assume two points of a solid body separated by the distance dl. This distance dl between the two points in the medium is changed by the stress and is then given by a new distance dl'. In a 3-dimensional coordinate system (x_1, x_2, x_3) the distance between two points can be written in the following form:

$$dl = \sqrt{{dx_1}^2 + {dx_2}^2 + {dx_3}^2} \longrightarrow dl' = \sqrt{{dx_1'}^2 + {dx_2'}^2 + {dx_3'}^2} \tag{3.19}$$

where the dx_i and dx_1' are the coordinates before and after the deformation. In other words the original coordinates were moved by a distance which we will call the displacements u_i. Hence we can express the new coordinates dx_1' in terms of the displacement u_i leading to the relationship $dx_i' = dx_i + \frac{\partial u_i}{\partial x_k} dx_k$. Inserting this relationship in equation 3.19 leads to:

$$dl'^2 = dl^2 + \left(\frac{\partial u_i}{\partial x_k} + \frac{\partial u_k}{\partial x_i} + \frac{\partial^2 u_l}{\partial x_i \partial x_k} \right) \cdot dx_i dx_k =: dl^2 + 2 \cdot \eta_{ik} \cdot dx_i dx_k \tag{3.20}$$

Equation 3.20 is used to define the strain tensor η_{ik} which describes how a body deforms in three dimensions when a force is applied. If the displacement u_i are small relative to the

distance between the lattice points itself the second order derivatives in 3.20 are negligible and the linearized strain tensor is given by:

$$\eta_{ik} = \frac{1}{2}\left(\frac{\partial u_i}{\partial x_k} + \frac{\partial u_k}{\partial x_i}\right) \tag{3.21}$$

With these considerations we can now write the generalized Hooke's law in vectorial form:

$$\sigma_{ik} = C_{iklm}\eta_{lm} \tag{3.22}$$

connecting the stress and the strain tensor with the elasticity tensor of the material C_{iklm}.

3.2.2 The acoustic wave equation

In analogy to the description of propagating optical waves and optical waveguides, we start our description of acoustics with the wave equation for acoustic waves. The wave equation for acoustic waves can be formulated in terms of the previously described stress σ or the displacements u_i. However, here we want to focus on longitudinal acoustic waves traveling through a medium. As shown in figure 3.4a) a longitudinal displacement changes the density of the medium (as opposed to, e.g., shear waves). Hence we can describe the longitudinal acoustic wave in terms of a spatially and temporally varying density ρ. This description of the acoustic wave as a traveling density wave leads to an intuitive way of coupling an acoustic wave to an optical wave, which will be described in the later this chapter. The acoustic wave equation for a longitudinal density wave has the following form:

$$-\nabla^2\rho + \frac{1}{v_a^2}\frac{\partial^2\rho}{\partial t^2} = 0 \tag{3.23}$$

with the longitudinal acoustic velocity v_a. As we have seen previously a common solution of the wave equation are plane waves. In the following section, we will have a look at the boundary conditions these plane waves have to fulfill in an acoustic waveguide.

3.2.3 Acoustic waveguides

This section serves to provide the reader some intuition how to guide acoustic waves in waveguides and what requirements need to be fulfilled to provide acoustic guidance. Here the analogies to optical waveguides are emphasized. As we will see in the next section, where optical and acoustic waves are coupled together, it is crucial for the strength of this interaction to guide both, the acoustic and the optical waves, simultaneously in the waveguide

core.
In analogy to optical waveguides, we start the description from the wave equation. Considering a waveguide aligned with the z-axis of a coordinate system. We now separate the density $\rho(x,y,z,t)$ into a transverse field in the xy-plane and a plane wave propagating in the z direction.

$$\rho(x,y,z,t) = \rho(x,y) \cdot \exp\{(i(q_z z + \Omega t)\} \tag{3.24}$$

with the z component q_z of the acoustic wavevector $\mathbf{q}$ and the frequency of the acoustic wave Ω. We are now interested in the boundary conditions required in the xy-plane to form a guided acoustic mode. Therefore we insert our ansatz 3.24 in the wave equation 3.23 and receive the following relationship:

$$\left(\nabla^2 - q_z^2 + \frac{\Omega^2}{v_{a_{1,2}}^2}\right)\rho(x,y) = 0 \tag{3.25}$$

Furthermore the longitudinal sound velocity of the waveguide core v_{a_1} and the surrounding material v_{a_2} are introduced.
The transverse density profile has to satisfy the following boundary conditions. The first condition requires the continuity of the z-component of the displacement field, hence the density variation, and the second condition requires the continuity of the stress tensor at the boundary between the waveguide and the cladding [109].

$$\rho|_{\partial C^+} = \rho|_{\partial C^-} \tag{3.26}$$

Here ∂C is the interface between the waveguide core and the surrounding material. The boundary condition for the normal components of the stress tensor has the following form [109]:

$$\mu_1 \frac{\partial \rho}{\partial n}|_{\partial C^+} = \mu_2 \frac{\partial \rho}{\partial n}|_{\partial C^-} \tag{3.27}$$

with $\mu_{1,2}$ being the shear modulus of the waveguide core and cladding, respectively.
The different acoustic properties of the core and the surrounding hence lead to an impedance mismatch. Therefore acoustic waves reflect from the interface and can be guided analog to optical waves. The acoustic impedance is given by [109]:

$$R = \frac{Z_2/(\mu_2\rho_2) - Z_1/(\mu_1\rho_1)}{Z_2/(\mu_2\rho_2) + Z_1/(\mu_1\rho_1)} \tag{3.28}$$

with $Z_{1,2} = \rho_{1,2} v_{1,2}/\cos\Theta_{1,2}$, where $\Theta_{1,2}$ is the incidence and reflection angle of the acoustic mode, respectively.

Here, pure longitudinal waves are assumed as it is the case for large core waveguides where boundary effects only play a negligible role. Hence there is no coupling at the boundary from longitudinal to shear waves and the main acoustic mode in the waveguide is a compression mode. In analogy to optical waveguides an acoustic V_{ac} parameter can be defined (here for a circular waveguide with a radius r that is much larger than the acoustic wavelength) [109]:

$$V_{\mathrm{ac}} = \Omega r \sqrt{\frac{1}{v_{\mathrm{a}_1}^2} - \frac{1}{v_{\mathrm{a}_2}^2}} \tag{3.29}$$

One can see from the acoustic V-parameter that the longitudinal sound velocity plays the same role as c/n in optical waveguides. Hence the acoustic waveguide needs to be designed in a way that the longitudinal sound velocity in the core is lower than the surrounding cladding. The chalcogenide waveguides investigated in this thesis surrounded with a silica cladding fulfill these requirements. Note: in acoustics, the sound velocity in a medium is usually higher than in air, and hence it is the opposite situation to optical waves where the refractive index of air is approximately 1. However, hypersound waves, e.g., in suspended silicon waveguides surrounded by air are still guided in the waveguide. The reason lies in the large impedance mismatch between the silicon waveguide and the surrounding air (see equation 3.28). The sound velocity in silicon is more than an order of magnitude larger than in air.

3.3 Coupling optical and acoustic waves - stimulated Brillouin scattering

After describing the propagation of optical and acoustic waves separately in the previous sections, we now bring them together introducing a coupling between the two types of waves. This description will lead to the coupled mode equations that describe SBS. We will see that the electric field will act as a driving term for the acoustic wave. At the same time that the acoustic wave will back-act on the optical waves, connecting the pump and Stokes wave. Again as described in the introduction 2.2 we see the two-fold nature of SBS - light acting on sound and sound back-acting on light. Hence our theoretical description will lead to three coupled mode equations, one for the optical pump, one for the optical Stokes wave and one for the acoustic wave.

As the focus of this thesis lies on SBS in photonic-phononic waveguides, we will derive the coupled equations using modes instead of just traveling acoustic and optical plane waves in free space. A crucial property of this description is the overlap of the optical and acoustic

modes. This overlap integral determines how strong the SBS interaction will be in a given waveguide and plays an important role in the design of photonic-phononic waveguides.
This chapter focuses on providing the basic understanding of the coupling between optical and acoustic waves; for a more detailed derivation of the SBS coupled mode equations the reader is referred to [108, 184, 107].

We start our description from the acoustic wave equation 3.23, however here we introduce two additional terms: first we add a (generic) driving term $-\nabla f$ to the right hand side of the equation and second we introduce an acoustic loss / damping term $\Gamma\nabla^2\frac{\partial\rho}{\partial t}$. The driving term provides the coupling to the optical waves. The damping constant Γ, on the other hand, is important to determine the linewidth of the Brillouin interaction. The driven acoustic wave equation with damping has the following form [108]:

$$\frac{\partial^2\rho}{\partial t^2} - \Gamma\nabla^2\frac{\partial\rho}{\partial t} - v_a^2\nabla^2\rho = \nabla f \tag{3.30}$$

The driving term is given by the force per unit volume f generated by the optical wave that changes the density ρ. We now have a closer look at this driving term to understand its origin and connect it to the electric field.
In a microscopic picture the electric field acts on the dipole moments $p_{\text{dip}} = \varepsilon_0\alpha E$ in the material, with α being the polarizability. Hence the electric field leads to a polarization in the material, which is associated with a change in the potential energy U. The underlying optical force F associated with the change in energy can be calculated via [108]:

$$F = -\nabla U = \nabla\int_0^E p_{\text{dip}}dE' = \frac{1}{2}\varepsilon_0\alpha\nabla(E^2) \tag{3.31}$$

In a macroscopic picture this force causes a change in the dielectric constant $\Delta\varepsilon$ due to a pressure p induced by the optical wave. This process is known as electrostriction, i.e. an optical field causes a change in the material density accompanied with a change in the dielectric function of the material [108].

$$\Delta\varepsilon = \frac{\partial\varepsilon}{\partial\rho}\Delta\rho \tag{3.32}$$

A change in the dielectric constant, however also changes the potential energy U in the system:

$$\Delta U = \frac{1}{2}\varepsilon_0\Delta\varepsilon E^2 \tag{3.33}$$

This change in the potential energy must be equal to the work W on the system. This consideration allows us to relate the change in the dielectric constant to an optically induced pressure p from which we receive the drive term in the wave-equation 3.30.

$$\Delta W = p\frac{\Delta V}{V} = -p\frac{\Delta\rho}{\rho} \stackrel{!}{=} \Delta U = \frac{1}{2}\varepsilon_0\Delta\varepsilon E^2 = \frac{1}{2}\varepsilon_0\frac{\partial\varepsilon}{\partial\rho}\Delta\rho E^2 \tag{3.34}$$

$$\Rightarrow p = -\frac{1}{2}\varepsilon_0\gamma_e E^2, \tag{3.35}$$

with the electrostrictive constant $\gamma_e = \rho(\frac{\partial\varepsilon}{\partial\rho})$. As the force per volume f on the right hand side of equation 3.30 is simply given by $f = \nabla p$ [108] we now have an impression for the driven acoustic wave equation with the electric field as a source term [108]:

$$\frac{\partial^2\rho}{\partial t^2} - \Gamma\nabla^2\frac{\partial\rho}{\partial t} - v_a^2\nabla^2\rho = -\frac{1}{2}\gamma_e\nabla^2 E^2 \tag{3.36}$$

The most common approach to solve the driven wave-equation is a simple plane wave approximation. However, as we want to investigate the interaction of optical and acoustic waves in waveguides, we use a slightly modified approach based on optical and acoustic modes (a detailed derivation using this approach can be found in [107]). This approach will naturally provide the overlap integral between said modes, which is crucial for SBS in guiding structures.
We use the following ansatz for the electric field $\mathbf{E}$ and the density ρ, respectively:

$$\mathbf{E}(r,z,t) = \frac{1}{2}f(r)(A_1(z,t)e^{i(\omega_1 t-\beta_1 z)}\mathbf{u}_1 + A_2(z,t)e^{i(\omega_2 t+\beta_2 z)}\mathbf{u}_2) + c.c. \tag{3.37}$$

$$\rho(r,z,t) = \frac{1}{2}\xi(r)Q_1(z,t)e^{i(\Omega t-qz)} + c.c. \tag{3.38}$$

For the electric field we assume forward and backward traveling waves in the direction of the unit vectors $\mathbf{u}_1$ and $\mathbf{u}_2$ and introduced also the envelopes A_i of the optical field and the mode profile $f(r)$. The acoustic wave has formally a very similar structure, consisting of an envelope Q and a mode profile $\xi(r)$. Compared to the approach described in [107] we assume only one acoustic mode, however the same approach can be straightforwardly extended to multiple acoustic modes that can be summed up in a linear combination (Note that the acoustic modes are technically only approximately orthogonal to each other.).
Inserting our ansatz for the optical and acoustic waves in the driven acoustic wave equation 3.36 we can derive an expression for the acoustic amplitude Q. Here several assumptions can reduce the amount of significant terms:

- First we assume a slowly-varying envelope approximation for the optical and the acoustic mode and hence can discard higher order derivatives.
- Second we only keep the phase matched terms $\Omega = \omega_1 - \omega_2$. We only want to consider the case of backward SBS here, hence we only keep terms with propagation constant q approximately twice the optical propagation constant $q = \beta_1 + \beta_2 \approx 2\beta_1$ (compare chapter 2.2).
- Furthermore we assume that the propagation of the acoustic mode is negligible due to the strong damping which allows to neglect the term proportional to $\frac{\partial \rho}{\partial z}$.
- Finally we assume a steady state and hence neglect the time dependent derivatives.

With all the above approximations we end up with the following equation:

$$i\xi(r)\,Q q^2\,\Omega\Gamma - Q v_\mathrm{a}^2\left[\nabla^2\xi(r) + \left(\frac{\Omega^2}{v_\mathrm{a}^2} - q^2\right)\xi(r)\right] = \frac{1}{2}\gamma_\mathrm{e} f^2(r) q^2 A_1 A_2^* \tag{3.39}$$

If we now assume that neither the presence of the optical field, i.e. the right hand side of equation 3.39, nor the acoustic damping term, i.e. first term on the left proportional to Γ, alter the structure of the acoustic mode itself, we can use the modal equation (see also equation 3.13) to find the optical modes with the eigenfrequencies Ω_B:

$$\nabla^2\xi(r) + \left(\frac{\Omega_\mathrm{B}^2}{v_\mathrm{a}^2} - q^2\right)\xi(r) = 0 \tag{3.40}$$

using the modal equation 3.40 we can further simplify the acoustic wave equation 3.39 and get:

$$i\xi(r)\,Q q^2\,\Omega\Gamma - Q\,\xi(r)\,(\Omega^2 - \Omega_\mathrm{B}^2) = \frac{1}{2}\gamma_e f^2(r) q^2 A_1 A_2^* \tag{3.41}$$

From here we finally get an expression for the amplitude Q of the acoustic wave. We multiply both sides of the equation with the mode profile ξ and integrate over the transverse plane. This is required as we have separated the variables in longitudinal and transverse components in our initial ansatz 3.37 and 3.38. We receive the following expression for the acoustic wave amplitude [107]:

$$Q(z,t) = \frac{\gamma_\mathrm{e} q^2 A_1(z,t) A_2^*(z,t)}{2(\Omega_\mathrm{B}^2 - \Omega^2 + i\Omega\Gamma q^2)} \frac{\langle \xi(r) f^2(r)\rangle}{\langle \xi^2(r)\rangle} \tag{3.42}$$

The last term in 3.42 is the overlap integral between the acoustic and the optical modes. The angle brackets denote an integration over the transverse plane.

We described how an optical mode drives an acoustic mode in a waveguide and received an expression for the acoustic wave amplitude depending on the electric fields and the mode overlap between the acoustic and the optical mode.
Now we want to examine the effect of the acoustic mode on the optical waves. We start with the optical wave equation derived in section 3.1 but again including a driving term in analogy to the previous treatment of the acoustic wave. However, there is no optical loss term included as the optical losses are negligible compared to the acoustic losses. For a treatment of SBS in lossy waveguides, a loss term can be added in a straightforward manner. The driven optical wave equation has the following form:

$$-\nabla^2\mathbf{E}+\frac{1}{c^2}\frac{\partial^2\mathbf{E}}{\partial t^2}=-\frac{1}{\varepsilon_0 c^2}\frac{\partial^2\mathbf{P}}{\partial t^2} \tag{3.43}$$

The polarization **P** acts as the driving term on the right-hand side of equation 3.43 and can be linked to the electric field via the susceptibility χ (see section 3.1.2). Here, we consider a change in the dielectric constant of the medium due to the presence of the acoustic wave. Hence we write the polarization **P** in the following form:

$$\mathbf{P}=\varepsilon_0\Delta\chi\mathbf{E}=\varepsilon_0\Delta\varepsilon\mathbf{E}=\varepsilon_0\frac{\gamma_e}{\rho_0}\Delta\rho\mathbf{E} \tag{3.44}$$

Hence a change in the density is now linked to the optical wave in the form of a driving term in the wave equation. This approach will lead us to the coupled mode equations for SBS. These equations can be categorized in steady state equations and dynamic equations which will be described in the following two sections.

Steady state coupled SBS equations

In this paragraph, the steady state coupled equations are given which provide critical insights in the exponential build-up of the Stokes waves and key parameters such as the Brillouin gain linewidth.

Again we use the ansatz 3.37 for the electric field but this time insert it in the optical wave equation 3.43. As in the previous section several assumptions are made to reduce the amount of relevant terms. The slowly varying envelope approximation is applied again to remove any higher order derivatives. Furthermore it is assumed that the change in the dielectric function is small and also approximately the same for the optical pump and Stokes wave. The optical fields are assumed to be monochromatic and the polarization is maintained, which allows the use of a scalar approximation. Lastly we assume a steady state which removes the temporal

derivatives. This leads us to the two coupled envelope equations:

$$\frac{dA_1}{dz} = -i\,\zeta\,A_1\,|A_2|^2 \tag{3.45}$$

$$\frac{dA_2}{dz} = +i\,\zeta^*\,A_2\,|A_1|^2 \tag{3.46}$$

with

$$\zeta = \frac{n^9 \varepsilon_0 p_{12}^2 \omega^3}{2\rho_0 c^3(\Omega_B^2 - \Omega^2 + i\Omega\Gamma)} \frac{\langle \xi(r) f^2(r)\rangle^2}{\langle \xi^2(r)\rangle\langle f^2(r)\rangle} \tag{3.47}$$

Here we used the electrostrictive tensor p_{12} that is connected to the electrostriction constant γ_e via $\gamma_e = n^4\varepsilon_0 p_{12}$.
The two coupled equations 3.45 and 3.46 describe the evolution of the optical field envelopes. However, the more intuitive description - in particular from an experimentalist point of view - is a description based on optical power P. The envelopes of the electric field are linked to the power P via [107]:

$$P = \langle I\rangle = \frac{1}{2}\varepsilon_0\, c\, n |A|^2 \langle f^2(r)\rangle \tag{3.48}$$

And hence one receives the coupled mode equations for the optical power (for the case of low optical loss waveguides) [107]:

$$\frac{dP_1}{dz} = -gP_1P_2 \tag{3.49}$$

$$\frac{dP_2}{dz} = -gP_1P_2 \tag{3.50}$$

Here we use the Brillouin coupling parameter g that is given by:

$$g = \frac{g_B\, L(\omega)}{A_{\text{eff}}^{\text{ao}}}, \tag{3.51}$$

where $L(\omega)$ gives the Lorentzian lineshape of the Brillouin gain spectrum with the full-width-of-half-maximum Γ_B given by:

$$\Gamma_B = \frac{8\pi n^2 \Gamma}{\lambda_p^2} \tag{3.52}$$

The Brillouin gain coefficient g_B is given by (see also 2.2):

$$g_B == \frac{4\ \pi\ n^8\ p_{12}^2}{\lambda_p^3\ c\ \rho_0\ \Omega_B\ \Gamma_B} \tag{3.53}$$

And the effective acousto-optic area $A_{\text{eff}}^{\text{ao}}$, which is given by [107]:

$$A_{\text{eff}}^{\text{ao}} = \left(\frac{\langle f^2(r) \rangle}{\langle \xi(r) f^2(r) \rangle} \right)^2 \langle \xi^2(r) \rangle \tag{3.54}$$

As one can see from equation 3.49 and 3.50 SBS leads to an exponential power build-up of a small Stokes seed, as already described in the section about the fundamental properties of SBS 2.2. The steady state description can provide valuable insights in the SBS process, however cannot describe the temporal dynamics of the effect, that will be described in the next section.

Dynamic coupled SBS equations

Here the dynamical SBS coupled mode equations are provided. The derivation is done in a very similar fashion than in the previous section, with the difference that additional to the first order spatial derivatives of the optical wave also the first order time derivatives are kept. For the acoustic wave the first order time derivative is kept as well, however the first order spatial derivatives are still negligible due to the short lifetime (in the order of nanoseconds) and the low velocity (below a few thousand m/s) of the acoustic wave that leads to negligible spatial movement of the acoustic wave. This approach leads to three partial differential equations that are coupled together - one for the optical pump wave, one for the optical Stokes wave and one for the acoustic wave.
The equation for an acoustic wave propagating in z-direction has the following form [189, 132]:

$$\frac{\partial}{\partial t} Q = \frac{\Gamma_{\text{B}}}{2} (A_1 A_2^* - Q) \tag{3.55}$$

Here we assumed that the optical pump wave A_1, the optical Stokes wave A_2 and the acoustic wave Q are phase matched. For not perfect phase matching one would require introducing a complex term proportional to the frequency detuning and Q in the equation.
For the optical pump wave we receive the following equation [189, 132]:

$$\frac{\partial}{\partial z} A_1 + \frac{n}{c} \frac{\partial}{\partial t} A_1 = -\frac{g_B}{2A_{\text{eff}}^{\text{ao}}} A_2 Q \tag{3.56}$$

And the optical Stokes wave is given by:

$$-\frac{\partial}{\partial z} A_2 + \frac{n}{c} \frac{\partial}{\partial t} A_2 = \frac{g_B}{2A_{\text{eff}}^{\text{ao}}} A_1 Q^* \tag{3.57}$$

These are the three coupled mode equations for SBS. Here we neglected the optical loss which can be introduced in the equations in a straightforward manner using the loss coefficient α, adding a term $-\frac{\alpha}{2}A_{1,2}$ to the right-hand side of the optical equations. Furthermore, other nonlinear effects such as self-phase modulation (SPM) and cross-phase modulation (XPM) were ignored in the derivation as the emphasis was put on the coupling mechanism of optical and acoustic modes. As we have seen in the section about nonlinear optics, SPM and XPM arise from the nonlinear polarizability of a medium. Taking these additional nonlinear terms into account during the derivation one ends up with the following additional term on the right hand side of the optical equations [108]: $i\gamma(|A_{1,2}|^2+2|A_{2,1}|^2)A_{1,2}$, with the nonlinear coefficient γ.

Vectorial description of Brillouin interactions

The previous sections describe the coupling between optical and acoustic modes via electrostriction and the photo-elastic effect. Both effects are known as bulk effects and are sufficient to describe SBS in standard single mode fiber or chalcogenide waveguides with a cross-section large compared to the wavelength in the material. However, for small ($<\lambda/n$) high index contrast waveguides, such as e.g. silicon nanowires, additional effects from the waveguide boundaries have to be considered; hence a fully vectorial description of the Brillouin interaction is required. However, as the scalar description given in the previous section is sufficient to understand and describe SBS in the chalcogenide waveguides investigated in this thesis, the description of the vectorial model of SBS is kept short and the reader is referred to the literature for a more in-depth description [190, 67, 191, 34].

Initial theoretical studies of SBS in small core, high index contrast waveguides predicted a large enhancement of the SBS gain that would allow harnessing SBS in silicon [67]. The large SBS gain enhancement can be assigned to the small mode area and the additional radiation pressure forces at the waveguide boundaries. The description presented in this work was approaching the SBS interaction not in terms of an overlap integral (as described section 3.3) but from the perspective of the induced optical forces that create the acoustic wave, where the overall force consists of bulk terms and boundary terms that originate from radiation pressure. The total optical force determines the generation rate of the acoustic phonons, which, due to particle conservation, is equal to the Stokes photon generation rate. Hence, the Brillouin gain can be inferred from solely knowing the optical forces in the waveguide.

The vectorial treatment of SBS can also be derived in an analog framework as described in section 3.3; namely starting from the optical and acoustic wave-equation and introducing a coupling of the two types of waves via an overlap integral but including now bulk and boundary terms [191]. In this case, the optical wave is acting on the acoustic wave not only via electrostriction but also via radiation pressure. The acoustic wave acts back on the optical mode, on the other hand, via the photoelastic effect and the effect of an index change caused by the moving boundaries, which is also known as moving boundary scattering [191]. A schematic visualization of these effects is shown in figure 3.5 a). The photoelastic effect causes a small change in the electric field but over a relatively large area. The moving boundary effect, on the other hand, causes a large change of the field over a small area at the waveguide surface and hence can be calculated using a contour integral instead of an integration over the whole waveguide cross-section. It also means that the moving boundary contribution becomes more relevant as the cross-section of the waveguide decreases.

In the following a short description of this treatment of the nonlinear interaction is given following the article by Wolff et al. [191]. The basic derivation of the SBS interaction using a vectorial description is similar to the scalar case, with the main difference, however, lying in the description of the acoustic mode and the overlap integrals between the optical and the acoustic modes. In the vectorial description we write the acoustic wave equation in terms of the displacement field $\mathbf{U}$ instead of the previously used (scalar) density variation. The vectorial acoustic wave equation reads the following [191]:

$$-\rho\,\partial_t^2 U_i + \sum_{jkl} \partial_j [c_{ijkl} + \Upsilon_{ijkl}] \partial_k U_l = -F_i \tag{3.58}$$

Here, ρ is the density of the material, c_{ijkl} is the stiffness tensor and Υ_{ijkl} is the viscosity tensor, which is related to the acoustic damping that will determine the linewidth of the Brillouin interaction. As before, a driving term is introduced on the right hand side, which is in equation 3.58 the force field per volume F_i. This source term couples the acoustic wave to the optical field.

Using equation 3.58 one can derive, in a similar manner as outlined in section 3.3, coupled mode equations for the optical pump and the Stokes wave. The overlap integrals, however, are now fully vectorial including photoelastic and moving boundary components. The overlap integral for the photoelastic part reads [191]:

$$O_v^{\mathrm{PE}} = \varepsilon_0 \int_A d^2 r \sum_{ijkl} \varepsilon_r^2 [e_i^{(1)}]^* e_j^{(2)} p_{ijkl} \partial_k u_l^* \tag{3.59}$$

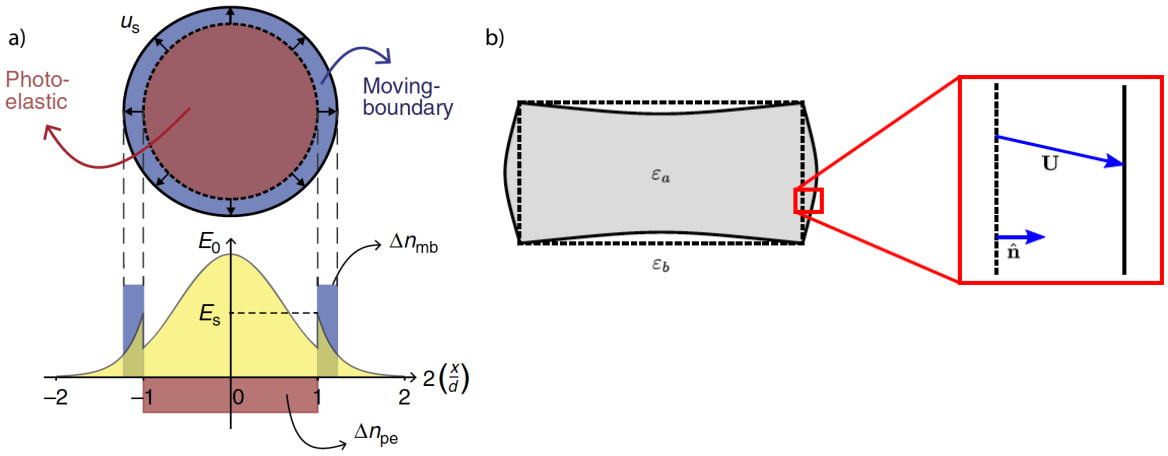

Fig. 3.5 a) Schematic visualization of SBS bulk and boundary effects [34]. b) Schematic of the moving boundary effect [191].

with the photoelastic tensor p_{ijkl}, the dielectric constant ε_r, and the electrical fields $e_i^{(1)}$ and $e_j^{(2)}$ of the phase-matched pump and Stokes fields, respectively.

We now want to describe the contribution of the moving boundaries of a waveguide to the SBS interaction. For illustration, we assume a rectangular nanowire with dielectric constant ε_a and a surrounding with a permittivity ε_b (in many cases the surrounding is air in which ε_b is approximately 1). Hence at the interface of the waveguide there is a contrast in permittivity and Maxwell equations dictate that the normal component of the **D** field and the transverse (in plane) component of the **E** field are continuous across the interface. If the interface moves, the **E** and **D** field have to change from their static value ($\mathbf{E}^\mathrm{static}$ and $\mathbf{D}^\mathrm{static}$) before the movement of the boundaries to the state of the moved boundary ($\mathbf{E}^\mathrm{mb}$ and $\mathbf{D}^\mathrm{mb}$):

$$\mathbf{E}^\mathrm{static} = \mathbf{E}_\parallel + \varepsilon_\mathrm{b}^{-1}\,\varepsilon_0^{-1}\mathbf{D}_\perp \rightarrow \mathbf{E}^\mathrm{mb} = \mathbf{E}_\parallel + \varepsilon_\mathrm{a}^{-1}\,\varepsilon_0^{-1}\mathbf{D}_\perp \tag{3.60}$$

$$\mathbf{D}^\mathrm{static} = \mathbf{D}_\perp + \varepsilon_\mathrm{b}\,\varepsilon_0\mathbf{E}_\parallel \rightarrow \mathbf{D}^\mathrm{mb} = \mathbf{D}_\perp + \varepsilon_\mathrm{a}\,\varepsilon_0\mathbf{E}_\parallel \tag{3.61}$$

Hence the movement of the boundaries causes a perturbation in the fields $\Delta\mathbf{E}$ and $\Delta\mathbf{D}$:

$$\Delta\mathbf{E} = (\varepsilon_\mathrm{b}^{-1} - \varepsilon_\mathrm{a}^{-1})\varepsilon_0^{-1}\mathbf{D}_\perp \tag{3.62}$$

$$\Delta\mathbf{D} = (\varepsilon_\mathrm{a} - \varepsilon_\mathrm{b})\varepsilon_0\mathbf{E}_\parallel \tag{3.63}$$

To describe the displacement of the waveguide boundary quantitatively we introduce the normal vector $\hat{n}$ (see figure 3.5). It allows us to calculate the amount the interface is displaced simply by the product of $\hat{n}$ with the displacement field **U**, assuming a quasi-parallel shift of the surface and neglecting any higher order terms. In this case, we can write the overlap integral of the moving boundary effect over the waveguide cross-section as a line integral over the boundary contours C. The overlap integral, that is the contour integral of the normal displacement of the waveguide boundary and the sum of the induced changes in the fields at the boundary is given by [192]:

$$O_v^{\mathrm{MB}} = \int_C d\mathbf{r}(\mathbf{u}^* \cdot \hat{n})[(\varepsilon_a - \varepsilon_b)\varepsilon_0(\hat{n} \times \mathbf{e}^{(1)})^*(\hat{n} \times \mathbf{e}^{(2)}) + (\varepsilon_b^{-1} - \varepsilon_a^{-1})\varepsilon_0^{-1}(\hat{n} \cdot \mathbf{d}^{(1)})^*(\hat{n} \cdot \mathbf{d}^{(2)})] \tag{3.64}$$

The total overlap integral that determines the strength of the SBS interaction is then given by the sum of the photoelastic and moving boundary contribution:

$$O_v^{\mathrm{total}} = O_v^{\mathrm{PE}} + O_v^{\mathrm{MB}} \tag{3.65}$$

Note that there is also a moving polarization effect due to the movement of charges in the material caused by the acoustic wave [192]. It was shown, however, that this effect is usually very small [192].

Chapter 4

Physics of Bragg gratings and slow-light propagation

4.1 Bragg gratings

A fiber Bragg grating is a periodic modulation of the refractive index of a waveguide. If the period of the modulation fulfills the Bragg condition a significant amount of the signal is backscattered. The first record of a Bragg grating was in 1978 when Hill and co-workers realized that the transmission through their fiber under test decreased over time and at the same time a reflected signal could be observed [193]. The origin of this backscattered signal could be associated to a periodic modulation of the refractive index induced by the pump laser. As the period of the modulation was given by the wavelength of the laser itself, it fulfilled the Bragg condition, and the light got reflected back. This observation was also the first account of the photosensitivity of an optical fiber, i.e., the ability to alter the refractive index of an optical fiber using laser light.
Following this initial discovery fiber Bragg gratings found a manifold of applications, from filtering to sensing and signal processing and the interested reader is referred to the following (by no means complete) list of examples, review papers, and books [194–199].
The method of writing and inducing grating structures greatly evolved since its first discovery. In the case of Hills experiment, the grating was formed by a high-intensity interference pattern of the pump laser caused by back reflections. This method of writing a grating is termed "Hill method". However, many other methods to generate the required interference pattern in the waveguide were developed such as side illumination techniques based on an interferometer [200] and a phase mask [201]. This method greatly increases the control over the grating properties. A more detailed description of grating writing is given in chapter 5,

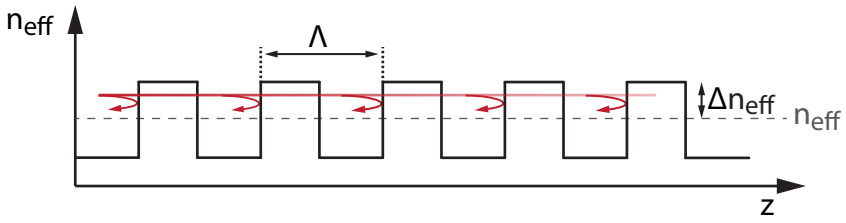

Fig. 4.1 Schematic representation of the periodic index modulation of a Bragg grating.

whereas this chapter focuses on providing the theoretical foundation of Bragg gratings. We start by describing the spectral response of Bragg gratings and segue into a description of the strong dispersion introduced by the grating that leads to slow-light propagation, which we then compare to SBS induced slow-light.

Our description of the mathematical framework of Bragg gratings starts from the periodic index modulation that couples forward and backward propagating optical modes and, as we will see later, can be described by coupled mode equations (detailed descriptions of coupled mode theory in the context of Bragg gratings can be found in several textbooks and review papers [194, 195, 202]). A scheme of the index modulation of a Bragg grating is shown in figure 4.1.

We can describe a periodic index modulation in z-direction in its most general form using the following formula:

$$\Delta n_{\mathrm{eff}}(z) = n_{\mathrm{av}}(z)\left[1 + V_{\mathrm{fr}}\cos\left(\frac{2\pi}{\Lambda}z + \Phi(z)\right)\right] \tag{4.1}$$

As we are dealing with waveguide structures the index to consider is the effective index n_{eff} instead of the refractive index n. From here onwards the average "DC" effective index over a grating period Λ is called $n_{\mathrm{eff}}(z)$. Furthermore we introduced in equation 4.1 the fringe visibility $V_{\mathrm{fr}} = \Delta n_{\mathrm{eff}}/n_{\mathrm{eff}}$ of the index change and the phase term $\Phi(z)$, which describes a possible chirp along the grating. Here we assume a shallow grating, i.e. the change in the effective refractive index $\Delta n_{\mathrm{eff}}(z) << n_{\mathrm{eff}}(z)$. The key condition for a Bragg grating is the fulfillment of the Bragg condition that is given by:

$$\lambda_{\mathrm{Br}} = 2n_{\mathrm{eff}}\Lambda \tag{4.2}$$

The Bragg condition ensures that light that is Fresnel reflected at the index contrast of one grating period is in phase with the reflection from the next, and all other periods of the grating. So even for a shallow grating with only a small modulation of the effective refractive

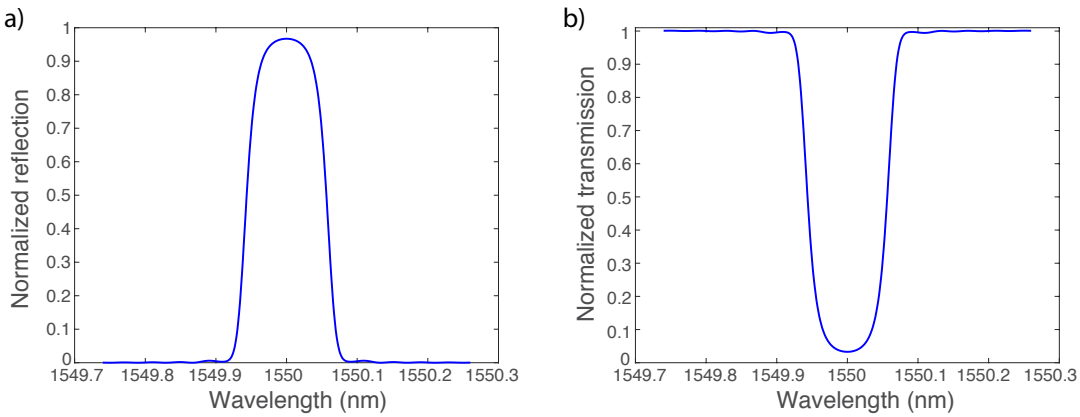

Fig. 4.2 Calculated reflection spectrum of an apodised Bragg grating (a) and a transmission spectrum (b).

index almost 100% of the light at the Bragg wavelength can be reflected if the grating is long enough. This reflection occurs over a finite spectral width $\Delta\lambda$:

$$\frac{\Delta\lambda}{\lambda_{\mathrm{Br}}} = \frac{\Delta n_{\mathrm{eff}}}{n_{\mathrm{eff}}} \tag{4.3}$$

As an example the calculated transmission and reflection spectrum of a typical grating is shown in figure 4.2 (here shown for an apodised fiber Bragg grating).

Coupled mode theory can be applied to describe the propagation of light in a fiber Bragg grating and hence calculate the transmission and reflection spectrum. In an unperturbed waveguide different modes usually do not couple to each other or exchange energy. A grating, however, introduces a coupling between the forward and backward traveling modes in a waveguide.

These coupled modes obey the optical wave equation 3.5 given previously. We introduce a coupling parameter κ that describes the introduced coupling by the Bragg grating of the forward traveling optical mode to the backward traveling mode and vice versa. Again we use the *slowly varying envelope approximation* which allows to neglect all rapid oscillating terms and second order derivatives. We arrive at the common coupled mode equations for forward $E^+(z,t)$ and backward $E^-(z,t)$ traveling modes:

$$\frac{\partial E^+(z,t)}{\partial z} + \frac{n_{\mathrm{av}}}{c}\frac{\partial E^+(z,t)}{\partial t} = -i\kappa E^-(z,t) \tag{4.4}$$

$$-\frac{\partial E^-(z,t)}{\partial z} + \frac{n_{\mathrm{av}}}{c}\frac{\partial E^-(z,t)}{\partial t} = -i\kappa E^+(z,t) \tag{4.5}$$

We can now separate the time dependence in equation 4.4 and 4.5 by using an ansatz proportional to $E^{\pm}(z,t) = E^{\pm}(z)\exp(\omega t)$

$$\frac{dE^{+}(z)}{dz} = -i\sigma E^{+}(z) - i\kappa E^{-}(z) \tag{4.6}$$

$$\frac{dE^{-}(z)}{dz} = i\sigma E^{-}(z) + i\kappa^{*} E^{+}(z) \tag{4.7}$$

The coupling coefficient κ describes the strength of the grating, σ on the other hand is a self-coupling coefficient. These two coupling coefficients are given by the following two relations. The coupling coefficient κ is connected to the refractive effective index modulation $\Delta n_{\text{eff}}(z)$ in the following way:

$$\kappa = \kappa^{*} = \frac{\pi}{\lambda_{\text{Br}}}\Delta n_{\text{eff}} = \frac{\pi n_{\text{eff}}\Delta\lambda}{\lambda_{\text{Br}}^{2}} \tag{4.8}$$

Here equation 4.3 is used to make the connection between the grating strength κ and the grating spectral width $\Delta\lambda$. The self-coupling coefficient σ is defined in the following way:

$$\sigma = \delta + \sigma' - \frac{1}{2}\frac{d\phi}{dz} \tag{4.9}$$

with the detuning δ from the Bragg wavelength, i.e. the center of the grating spectrum. Therefore δ can be written as:

$$\delta = 2\pi n_{\text{eff}}[\frac{1}{\lambda} - \frac{1}{\lambda_{\text{Br}}}] \tag{4.10}$$

Note that for $\delta \to 0$ one obtains the canonical Bragg condition, as one would expect. The second term in equation 4.9 is the "DC" coupling coefficient σ' and is given by:

$$\sigma' = \frac{2\pi}{\lambda_{\text{Br}}} n_{\text{eff}} \tag{4.11}$$

The last term in 4.9 describes a phase change along the grating, i.e. a chirp of the grating period. Grating spectra for different grating strengths κ are shown in figure 4.3. One can see in figure 4.3 that the grating shows strong sidelobes next to the main reflection region of the grating. These sidelobes emerge for a uniform grating where the envelope of the index modulation is a rectangular function. By altering the envelope function of the index modulation to e.g. a gaussian profile, one can get rid of the sidelobes. Depending on the underlying envelope of the index modulation one distinguishes between uniform or apodized gratings. Figure 4.4 shows a spectra of a uniform and a guassian apodized grating, respectively.

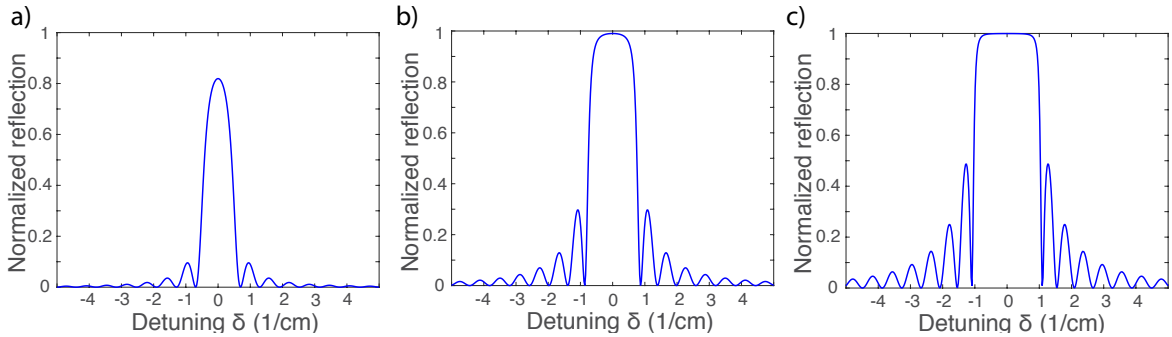

Fig. 4.3 Grating reflection spectra of a uniform grating for different grating strength κ. a) $\kappa = 30$ b) $\kappa = 60$ c) $\kappa = 90$

As a final remark in this section a direct expression that relates the grating strength κ with the maximum reflectivity $r_{\max}$ of a strong grating (> 3 dB) is given [195]:

$$r_{\max} = \tanh^2(\kappa L) \tag{4.12}$$

where L is the length of the grating. Equation 4.12 follows from an analytical solution of 4.6 and 4.7 for a uniform grating without chirp.

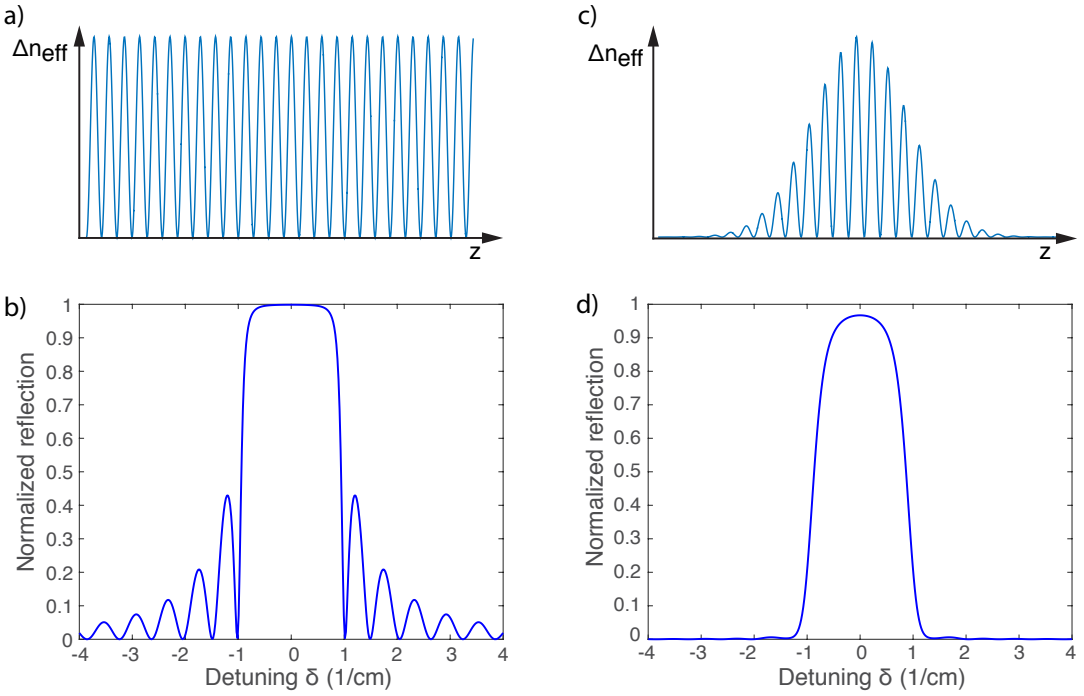

Fig. 4.4 a) Uniform index modulation and b) corresponding grating spectrum. c) Gaussian apodized index modulation. d) Gaussian apodized grating spectrum with greatly reduced sidelobes compared (a).

4.1.1 Photonic bandgap and group velocity

In the last section, the fundamental physics of Bragg gratings and the underlying equations have been introduced. To this point, we have only described the spectral response of Bragg gratings. The spectral response of a grating allows for the construction of narrowband reflectors and filters. The grating structure, however, also strongly alters the dispersion of a waveguide. In this section, we have a closer look at the dispersive nature of Bragg gratings and its effects on the group velocity of a light pulse.
From the dispersion relation of the Bragg grating, we will see that a Bragg grating can be described as a one-dimensional photonic bandgap structure. In analogy to the electronic bandstructure in solid-state physics, many interesting properties and phenomena can be derived and explained from the knowledge of the bandstructure.

To derive the photonic bandgap we start again from the coupled mode equations for forward and backward traveling optical modes:

$$\frac{\partial E^+(z,t)}{\partial z} + \frac{n_{\mathrm{av}}}{c}\frac{\partial E^+(z,t)}{\partial t} = -i\kappa E^-(z,t) \tag{4.13}$$

$$-\frac{\partial E^-(z,t)}{\partial z} + \frac{n_{\mathrm{av}}}{c}\frac{\partial E^-(z,t)}{\partial t} = -i\kappa E^+(z,t) \tag{4.14}$$

To obtain the dispersion diagram from the coupled equations 4.4 - 4.5 we use again a plane wave ansatz, however we introduce a detuning term δ_{d} here [202]:

$$E^{\pm}(z,t) = A_0^{\pm} \cdot e^{i(K_d \cdot z - \delta_{\mathrm{d}} \frac{c}{n_{\mathrm{av}}} \cdot t)} \tag{4.15}$$

Here we use the detuning δ_{d} instead of the frequency ω which is defined relative to the center frequency of the Bragg grating (i.e. the Bragg frequency ω_{Br}): $\delta_{\mathrm{d}} = \frac{n_{\mathrm{av}}}{c}(\omega - \omega_{\mathrm{Br}})$. Also the z component of the k-vector K_d in the ansatz 4.15 is defined relative to the z component of the Bragg wave vector: $K_d = k - k_{\mathrm{Br}}$. We insert the plane wave ansatz 4.15 into the coupled mode equations 4.4 - 4.5 and rewrite the obtained expression into a matrix equation:

$$\begin{pmatrix} -K_d + \delta_{\mathrm{d}} & \kappa \\ \kappa & K_d + \delta_{\mathrm{d}} \end{pmatrix} \begin{pmatrix} A_0^+ \\ A_0^- \end{pmatrix} = 0 \tag{4.16}$$

From the matrix equation 4.16 one receives a relationship between the detuning δ_{d} from the grating center frequency and the wavevector K_d and the grating strength κ by setting the

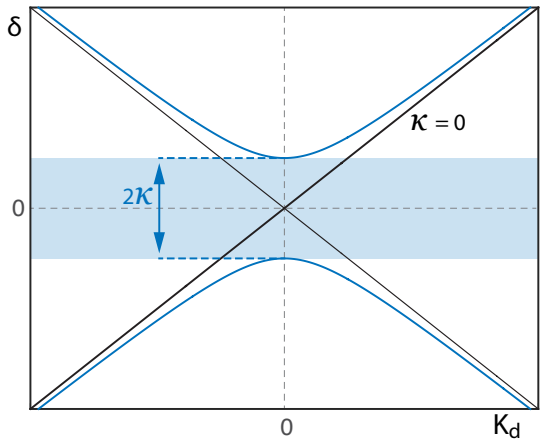

Fig. 4.5 Dispersion relation of a Bragg grating showing a photonic bandgap. The black curves shows the linear dispersion without grating, whereas the blue line show a bandgap openeing proportional to 2κ.

determinant to 0. This leads to the following relationship:

$$\delta = \pm\sqrt{K_d^2 + \kappa^2} \tag{4.17}$$

The disperion curve given by equation 4.17 is shown in figure 4.5. It shows the linear dispersion for the case without a grating and how the presence of the grating opens up a bandgap. The width of the bandgap is proportional to the grating strength κ. This means, that for certain frequencies there are no propagating waves present in the structure. Therefore this can be seen as a direct analogue to the bandgap in semiconductors.
The next step is to investigate the dispersion properties of the grating around the bandgap, in particularly the change in the group velocity v_g. From the dispersion relation 4.17 one can get the group velocity, i.e. the slope of the band, via the following relation:

$$v_g \approx \frac{d\omega}{dk} = \frac{c}{n_{\text{eff}}}\sqrt{1 - \frac{\kappa^2}{\delta^2}} \tag{4.18}$$

One can see that for large detuning δ_d one receives $\frac{c}{n_{\text{eff}}}$, as one would expect, for δ_d approaching κ, however, the group velocity approaches 0, as one can also see directly from the flat dispersion diagram shown in figure 4.5. Another, maybe more intuitive way to look at the low group velocity in the vicinity of the grating is to consider that light traveling through the Bragg grating structure gets reflected forth and back, and hence it takes the light pulses much longer to transit through a waveguide with grating compared to without it.
We have seen that dispersion can alter the group velocity of the pulse traveling in a waveguide.

This effect is commonly referred to as slow-light and occurs in a variety of resonant effects. The next section will give a general introduction to the effect of slow-light.

4.2 Slow-light

We have seen in the previous section that a Bragg grating forms a one-dimensional photonic bandgap. The change in dispersion leads to flat dispersion bands close to the bandgap, which causes the group velocity to reduce dramatically. The same concept can be directly applied in two dimensions, by periodically patterning a two-dimensional slab. It is usually achieved by etching holes in a material slab, often silicon. A line defect between the holes acts as a waveguide. These structures are called photonic crystals [203, 204]. As in the case of a Bragg grating, a bandgap opens up, and the group velocity greatly reduces.
However, the concept of slow-light (that is a reduction of the group velocity v_g of optical pulses much smaller than the speed of light c in vacuum) is far more universal than just periodic structured waveguides and can be found in any structure that provides an optical resonance.
Record low group velocities down to just 17 m/s could be achieved in cold atoms [205] and record fractional pulse delays of 80 pulse widths have been shown in a Cesium vapor [206]. Other schemes that are able to reduce the group velocity of light are coupled-resonator optical waveguides (CROW) [207] or SBS in optical fibers [208, 180] and waveguides [77]. Even though the presented slow-light implementations are very different in their nature, the underlying physical cause for the change in group velocity is the same. In all cases, it is a change in the group index due to a rapid change in the dispersion. The group index is given by the following equation:

$$n_g = n + \omega \frac{dn}{d\omega} \tag{4.19}$$

From equation 4.19 one can see that to achieve the largest possible group index one needs to realize a large index change over a relatively small bandwidth. The Kramers-Kronig relation dictates that every optical resonance is also accompanied by a change in the refractive index and follows directly from causality. In the case of atomic vapors e.g. the bandwidth of the resonance is very sharp and hence a large change in the group index can be achieved.

Even though the underlying physics causing the light to slow down is the same in all the presented schemes, there are two overarching categories for slow-light: structural slow-light and material slow-light. In material slow-light, the slow-down effect originates from a resonance in the material, e.g., an atomic transition. In structural slow-light, the effect arises

from structuring the waveguide as in the case of Bragg gratings and photonic crystals. The main difference is that in structural slow-light the intensity of the light signal builds up proportional to the group velocity reduction. It was shown that this field enhancement effect can be used to enhance nonlinear effects [209, 210]. The slow-light enhancement effect will be analyzed in more detail in chapter 5.
In the last section of this chapter, we will have a closer look at SBS induced slow-light. On the one hand, as it serves as an example of how a resonant effect can slow-down light pulses and on the other hand, it will give the necessary context to distinguish the delays achieved using a BBM technique compared to a Brillouin-based slow-light scheme.

4.2.1 SBS slow-light

Here, we want to introduce SBS slow-light. As we have seen in the previous section, slow-light relies on a rapid change of the group index n_g in the vicinity of a resonance. As SBS is a fairly narrow-band (MHz range) optical resonance, it can be harnessed to slow down light pulses. The advantages of an SBS based slow-light approach are room-temperature operation and full compatibility with standard telecommunication technologies. As SBS, in fact, consists of two resonances, the SBS Stokes resonance (gain) and the anti-Stokes resonance (loss), SBS can also be used for fast light generation. However, for the rest of this chapter, we will focus on SBS slow-light.
The first demonstrations of SBS slow-light were reported by two groups almost simultaneously in 2005 [208, 180]. Both these demonstrations were performed in optical fiber, and the first on-chip SBS slow-light demonstration followed in 2012 [77]. In the following we want to outline the underlying physics that cause a change of the group index in the vicinity of the Stokes resonance.

We start the description from the coupled-mode equations derived in chapter 3.3. We only look at the equation for the Stokes wave as we want to investigate the effect of the gain resonance on the group index. The coupled mode equation of the Stokes wave has the following form (see 3.57):

$$-\frac{\partial A_2}{\partial z}+\frac{n}{c}\frac{\partial A_2}{\partial t}=\frac{g_B}{2A_{\text{eff}}^{\text{ao}}}A_1Q^* \tag{4.20}$$

To calculate the acoustic mode envelope Q^* we assume the steady state for the acoustic mode (compare chapter 3.3). The following derivation follows the description given in ref. [184]. In contrast to the derivation presented in section 3.3, we do not assume anymore that the

acoustic and optical modes are perfectly phase-matched. Instead we introduce a complex detuning term $i(\Omega_B - \Omega)$. Inserting the steady state solution for Q^* in equation 4.20, we receive:

$$-\frac{\partial A_2}{\partial z} + \frac{n}{c}\frac{\partial A_2}{\partial t} = \frac{g_B}{2A_{\text{eff}}^{\text{ao}}} A_2 |A_1|^2 \left(\frac{1}{1+i\delta}\right) \tag{4.21}$$

Here we have introduced the fractional detuning $\delta = 2(\Omega_B - \Omega)/\Gamma_B$. Furthermore we can identify $|A_1|^2$ with the power of the pump P_p wave. This allows us to summarize the right hand side of equation 4.20 using a complex gain coefficient $g_c(\delta)$:

$$-\frac{\partial A_2}{\partial z} + \frac{n}{c}\frac{\partial A_2}{\partial t} = g_c(\delta) A_2 \tag{4.22}$$

The complex gain coefficient $g_c(\delta)$ is given by:

$$g_c(\delta) = \frac{g_B P_p}{A_{\text{eff}}^{\text{ao}}} \left(\frac{1}{1+i\delta}\right) \tag{4.23}$$

The real part of the complex gain $g_c(\delta)$ gives the canonical Brillouin gain coefficient $g_B(\Omega)$. The imaginary part, however, is responsible for a Brillouin induced change in the refractive index Δn_B, which is given by [184]:

$$\Delta n_B = \frac{c}{2\omega_S} \text{Im}(g_c) = \frac{c}{2\omega_S} \frac{g_B P_p}{A_{\text{eff}}^{\text{ao}}} \left(\frac{\delta}{1+\delta^2}\right) \tag{4.24}$$

with the Stokes frequency ω_S. This change in the index follows directly from the Kramers-Kronig relations and is a consequence of causality. Even though the absolute changes in refractive index are usually small ($\approx 10^{-8}$) the group index still can change significantly as the refractive index change occurs over a narrow frequency bandwidth $\Delta\omega$ (recall equation 4.19 for the group index). This index change is about two orders of magnitude larger in chalcogenide waveguides due to the larger Brillouin gain coefficient g_B and the smaller effective acousto-optic mode area $A_{\text{eff}}^{\text{ao}}$. The SBS induced index change in a chalcogneide waveguide in the vicinity of the Stokes resonance is shown in figure 4.6a) for 100 mW pump power at a wavelength of 1.55µm (the parameters of the photonic waveguide can be found in reference [75]).

The induced index change can be translated into a change of the group index using equation 4.19. This leads us to the following expression for the group index n_g in the presence of SBS:

$$n_g = n + \frac{c\, g_B}{\Gamma_B A_{\text{eff}}^{\text{ao}}} \frac{1-\delta^2}{(1+\delta^2)^2} \cdot P_P \tag{4.25}$$

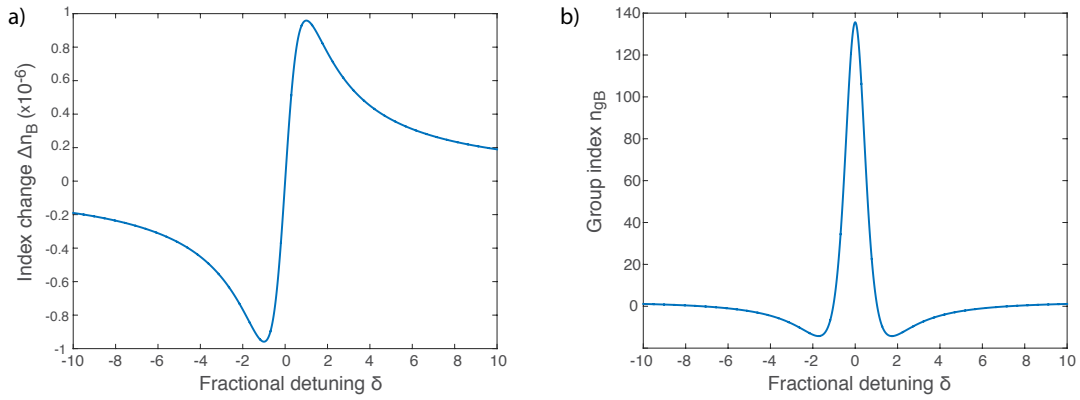

Fig. 4.6 a) Refractive index change induced by the Stokes resonance in a chalcogenide waveguide. b) Group index change induced by SBS.

The SBS induced group index change in a chalcogenide waveguide is shown in figure 4.6 b). From equation 4.25 one can see another advantageous property of SBS slow-light, i.e. the control of the group index via the pump power P_p. This makes the SBS slow-light approach even more versatile. Even though being a very promising approach to delay optical signals, SBS research was facing major challenges, such as bandwidth, fractional delay and pulse distortions. Different techniques were proposed and implemented to address these challenges, and an overview is given in chapter 5.

Chapter 5

Enhancing and inhibiting Stimulated Brillouin scattering

In this chapter results on tailoring the SBS interaction strength, by either enhancing or fully suppressing the effect, in a waveguide are presented. This control of the nonlinear interaction is achieved by inscribing a Bragg grating in a highly nonlinear photonic waveguide. These results were published in Ref. [33].

5.1 Introduction

This section provides the required background leading to the publication presented later in this chapter (section 5.2). It gives a general introduction to enhanced optical nonlinearities in periodic structures and introduces the concept of a stopband in the context of inhibiting optical effects. The final section of the introduction describes how these periodic structures actually are inscribed into an integrated photonic waveguide.

Slow-light enhanced nonlinearities

We have seen in chapter 4.1.1 that Bragg gratings are able to reduce the velocity of light. As slow-light induced by a Bragg grating is a form of structural slow-light, it also enables to enhance nonlinear optical interactions. Here an introduction of slow-light enhanced nonlinear optical effects is given to contextualize the SBS enhancement [33] presented later in the chapter.
In the case of structural slow-light, there is not only a reduction of the group velocity of light, that is accompanied with a larger transit time τ_t through a waveguide under test, but also an enhancement of the electric field strength within the waveguide [211–213, 209]. We can

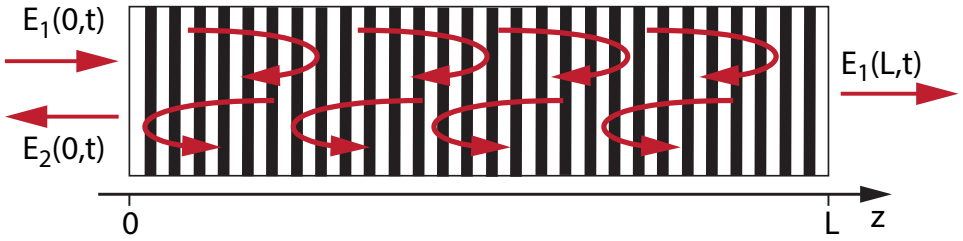

Fig. 5.1 Schematic explanation of the slow-light and energy build-up effect in a Bragg grating.

understand this field build-up intuitively; if we consider a one-dimensional periodic structure, a waveguide with a Bragg grating, then the light is reflected forth and back by the periodic index modulation, in contrast, to simply passing through an unpatterned waveguide (figure 5.1). Hence the transit time τ_t is increased. But as the forward and backward scattered waves carry a certain power there is also a build-up of energy within the grating (as compared to the light just passing through an unpatterned waveguide). In structural slow-light, none of this energy is transferred to the material [213] and hence the electric field is building up (if absorption in the waveguide is negligible).

It was shown by Winful [214] that the normalized group delay $\tau_{gn} = \tau_g/\tau_t$ can be related to the normalized stored energy $U_{gn} = U_g/U_t$ and is in fact equal. Here τ_g and U_g are the transit time and stored energy in the waveguide with a grating, respectively, and τ_t and U_t are the respective quantities without a grating.

Therefore slow-light can enhance linear and nonlinear optical effects twofold: on the one hand there is the increased interaction length due to the reduced group velocity, and on the other hand there is the build-up of the electrical field in the structure. A parameter to quantify the enhancement effect is the slow-down factor S that is generally defined as $S = n_g/n$ with the group index n_g and the refractive index of the material n. However, as we investigate slow-light in waveguides an effective index description of the index is more appropriate, where $n_{g,eff}$ is given by $n_{g,eff} = c/v_{g,eff} = c/L \cdot \tau_g$ with L being the length of the waveguide. The slowdown factor S is then simply the effective group index $n_{g,eff}$ over the effective waveguide index n_{eff}.

Many nonlinear effects have been studied in periodic structures with a good overview given in [209]. In particular, photonic crystals were used to study the scaling laws of enhanced linear and nonlinear effects. Photonic crystals are particularly suitable to study these effects, as they achieve very high slow-down factors S, that can exceed 100 [215], but also as they allow for engineering the dispersion [216]. Dispersion engineering is crucial for many nonlinear effects such as 4WM to ensure phase matching. Two examples of SEM images of typical photonic crystals are shown in figure 5.2.

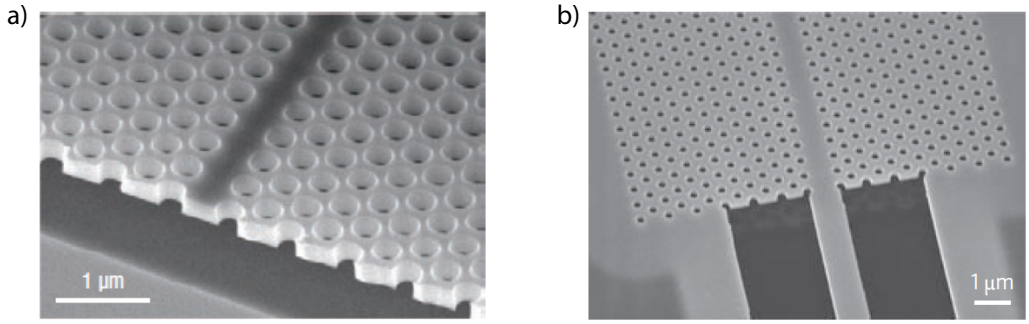

Fig. 5.2 a) SEM image of a crystal slab [204] b) SEM image of a photonic crystal waveguide connected to a tapered ridge waveguide [210].

Linear optical effects scale linear with the slow-down factor S, simply reflecting the increased path length due to the slower group velocity of the light. Hence a lot of effort was put into engineering the linear scattering losses in photonic crystals [217]. Note, that the scaling of the loss mechanisms in photonic crystals can be more complicated; e.g., for very low group velocities the scaling of the losses starts to deviate from the linear dependence on the slow-down factor S and follows a quadratic trend [218].

The scaling of enhanced nonlinear optical effects fundamentally differs from that of linear optical effects, as nonlinear effects depend on the intensity as well as the path length. As structural slow-light effects enhance both the intensity and the optical path length, a strong enhancement of nonlinear optical effects is expected.

So does, for example, the nonlinear effect of SPM scale quadratically with the slow down factor [211]. Intuitively one can understand this by combining the contribution from the enhanced path length, that is proportional to S and the effect of the field enhancement, also proportional to S. In reality the scaling is slightly more subtle and the nonlinear coefficient Γ is given by [219, 209, 220]:

$$\Gamma = (\frac{3 - S^{-2}}{2})S^2\gamma_0 \tag{5.1}$$

where γ_0 is the nonlinear coefficient of the unstructured waveguide given by $\gamma_0 = 2\pi n_2/\lambda A_{\text{eff}}$ with the nonlinear index n_2 [108].

The slow-light enhancement effect was investigated for a manifold of nonlinear effects. In the case of 4WM an enhancement that scales to the fourth power of S has been theoretically predicted and experimentally confirmed [221, 222, 216]. Also, the possibility to enhance higher order nonlinearities such as third harmonic generation was investigated [210]. Here green light generated in a photonic crystal pumped at 1550 nm was observed.

We have seen that slow-light has great potential to enhance nonlinear effects and was investigated for many different effects. It offers the ability to achieve large nonlinear phase-shifts in compact structures with reduced power consumption. The enhancement of SBS, however, was not studied in this context. Here we present the enhancement of the cascading of SBS in a grating structure in a highly nonlinear waveguide. The used grating structure is carefully designed, so the band edges align with the multiple Stokes lines.

Photonic bandgap to inhibit nonlinear effects

We have seen how a photonic bandgap structure can be harnessed to enhance nonlinearities. We now want to discuss how the bandgap can be used for suppressing unwanted nonlinear effects. It was first realized and discussed by Purcell that the emission from two-level atoms is altered when surrounded by a resonant cavity and is enhanced proportional to the Q-factor of the cavity [223]. Following Purcell's initial realization, it was shown by Kleppner that spontaneous emission is inhibited in the off-resonance case when the transition frequency of the atom is below the fundamental frequency of the cavity [224].
The seminal works by Yablonovitch and by John, which developed the concept of the photonic bandgap, build on the realization that spontaneous emission will be inhibited in a photonic bandgap structure [225, 226]. Yablonivitch states in the abstract of this first proposal of a photonic bandgap structure [225], that: *"If a three-dimensionally periodic dielectric structure has an electromagnetic bandgap which overlaps the electronic band edge, then spontaneous emission can be rigorously forbidden"*.
The concept of inhibiting spontaneous emission by the photonic bandgap was intensely studied over the following decades and is still an active research field today. Shortly after the initial proposal, it was shown that spontaneous emission rates could be altered in semiconductor heterostructures made out of AlGaAs / GaAs [227]. Demonstrations of inhibited emission in dielectric structures followed, first for microwave signals [228] and later for optical frequencies [229]. In the latter case, dye molecules were embedded in a matrix of dielectric spheres [229].
In more recent years this concept was extended to the emission of "artificial atoms", also known as quantum dots. It was demonstrated that the emission of quantum dots [230] and quantum wells [231] can be altered in photonic crystals. An overview of demonstrations that control the spontaneous emission in photonic crystals and nanocavities is given in review paper [232]. In 2011 the first demonstration of inhibited emission from a quantum dot in a three-dimensional photonic crystal could be shown experimentally [233].

With the great focus in the development of photonic bandgap structures on inhibiting *spontaneous* emission, it is almost surprising that photonic bandgaps did not find much attention for inhibiting *stimulated* processes, such as SBS or in general nonlinear optical effects. The ability to selectively suppress unwanted nonlinearities has great potential for many signal processing applications, in particular with the growing importance of integrated photonic circuits that rely on highly nonlinear waveguides. The high nonlinearity in these circuits is required for efficient signal processing but makes them also prone to nonlinear distortions due to unwanted competing nonlinear effects. In particular SBS is a nuisance in many communication systems (compare section 2.3).
In 2003, Lee and Agrawal theoretically proposed to utilize a photonic bandgap to prevent the build-up of the Stokes wave and hence suppress SBS [29]. In their numerical study, they considered the propagation of 15 ns long pump pulses with a peak power in the kW range through a 1m-long Bragg grating. The grating is designed in a way that the Stokes frequency falls inside the stopband. The numerical study shows that without the grating the pump pulse is strongly distorted after the transmission through the 1m-long fiber segment due to pump depletion caused by the build-up of the counter-propagating Stokes wave (see figure 5.3 a)). With the grating, on the other hand, the Stokes wave is not building up (figure 5.3 b)). In the latter case, no depletion of the pump wave can be observed.

After the theoretical proposal from Lee and Agrawal to use a photonic bandgap to suppress SBS, it was shown theoretically by Gomila that a photonic bandgap can inhibit spontaneous modulation instabilities in nonlinear cavities [234, 235]. Experimental demonstrations of the proposed scheme followed shortly after in the context of pattern formations in two-

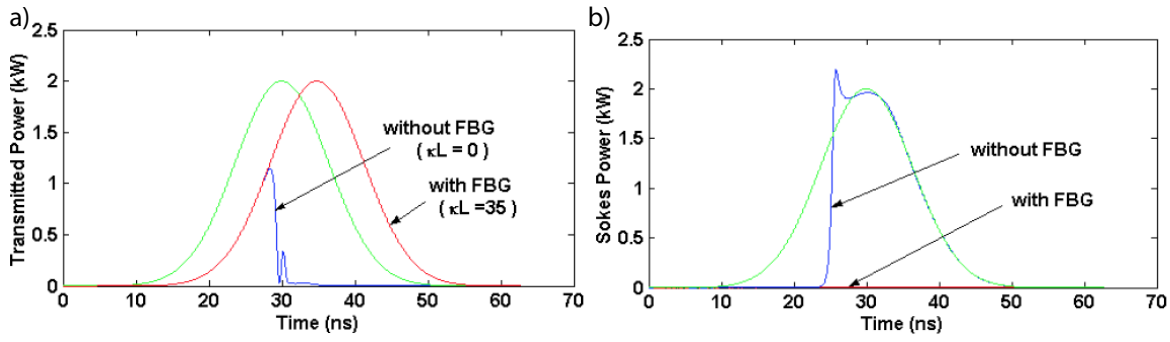

Fig. 5.3 a) Pump pulses after they were transmitted through a fiber segment with a grating (red curve) and without grating (blue curve) [29]. Without the grating, the pump pulse is depleted and b) a counter-propagating Stokes pulse builds up. The green curves show the input pulse [29].

dimensional nonlinear cavities [236, 237].

In this thesis we show the first experimental demonstration of inhibiting the build-up of a Stokes wave, and hence full suppression of SBS, utilizing a photonic bandgap structure [33]. However, before presenting the experimental results on inhibiting and enhancing SBS by harnessing a photonic bandgap, we first want to describe how these photonic bandgap structures can be implemented into a highly nonlinear waveguide. The next section introduces and describes methods to inscribe Bragg gratings in waveguides.

Multi-wavelength Hill gratings

As we have seen in the Bragg grating section 4.1 a grating is a periodic modulation of the waveguide refractive index. Hence to inscribe a grating one must induce a change of the refractive index with a period that is in the range of the wavelength of interest, therefore writing methods usually rely on laser inscription (with the exception of lithographically fabricated waveguide gratings). The physical effect that allows the refractive index to change under illumination is called photosensitivity [238].
In a photosensitive process, the incoming light alters the chemical bonds in the material. This change can be achieved directly by illuminating the material with light with an energy above the electronic bandgap or with laser light that has an energy that corresponds to the energy of defect states in the glass matrix, which could be within the bandgap. The laser light will be absorbed by the glass and in this process create electron-hole pairs. This process can lead to the formation of new bonds and hence an alteration of the materials refractive index. Glass matrices with many defects are often particularly receptive to this process as the deposited energy by the laser light can lead to relaxation of these defects and reform or recreate bonds. Besides the absorption in defect states within the bandgap, there is a second mechanism of photosensitivity induced by light with sub-bandgap energy, that is nonlinear absorption. In this case, the electron-hole pairs that are altering the bonds in the glass matrix are formed by for example of two-photon absorption (TPA) and hence light with around half the bandgap energy can induce photosensitivity.

Different methods are used to generate an intensity pattern that generates the periodic index variation required to form a Bragg grating. The initial technique pioneered by Hill et al. relied on an interference pattern generated from counter-propagating optical waves, which were forming a standing wave in the waveguide [193]. As a light source, an ultraviolet (UV) laser source was used, and a periodic change of the refractive index of the germanium-doped fiber core was observed.

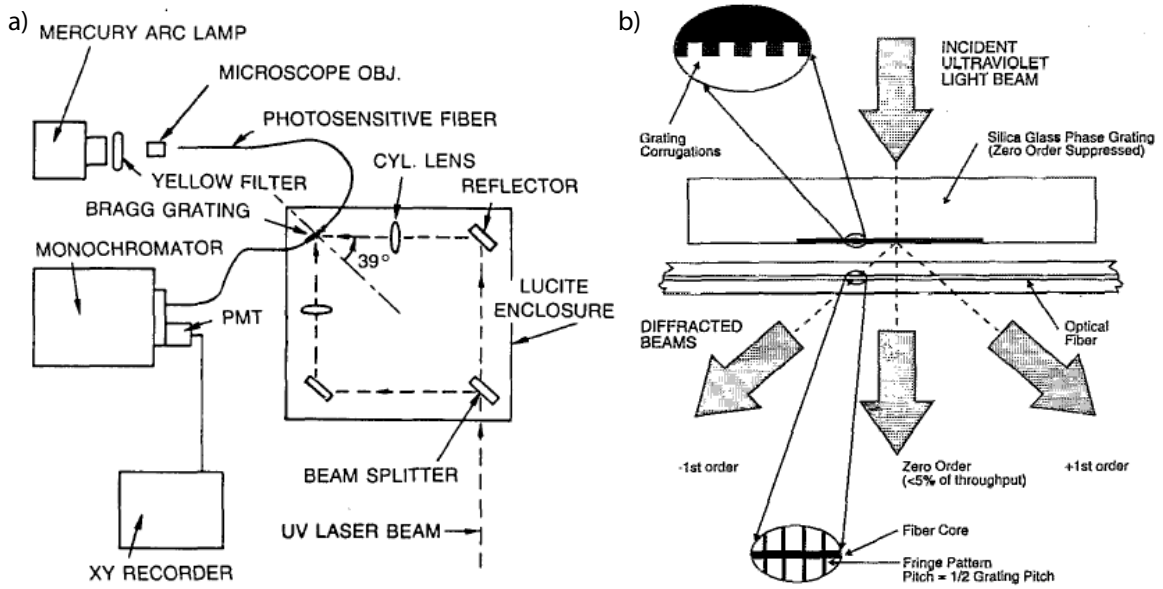

Fig. 5.4 a) Holographic grating writing technique [200]. b) Inscription method based on a phase mask [201].

Hill's method of writing a grating has the advantage of only requiring access to the fiber facets, however, nowadays gratings writing techniques that access the fiber from the sides are more common. The reason lies in the increased control over the grating profile. The first such side grating inscription techniques relied on a holographic method [200]. A UV laser is split into two paths that interfere at the fiber core and are forming an interference pattern that writes the Bragg grating.
The side inscription methods were further developed, and instead of interfering two laser beams techniques based on a phase-mask were put forward [201]. In this case, a UV laser is transmitted through the phase-mask and hence forms an interference pattern at the fiber core. Schemes of the holographic and the phase-mask techniques are shown in figure 5.4.
In the results presented later in this chapter we exploit a multi-wavelength Bragg grating in a chalcogenide waveguide to enhance or suppress SBS. This imposes stringent requirements on the grating structure. First of all, a multiple-stopband grating is required as an enhancement of higher Stokes orders is required to form a cascade of Stokes waves - a Brillouin frequency comb (BFC). Hence the grating spectra, i.e., the grating's band edges, need to be very narrow and precisely match the Brillouin frequency shift Ω_B. The requirement of spectrally narrow stopbands (≈ 65 pm) also ensures that in the inhibition case the grating is narrow enough to selectively suppress the Stokes wave generation. Furthermore, the grating needs to be written in an integrated waveguide on a chip, which also requires a top cladding to ensure acoustic guidance (compare section 3.2.3).

It has been shown previously that Bragg gratings can be inscribed in chalcogenide waveguides [239, 240]. In both approaches sampled gratings were written into the waveguide by using a phase mask technique [240] or a shadow mask [239]. Even though in both cases gratings were successfully inscribed, achieving narrowband gratings that match precisely the Brillouin frequency shift Ω_B is challenging.

To address this challenge, we chose to use the Hill method combined with SBS itself to write a grating that perfectly matches the Brillouin shift Ω_B. As SBS itself is used to generate the multiple optical waves to inscribe the multi-stopband grating structure the spacing of the stopbands naturally matches the Brillouin frequency shift Ω_B. A schematic of this method is shown in figure 5.5.

The formation of a standing wave interference pattern (as required in the Hill method) is achieved via the reflections from the cleaved facets of the chalcogenide waveguides. These perpendicularly cleaved waveguide facets provide a feedback of about 17% due to the index contrast between the waveguide index $n_1 = 2.4$ and the surrounding air $n_1 = 1$. The amount of feedback can be simply calculated using the Fresnel equation for normal incidence:

$$r = \left| \frac{n_1 - n_2}{n_1 + n_2} \right|^2 \approx 0.17 \tag{5.2}$$

The feedback mechanism will form an interference pattern for the pump wave in the waveguide. However, as our chalcogenide waveguides are designed to have high Brillouin gain, the optical pump will also generate a 1st order Stokes wave. If the Stokes wave reaches a critical power it will act as a pump for the next higher order Stokes wave (see figure 5.5). Therefore one ends up with several standing wave interference patterns in the waveguide that will inscribe a multi-wavelength grating. As the multiple waves are written by optical waves that are generated via SBS the spacing between the grating stopbands will match perfectly the Brillouin frequency shift Ω_B.

A multi-wavelength grating written using a Brillouin assisted Hill method was previously shown in chalcogenide As_2Se_3 fiber [241]. The gratings were written at a wavelength of 1550 nm, which is in the order of twice the bandgap of 830 nm of the glass [242]. Hence, the energy of the pump light at 1550 nm is not enough to excite electrons above the bandgap and create electron-hole pairs. However, two pump photons have sufficient energy, and hence the nonlinear effect of TPA is able to provide the required excitation energy.

The waveguides used for the SBS experiments presented in this thesis, however, are made out of a different chalcogenide glass, i.e., As_2S_3. The electronic bandgap of As_2S_3 corresponds to a wavelength of 620 nm. Hence even two photons do not provide the required excitations energy and even higher order nonlinear effects - such as, e.g., three-photon absorption - are

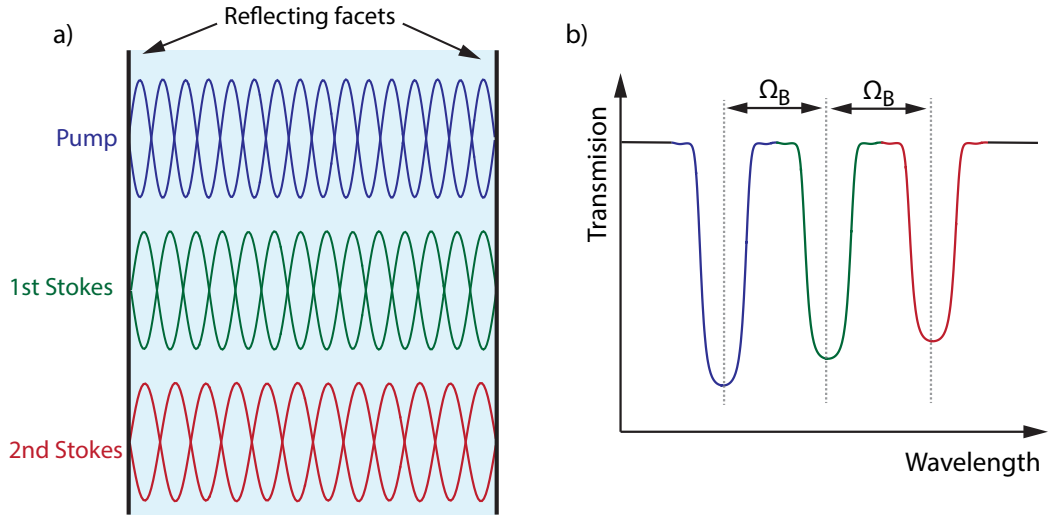

Fig. 5.5 a) Hill grating method with multiple optical waves generated by SBS. b) Resulting multi-wavelength grating spectrum.

necessary to excite electrons above the bandgap.
However, it is well known that thin films of chalcogenide glass are prone to defects in the glass matrix. Thus, usually many defect states are present in these thin films that are located within the electronic bandgap. These defect bonds can be altered by light illumination. As a consequence, the refractive index starts to deviate from the thin film refractive index and approaches the bulk refractive index of the glass [243]. These defect states are the main reason that strong photosensitivity in As_2S_3 at 1550 nm could be observed despite the large bandgap energy [244, 245].

5.2 Publication: Enhancing and inhibiting stimulated Brillouin scattering

This chapter is investigating how SBS can be enhanced or inhibited in a photonic circuit by applying the techniques introduced in the previous chapters on SBS. The rest of the chapter is based on the following publication:

M. Merklein, I. V. Kabakova, T. F. S. Büttner, D.-Y. Choi, B. Luther-Davies, S. J. Madden, and B. J. Eggleton, "Enhancing and inhibiting stimulated Brillouin scattering in photonic integrated circuits," Nature Communications **6**, 6396 (2015).

Abstract

On-chip nonlinear optics is a thriving research field, which creates transformative opportunities for manipulating classical or quantum signals in small-footprint integrated devices. Since the length scales are short, nonlinear interactions need to be enhanced by exploiting materials with large nonlinearity in combination with high-Q resonators or slow-light structures. This, however, often results in simultaneous enhancement of competing nonlinear processes, which limit the efficiency and can cause signal distortion. Here, we exploit the frequency dependence of the optical density-of-states near the edge of a photonic-bandgap to selectively enhance or inhibit nonlinear interactions on a chip. We demonstrate this concept for one of the strongest nonlinear effects, stimulated Brillouin scattering using a narrow-band one-dimensional photonic-bandgap structure: a Bragg grating. The stimluated Brillouin scattering enhancement enables the generation of a 15-line Brillouin frequency comb. In the inhibition case, we achieve stimulated Brillouin scattering free operation at a power level twice the threshold.

Introduction

Enhanced nonlinear interactions and spontaneous emission near the band edge of periodic structures [225, 226] have fascinated researchers for decades as a possible path towards power-efficient integrated photonics. The combination of strong field enhancement with prolonged light-matter interaction due to slow-light propagation [246, 204, 181] is a powerful technique for overcoming material constraints and can lead to a significant reduction in the size of photonic structures. Based on this idea, several milestone demonstrations [215, 247–249] in photonic circuits have been reported, including slow-light enhanced third harmonic generation [210], four-wave-mixing (4WM) [216], slow-traveling solitons [250] and gain enhancement in lasers [251]. Surprisingly, band edge effects on stimulated Brillouin scattering (SBS), one of the strongest nonlinear phenomena, have not been experimentally demonstrated to date. A power-efficient way to generate SBS, however, would advance on-chip SBS applications, in particular Brillouin lasers [130] and Brillouin frequency combs [132].

From another point of view, nonlinear interactions can limit the power efficiency in optical fiber communication links [252]. SBS, for example, is known to be detrimental for high-power continuous wave (CW) lasers and amplifiers [252, 28, 27] and degrades the performance of fiber and chip-based signal processors that exploit the Kerr nonlinearity [252]. In particular, the suppression of SBS in CW-pumped signal processing devices remains a significant challenge, calling for specially designed fibers with reduced Brillouin gain [252]. Similar problems arise in the context of on-chip phase-sensitive amplifiers and regenerators, which also rely on CW pumping [253, 254]. The ability to fully suppress SBS will therefore remove power limitations and lead to more efficient nonlinear interactions.

Current approaches minimize the generation of SBS by increasing the pump bandwidth via modulation of the pump phase and amplitude [253], or by using structures with poor acoustic guidance and hence low SBS gain such as silicon on insulator waveguides [254]. Nonlinear signal processing in silicon waveguides at telecommunication wavelengths has, however, its own limitations due to the presence of nonlinear absorption and free carrier generation [255, 256]. Here we present an experimental demonstration of an alternative approach, in which the efficiency of SBS is tailored by the presence of a photonic-bandgap (PBG).

The combination of SBS and a Bragg grating was previously studied in numerical models in the context of nonlinear pulse propagation [257] and improved delay line performance [258]. The latter study proposed a linear sequence of SBS-based slow-light and grating-based slow-light to increase the system's overall delay [258]. On the other hand, the use of a PBG structure has been suggested to suppress SBS inside the bandgap [29]. This concept is quite similar to the previously explored inhibition of spontaneous emission inside the bandgap of

photonic crystals [225, 231]. The experimental demonstration of SBS inhibition, however, remains challenging because the bandwidth of the periodic structure must be narrow enough to suppress the Stokes signal without impacting the pump and additionally the length of the periodic structure must match the length of the SBS gain medium. Therefore, 1m-long Bragg gratings were proposed to suppress SBS in silica fibers in the context of Q-switched lasers [29], whereas 4WM-based optical signal processing architectures usually use hundreds of meters of highly nonlinear fiber16 and would require prohibitively long periodic structures. The length of the SBS gain medium can be reduced to only a few centimeters by using highly-nonlinear materials to create photonic integrated circuits [259]. For example, very large Brillouin gain G_{SBS} can be achieved in an As_2S_3 chalcogenide waveguide (gain parameter $g_0 = 0.715 \cdot 10^{-9} m \cdot W^{-1}$) [75] due to the small effective mode area, A_{eff}, combined with high material refractive index and excellent overlap between optical and acoustical modes [75, 109]. Thus the Brillouin gain G_{SBS} can be about 500 times larger than in a silica single mode fibre [260]. The large value of G_{SBS} in such chalcogenide rib waveguides led to the first demonstration of on-chip SBS [75].

In this article we demonstrate both enhancement and inhibition of nonlinear scattering in a photonic integrated circuit by tailoring the optical density-of-states (DOS) associated with a one-dimensional photonic-bandgap, a stopband of a Bragg grating, written into a chalcogenide rib waveguide. We exploit slow-light enhancement of SBS to demonstrate a 15-line Brillouin frequency comb which is at least 5 Stokes orders broader than in demonstrations using chalcogenide waveguides reported previously [138]. In addition, we exploit the inhibition of nonlinear scattering inside the stopband to suppress SBS and achieve linear transmission at higher powers. Both demonstrations illustrate a unique capacity for tailoring the strength of a nonlinear interaction on a chip solely by means of frequency tuning.
Waveguide-long Bragg gratings in chalcogenide photonic chips can be written using interferometric techniques [240] or internal inscription [193, 241] and these enable both regimes, SBS enhancement and inhibition. The approach of using Bragg gratings provides several advantages over high-index contrast photonic crystals for the enhancement and inhibition of SBS, namely the narrow bandwidth of the stopband, low loss and potential tunability. The narrow bandwidth is crucial for the inhibition of SBS as only the Stokes wave should be affected by the stopband, whilst the pump wave will have full transmission. Although we demonstrate tailoring the strength of SBS in a chalcogenide chip, the same concept can be extended to other materials and nonlinear processes, e.g. 4WM and Raman scattering.

Results

The basic principle of enhancing and inhibiting SBS by a structure with a stopband in a highly nonlinear waveguide is illustrated in figure 5.6 a-c. A single-frequency laser is sent into a chalcogenide rib waveguide. If the pump power exceeds the threshold [108] for Brillouin scattering (P_{SBS}) a backscattered Stokes wave can be observed. The Stokes wave arises from the coherent backscattering of the pump wave from thermally excited acoustic phonons [108]. The phonons are moving along the waveguide at the speed of sound leading, via the Doppler effect, to a frequency downshift of the backscattered Stokes wave. This frequency shift equals the acoustic phonon frequency Ω_{B} and is typically in the gigahertz range ($\Omega_{\mathrm{B}} \approx 7.7\,GHz$ for As_2S_3 at $\lambda = 1550\,nm$).

Integrating a PBG structure in the gain medium gives an opportunity to tailor the nonlinear interaction strength, enabling both, enhancement and suppression of SBS. This concept is illustrated in figure 5.6b and c. Adjusting the pump wavelength so that the Stokes wavelength coincides with the edge of the photonic bandgap leads to an enhancement of the Stokes wave generation (b), whereas it is inhibited when the Stokes wavelength falls into the stopband (c). For wavelengths inside the stopband, light is not allowed to propagate, the transmission reaches a minimum and hence no field can build up at these wavelengths. Near the band edges, however, a light signal travels on average slower due to multiple coherent reflections from the refractive index modulation, leading to a field enhancement. This is similar to the description of electron behavior near the electronic bandgap and the DOS formulation in solid-state physics [225, 261, 262]. Using this analogy, the optical DOS is expected to change drastically in the vicinity of the photonic stopband: at the band edge, in the slow-light region, the DOS increases, while it approaches zero inside the stopband (figure 5.6d). We exploit the low DOS inside the stopband to inhibit the build-up of a Stokes wave and suppress SBS. On the other hand, the high DOS at the edge of the stopband can be used to enhance the generation of a Stokes wave.

If the power of the 1st Stokes wave exceeds P_{SBS}, SBS can be cascaded generating a 2nd-order Stokes wave shifted by $2\,\Omega_B$ from the pump. The power requirements for cascaded SBS can be reduced substantially in resonators [138, 88, 84]. For the rib waveguides we use, 17% reflectivity is expected from the cleaved facets due to the large index mismatch between As_2S_3 (≈ 2.43) and the surrounding air. The combination of high SBS gain material and feedback from the facets already enabled the observation of a 2nd order Stokes wave in a chip scale device [138]. However, for practical applications in microwave photonics and arbitrary waveform generation, on-chip sources with a larger number of spectral lines are necessary, thus the efficiency of the SBS cascading process has to be further improved.

PBG structures can be a solution for power-efficient SBS cascading and the formation of

broad-bandwidth Brillouin combs. This, however, requires a distinctive design of the PBG structure, featuring multiple stopbands exactly matching the Brillouin shift Ω_B and being narrow bandwidth. A schematic of such a structure is shown in figure 5.6e, which illustrates the alignment of the pump and several Stokes waves with the edges of the multiple stopbands, leading to simultaneous enhancement of several waves.

Enhancement of stimulated Brillouin scattering

First we demonstrate the enhancement of the SBS cascading process near the band edge of a grating. A measured spectrum of a Brillouin frequency comb generated by using this method is shown in figure 5.7a. The graph shows the output comb spectrum in transmission and the alignment of the comb lines with the edges of a multiple bands of the grating (red spectra in figure 5.7a). The superstructure grating was inscribed into the highly nonlinear rib waveguide beforehand, following the method discussed in ref. [241]. The three stopbands of this grating were formed by designing the writing beam to be a cascade of three waves (pump, 1st Stokes and 2nd Stokes). This ensured the separation between the gaps to be exactly the frequency shift Ω_B in the chalcogenide waveguide (≈ 64)pm [75]. A high-resolution spectrum of our multi-band grating is shown in figure 5.7b.
The enhancement effect at the band edges of the grating was demonstrated by scanning the pump laser wavelength across the grating spectrum (figure 5.7c) with the pump power ($P_P \approx 0.5$)W adjusted just below the measured power threshold $P_{SBS} \approx 0.6$ W. The measured value for P_{SBS} agrees well with the theoretically calculated threshold given by [40]:

$$P_{SBS} = \frac{2\pi^2 \cdot A_{eff}}{g_0 \cdot L_{eff} \cdot F^2} = 0.59\,\mathrm{W} \tag{5.3}$$

with the SBS gain parameter, $g_0 = 0.715 \cdot 10^{-9}\mathrm{m} \cdot \mathrm{W}^{-1}$, the effective length $L_{eff} = 5.5$ cm, $A_{eff} = 2.3\,\mu\mathrm{m}^2$ and the measured finesse of the cavity $F = 1.40$. The pump power P_P was kept constant during the wavelength sweep and no Stokes waves were generated at frequencies far from the photonic stopband (black curve in figure 5.7c). However, aligning the pump wavelength with the first band edge of the multi-band structure led to a strong enhancement of the SBS generation and cascading process (red curve in figure 5.7c). This enabled the formation of a Brillouin frequency comb with 4 Stokes waves (1S-4S) at a sub-threshold ($\leq P_{SBS}$) power level. Tuning the pump further towards the longer wavelength showed an enhancement effect, although more moderate, every time the pump wave hit one of the band edges of the multi-band grating.

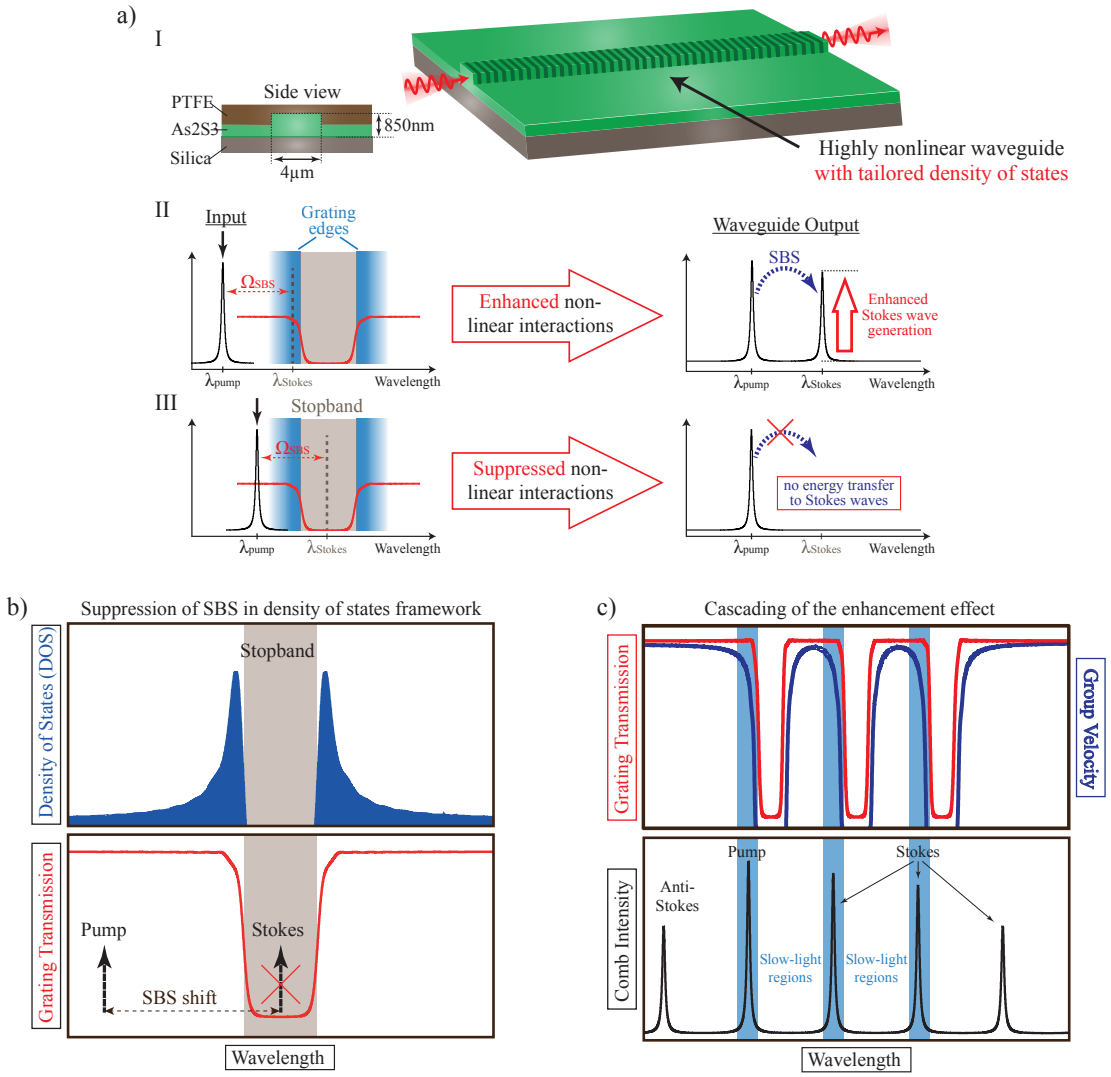

Fig. 5.6 **Figure 1 | Basic principle for enhancing or inhibiting SBS by tailoring the DOS in a waveguide.** a, Scheme of the 850 nm by 4 µm chalcogenide (As_2S_3) rib waveguide on a silica substrate with a Polytetrafluoroethylene (PTFE) over-cladding. b, Tuning the frequency of the optical waves (here shown for the 1st Stokes wave) into the slow-light region at the band edge of the PBG leads to an enhancement of the nonlinear interactions. c, Adjusting the pump frequency so that the Stokes frequency falls into the stopband, however, leads to an inhibition of the SBS process. d, Illustrates the distribution of the density-of-states and the stopband for a one-dimensional PBG structure. The DOS increases towards the band edge of the structure and approaches zero in the stopband, which enabled the full suppression of any Stokes wave generation. e, Shows schematically how the enhancement effect can be cascaded using a multi-band grating to form a Brillouin frequency comb. It illustrates the distinctive design of the multi-band grating, matching the Brillouin shift and each having narrow bandwidth, so that multiple comb lines are aligned with the grating edges.

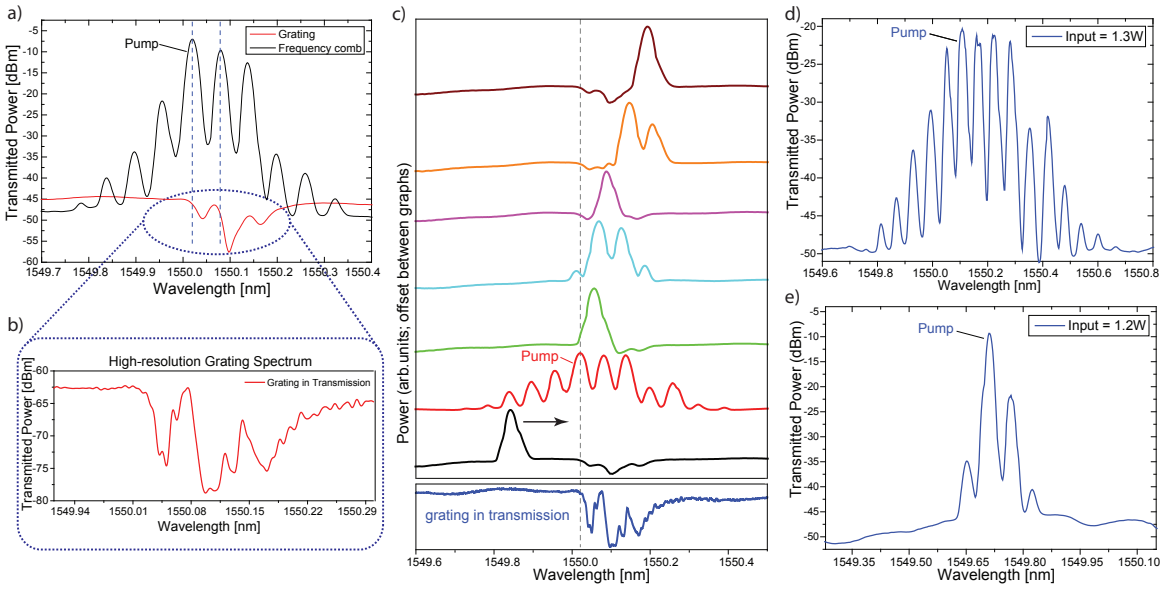

Fig. 5.7 **Figure 2 | Slow-light enhancement effect of stimulated Brillouin scattering.** a, Alignment of the Brillouin frequency comb with respect to the multi-stopband Bragg grating. The pump and lowest order Stokes waves lay at the edges of the individual stopbands, where the DOS was high but the normalised transmission was almost unity. b, High resolution spectrum of the multi-stopband structure. c, Wavelength scan across the grating spectrum. The SBS process was significantly enhanced in the slow-light regions. d, Brillouin frequency comb with 15 lines generated by harnessing the tailored DOS in the waveguide. e, Maximum SBS cascading in the waveguide without the grating.

The largest enhancement effect is observed when the waves with the highest intensities in the waveguide, namely the initial pump, 1st and 2nd Stokes wave coincide with the band edges of the grating. A Brillouin comb with 15 distinct comb lines could be generated by increasing the pump power to about $1.3\,\mathrm{W} \approx 2 \times P_{\mathrm{SBS}}$ (figure 5.7d). This is the broadest Brillouin frequency comb generated in a chip-scale low-Q waveguide, exceeding previous demonstrations by 5 Stokes orders [138]. Recently Büttner et al. [132] demonstrated that Brillouin frequency combs generated in a low-finesse chalcogenide fibre cavity show phase-locking mediated by an interplay of 4WM and SBS. This is an important find since phase-locking is crucial for all frequency comb applications. The enhancement effect demonstrated in this article provides a way to increase the effective SBS gain in a highly nonlinear waveguide and shows a path towards power-efficient, on-chip integrated GHz repetition rate light sources.

The enhancement of the nonlinear interactions at the band edge of the PBG can be attributed to an amplified light-matter interaction in the slow-light regime by a factor $S = n_{\mathrm{g}}/n$. This slow-down factor S determines how much slower a light signal travels in the PBG structure compared to the bare waveguide. Figure 5.8a shows a measured (blue) and simulated (red)

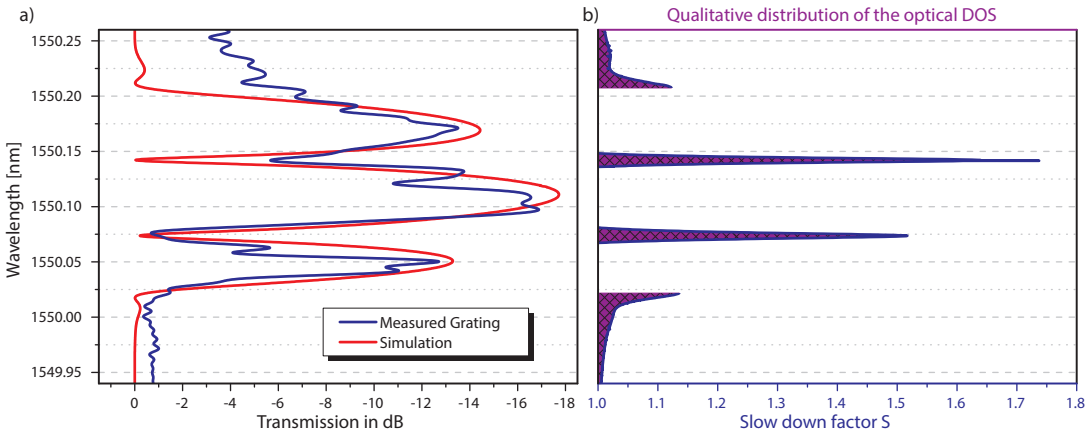

Fig. 5.8 **Figure 3 | Simulation of the PBG structure and the group index.** a, High resolution grating spectrum and simulated grating spectrum obtained by solving the coupled equations for the transmitted and reflected waves in the waveguide. b, Calculated slow-down factor S from the simulated grating. The graph also represents qualitatively the distribution of the DOS in the waveguide.

transmission spectrum, respectively, for the multi-wavelength Bragg grating used in our experiment. The red spectrum was obtained by solving the coupled-mode equations and presents a good fit to the experimental data. Based on the numerical fit we can determine the slow-down factor S for each frequency across the grating spectrum (figure 5.8b). The slow-down factor S can be deduced by normalizing the group delay [258] $\tau = \frac{d\varphi}{d\omega}$ that a light signal acquires during propagation through the Bragg grating to the transit time $\tau_{tr} = 550\,\text{ps}$ in the waveguide without grating (φ describes the phase transfer function of the optical wave). We find that the slow-down factor reaches its maximum value of $S = 1.75$ at the band edge of the second stopband (figure 5.8b). It is well known for photonic crystals that the optical DOS is proportional to S at the band edges [263] and approaches zero in the stopband. Figure 5.8b gives a qualitative distribution of the optical DOS in the vicinity of the PBG structure.

The SBS gain G_{SBS} increases exponentially with the Brillouin gain coefficient g_0 and the input pump power P_{P} [108]. In a similar approach as used to describe the gain enhancement of band edge lasers [251], G_{SBS} is expected to increase in the slow-light region due to a build-up of the local energy density proportional to S [213]. The energy build-up is a result of the coherent coupling of forward and backward traveling waves through the grating. However with $S < 2$ this approach cannot fully explain the significant enhancement in the SBS cascading process we observe in our experiments. Below we discuss additional factors that influence the comb formation and determine the power efficiency of this process.

Firstly, the high optical DOS at frequencies near the grating band edges leads to enhanced

spontaneous scattering at these frequencies by S [264, 265]. As shown by Smith [182], the Stokes power is given by the sum of all spontaneously scattered photons along the gain medium multiplied by the Brillouin gain. Thus, an increase in the optical DOS by a factor of S will lead to S-times higher Stokes power, in accordance with Fermi's golden rule which follows directly from second order perturbation theory [266].
Secondly, chalcogenide glass is a material with strong χ^3 nonlinearity as well as Brillouin gain. This implies strong multi-wave interactions between the comb components. As soon as the 1st Stokes wave is generated at frequency $\omega_{1S} = \omega_p - \Omega_B$ and is reflected by the waveguide facet, it co-propagates with the pump leading to 4WM and the generation of a signal at the frequency $\omega_{2S} = \omega_p - 2\Omega_B$ and an idler at the frequency $\omega_{1AS} = \omega_p + \Omega_B$. These, in turn, can excite higher order waves at frequencies $\omega_{nS} = \omega_p - n\Omega_B$ and $\omega_{nAS} = \omega_p + n\Omega_B$. In this manner generated optical waves act as seeds for the SBS process and, therefore, have the ability to reinforce SBS and lower the threshold for the generation of higher order Stokes waves. Previous studies demonstrated a 10-fold reduction of the SBS threshold when the Stokes wave was seeded instead of initiated from noise [267–269]. It is worth noting that for a given power (P), the 4WM gain in the chalcogenide rib waveguides is at least 30 times lower than the SBS gain. If we assume zero phase mismatch (largest gain) for the 4WM process we obtain the following expression for the 4WM and SBS gain coefficients, respectively [184]:

$$G_{FWM} = 2 \cdot \gamma \cdot P \cdot L_{eff} \approx 10.6 \cdot P \cdot L_{eff} << G_{SBS} = \frac{g_0 \cdot P \cdot L_{eff}}{A_{eff}} \approx 311 \cdot P \cdot L_{eff} \qquad (5.4)$$

with the nonlinear parameter γ. However, the strength of 4WM interactions that include comb components aligned with the band edges of the PBG structure increases [216] since the intensities of these components are enhanced due to a coherent energy build-up.The large amount of anti-Stokes components of the Brillouin frequency comb in figure 5.7 is a strong indicator that 4WM is present in the comb formation. However, the asymmetry of the comb spectrum demonstrates that SBS is the dominant process.

Inhibition of stimulated Brillouin scattering

As we have already noted, the wavelength-dependent DOS near the band edge of a periodic structure allows not only the enhancement of a nonlinear interaction but also its suppression. It is, therefore, possible to suppress spontaneous and stimulated Brillouin scattering completely if the frequency of the Stokes wave falls into the stopband. The pump wave, however, can lie outside the bandgap because it is shifted by the Brillouin frequency, Ω_B.

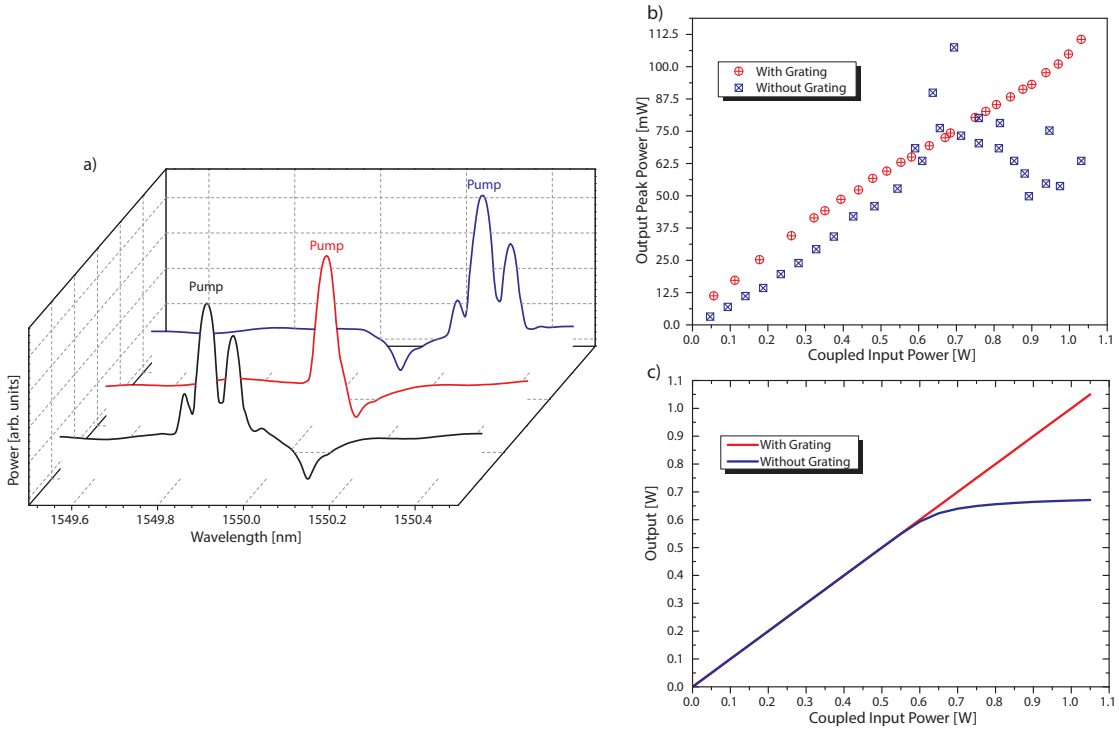

Fig. 5.9 **Figure 4 | Harnessing the tailored DOS to fundamentally inhibit SBS in the waveguide.** a, Spectra obtained as the wavelength of the pump ($P_P = 0.8\,W$) was scanned relative to the PBG structure. The power was just above the SBS threshold $P_{SBS} = 0.6\,W$ and a Stokes and Anti-Stokes wave was generated at frequencies outside the stopband. By positioning the pump so that the Stokes wave fell into the stopband, SBS was no longer generated. b, Pump power output with (red data points) and without (blue data points) the PBG structure. Without the grating the pump was depleted as soon as the SBS threshold was reached whilst with the grating the generation of SBS was inhibited and no pump depletion was observed. c, Simulations of the experiment obtained by solving coupled mode equations with and without grating confirming the measurements presented in (b).

Provided the bandwidth of the bandgap is narrower than Ω_B, the propagation of the pump is unaffected by the periodic structure. Since no Stokes wave is generated in this situation, the transmission of the pump wave remains linear at any power and pump depletion does not occur. Figure 5.9a demonstrates this concept using a single stopband Bragg grating. The pump wavelength was tuned across the stopband, whereas the pump power was fixed above the SBS threshold $P_P = 0.8W > P_{SBS}$. As can be seen in figure 5.9a, away from the grating stopband a strong Stokes wave was generated. The Stokes wave, however, was suppressed when the wavelength of the Stokes wave λ_S coincided with the center of the grating stopband λ_B. To quantify the inhibition of the Stokes wave we measured the output pump power for different input power levels with and without grating (figure 5.9b). A narrow bandpass filter

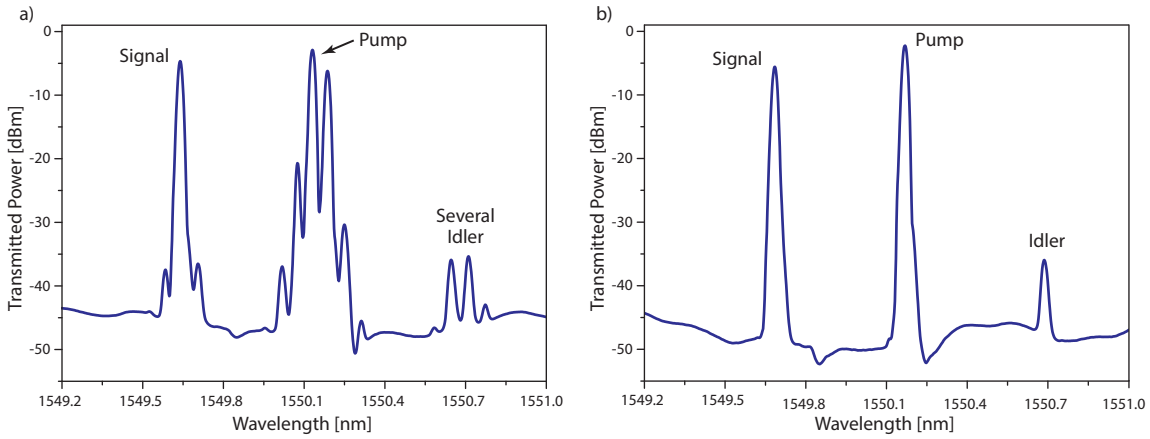

Fig. 5.10 Figure 5 | Utilizing the tailored DOS to inhibit SBS in a 4WM experiment. a, 4WM experiment without the Bragg grating. SBS generated several idlers and, therefore, limited the maximum input power and could lead to parasitic beat signals between several SBS lines. b, The same experiment in the presence of the grating. For the same input power no SBS was generated and therefore a single idler could be produced.

with 80 pm bandwidth was used before the detector to isolate the transmitted pump power from the Stokes power. For the Stokes wavelength $\lambda_S \neq \lambda_B$, SBS generation occurred and the pump power was depleted at power levels above the SBS threshold (blue squares in figure 5.9b). This, however, does not happen when $\lambda_S = \lambda_B$ and therefore the transmitted pump power grew linearly with the input power and no sign of depletion could be seen (red circles in figure 5.9b).

We modeled our system using coupled-mode theory, similarly to that in ref. [29]. The results of the numerical modeling are shown in figure 5.9c and show excellent agreement with the experiment. This demonstration of SBS suppression can have a significant impact on the efficiency of ultrafast chip-based all-optical signal processing [270, 271]. We note that complete SBS suppression for an arbitrary input pump power is only possible in theory for infinitely strong gratings. In practice, however, it is not required and doubling or tripling the SBS threshold can be substantial.

To demonstrate the practicality of our approach for suppressing SBS, we performed a 4WM experiment using our chalcogenide chip. A CW signal with an average power of 15 mW and a pump with a peak power of about 1 W were coupled into the waveguide. As the pump power exceeded the SBS threshold, several Stokes waves were generated in the waveguide (figure 5.10a). This led to the generation of multiple idler waves via four-wave mixing between the signal, the pump and the Stokes waves. To inhibit the generation of multiple waves at the signal and idler frequencies, we tuned the pump frequency close to the grating stopband, so

that SBS was inhibited and in these conditions only a single idler and signal were produced (figure 5.10b).

Discussion

We have demonstrated a powerful and flexible way to tailor the strength of nonlinear interactions, from strong enhancement to full suppression, at fixed input power in an on-chip highly-nonlinear waveguide. Inscribing a PBG structure in the waveguides and harnessing the high optical DOS at the band edge led to a significant enhancement in SBS cascading. We applied this method to generate a Brillouin frequency comb with 15 lines in a low-Q rib waveguide. Band edge enhanced cascaded SBS is a promising method for the generation of on-chip coherent Brillouin frequency combs and are an attractive alternative to 4WM based micro resonator frequency combs [272]. Brillouin frequency combs exhibit GHz line spacing and can be phase locked [132, 273, 134]. Furthermore, SBS cascading is known to suppress the pump phase and amplitude noise with each successive Stokes component [114]. This linewidth narrowing effect is expected to play a significant role for generating low-noise Brillouin frequency combs. High spectral purity and stability are greatly desirable for on-chip microwave generation and low noise chip-scale optical-to-digital synthesizers.
As well as enhancing nonlinear interactions, we demonstrated the feasibility of tailoring the optical DOS to fundamentally inhibit nonlinear processes. We showed that no Stokes wave was generated inside the bandgap of a PBG structure, where the DOS approaches zero. As the build-up of the Stokes wave was inhibited, no energy was transferred from the pump to the Stokes wave and, therefore, no pump depletion occurred. This technique can be exploited to improve the performance of high power lasers and amplifiers, to design power independent optical devices and chip-based 4WM architectures. We have demonstrated this concept in a 4WM experiment and achieved SBS-free operation. This could lead to improved communication links based on on-chip parametric amplification and all-optical signal processing schemes.

Methods

Experimental Setup

A schematic of the basic setup of the experiment is shown in figure 5.11. A narrow linewidth laser at 1550 nm with a bandwidth of 500 kHz was used as a pump source for the enhancement as well as the suppression experiments. The CW laser light was carved into 400 ns pulses with

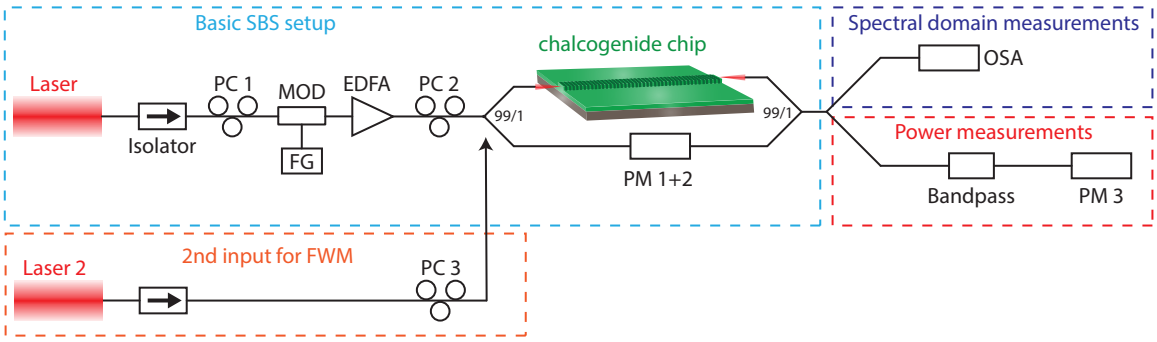

Fig. 5.11 Figure 6 | Schematic of the experimental setup. A narrow linewidth laser was coupled to a highly nonlinear rib waveguide (light blue box). The waveguide output was monitored in the spectral domain (dark blue box) and the power domain (red box). For the 4WM experiment a second narrow linewidth input laser was added to the setup and coupled into the waveguide. PC: polarisation controller, MOD: modulator, FG: function generator, EDFA: erbium doped fibre amplifier, PM: power meter, OSA: optical spectrum analyser.

a repetition rate of 40 kHz using a Mach-Zehnder modulator driven by a function generator. The bandwidth of the coupled laser light was, therefore, determined by the pulse length and was around 2.3 MHz. The pulses were much longer than the transit time of 550 ps for the chip. Operating in a quasi-CW regime allowed high peak power levels in the waveguide while keeping the average power low. Therefore, we are able to observe strong SBS without accumulative heating of the waveguides which prevented waveguide damage. An erbium doped fiber amplifier (EDFA) was used to amplify the laser pulses before coupling to the chip and a polarization controller allowed the coupled light to be in the TE mode, which is the lowest loss mode of the waveguide. The light was coupled into the waveguide using lensed fibers with a focal spot diameter of 2 µm and a measured fibre-to-fibre coupling loss of 2.5 dB. Overall the insertion loss of the 6.8 cm long rib waveguide was 10 dB, which was permanently monitored during the experiment using a 99/1 coupler at the waveguide input and output connected to a dual channel power meter. The refractive index of the guiding material was 2.43 leading to a maximum feedback of 17% from the cleaved facets because of the index mismatch to the surrounding air. The waveguide output was monitored with an optical spectrum analyser (OSA) with 8 pm resolution.

The high resolution spectra of the grating were measured with an OSA that is based on coherent detection and has a resolution of 1.2 pm. The spectra were Fourier filtered to remove the high frequency Fabry-Perot oscillations at about 900 MHz to obtain clear spectra of the grating itself. These Fabry-Perot fringes were about 1 dB deep, as the feedback from the facets is low. Therefore, the pump and the Stokes waves did not need to be perfectly aligned and stabilized to the cavity resonances to observe SBS.

For the SBS inhibition experiment a 99/1 coupler at the waveguide output was used to simultaneously measure the pump output power (99% port) and the optical spectra (1% port). To ensure that only the pump power was measured, we used an 80 pm bandpass filter between the waveguide output and the power meter.
A second narrow linewidth laser was added to the setup and coupled into the rib waveguide for the demonstration of SBS-free operation of a 4WM experiment (orange box in figure 5.11). Polarization controllers (PC 3 and PC 2 respectively) were used to ensure that both lasers are coupled to the TE mode of the rib waveguide.

Sample preparation

The highly nonlinear rib waveguide was fabricated by thin film deposition followed by several etching and annealing techniques [274]. An 850 nm thick As_2S_3 layer was deposited on a thermally grown 1.5 µm thick SiO_2 (n = 1.44)/silicon substrate by thermal evaporation. Thermal and photo annealing of the chalcogenide thin film, led to a bulk-like refractive index of 2.43 ref. [275]. The rib waveguide was fabricated by standard contact photo-lithography and inductively coupled plasma reactive ion etching using CHF_3 gas [276]. The etch depth for the 4 µm wide waveguides used in this work was 425 nm. As a protection layer a PTFE over-cladding was deposited on the chip [277].
The technique used for the inscription of a multi-stopband grating with the distinctive design (the stopband spacing matching the Brillouin shift) is based on the method by Hill et al. [193]. It utilized the photosensitivity of the As_2S_3 waveguide films [245, 244]. Gratings written using this method were reported previously by us for chalcogenide fiber [241] and the method is the same for the chip geometry.

Simulation methods

To simulate the suppression experiment we solved the coupled mode equations for the pump, 1st Stokes and the acoustic wave in the presence of a PBG structure and without the PBG structure using an implicit fourth-order Runge-Kutta method [278]. The coupled mode equations can be found in ref. [29].
For the simulation of the multi-wavelength grating we solved the steady state coupled equations for complex amplitudes E_1 of the forward-travelling wave and E_2 of the reflected backward-travelling wave, respectively, in the presence of the multi-bandgap structure. The equations had the following form:

$$\frac{dE_1}{dz} = i \cdot \kappa_1(z) \cdot E_2 \cdot exp(-2i \cdot \delta_1 \cdot z) + i \cdot \kappa_2(z) \cdot E_2 \cdot exp(-2i \cdot \delta_2 \cdot z) + i \cdot \kappa_3(z) \cdot E_2 \cdot exp(-2i \cdot \delta_3 \cdot z) \tag{5.5}$$

$$\frac{dE_1}{dz} = -i \cdot \kappa_1(z) \cdot E_2 \cdot exp(2i \cdot \delta_1 \cdot z) - i \cdot \kappa_2(z) \cdot E_2 \cdot exp(2i \cdot \delta_2 \cdot z) - i \cdot \kappa_3(z) \cdot E_2 \cdot exp(2i \cdot \delta_3 \cdot z), \tag{5.6}$$

where κ_1, κ_2 and κ_3 describe the maximum grating strength of the three stopbands and are 109, 174 and 144 m^{-1}; δ_1 to δ_3 are the detunings from the center of the stopband; and z is the spatial component along the waveguide. We solved these equations using a standard numerical ordinary differential equation solver integrating z over the length of the chip.

5.3 Outlook

In this section further investigations of cascaded SBS and an outlook of further applications of on-chip gratings, in the context of SBS and nonlinear optics in general, is presented.

Phase-locking of Brillouin frequency combs

We have seen that on-chip Bragg gratings are able to greatly enhance the cascading of SBS in chalcogenide waveguides. Pumping the waveguide with a single frequency laser leads to the generation of multiple new frequencies spaced by the Stokes shift Ω_B, i.e., a BFC can be generated [33]. However, any practical application of a frequency comb requires not only a cascade of multiple frequency components, but also a fixed phase relationship between the single comb lines. This effect is called phase-locking and ensures that the individual comb lines are equally spaced. Phase-locking, furthermore, leads to a stable pulse train at the output of the waveguide.

Before describing the phase-locking mechanism of the BFC we want to have a closer look at the generation of the BFC. Chalcogenide waveguides do not only possess a large Brillouin gain coefficient g_B but also a large nonlinear index $n_2 = 3.0 \times 10^{-}18\,\mathrm{m/W}$ [259]. This large nonlinear index n_2 leads to a strong Kerr effect and hence 4WM (see also figure 5.10). 4WM is a third order nonlinear process that mixes multiple optical waves and generates optical waves at new frequency components given that a phase-matching condition is fulfilled [108]. We will see below that 4WM plays a crucial role in the phase-locking of the BFC.

The comb formation starts with an optical pump wave generating a Stokes wave that is frequency shifted by the Brillouin frequency shift Ω_B. 4WM can then create new frequency components separated by $2\Omega_B$ and $-\Omega_B$ from the optical pump frequency. 4WM of counter-propagating optical waves, however, is usually weak due to the required phase matching condition of 4WM. In the waveguides used for the experiments in this chapter the cleaved facets provide around 17% feedback, which leads to a build-up of pump and Stokes waves that are traveling in both directions within the waveguide. As the Brillouin shift is very small (around 64 pm) phase matching between the co-propagating waves is fulfilled, and strong 4WM could be observed. This effect is further amplified by the presence of the Bragg grating. The optical waves generated at multiple frequencies of Ω_B act as seeds for the SBS process. SBS further amplifies the seed waves generated via 4WM.

The most direct way to confirm that the individual Brillouin comb lines are phase locked is to measure a stable pulse train at the waveguide output with a fast real-time oscilloscope [133, 132]. A trace of such a measurement is presented in figure 5.12.

A pulse train can be clearly identified in figure 5.12. The phases of the BFC are fully

deterministic as the same pulse train can be observed for individual quasi-CW pump pulses. This behavior is visualized in figure 5.12 b), in which the output traces of 11 pulse trains recorded over 5 ms are superimposed on each other.

The underlying physics behind the phase-locking mechanism of the on-chip BFC is rather complex and was studied in detail in [133, 132]. As SBS is a coherent interaction, there is a certain fixed phase relationship between the pump and the first order Stokes wave. Therefore it was realized from early on that SBS can lead to phase-locking [36, 38]. However, the situation changes if one considers higher order Stokes waves in the case of backward SBS, which can be seen directly from the dispersion diagrams shown in section 2.2. The dispersion of the acoustic wave in backward SBS is not entirely flat, and hence the Stokes frequency shift Ω_B changes slightly with every cascading step. This is in stark contrast to forward Brillouin interactions where the acoustic frequency band is flat. Hence forward cascading and pulse train generation could be observed to many orders [139, 140] and passive mode-locking to the 337th harmonic of a fiber laser cavity could have been demonstrated using forward Brillouin interactions [139].

In the case of backward SBS the acoustic dispersion is not flat. Hence the Brillouin frequency shift Ω_B changes a tiny amount with every cascading order. As a consequence multiple order Stokes waves cannot couple to a single acoustic wave. In the case of backward SBS, phase-locking is achieved by 4WM, as it couples optical waves in a phase-sensitive manner [133, 132]. The crucial role of 4WM for the phase-locking of BFC was confirmed in an

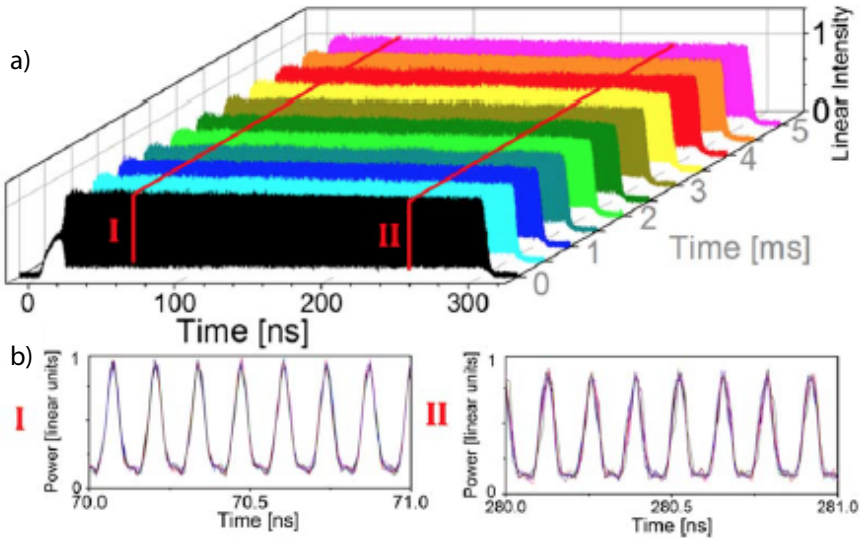

Fig. 5.12 a) Show 11 time traces of the quasi-CW 300 ns long pulses recorded over 5 ms [133]. b) Shows two zoom-ins on the pulses at two positions. All 11 traces are superimposed on each other [133].

extensive numerical analysis [132], in which the 4WM interaction was selectively switch on or off.
The stable pulses generated via cascaded backward SBS in chalcogenide waveguides are below 100 ps in pulse length and have a repetition rate of around 7.5 GHz. The repetition rate is given by the Brillouin frequency shift Ω_B and hence distinguishes the BFC from other types of frequency combs such as mode-locked lasers or microresonator combs. In the two later cases, the repetition rate is given by the roundtrip time of the cavity/ FSR of the cavity. This puts the BFC in a niche spot between the free-space mode-locked lasers and micro-resonator combs. Mode-locked laser cavities usually provide a repetition rate in the order of up to a GHz, with further increase in frequency being challenging as it requires a further reduction of the cavity length which is difficult due to the size of most laser components (a heroic effort of a 10 GHz mode-locked laser forms an outstanding exception [279]). Most microresonator combs rely on very small cavities, usually in the tens to hundreds of micrometer range (excluding the up to mm sized silica resonators [85] presented earlier). Hence they generate frequency combs with repetition rates in the order of THz to hundreds of GHz.

Future directions of Brillouin frequency combs

As described in the previous section the here generated BFCs have a repetition rate given by the Brillouin frequency shift and not the FSR of the cavity. The generated combs were furthermore free running without the need for further stabilization. The reason for not requiring external stabilization lies in the low Q-factor of our cavity. But on the other hand, the low Q-factor limits the amount of feedback and hence restricts a number of comb lines that can be generated. Hence to generate a broader frequency comb with more comb lines the quality factor of the cavity should be increased.
An increase of the Q-factor of the waveguide cavity could be achieved by coating the facets of the waveguide with a gold layer, which increases the reflectivity of the facets. An increase of the Q-factor, however, imposes additional considerations: first of all, in the case of a high-Q cavity, the Brillouin frequency shift Ω_B needs to match precisely the FSR of the cavity. Hence extra care has to be taken during the fabrication to precisely control the length of the waveguide. Second, a cavity with increased Q-factor would require additional stabilization to lock the pump laser to the cavity resonance and avoid thermal drifts.
It would be interesting to investigate a Brillouin based frequency comb in such a high-Q waveguide resonator and compare the performance to a comb solely based on 4WM. Interesting in this context would be in particular the noise properties of the generated higher order Stokes waves. It was shown that the pump laser noise is reduced for the first and second Stokes wave; however, it is yet to be determined what happens for even higher orders. This

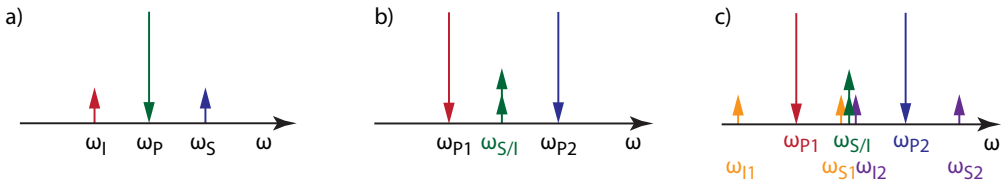

Fig. 5.13 a) Spontaneous single pump 4WM. b) Ideal dual pump 4WM scheme and c) dual pump scheme with spurious idler and signal photons.

study would require a carefully stabilized set-up, as otherwise, the drift of the cavity will be the main noise source observed. However, several stabilizations techniques based on feedback loops have been developed over the years and show the feasibility of the suggested study.

Suppression of spurious photons for quantum experiments

As fleshed out in the publication presented in this chapter, suppressing SBS can have a large impact on many optical signal processing schemes based on nonlinear optics. However, the concept of using a photonic bandgap can also be extended to other nonlinear effects beyond SBS. Based on the here presented technique, an interesting theoretical study proposes to suppress spurious photons in a single photon generation experiment [280] and hence extends the concept from applications in classical optical signal processing to the quantum regime.
It is known that spontaneous 4WM can produce non-classical states of light [281, 282]. In general there are two different 4WM configurations in a waveguide: First, there is the single pump configuration that creates a signal and an idler wave at each side of the pump spectrum (see figure 5.13 a)). Due to energy conservation the frequencies of these two generated photons are connected to the pump photons via $2\omega_\mathrm{p} = \omega_\mathrm{S} + \omega_\mathrm{I}$.
The second configuration relies on two detuned optical pumps and the single photons generated in the frequency range between the two (see figure 5.13 b)). The energy conservation dictates $\omega_{\mathrm{P1}} + \omega_{\mathrm{P2}} = \omega_\mathrm{S} + \omega_\mathrm{I}$. This second configuration is preferred for single photon generation experiments as it provides spectrally degenerate single photons. However, it faces the challenge that the two pumps can also individually act as a pump for the generation of signal and idler photons (as shown in the single pump configuration in figure 5.13 a)). Hence spurious signal and idler photons are generated in the region between the two pumps (see figure 5.13 c)).

It was theoretically shown [280] that these spurious single photons can be suppressed using a bandgap structure to inhibit the generation of the signal photons ω_{S2} from the higher frequency pump ω_{P2} and the generation of the idler photons ω_{I1} of the lower frequency pump

ω_{P1}. In this way, the generation of the spurious single photon in between the two pumps $\omega_{P1/P2}$ will also be suppressed, and the coincidence to accidental ratio of the single photon source will be improved.
As chalcogenide waveguides have large Kerr nonlinearity, a 4WM based quantum experiment with suppressed spurious photons is feasible. It would not only extend the bandgap engineered suppression technique to other nonlinear optical effects but also extend it to the quantum regime.

Potential further studies of the interaction of SBS and on-chip gratings

Recently a Brillouin-based distributed sensing technique was shown in integrated chalcogenide waveguides [175] - a breakthrough that was enabled by achieving record resolution of sub-mm in a Brillouin distributed sensing technique. With this technique one can map the Brillouin gain along the waveguide. It would be interesting to scan a waveguide that includes a Bragg grating and monitor locally the Brillouin gain and Brillouin frequency shift. This mapping could provide crucial information about the uniformity of the grating and its influence on Brillouin shift and gain enhancement.

So far the gain enhancement and the suppression effect were treated separately, however, an idea that would harness both effects simultaneously is Brillouin cooling. As stated by Chen and Bahl [283] for cooling based on Raman scattering, there are
"two fundamental requirements for achieving spontaneous Raman cooling: suppressing the dominance of Stokes (heating) transitions and the enhancement of anti-Stokes (cooling) efficiency".
This asymmetry can be achieved by tailoring the DOS. The same underlying physics, however, applies for optomechanical cooling [57, 94, 284, 285]. The Stokes wave needs to be suppressed while the anti-Stokes is responsible for the cooling effect. In a resonator configuration, this asymmetry is usually achieved by aligning the anti-Stokes wave with a cavity resonance while the Stokes wave falls in between the cavity lines, and therefore it is not building up at the same rate as the anti-Stokes wave.
In the experiment presented in this chapter, we can suppress and enhance Brillouin interactions selectively. Hence one could use the photonic bandgap structure to suppress the Stokes wave generation and at the same time enhance the anti-Stokes generation and perform a Brillouin cooling experiment in a waveguide instead of a resonator.

Another potential direction of Brillouin interactions in high gain waveguides, which include Bragg gratings, is a chip-scale random Brillouin laser. These types of lasers have been

recently shown in fibers [127–129]. Demonstrating an on-chip Brillouin random laser would require the inscription of a random grating [286–288]. Besides the obvious improvement in size and overall footprint, an on-chip Brillouin random laser implementation would greatly benefit from the two orders of magnitude larger Brillouin gain. Random lasers are for example of great interest for imaging due to their speckle-free operation [131] and displays with advanced functionalities, such as temperature sensitivity [289].

Concluding remarks

We have demonstrated that on-chip gratings have great potential to control the interaction strength of SBS. It was shown that band edge enhancement effects that were previously studied for other nonlinear effects can also be applied to SBS, and lead to a lower threshold and higher efficiency. It also enables cascading SBS in waveguides, which lead to the generation of on-chip phase-locked frequency combs.
Furthermore, we demonstrated that periodic structures can be applied to suppress nonlinear optical effects selectively - an effect not widely studied in nonlinear optics yet. Also extending the presented concepts to the quantum regime offers promising new opportunities.

Chapter 6

SBS with radio frequency feedback

In this chapter, we show how SBS can produce stable microwave oscillations when operated in a hybrid optical-electrical RF cavity. This type of hybrid cavity approach is known as an OEO and was pioneered by Yao and Maleki [290]. The OEO has proven to overcome challenges commonly faced in electronics when it comes to high-frequency microwave synthesis.
Here, we show that harnessing on-chip SBS in such a configuration enables not only the generation of a stable single frequency microwave tone but also allows for ultra-wide frequency tunability. However, before providing and discussing the performance of an on-chip SBS OEO configuration, a general introduction to OEOs is given.

6.1 Introduction

Oscillators are one of the most ubiquitous building blocks in many applications. Their ability to produce a stable periodic signal is used for timekeeping, distance measurement, as a local reference to identify and generate signals and many more. Hence the most important quantity of an oscillator is to keep the oscillation period preciously. In more technical terms, it means that the generated oscillations have to exhibit high spectral purity, i.e., only minimum fluctuations in the frequency which can be expressed in terms of the phase noise of the signal. The stability or purity of any oscillator depends on its capability to store energy. A figure of merit for this capability is given by the Q-factor of an oscillator:

$$Q = \frac{\text{frequency}}{\text{loss rate}} \tag{6.1}$$

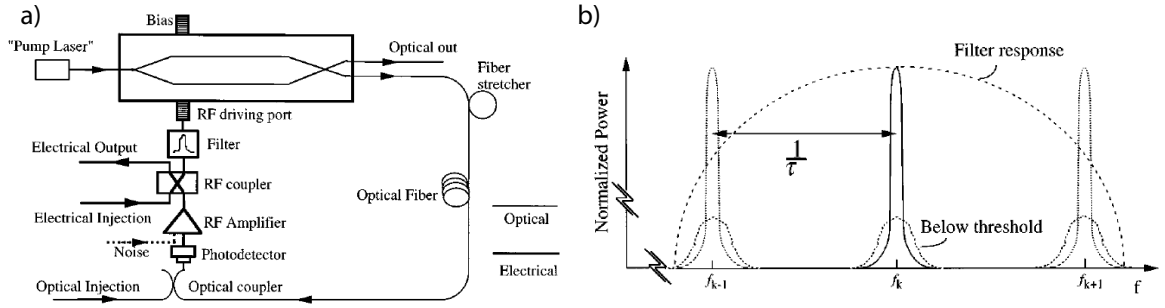

Fig. 6.1 a) Setup of the OEO consisting of optical and electrical components [290]. b) Cavity modes of the OEO output above and below threshold and the filter response [290].

This simple dependence imposes real challenges for the generation of high-frequency microwave oscillations in the GHz to tens of GHz range. Electronic oscillators, commonly based on a LC-circuits, suffer from decreasing Q-factors for increasing frequencies, simply due to the higher losses of electronic components at higher frequencies. Quartz oscillators offer great stabilities, however, usually have an oscillation frequency in the MHz range. Frequency multiplication techniques can be applied to generate higher frequency signals from the Quartz oscillator. However, with every multiplication step, the noise performance of the signal degrades.

As a solution to these challenges, the OEO was proposed and demonstrated [290]. The idea behind the OEO is to use the low losses, high speed and efficiency of photonics to construct an oscillator that produces pure GHz-RF-signals.

A scheme of the setup of such an oscillator is shown in figure 6.1 a). The operation principle of the OEO is the following. The optical part of the setup consists of a laser that passes through an intensity modulator and a fiber delay and gets eventually detected by a photodetector. The detected signal is fed back (electronically) to the intensity modulator. RF amplification might be required in this step in order to achieve a signal that is strong enough to drive the modulator. Feeding back the RF signal to the modulator closes the hybrid cavity; hence cavity modes are detected at the output with an FSR depending on the overall cavity length (see figure 6.1 b). If the overall gain in the cavity exceeds a threshold, the cavity starts to oscillate at the cavity mode frequencies. A filter is required to select one cavity mode and achieve single tone oscillations.

The threshold is reached when the overall gain G in the cavity exceeds unity. Hence a critical output photovoltage V_{out} from the photodetector is required to drive the modulator V_{in} in the setup. The optical output power $P(t)$ of a modulator is given by [290]:

$$P(t) = \frac{1}{2}\alpha P_0 \left[1 - \eta \sin\left(\pi \left(\frac{V_{\text{in}}(t)}{V_\pi} + \frac{V_{\text{B}}}{V_\pi}\right)\right)\right] \tag{6.2}$$

with the fractional insertion loss α, the optical input power P_0, the modulators extinction ratio, that is determined by η, the modulators half-wave voltage V_π, and the bias voltage V_B. The photovoltage V_out of the photodetector is given by [290]:

$$V_\mathrm{out}(t) = \rho\, P(t)\, R\, G_\mathrm{A} \tag{6.3}$$

with the responsitivity of the detector ρ, the load impedance R and the voltage gain G_A coming from an RF amplification step. With these two quantities, we can now calculate the cavity gain and find the threshold condition. The overall cavity gain is defined as [290]:

$$G = \left.\frac{dV_\mathrm{out}}{dV_\mathrm{in}}\right|_{V_\mathrm{in}=0} = \frac{1}{2}\frac{\rho\, R\, G_\mathrm{A}\, \alpha\, P_0\, \eta\, \pi}{V_\pi}\cos\left(\frac{\pi V_\mathrm{B}}{V_\pi}\right) = \eta\,\pi\frac{V_\mathrm{ph}}{V_\pi}\cos\left(\frac{\pi V_\mathrm{B}}{V_\pi}\right) \tag{6.4}$$

Here we introduced the photovoltage from the photodetector $V_\mathrm{ph} = 1/2\,\rho\, R\, G_\mathrm{A}\,\alpha P_0$. The maximum loop gain is achieved for a bias voltage $V_\mathrm{B} = 0$ or $V_\mathrm{B} = V_\pi$. With the condition that the loop gain has to be larger than unity for the OEO to oscillate, equation 6.4 leads to the following threshold condition [290]:

$$V_{ph} = \frac{V_\pi}{\pi} \tag{6.5}$$

The threshold is given by a relation between the output photovoltage of the detector V_ph and the half-wave voltage of the modulator V_π. Hence we see that a photodetector with a high output voltage and a modulator with a low V_π are preferential as it reduces the requirement of additional gain in the cavity, either by optical or RF amplification, that will degrade the noise performance.

As motivated at the beginning of the chapter, the OEO can produce low-phase noise microwave oscillations due to the high Q-factors photonics is able to provide. It is convenient to rewrite our definition of the Q-factor in a slightly different form:

$$Q = \omega \cdot \tau_\mathrm{d} \tag{6.6}$$

Here the loss rate is written in the form of the decay time τ_d. Due to the ultra-low propagation loss of optical fiber, we can relate the decay time τ_d to the delay time provided by the fiber loop in setup 6.1 a). The longer the fiber delay line, the more energy is stored in the OEO cavity. Hence the phase-noise is expected to decrease with longer fiber length. Experimental results confirm the expected behavior (see figure 6.2).

The longer the cavity length, however, the more stringent are requirements on the filter that

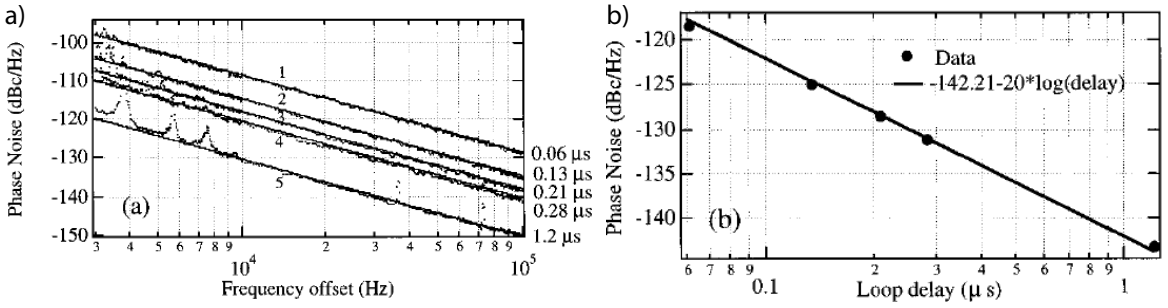

Fig. 6.2 a) Phase noise of an OEO with different cavity lengths [290]. b) Phase noise at 30 kHz offset for different fiber delays [290].

selects the cavity mode, as with longer delays the FSR decreases and the cavity modes get closer together. Therefore the filter needs to get narrower, in addition, to operate at GHz RF frequencies. This stringent requirement is difficult to match with RF filters and usually leads to a high insertion loss and lack of frequency tunability. In particular, the limited tunability is a drawback as it quenches one of the big advantages of photonics, that is the wide bandwidth. Following the first OEO demonstration, many schemes were proposed to solve the challenge of having a long fiber loop but still selecting a single cavity mode. Multi-loop OEOs are one promising solution; the OEO consists of a long loop to achieve the maximum delay, and a short loop to select the cavity [291]. Other techniques are based on optical selection techniques such as 4WM [292]. Also using SBS as a narrowband amplifier was proposed and applied [144, 293, 294].

Phase noise

As pointed out previously in this chapter the most important property of an oscillator is its stability. A common way to determine the stability and hence characterize an oscillator is by measuring the phase noise of the oscillator signal. A scheme of a perfect sinusoidal oscillation and the impact of phase or amplitude fluctuations is illustrated in figure 6.3.

Here we focus on the phase fluctuations and for the most part neglect amplitude noise. Phase noise is directly correlated to frequency noise and hence crucial for any applications relying on the precise frequency of the oscillator. The quantity describing the phase noise of an oscillator is known as $\mathscr{L}(f)$ and is given in $dBc\,/\,Hz$ where dBc stands for dB relative to the carrier power. The original definition of $\mathscr{L}(f)$ was the single sideband power in 1 Hz bandwidth over the carrier power. As this definition is ambiguous (e.g., it does not discriminate between contributions from amplitude and phase noise), it is now replaced. The

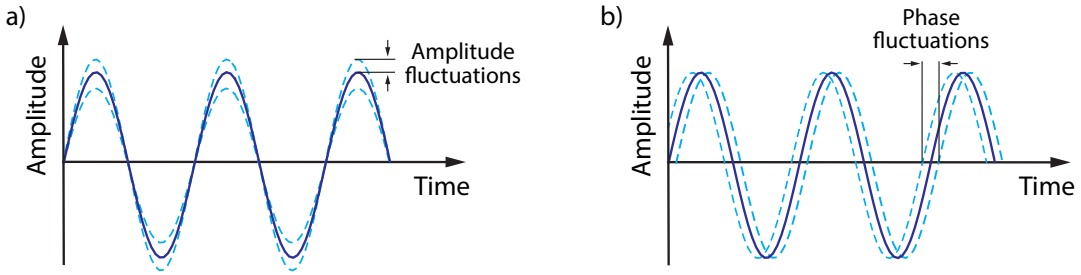

Fig. 6.3 a) Illustration of amplitude noise. b) Illustration of phase noise.

new definition of $\mathscr{L}(f)$ is given by:

$$\mathscr{L}(f) = \frac{1}{2} S_\phi(f) \tag{6.7}$$

where $S_\phi(f)$ is defined as single sideband power spectral density of the phase fluctuations $\phi(t)$ [295]. $S_\phi(f)$ is related to the power spectral density $S_\mathrm{f}(f)$ which describes the frequency noise via [295]:

$$S_\mathrm{f}(f) = \frac{f^2}{f_\mathrm{c}} S_\phi(f) \tag{6.8}$$

with the carrier frequency f_c.

We now have a look at the phase noise of the OEO. It was shown that the phase noise of an OEO does not increase with frequency [290]. This differentiates the OEO from all electrical synthesizers and oscillators that rely on frequency multiplication.
There are different sources of noise in an OEO that influence the generated signal, such as thermal noise, shot noise and relative intensity noise (RIN). These different noise sources can all be summed up in an overall noise density ρ_N [290].

$$\rho_\mathrm{N} = \rho_\mathrm{thermal} + \rho_\mathrm{shot} + \rho_\mathrm{RIN} = 4\,k_\mathrm{B}\,T\,(NF) + 2\,e\,I_\mathrm{ph}\,R + N_\mathrm{RIN}\,I_\mathrm{ph}^2\,R \tag{6.9}$$

with the Boltzman constant k_B, the temperature T, the noise factor of the RF amplification NF, the electron charge e, the photocurrent I_ph and the relative intensity noise (RIN) of the laser N_RIN.
The sum of all these noise contribution can be lumped together and hence described, in a simplistic model, as they would enter the OEO cavity at the output of the photodetector before entering the RF amplifier (compare figure 6.1 a)). The input signal to the RF amplifier is given by $P_\mathrm{osc} \,/\, G_\mathrm{A}^2$, with the oscillating power P_osc and the amplifier gain G_A. This allows

us to define a noise-to-signal ratio (NSR) [290] :

$$NSR = \frac{\rho_{\mathrm{N}}}{P_{\mathrm{osc}} / G_{\mathrm{A}}^2} = \frac{|G|^2}{1 - 1/|G|} \frac{4 k_{\mathrm{B}} T (NF) + 2 e I_{\mathrm{ph}} R + N_{\mathrm{RIN}} I_{\mathrm{ph}}^2 R}{4 \eta^2 \cos\left(\pi V_{\mathrm{B}} / V_{\pi}\right) I_{\mathrm{ph}}^2 R} \tag{6.10}$$

Here we used the dependence of the oscillating power P_{osc} on the photocurrent I_{ph} and the gain of the RF amplifier G_{A}, which we was than related to the overall loop gain G (compare equation 6.4; a detailed derivation of equation 6.10 is given in [290]).
Equation 6.10 allows us to draw some conclusions about the noise dependence in an OEO on the photocurrent. First of all the noise-to-signal ratio is decreasing with increasing photocurrent. For high photocurrents, the NSR levels and follows the RIN of the carrier laser and thermal and shot noise only play a minor role.

We now want to look at the spectrum of the OEO, or in other words want to describe the noise of an OEO depending on the frequency relative to the output signal and give an expression for the full width at half maximum (FWHM) of the output signal Δf_{FWHM}. The Δf_{FWHM} is given by [290]:

$$\Delta f_{\mathrm{FWHM}} = \frac{1}{2\pi} \frac{NSR}{\tau^2} = \frac{1}{2\pi} \frac{G_{\mathrm{A}}^2 \rho_{\mathrm{N}}}{\tau^2 P_{\mathrm{osc}}} \tag{6.11}$$

The FWHM of an OEO signal resembles closely the Shawlow-Townes formula for the linewidth of a laser signal. In the latter case of the laser, the numerator $G_{\mathrm{A}}^2 \rho_{\mathrm{N}}$ is replaced by the spontaneous emission rate and the delay time τ in the denominator with the laser cavity decay time.
In a similar way one can receive the power spectral density $S_{\mathrm{RF}}(f)$ of the RF noise of the OEO for frequencies much larger than $\Delta f_{\mathrm{FWHM}} / 2$ [290]:

$$S_{\mathrm{RF}}(f) = \frac{1}{4\pi^2} \frac{NSR}{\tau^2 f^2} = \frac{1}{4\pi^2} \frac{\rho_{\mathrm{N}} G_{\mathrm{A}}^2}{P_{\mathrm{osc}} \tau^2} \frac{1}{f^2} \tag{6.12}$$

Equation 6.12 is the power spectral density $S_{\mathrm{RF}}(f)$ of all noise contributions, i.e., amplitude and phase noise. However, in most practical cases the amplitude fluctuations are much smaller than the phase fluctuations (amplitude fluctuations are greatly reduced by saturating RF components within the OEO cavity); hence the $S_{\mathrm{RF}}(f)$ can be approximated as the single sideband phase noise of the OEO [290]. From equation 6.12 one can identify the typical f^{-2} decay of the phase noise with frequency offset from the carrier.
This f^{-2} decay is valid for frequencies above 1 kHz frequency offset that complies with the previous assumption of frequencies much larger than the FWHM of the output signal Δf_{FWHM}. Other noise sources closer to the carrier have been identified [296–298]. The very

low-frequency range from 1 Hz to 10 Hz can be identified as environmental fluctuations of the length of the long fiber delay. These fluctuations can originate from temperature or acoustic variations. These noise contributions usually fall off with a f^{-4} slope.
The frequency range from 10 Hz to about 1 kHz is usually dominated by flicker noise from the RF amplifiers and the noise falls of with a f^{-3} slope. Higher frequency offsets from the carrier are dominated by the previously described f^{-2} decay. This f^{-2} decay flattens out and becomes white phase noise $\propto f^0$ at the frequency that is the inverse of the cavity delay time τ. This flat phase noise is due to the non-oscillating higher order cavity modes. For example for a cavity length in the range of a km the sidemodes appear in the range of 100 kHz.

We have seen the basic operation principle of an OEO. In the rest of this chapter, we show an OEO approach, which is based on high Brillouin gain waveguides and generates pure microwave signals with a frequency tunability of almost 40 GHz while maintaining low phase noise.

6.2 Publication: A widely tunable, low phase noise microwave source

This chapter presents an OEO based on a photonic waveguide that harnesses SBS as an active filter. The following of this chapter is based on the publication:

M. Merklein, B. Stiller, I. V. Kabakova, U. S. Mutugala, K. Vu, S. J. Madden, B. J. Eggleton, and R. Slavík, "Widely tunable, low phase noise microwave source based on a photonic chip," Optics Letters **41**, no. 20, 4633 (2016).

Abstract

Spectrally pure microwave sources are highly desired for several applications ranging from wireless communication to next generation radar technology and metrology. Additionally to generating very pure signals at ever higher frequencies, these advanced microwave sources have to be compact, small weight and low energy consumption to comply with in-field applications. A hybrid optical and electronic cavity, known as an opto-electronic oscillator (OEO), has the potential to leverage the high bandwidth of optics to generate ultra-pure high-frequency microwave signals. Here we present a widely tunable, low phase noise microwave source based on a photonic chip. Using on-chip stimulated Brillouin scattering (SBS) as a narrowband active filter allows single mode OEO operation and ultrawide frequency tunability with no signal degeneration. Furthermore we show very low close-to-carrier phase noise. This work paves the way to a compact, fully integrated pure microwave source.

Introduction

Ultra-pure microwave signals are essential for radar technology to precisely measure the distance of objects, as reference clocks for communication networks or data carriers for wireless communication. Especially with mobile communication being omnipresent in every-day's life the demand for bandwidth in wireless communication schemes is steadily increasing and therefore microwave sources which are able to generate stable high-frequency microwave signals (several tens of GHz) in a small form factor are needed.
The generation of high frequency microwave signals as data carriers, however, is challenging when done electronically, because the losses are increasing with higher frequencies and electronic systems are known to suffer from parasitic electromagnetic interferences. Microwave photonics, in particular integrated microwave photonics, offers great potential to overcome these barriers and provides solutions for problems known to be notoriously challenging in electronics [299]. A good example is an optoelectronic oscillator (OEO), which harnesses optics to generate ultra pure microwave signals [300, 301, 294, 302].

It was shown that these oscillators - consisting of a cavity which is half optical and half electrical - can be used to generate pure single frequency microwave sources with very low phase noise [303]. However, most of the demonstrated OEOs did not take advantage of the large bandwidth optics is able to provide. The main reason for this limitation is the fact that the OEO relies on a narrow-band filter to ensure that only one cavity mode is oscillating. This filter needs to fulfill quite stringent requirements: on the one hand it needs to operate in the range from GHz to tens of GHz, and on the other hand exhibit very narrow bandwidth in the orders of a few MHz or less. This filter can be implemented in either the optical or the electrical part of the cavity. However, electrical filter with the above-mentioned requirements

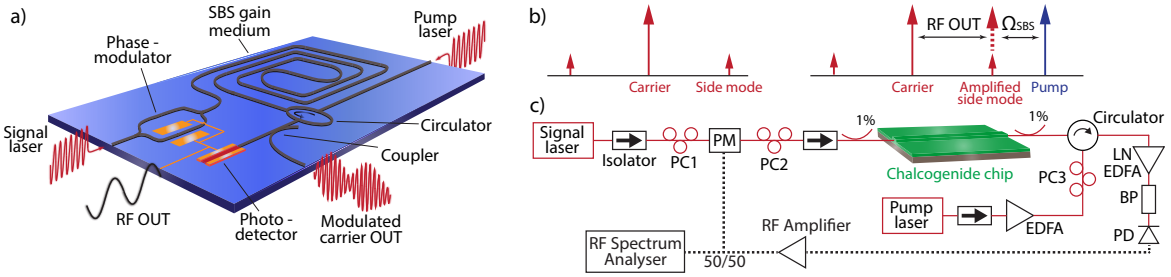

Fig. 6.4 a) Artist's impression of a fully integrated OEO. b) Basic principle of the SBS-based OEO. The narrow band Brillouin gain amplifies one of the side modes converting the phase modulation into an amplitude modulation which can be detected at a photodetector. c) Experimental setup of the chip-based OEO. PC1-3: Polarisation controller; PM: Phase modulator; EDFA: Erbium-doped fibre amplifier; LN EDFA: Low-noise EDFA; BP: Bandpass filter; PD: Photodetector.

usually have a high insertion loss (typically around 10 dB) and lack tunability. The high loss also degrades the noise performance of the OEO as it requires reamplification of the signal. Similar problems occur for narrow-band optical filters, such as e.g. high finesse Fabry-Perot cavities.

Here we show the first photonic-chip based OEO employing a narrow-band active Brillouin filter. Besides being chip-scale size with the potential to be fully-integrated, the Brillouin filter provides gain to the cavity and therefore no additional reamplification to compensate filter losses is required, allowing low phase noise (< -100 dBc/Hz at 100 kHz offset frequency). The active Brillouin filter also allows ultra-wide tunability of the generated microwave signal without any degradation of performance (in our demonstration up to 40 GHz).
Harnessing the large Brillouin gain of chalcogenide rib waveguides allows to employ the Brillouin filter in a short length [75, 81, 106], which makes this demonstration the first truly single mode OEO based on a Brillouin filter. Therefore the stability of the OEO is increased as there is no mode-hopping occurring. Relying only on very few components - which all have been demonstrated on-chip already [304–310, 101] - the design and construction of a fully integrated OEO is feasible (see Fig. 6.4 a). Therefore this work paves the way to a cost effective, due to scalability in the fabrication process, small-footprint ultra-pure microwave source.

Basic Principle and Experimental Setup

The basic principle and the experimental setup of the chip-based OEO is depicted in Fig. 6.4 b) and 6.4 c), respectively. A signal laser, a distributed feedback (DFB) laser, passes through a phase-modulator and is coupled to a 6 cm long highly nonlinear chalcogenide rib waveguide with a cross-section of 850 nm $\times$ 2.6 µm. A second DFB laser serves as a pump and is coupled from the opposite side to the chip, generating the narrow-band SBS response. SBS describes a nonlinear interaction between an optical pump ω_{pump}, an acoustic wave Ω_{SBS} and an optical Stokes wave ω_{S}. In this process the optical Stokes wave experiences exponential gain [108]. Initially the phase modulator gets just seeded by white noise. However, as SBS provides a narrow-band gain inside the cavity one of the side modes gets amplified. The bandwidth of the SBS gain is around 30 MHz in chalcogenide glass [75], which is significantly wider than the linewidth of the used pump laser (sub-MHz).
The radiofrequency (RF) beat frequency gets fed back into the phase modulator, and above a threshold the OEO starts oscillating at this particular frequency, which is given by $\omega_{\text{OEO}} = \omega_{\text{pump}} - \Omega_{\text{SBS}} - \omega_{\text{carrier}}$. As only one side mode gets amplified the phase modulation is converted into amplitude modulation, which can be detected at a photodetector.

Therefore the Brillouin active filter allows the use of a phase modulator instead of the intensity modulator commonly used in OEOs. A phase modulator does not require a DC bias, which would otherwise need to be controlled with a low-noise phase-lock loop. It also has lower insertion loss, further reducing the cavity loss and thus the noise of the OEO signal.

Characterisation of the On-Chip OEO

An optical spectrum of the built OEO is presented in Fig. 6.5. It shows the OEO in open loop operation with 10 dBm RF seed power from an RF signal generator at the phase modulator. One can see that SBS amplifies the upper side mode leading to 12 dB difference in optical power of the two side modes, matching the power of one side mode with the carrier power. In the right corner of Fig. 6.5 one can see the residual SBS pump, backreflected from the facet of the chip.

In our measurement an optical bandpass filter is used to remove this backreflection to avoid any detrimental beat signals. We want to clarify that the optical bandpass filter in the setup shown in Fig. 6.4 c) serves the only purpose to suppress this backreflected SBS pump laser signal. The backreflected pump signal, however, could be strongly suppressed by moving to a fully integrated chip, using wire bonding [311] or photonic chips with tapers and anti-reflection coatings [312].

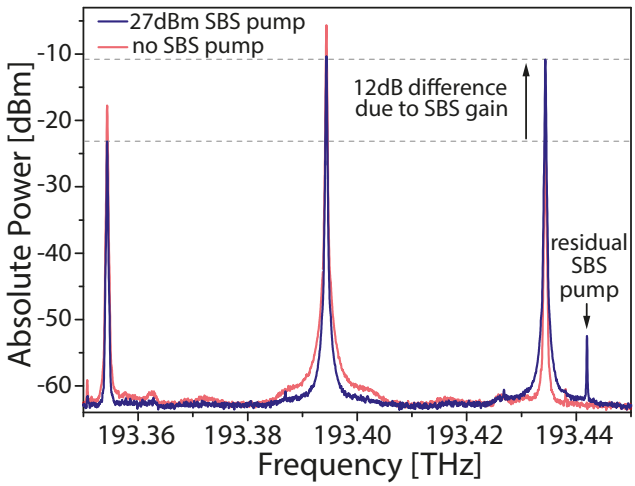

Fig. 6.5 Optical spectrum of the OEO in open-loop operation with 10 dBm RF seed power at the PM. The upper side mode gets amplified by SBS leading to a 12 dB difference in the side mode power.

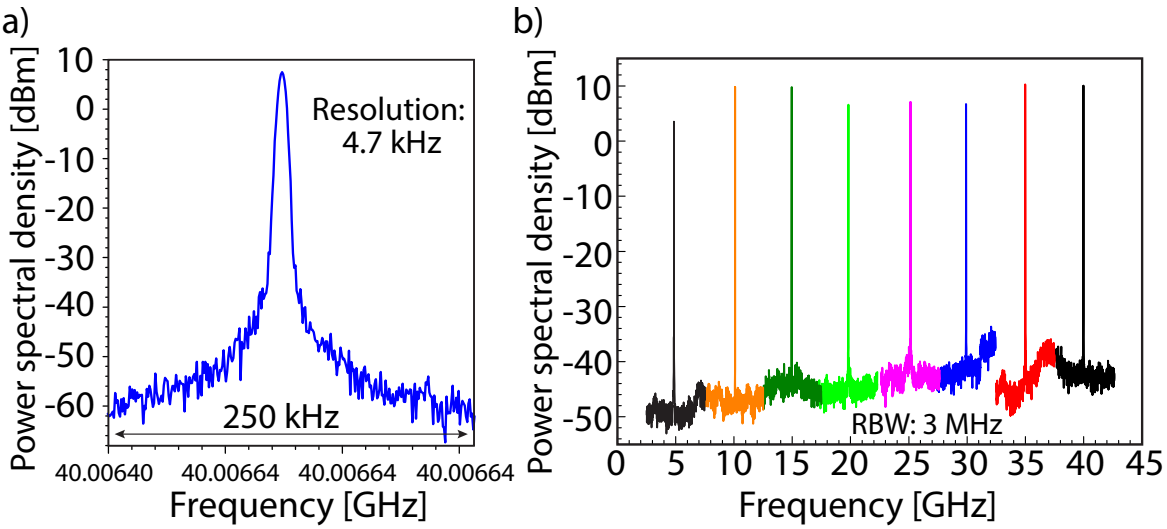

Fig. 6.6 a) RF spectrum of the OEO output signal at around 40 GHz. b) Ultra-wide tunability of the OEO output signal. The tuning is achieved by tuning the pump laser frequency relative to the carrier frequency (RBW: Resolution bandwidth).

The oscillating microwave mode of the OEO is shown in Fig. 6.6 at a frequency of around 40 GHz. The total span of Fig. 6.6 is only 250 kHz showing the narrow linewidth character of the OEO. In Fig. 6.6 b) we show the ultra wide tunability of the SBS-based OEO. This is one of the key advantages of photonics compared to electronics - there is no degradation in the signal when going to higher frequencies. Whereas the high quality microwave output is a typical characteristic of an OEO, the wide tunability is a specific feature of the dual pump SBS based setup. Here the OEO output frequency can be simply changed by tuning the frequency of the carrier laser relative to the SBS pump laser. The spectra were measured in 5 GHz windows and stitched together to obtain better resolution. We want to emphasize that there were no other cavity modes oscillating over the whole span, besides the main OEO output mode. Here we show tunability up to 40 GHz, which is only limited by our equipment - namely the modulator and the photodetector. However it was shown that all-integrated modulators can exceed modulation speeds of 100 GHz [306–309] and recent research on graphene photodetectors predicts operational speeds of up to 500 GHz [313].

Purity of the Generated Microwave Signal

The most important figure of merit for microwave sources is its stability, which can be quantified by measuring the phase noise of the source. This gives a direct indication of the stability and purity of the source. Fig. 6.6 a) shows the measured phase noise of our

SBS based OEO and compares it to a high-range commercial microwave source (Agilent N5183A). The phase noise is measured using an microwave spectrum analyser (Agilent E4448A).

In the range up to 1 MHz we see no detrimental cavity side modes present. This is a result of the high SBS gain on-chip enabling a short cavity (in total about 25 m), which results in a truly single moded OEO with great stability and no detrimental mode-hopping. Furthermore, we see that the phase noise of the OEO at close-to-carrier frequencies is orders of magnitude lower than the Agilent microwave source. The flat and low noise of the OEO at low frequencies is a result of the noise properties associated with SBS. At low frequencies (below 10 kHz offset frequency), SBS was reported to generate an optical signal with unusual relative intensity noise (RIN) characteristics. At low offset frequencies (< 10 kHz) the SBS signal RIN is decreasing at about an f^2 rate [314], whereas the RIN of optical signals usually increases at f^{-1} rate or is white f^0. As white RIN produces the typical f^{-2} OEO phase noise [300], SBS RIN (with f^2 slope) is expected to produce flat phase noise, which is perfectly in line with our experimental observations.

Furthermore it is known that operating the SBS filter / amplifier in saturation leads to an improved noise performance [315]. Operating at relative high pump powers (around 23 dBm) also provides the maximum gain for the selected sideband mode, giving the steepest response of the active Brillouin filter. It is worth mentioning that the photocurrent from the photodiode of our OEO was high, about 20 mA, making optical RIN the dominant contribution of the noise [300]. This is opposed to most OEO demonstrations, where thermal or shot noise was the limiting factor. Besides a slight bump in the phase noise curve at around 10 kHz the phase

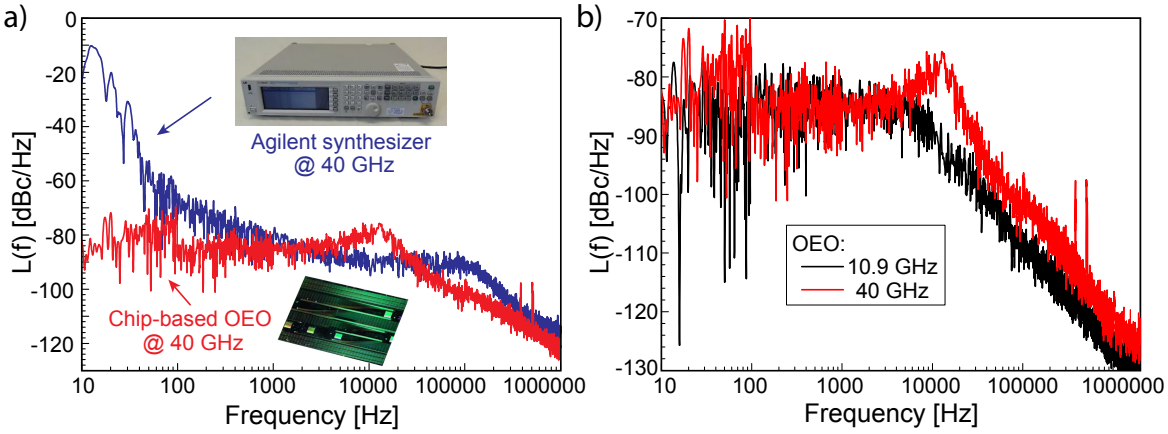

Fig. 6.7 a) Comparison of the phase noise performance of the OEO (red curve) and a high range commercial RF synthesizer (blue curve). b) phase noise performance of the OEO at different RF frequencies. Note the slightly worse noise performance at 40 GHz is due to limitations in the used RF components.

noise of the OEO is below the commercial microwave source.
Fig. 6.6 b) compares the noise performance of the OEO at 40 GHz and at 10 GHz. It was shown previously [300] that the phase noise of an OEO does not depend on the operation frequency, which we also observed experimentally for frequencies up to 30 GHz. Beyond this frequency, we saw slight signal degradation due to the limited bandwidth of the used RF components. The phase noise at 40 GHz (limited by the used RF components) and 10.9 GHz (typical performance up to 30 GHz) is shown in Fig. 6.7 b). However, these limitations can be overcome with better components and therefore the noise performance of the OEO could be further improved at high frequencies.

Conclusion and Outlook

We demonstrated a chip-based highly pure microwave source harnessing SBS. We show that the noise performance of our on-chip OEO is comparable with high-range commercial microwave sources. The strong photon-phonon interaction in chalcogenide waveguides enabled us to utilize high Brillouin gain in a short length scale, realising the first single-mode OEO based on SBS. Furthermore replacing the commonly used electronic filter in the OEO cavity with an active SBS filter enabled ultra-wide tunability of the OEO output frequency.

This work paves the way to more compact stable microwave sources. As the whole setup can be integrated on one photonic chip (Fig. 6.4a) there is great potential to leverage existing nano-and microfabrication facilities with great advantages concerning costs and scalability. A chip-scale source of highly pure microwaves would have a big impact on applications where the size and weight are key demands: such as mobile communication and on-field radar applications. An all-integrated OEO (Fig. 6.4a) could be interfaced with further photonic components using wire bonding [311]. Additionally to the microwave output an OEO is also able to output the microwave signal modulated on an optical carrier. Therefore it could be used directly in microwave photonic circuits without the need of additional conversion/modulation or be transmitted as radio over fibre signal.

The chip depicted in Fig. 6.4 a) relies only on very few components - of which all are already demonstrated in all-optical chip-scale platforms. Fast photodetectors are available on chip [304, 305] and are steadily improving concerning conversion efficiency and speed. Several different modulators - based on graphene, plasmonics or hybrid organic structures - were also demonstrated on chip recently [306–309]. These on-chip modulators and photodetectors do not only have a very small footprint but also offer operation speeds not seen in commercially available products today. For the SBS waveguide one could either think of a

hybrid chalcogenide-on-silicon structure or use silicon waveguides, as Brillouin net gain in silicon was demonstrated recently [101]. Chip integrated isolators or circulators, however, are notoriously challenging [316]. In recent years there was a lot of progress and there are demonstrations with sufficient isolation between the respective ports [310, 317]. On the other hand our concept of an all-integrated OEO does not rely on the circulator - a simple coupler combined with a bandpass filter would also work [318, 319]. Both are standard components in photonic chips today.

6.3 Outlook

Further directions of the Brillouin OEO

Here an outlook on further directions for an on-chip Brillouin based OEO is given. First of all, a few adjustments to the current setup will potentially improve the noise performance of the demonstrated OEO configuration. In particular waveguides with larger gain and lower insertion loss could improve the noise performance of the OEO. With larger SBS gain in the cavity, one could remove the low-noise EDFA in the cavity which directly should positively affect the noise performance. Furthermore, a photodiode with a higher current output and a modulator with a lower V_π could potentially allow to fully remove the RF amplifier, reducing system complexity, power requirements and further boosting performance. Moreover, these two components are setting the upper limit of the frequency tunability to 40 GHz in the current experiment. The basic operation principle of the Brillouin OEO, however, would allow a much wider frequency tuning range to even higher frequencies.
Also, a single laser setup that uses a single sideband modulator could improve the performance by avoiding relative drift of the two lasers. For the latter case, however, initial experiments did not show a significant improvement in performance but might have been simply limited by the performance (loss, conversion efficiency) of the available single sideband modulator.
Based on the here demonstrated Brillouin OEO a similar OEO configuration was suggested by Peng et al. [320]. Instead of using the Brillouin gain resonance the Brillouin loss is used to filter one of the sidebands of the phase modulator in the OEO cavity and hence convert the phase modulation to an amplitude modulation that can be detected by the photodiode. This proposed scheme was implemented in a dual-fiber OEO configuration and showed improved noise performance compared to the amplification based configuration. The given explanation is that in the loss configuration there is less pump laser noise transferred to the OEO cavity as compared to the amplification configuration. So far this scheme was only shown in fiber and could be implemented on-chip.
Recently it was shown that a chalcogenide waveguide can be interfaced with a silicon chip manufactured in a state-of-the-art CMOS foundry via hybrid integration [122]. The chalcogenide waveguide was interfaced with silicon waveguides and showed more than 20 dB gain. With this result, the vision of an all-integrated OEO presented in the paper in figure 6.4a) is coming closer to realization. As elaborated in this chapter interfacing the chalcogenide gain medium with other on-chip components can not only reduce the footprint but also increase performance, in particular in terms of high-frequency operation.
An interesting approach would be to interface the nonlinear chalcogenide waveguides with linear spiral waveguide delay lines [321]. On-chip delay lines with up to 39 m optical path

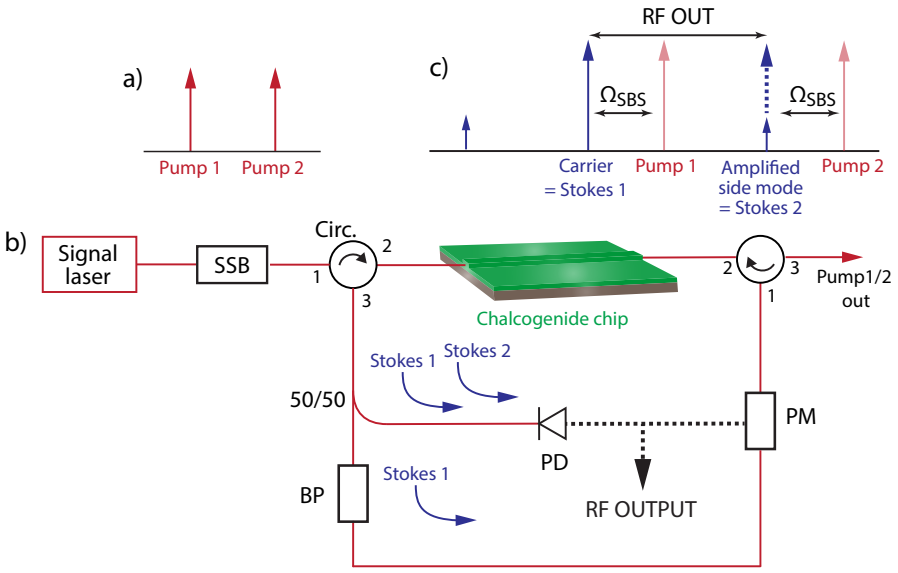

Fig. 6.8 Proposal of a dual cavity hybrid Brillouin OEO. a) Two input pumps generated via a single sideband modulator. b) Scheme of a potential setup. The outer fiber loop forms an optical cavity for the 1st Stokes wave. The inner cavity is a half electrical half optical OEO cavity. c) One Stokes wave acts as a pure carrier while the second Brillouin process acts as a selective amplifier for one of the sidebands. The pumps are counter-propagating and do not oscillate or beat on the photodiode. SSB: single-sideband modulator; Circ: circulator; BP: bandpass filter; PM: phase modulator; PD: photodiode.

length, have been shown [321] with the same paper proposing delay lines up to a length of 250 m. Including these ultra-long delays in the OEO cavity should greatly reduce the noise performance of the OEO [290]. The longer cavity, however, would cause several cavity modes to be within the Brillouin gain resonance; hence mode competition and hopping would be a likely consequence. To maintain single mode operation, one would need to narrow down the Brillouin gain resonance which was successfully demonstrated previously [322, 323]. Combining a tailored gain spectrum with a long OEO cavity could lead to significant performance improvements. The question whether this configuration can reach the superb noise performance of OEOs based on ultra-high Q resonators is not easy to answer. However, the Brillouin based OEO has the advantage of continuous frequency tunability, simplicity and robustness, not requiring locking and stabilization of a cavity mode.

With these suggested approaches the phase noise of the OEO could improve further, however the one limiting factor will always be the noise of the laser that acts as the carrier for the beat note which is detected by the photodiode and fed back into the cavity. To improve the stability and noise of the carrier one could imagine using a Brillouin laser configuration in combination with the Brillouin OEO. A schematic of such a setup is shown in figure 6.8.

As shown in the introduction chapter 2.3 Brillouin laser can lead to linewidth narrowing of the pump laser and hence generate ultra narrow laser signals [80, 89, 120]. The inner cavity is the half optical half electrical cavity used in the OEO setup presented in the previous section (compare figure 6.4). The outer cavity is an optical Brillouin laser cavity to generate a more stable carrier signal that is fed into the OEO cavity. A narrow bandpass filter is used to make sure only one Stokes wave oscillates. The tunability would then be achieved by tuning the second pump laser relative to the pump laser that generates the first Stokes wave in the Brillouin laser configuration. Note that the two pump waves in this configuration are co-propagating through the nonlinear chalcogenide waveguide and therefore one should consider and mediate other nonlinearities, such as 4WM. This is a task, however, that can be managed by dispersion engineering the waveguide.

Concluding remarks

A chip-based OEO harnessing Brillouin scattering in a waveguide was shown. Impressive performance was achieved, and the concept has large potential for further investigation. In particular the prospect of hybrid integration and the possibility of combining nonlinear and linear elements on one photonic chip. For ultimate phase-noise performance in a small footprint, high-Q resonators are still the best option due to their high energy storage capabilities. The SBS waveguide approach, however, has advantages when it comes to frequency tunability. Furthermore, the fabrication demands for a waveguide approach are relaxed compared to high-performance resonators, no cavity locking is required, and the output power can be high because there is no field build-up like in a high-Q resonator. Recent progress in integrated optics and fabrication methods, on the other hand, could enable a hybrid OEO consisting of a high-Q ring as an energy storage element and SBS as a mode selector and hence combining both worlds for the maximum performance.

Chapter 7

Advanced SBS based signal processing: A photonic-phononic memory

In this chapter, a BBM is presented that allows the storage of optical data pulses in a photonic integrated circuit. In this concept, SBS is used to efficiently transfer optical information to traveling acoustic waves and unambiguously retrieve it again afterward. Due to the large difference in the optical and acoustic velocity the signals are effectively delayed. But why do we want to delay an optical signal in the first place? In the next section, an introduction to optical delay schemes is given to contextualize the results presented in [324].

7.1 Introduction

Altering the speed of light is an endeavor that has excited researchers for many decades due to its large potential impact on future technologies but also because it is intriguing from a fundamental science point of view. How slow can we make a light pulse propagate that usually travels with the fastest velocity known to us?
The fast speed of light allows us today to communicate all around the globe with minimum latency by using modern optical communication schemes. However, this large speed of light becomes a real challenge when processing data all-optically, in particular in compact integrated circuits. Also for "simple" optical interconnects on a chip between different processors it becomes a challenge, as it requires temporarily storing the optical information while a processor is occupied, to provide enough time to reroute it to a different processor or to synchronize it with a separate data stream.
Therefore the ability to control and reduce the speed of light and hence the flow of information

in optical data transmission and all-optical signal processing schemes would greatly excel the performance of these systems. It would allow to temporarily slow down or store optical information without the need to convert it into an electrical signal, that is then parked in a conventional binary electronic memory. The ability to store and delay information carried by light in a direct fashion would release many constraints in current systems.
There is the obvious speed advantage of avoiding any additional electro-optical conversion, along with the prospect of greatly reduced energy consumption. Light can carry a large amount of data due to advanced telecommunication schemes that harness many different degrees of freedom of the optical wave. So is data encoded in multiple amplitudes and phase levels, sent simultaneously in many wavelength channels, as well as polarization states and modes. The advantage of delaying such complex encoded signals directly, without the need of decoding and re-encoding, is greatly reducing system complexity, energy consumption and latency.
However, delaying optical signals while maintaining all the aforementioned properties - in particular amplitude, phase, and frequency - without inducing distortion is very challenging. The requirement of a large bandwidth ($>$ GHz) and a large fractional delay makes it even harder.

Researchers proposed many different solutions to address and solve this challenge. We have seen in section 4.2, that optical resonances are accompanied by a change in the refractive index that can lead to the phenomena of slow-light. As this phenomena is universal it was implemented in a manifold of platforms, such as photonic crystals [203, 204], coupled-resonator optical waveguides (CROWs) [207], high-Q resonators [325], atom clouds and Bose-Einstein condensates [205, 206]. Very low group velocities and large fractional delays were achieved in pioneering experiments in the latter two platforms [205, 206]. However, even though these delay schemes were achieving impressive performance, they are not readily transferable outside a laboratory environment. Furthermore, the wavelength of the resonance often does not fall within the telecommunication wavelength band around 1.5 μm. For this reason, we want to focus the following discussion on signal delay schemes that can be achieved in an optical fiber or chip-scale platforms.

It turned out that the interaction between photons and phonons offer flexible and powerful ways to delay optical signals and has been implemented in many different platforms, from standard optical fiber to optomechanical resonators and crystals to photonic-phononic waveguides. On the one hand, phonons induced by SBS in standard telecommunication fiber and on-chip waveguides can be utilized to slow down optical information, which is known as

SBS slow-light. On the other hand phonons itself can store optical information - either in the form of long-lived mechanical excitations in resonators or traveling acoustic wave in phononic waveguides. In the following, we will provide an overview of phonon-based optical delay or storage schemes.

Fiber based approach - delaying signals with SBS

Different SBS based delay schemes in fiber have been realized over the years. This chapter gives an overview of the different approaches, ranging from SBS slow-light, SBS *quasi*-light storage to SBS light storage.

SBS based slow-light: We have seen that the narrowband Stokes resonance generated via SBS induces slow-light in an optical fiber [181, 326] (see chapter 4.2). The advantages of this approach seem to be evident: it only relies on telecommunication components, works at room-temperature and the delay can be dynamically controlled via the pump power (see equation 4.25). In the pioneering work from Okawachi et al. [180] the delay of a 15 ns pulse using SBS slow-light in optical fiber was shown (see figure 7.1 a). At the same time, the seminal work from Song et al. [208] showed the dependence of the delay on the Brillouin gain / pump power (see figure 7.1 b).
The concept of SBS slow-light was later also successfully implemented in on-chip waveguides [77]. In this demonstration, large changes in the group index Δn_g were achieved due to the orders of magnitude larger Brillouin gain compared to standard silica fibers (see figure 7.1 c). However, even though large changes in the group index could be shown, the fractional delay (the number of pulse widths the pulse can be delayed), was still limited to only around one pulse width.
Achieving large fractional delays is one of the main challenges in SBS slow-light research and is well described by a statement from Luc Thevenaz [181]:

"In practice the maximum delay only amounts to one to two pulse widths, and breaking this deadlock remains a major challenge for research on slow light based on spectral resonances."

In the following years, many attempts were pursued to increase the fractional delay, extend the bandwidth and to minimize distortions in SBS slow-light schemes [327–334]. One great advantage of SBS slow-light is that the resonance that generates the slow-light behavior can be altered and tailored by the profile of the pump laser and as opposed to a resonance given by a material or structure. The first demonstration of altering the SBS gain profile relied on two optical pumps in close vicinity to each other [335]. Using a pump that included

two frequencies provided a great increase in control of the dispersion of the generated SBS resonance and even allowed to switch between SBS slow- and fast-light [335].
Following these seminal demonstrations, different forms of tailoring the pump profile emerged that can be categorized in the following way: using multiple discrete frequency pumps or continuously broadening a single pump profile. In the first case, best slow-light performance was achieved using three separate tones [336, 337]. Continuously broadening the pump spectrum allowed to slow down light signals with much larger bandwidth (exceeding 10 GHz), compared to the narrowband intrinsic Brillouin linewidth [327–331, 333].
However, broadening the SBS gain to delay broadband signal did not come without an additional cost; the required pump power to maintain the same normalized delay increases proportionally to the broadening. If one wants to maintain the same absolute delay the required pump power increases quadratically, as the achievable delay is not only proportional to the peak power but also proportional to the bandwidth of the resonance. Hence to achieve the same fractional delay for a 10 GHz broadband signal compared to a signal narrower than the intrinsic Brillouin linewidth, 350 times higher pump power is required [181].
Further efforts were undergone to increase the fractional delay in SBS slow-light schemes which have been limited to a few pulse widths even with the great achievements in broadening the spectral response. Cascading several slow-light segments allowed increasing the fractional delay [179], however with the cost of system complexity and only a small improvement in overall delay.
With all the aforementioned challenges and proposed solutions it was shown by Khurgin [338] that a delay scheme based on optical amplification, such as SBS slow-light, still is only able to delay a sequence of maximum five bits. The number five follows from realistic power budget considerations in a fiber-based slow-light setup and is a consequence of the fact that the required gain in such a delay scheme increases in a nonlinear way with the number of

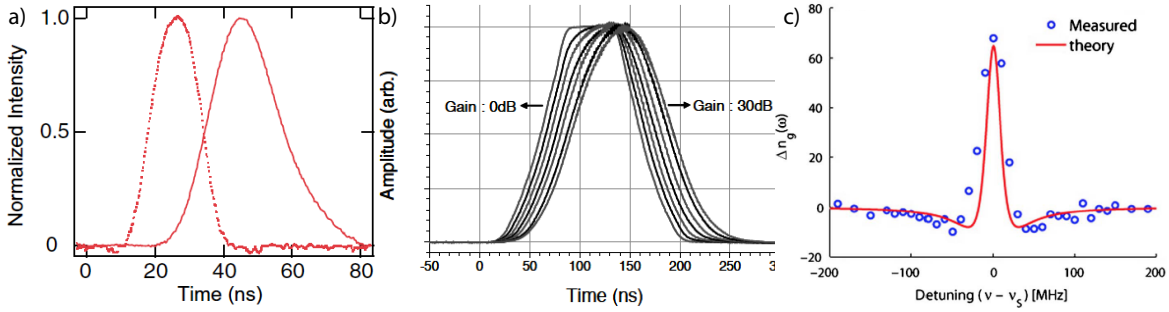

Fig. 7.1 a) Pulse delay of a 15 ns Stokes pulse [180]. b) Tunable delay of a 100 ns pulse for different Brillouin gain values [208]. c) Change of the group index of an on-chip SBS slow-light implementation [77].

delayed bits [338].

SBS based quasi-light storage: SBS based quasi-light storage is a concept that was proposed and demonstrated in 2009 to overcome the shortcomings of SBS slow-light if it comes to large fractional delays [339–342]. This scheme uses SBS to sample a data pulse with a frequency comb. The sampling produces a pulse train of identical copies of the original data pulses. Hence the term *quasi*-light storage was introduced, as the information is not stored but copied many times. The delay of the data is achieved by selecting one of the copies,

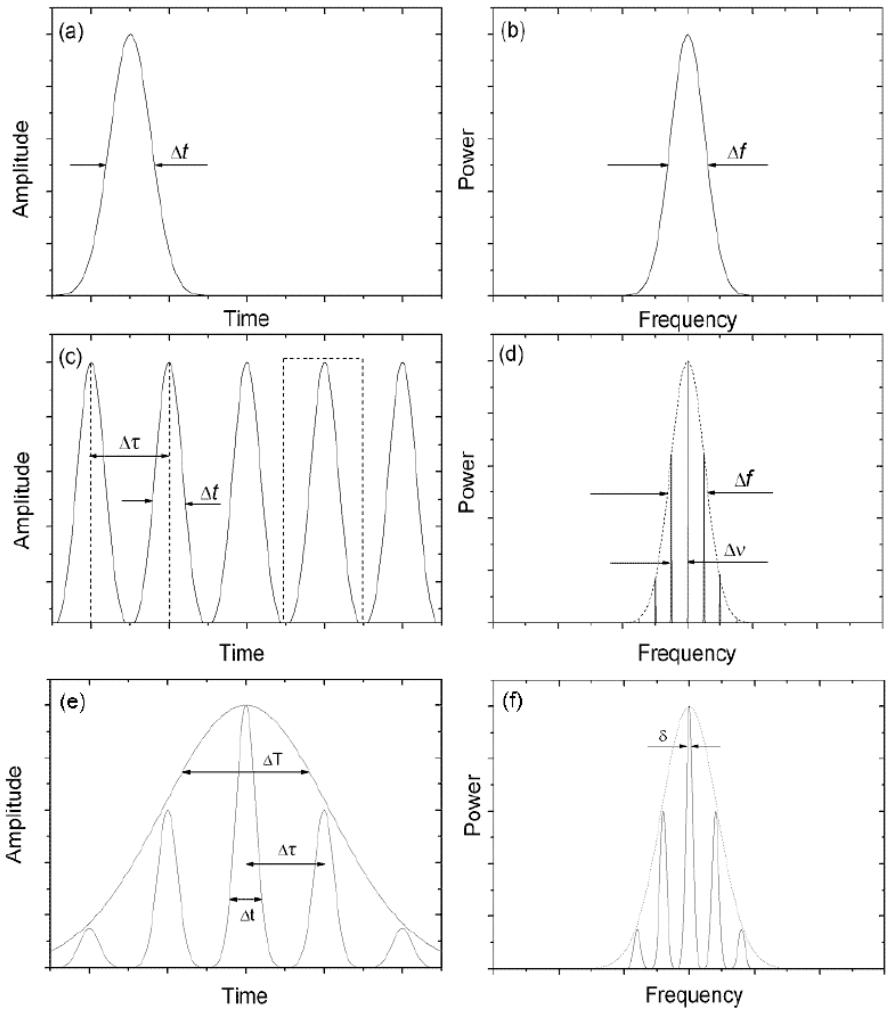

Fig. 7.2 Juxtaposition of signals in the time domain and the corresponding frequency spectrum [339]. a) Pulse in the time domain and b) corresponding spectrum. c) Ideal pulse train and d) corresponding ideal sampled frequency spectrum. e) and f) show a pulse train and frequency spectrum when sampled with a finite bandwidth.

which succeed the original data pulse.

The basic principle of this light storage technique is shown in figure 7.2. The underlying principle of quasi-light storage relies on the correspondence between the time and frequency representation of a pulse. A frequency comb corresponds to a pulse train in the time domain. Multiplying a pulse with a frequency comb in the frequency domain corresponds to a convolution in the time domain and hence a pulse train consisting of copies of the original data pulse.
In the quasi-light storage scheme, SBS is used to multiply the optical data pulse with a frequency comb in the frequency domain. The frequency comb counter-propagates the optical data pulse, and via Brillouin amplification "samples" the data pulse. The separation in the time domain between these copies is given by the frequency spacing of the individual comb lines. Selecting one of the copies with a photonic switch allows retrieving a copy of the original data pulse, however at a delayed time. The maximum delay of these copies is given by the width of the comb lines, which is given by the Brillouin linewidth. Operating the quasi-light storage scheme in the high pump power regime, which reduces the Brillouin bandwidth to around 10 MHz, allows for a storage time of around 100 ns [339].
The delay time can be increased even further by narrowing the Brillouin gain spectrum. It was shown that by overlying the Brillouin gain spectrum with two Brillouin loss (anti-Stokes) spectra, the Brillouin gain bandwidth could be reduced to 3.4 MHz [343].
Applying the gain narrowing technique to the light storage scheme allowed to further increase the delay time up to 140 ns. A measurement of a train of copies of a data bit pattern using quasi-light storage with narrowed Brillouin spectrum is shown in figure 7.3. A fast optical switch is used to select one of the delayed bit patterns after the desired delay time.

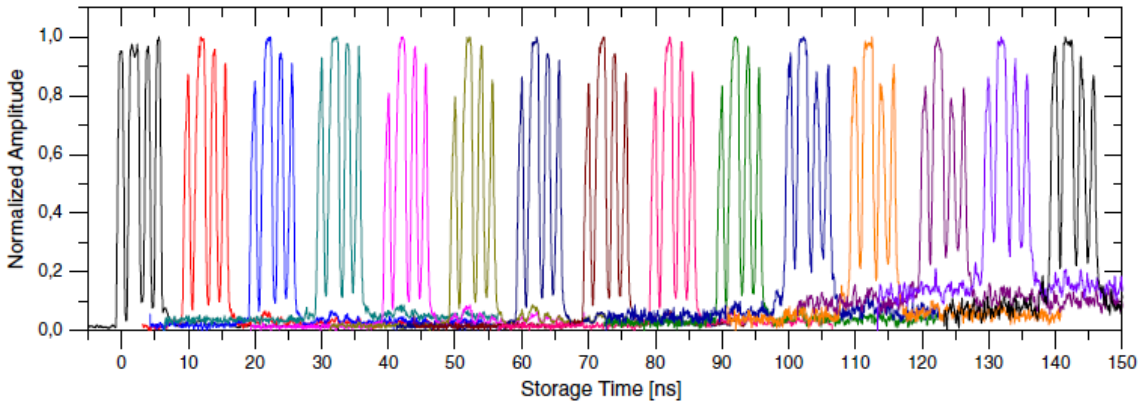

Fig. 7.3 Train of copies of a bit pattern generated in an SBS quasi-light storage scheme [341].

Quasi-light storage could overcome many of the shortcomings of SBS slow-light to delay bursts of data packages. A fast switch is required to select the desired optical pulses. Ways to extend this concept to streams of data are not obvious at this point. However, SBS can also be used to achieve light storage in the acoustic wave, which will be described in the next section.

SBS based light storage: In this approach SBS is used to store light in the form of an acoustic wave. SBS acts as a coherent coupling mechanism between optical data pulses and acoustic waves, where the information is completely transferred from the optical domain to acoustic waves, which travel orders of magnitude slower than the speed of light. In this scheme, the optical pulse does not experience a different group velocity as in SBS slow-light but are actually stored as an acoustic excitation. An optical read pulse subsequently transfers the information back from the acoustic to the optical domain.
The first proof-of-principle implementation of this idea was realized in highly-nonlinear fiber [344]. The main results of this demonstration are summarized in figure 7.4.

With this approach Zhu et al. were able to store 2 ns long pulses for up to 12 ns, which is a fractional delay of 6 and hence exceeding most SBS slow-light demonstrations. The required power, however, was exceeding 100 W and the storage time is limited by the short acoustic lifetime of the hyper-sound phonons. To overcome the high power requirements and to enable longer storage times the idea of storing photons as phonons was transferred to high-Q resonator structures. In these resonator structures, the acoustic lifetime of acoustic modes can be orders of magnitudes larger than the high frequency traveling acoustic waves

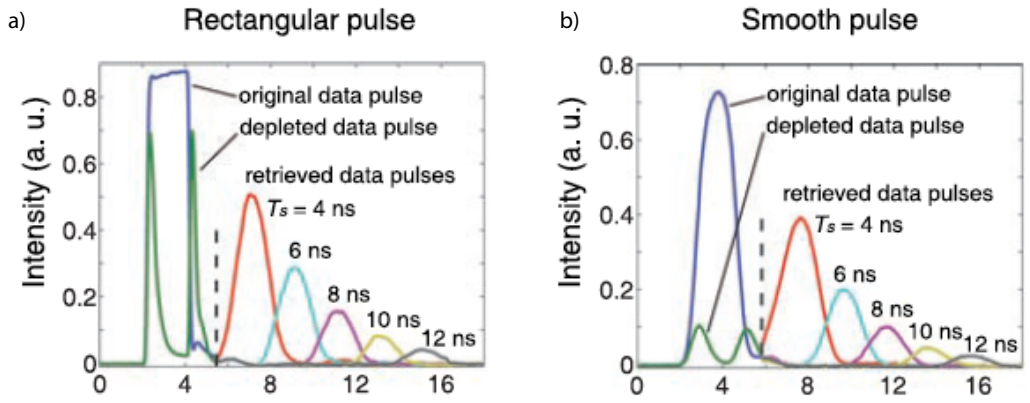

Fig. 7.4 a) Stored rectangular pulse in an optical fiber [344]. Note that the pulses right of the dashed line were multiplied by a factor of two. b) Storage and retrieval of smooth pulses with the retrieved pulses multiplied by a factor of two [344].

in an optical fiber. The resonator based light storage schemes will be described in the next section.

Micro-resonator based approach

Optomechanical resonators are resonators that efficiently couple optical cavity modes to mechanical degrees of freedom. Due to the high Q-factors of these resonators the power requirements to couple, the two waves are greatly reduced. More importantly, the acoustic lifetime achieved in these resonators is much longer and hence when used to store light pulses, much longer storage times can be achieved.
It was demonstrated by Fiore et al. that the previously described light storage concept can be transferred from optical fiber to silica resonators [345]. The resonators used in this demonstration have a diameter of around 30 µm and offer acoustic and optical Q-factors of 3000 and 0.5×10^5, respectively. With the much larger acoustic Q-factor compared to optical fiber, storage times in the µs range could be demonstrated (see figure 7.5). The optical modes couple to a transverse breathing mode. It was shown by Fiore et al. [346] in a follow-up paper that this storage process is fully coherent (see figure 7.6).

We have seen that the resonator approach has greatly increased the storage time is fully coherent and hence can in principle preserve the quantum state of light [345]. Besides the higher Q-factors compared to SBS based fiber approaches the nature of the acoustic mode that stores the optical information is quite different. In the SBS based approach, it is a traveling acoustic wave with stringent phase matching conditions, whereas in the resonator based approach it is a transverse breathing type acoustic mode. In the latter case, there is only

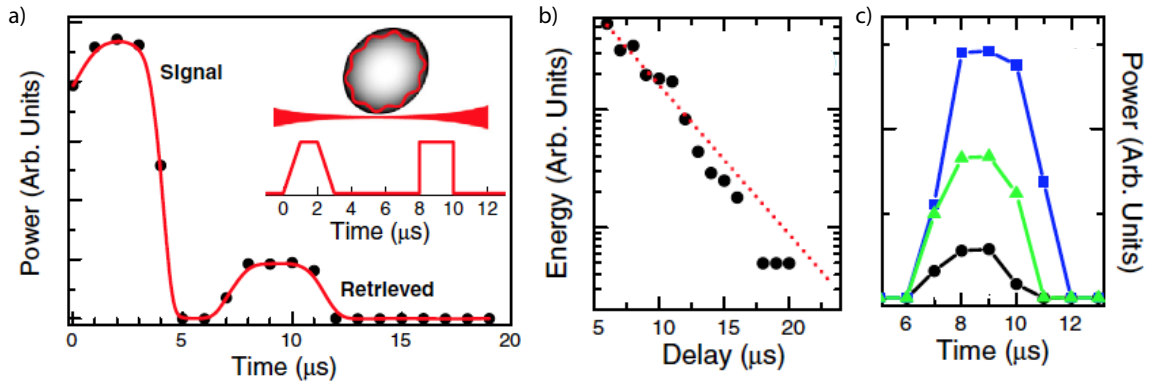

Fig. 7.5 a) Heterodyne measurement of a stored and retrieved optical pulse [345]. b) Exponential decay of the energy of the readout pulse [345]. c) Temporal profile of the readout pulse for different read pulse durations (blue 0.3 µm, green 0.6 µm, black 1.4 µm) [345].

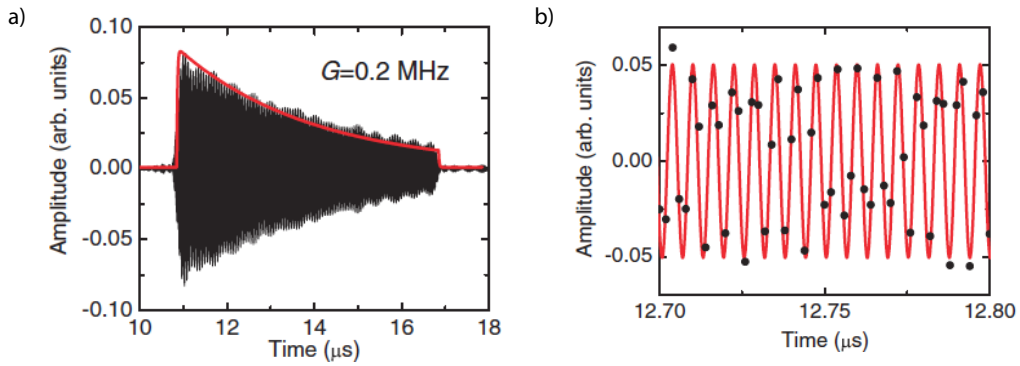

Fig. 7.6 a) Heterodyne beat between the read pulses and the retrieved pulses [346]. b) Zoomed in version of (a) [346].

a minimum change in the k-vector of the involved light waves. The nature of the involved acoustic wave has wide-reaching consequences.
The mechanical breathing mode can be excited at a certain optical frequency and afterward read out by any other optical cavity mode. Hence it allows transferring a quantum state from a certain frequency to another, which has potential applications in quantum signal processing [347]. Whereas state conversion is a desired feature for quantum networks, this non-frequency preserving nature can be disadvantageous in light storage for classical communication applications, as it prevents multiplexing of data streams in different wavelength channels.
Another challenge the resonator based memory faces is the fact that the retrieved data pulse depends on not only the wavelength but also the profile and intensity of the read pulse. This dependence on the read pulse condition might be a hindrance when encoding bit streams with information encoded in the amplitude, as particular care has to be put on the writing and reading conditions.

To overcome some of the aforementioned challenges a Brillouin based resonator approach was pursuit [96, 95]. Here the light field does not couple to a radial breathing mode but a mechanical whispering gallery mode that travels around the circumference of the resonator. The pump, Stokes and mechanical wave have to fulfill the well known Brillouin phase matching conditions (see figure 7.7 a). Hence this approach combines some of the advantages of both schemes - the SBS approach and the micro-resonator approach.
In particular, the phase matching condition distinguishes the Brillouin resonator approach from the previously described light storage scheme. The phase matching assures that only certain optical waves can be coupled via the acoustic wave. Furthermore, it only couples optical signal waves that co-propagate with the write and read pulses. Hence this approach

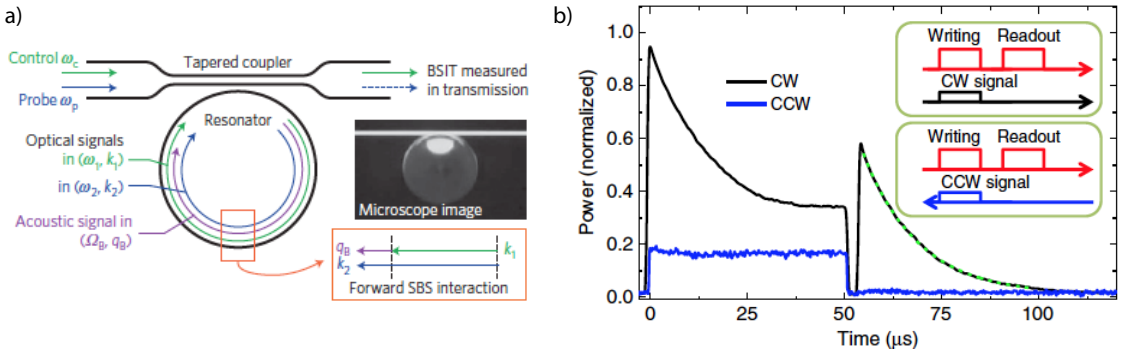

Fig. 7.7 a) Basic principle and phase matching of Brillouin interactions in a resonator [95]. b) Non-reciprocal storage of light pulses using Brillouin optomechanical interactions in a resonator [96].

allows for non-reciprocal light storage [96, 95] (see figure 7.7 b). Note that more recently optomechanically induced non-reciprocity in micro-resonators was also shown, where only co-propagating laser fields couple to a radial mechanical mode [348].
The phase-matching in the Brillouin light storage scheme assures that the frequencies of the pulses in the storage process are preserved, which solves one of the main issues of previous resonator based approaches for light storage. However, the frequencies are still bound to the resonances given by the resonator, and therefore cannot be continuously tuned or adjusted. Also, the bandwidth of the stored pulses is still very limited. This limitation arises due to the narrowband nature of the resonances in the resonator configuration. Furthermore, the pulse shape was preserved neither in these demonstrations (see figure 7.7).

We want to point out the similarity between the so far described light storage schemes in micro-resonators and optomechanically induced transparency (OMIT), which was demonstrated previously in toroids [56] and optomechanical crystals [59]. Even though being conceptually very different, the coupling mechanism between optics and acoustics relies on the same underlying physics. In both cases, optomechanical light storage and induced transparency, a light field is coherently coupled to a mechanical mode.
In the case of induced transparency a probe laser field interferes with the anti-Stokes field of a control laser in such way that a narrow band transmission window opens (see figure 7.8 a) and b)). The same behavior can be achieved using Brillouin interactions in the resonator (see figure 7.8 c, d and e)). As this effect creates a narrowband resonance (as in electromagnetically induced transparency (EIT) in atomic vapor), it is also accompanied by a slow-light effect that can lead to large delays due to the narrow bandwidth of the resonance.
In the optomechanical light storage case, optical control and probe fields also couple coher-

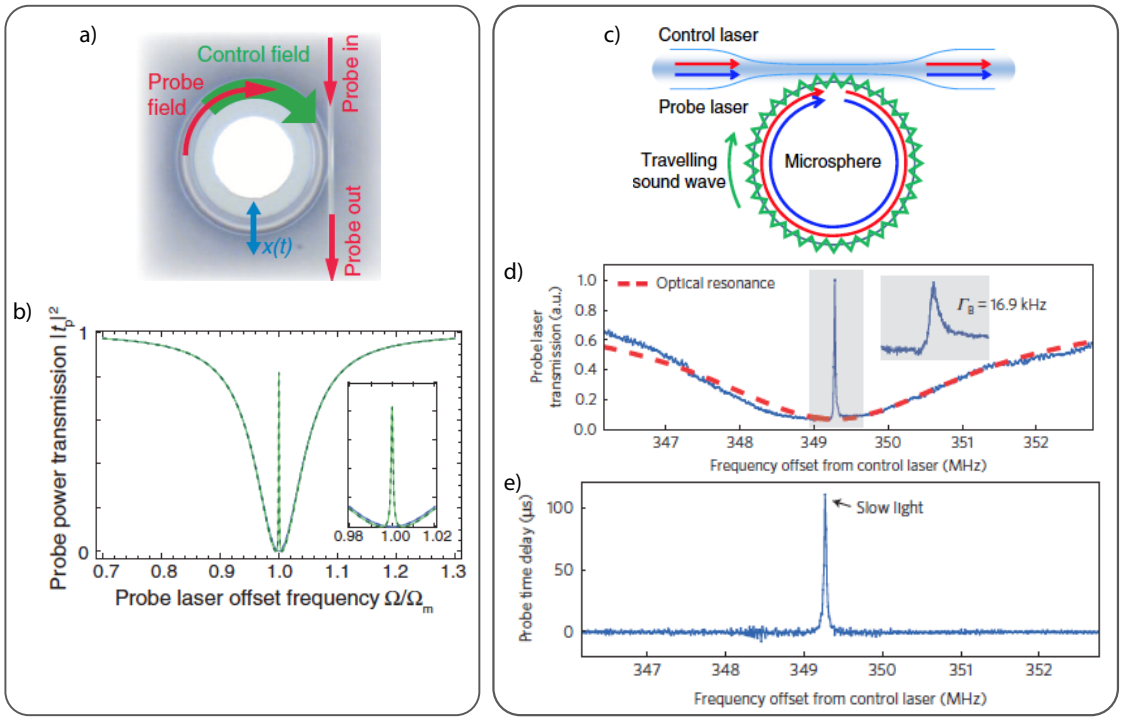

Fig. 7.8 a) Microcavity with a probe and control field that are coupled via a mechanical excitation [56]. b) Narrowband transmission window generated via OMIT [56]. c) Schematic of Brillouin induced transparency [96]. d) Narrowband transmission window generated via Brillouin induced transparency [95] and e) accompanied slow-light effect [95].

ently to a mechanical mode. However, here an optical signal is not delayed by the strong resonance in the transmission spectrum caused by the acoustic resonance. The delay rather arises from a delayed retrieval via an optical read pulse of the information that was imposed on the acoustic wave itself in the coherent writing process.

These effects - optomechanical light storage and induced transparency - in micro-resonators can also be achieved in carefully engineered optomechanical crystals that support optical and mechanical modes. Achievements based on these structures in the context of storing and delaying signals are presented in the next section.

Optomechanic crystals to delay signals

Optomechanical crystals are periodically patterned structures that co-localize optical and mechanical modes and allow strong interactions between the two [349, 350]. These structures are quite similar to the previously described photonic crystals but exhibit, besides the optical bandgap, also an acoustic bandgap [349, 350]. These optomechanical structures allowed for many impressive demonstrations such as ground state cooling of a mechanical oscillator [57]

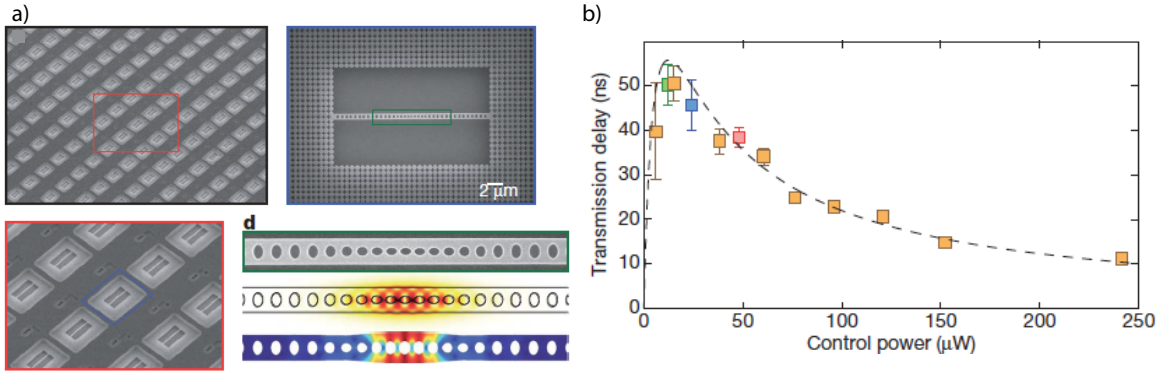

Fig. 7.9 a) SEM image of an array of optomechanical cavities with different levels of zoom-ins. Bottom right panel shows from top to bottom, the defect region of the optomechanical crystal, finite element method (FEM) simulations of the electric field intensity and the mechanical displacement [59] b) Signal delay for different pump powers [59].

and the previously mentioned induced transparency phenomena [59].
An array of optomechanical cavities is shown in figure 7.9 a). Figure 7.9 b) shows the achieved delays in an electromagnetically induced transparency demonstration in such a cavity [59]. Transferring the induced transparency phenomena from atom clouds to optomechanical crystals, greatly increases the control and tailorability of this slow-light technique. Impressive delays could be achieved using this approach, however over a limited bandwidth.

It was theoretically proposed by Safavi-Naeini et al. [351] that optomechanical crystal cavities can not only be used to slow down signals via induced transparency phenomena but also by transferring the optical pulse to a traveling phonon. A schematic of the proposed scheme is shown in figure 7.10. An optical wave excites a phonon that then travels in an acoustic waveguide where it gets reflected at a phonon reflector and travels back to the cavity. There the phonon couples back to an optical wave. The retrieved signal acquires a delay due to the time associated with the phonon traveling forth and back.

An experimental demonstration of this proposed scheme was shown in a double cavity configuration for microwave pulses [352] (see figure 7.10 b) and c)). Two optomechanical cavities, R and L, are connected via a phononic waveguide. Figure 7.10 c) shows a phonon pulse that is excited by a 20 ns microwave pulse in one cavity and travels forth and back between the two. As outlined in the theoretical proposal [59] the signal acquires a delay related to the travel time, in this case, between the two resonant cavities.

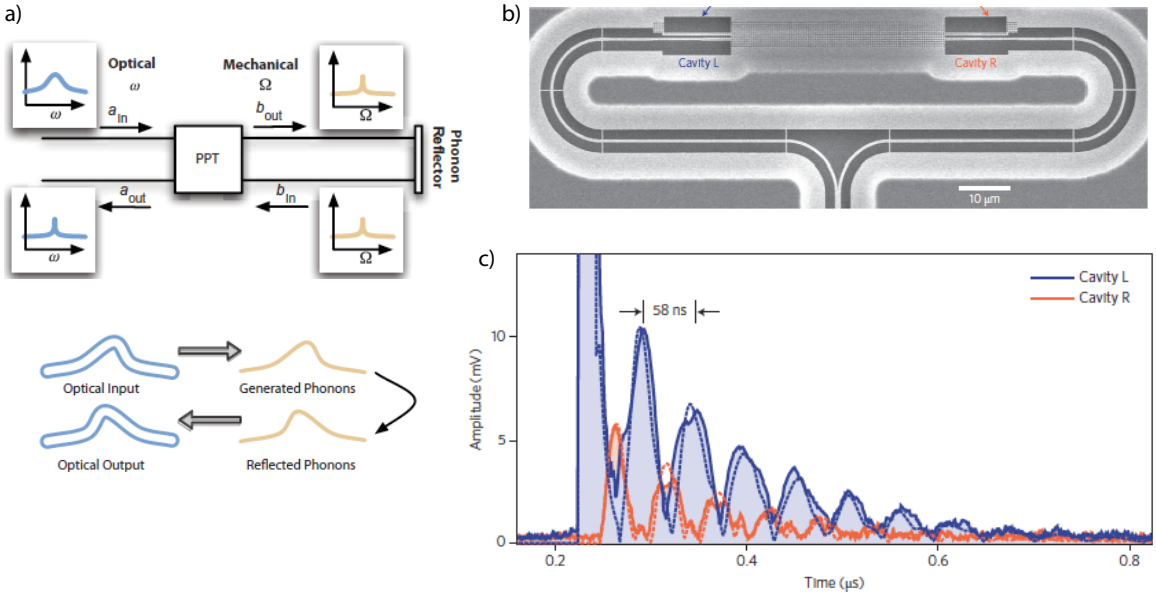

Fig. 7.10 a) Scheme of a delay line based on a photon-phonon translator (PPT) [59]. b) SEM image of an optomechanical crystal with a double cavity (L and R) connected via a phononic waveguide [352]. c) A short microwave phonon pulse gets excited in cavity L and bounces between the two cavities L and R [352].

Photonic-Phononic waveguides

In the following chapter, we present an approach based on a Brillouin scattering induced state transfers from optical to acoustic waves [324]. We show that the capabilities of this delay scheme go far beyond the initial demonstration in highly nonlinear fiber [344]. We show that the memory is able to store phase and amplitude information and works at multiple wavelengths.

These results were achieved in a small footprint chalcogenide waveguide that provides large Brillouin gain. This large Brillouin gain allows performance that goes far beyond what is possible in the fiber-based approach, as it allows operational bandwidths in excess of a GHz (which would require hundreds of Watts of peak power in optical fiber and is hence not feasible).

7.2 Publication: An on-chip photonic phononic memory

This chapter presents a BBM showing the storage of light pulses in an integrated photonic circuit. The following of this chapter is based on the following publication:

M. Merklein, B. Stiller, K. Vu, S. J. Madden, and B. J. Eggleton, "A chip-integrated coherent photonic-phononic memory," Nature Communications **8**, no. 1, 574 (2017).

Abstract

Controlling and manipulating quanta of coherent acoustic vibrations - phonons - in integrated circuits has recently drawn a lot of attention since phonons can function as unique links between radiofrequency and optical signals, allow access to quantum regimes and offer advanced signal processing capabilities. Recent approaches based on optomechanical resonators have achieved impressive quality factors allowing for storage of optical signals. However, so far these techniques have been limited in bandwidth and are incompatible with multi-wavelength operation. In this work, we experimentally demonstrate a coherent buffer in an integrated planar optical waveguide by transferring the optical information coherently to an acoustic hypersound wave. Optical information is extracted using the reverse process. These hypersound phonons have similar wavelengths as the optical photons but travel at 5-orders of magnitude lower velocity. We demonstrate the storage of phase and amplitude of optical information with Gigahertz-bandwidth and show operation at separate wavelengths with negligible cross-talk.

Introduction

Storing or delaying optical signals has been a major driving force for a wide variety of research efforts as it offers new possibilities in all-optical processing and enhanced light-matter interactions. An optical buffer that is able to maintain the coherence of the optical signal, i.e. storing amplitude and phase information, and is able to operate at multiple wavelengths would greatly enhance the capacity of photonic integrated circuits and optical interconnects. Coupling light to coherent acoustic phonons in optomechanical systems offers not only the opportunity to slow down the velocity of an optical pulse [56, 59], but also enables a full transfer of an optical wave to an acoustic wave [62, 345, 353, 63], which subsequently can be transferred back to the optical domain after a certain storage time. Recent years have seen great progress in increasing the storage time in photonic-phononic whispering gallery mode resonators [96, 95, 348, 345] and optomechanical cavities [352, 354, 355], with reported storage times on the order of microseconds. Furthermore, the photon-phonon-photon transfer can be fully coherent [62, 354, 346]. However, there are several major challenges which need to be addressed before an optical memory based on this approach is compatible with all-optical information processing and transmission techniques.

First, any practical optical buffer needs, amongst other requirements, at least a GHz bandwidth. Previous demonstrations relied on structural resonances – either in the form of high-Q resonators or suspended optomechanical cavities, in which the bandwidth is limited to sub-MHz. There are several theoretical proposals to increase the bandwidth in optomechanical systems [351, 356] but there has been no experimental demonstration to date.

Second, optical data transmission schemes usually harness multiple wavelength channels to increase the overall capacity. This means the storage process needs to work over a wide frequency range (a large number of channels); and it needs to preserve the frequency of the optical signal (no cross-talk between the channels). These requirements are challenging to fulfill in photonic-phononic systems relying on structural resonances, e.g. silica fibre-tip whispering gallery mode resonators or photonic-phononic crystal defect modes, since the optical wavelength is strictly bound to the resonance frequency. In the case of whispering gallery mode resonators, an optical pulse transferred to a phonon can be retrieved by a read pulse at a different wavelength [345], so several wavelength channels cannot be stored and retrieved unambiguously, since the storage/retrieval process is not frequency preserving [347, 357].

Finally, a practical optical buffer must be chip-integrable and able to be interfaced with other on-chip components, criteria not easily satisfied with other optomechanical platforms investigated to date. Fused silica fibre-tip resonators are micrometre size [96, 95, 348, 345, 346] but cannot be easily implemented onto a planar chip platform. Lithographically-produced

photonic-phononic crystals, which form resonant cavities for the acoustic and optical modes, possess the requisite small footprint [352, 354]. Despite this, they either rely on fibre taper coupling [358, 359] that can be challenging to operate outside a laboratory environment or require complicated under-etching processes to maximize the optical and acoustic Q-factor [350]. The underetching step is required to confine the optical and acoustic modes in the out-of-plane direction and avoid leakage to the substrate, but limits compatibility with planar integrated photonic circuits.

Here, we demonstrate a different approach for coherent optical storage, harnessing travelling acoustic phonons in a planar integrated waveguide. We transfer the information carried by the optical signal to these acoustic phonons using stimulated Brillouin scattering (SBS) [108, 344]. We demonstrate that this transfer is fully coherent by storing and retrieving different phases. Our buffer does not rely on a structural resonance, so is not limited to a narrow bandwidth or single wavelength operation. We show that the unique phase matching condition between travelling acoustic and optical waves allows the unambiguous storage and retrieval at several different wavelengths without cross-talk.
This result was enabled by a recent paradigm shift in SBS research from long lengths of optical fibre to chip-scale devices, allowing the excitation of coherent acoustic phonons on a chip using optical forces [75, 98, 101, 81, 106]. The opto-acoustic interaction strength is increased by several orders of magnitude by using carefully designing waveguides that guide optical as well as acoustic waves, allowing us to store broadband optical signals in a planar waveguide without relying on a resonator geometry. The acoustic phonons travel in the waveguide at a velocity that is 5-orders of magnitude slower than in the optical domain and do not suffer from effects of optical dispersion and other detrimental optical non-linearities during the delay process. Transferring the signal back to the optical domain leads to a delay of the optical signal by approximately the time the signal was encoded as acoustic wave.

In this article, we exploit this ultra-strong local opto-acoustic interaction in a highly non-linear chalcogenide spiral waveguide to demonstrate storage of several optical bits with sub-ns pulse-width corresponding to a broad GHz bandwidth. We show the retrieval of the phase and amplitude information, multi-wavelength operation and continuously adjustable storage time over 21 pulse widths. We confirm our measurements using simulations based on coupled-mode equations showing excellent agreement with the experimental results. Our photonic-phononic memory operates at room temperature and only relies on a planar waveguide that can be interfaced with other on-chip components in a straight forward manner.

Results

Experimental approach

We use SBS - one of the strongest nonlinear effects - to coherently couple two optical waves and an acoustic wave. The optical data signal is transferred to the acoustic wave by a strong counter-propagating optical write signal. Using this nonlinear effect as a memory was first proposed in highly nonlinear fibre[344, 360]. The storage of only one amplitude level of several nano-second long pulses has been shown to date[344]. This is only a fraction of the capability this memory concept can offer.

Our approach to write and retrieve the optical data pulses as acoustic phonons is schematically shown in figure 7.11 a) and 7.11 b). A strong optical write pulse ω_{write}, offset by the acoustic resonance frequency of the optical waveguide material, propagates counter to the optical data pulse ω_{data}. When the two pulses encounter each other, the beat pattern between the two compresses the material periodically through a process known as electrostriction, exciting resonantly and locally a coherent acoustic phonon $\Omega = \omega_{\text{data}} - \omega_{\text{write}}$.
The required power depends on the local Brillouin gain, which is orders of magnitude higher in chalcogenide As_2S_3 rib waveguides than, for example, in standard silica fibre. The optical and the acoustic modes are guided in the rib waveguide structure by the refractive index contrast and the acoustic impedance between the chalcogenide glass and the silica surrounding, respectively [109]. Once transferred to the acoustic wave the information on the optical data pulses can be retrieved after a storage time of several nanoseconds, corresponding to several tens of data pulse widths.
The process is shown in figure 7.11 b). A strong read pulse is coupled into the waveguide and retrieves the optical information by depleting the acoustic wave, the inverse process of the writing step. The setup for the photonic buffer is schematically shown in figure 7.11 c) (a detailed description of the setup can be found in the methods section 7.2 and in supplementary figure 7.15).

Photonic chip

As a storage medium we use a small footprint spiral waveguide made from the chalcogenide glass As_2S_3 comprising a rib waveguide structure with a cross-section of 2.2 μm by 800 nm. A photo of the chip is depicted in the inset of figure 7.11 c) next to an Australian 50-cent coin.
Every chip consists of spirals with several lengths ranging from around 9 cm to 24 cm. The

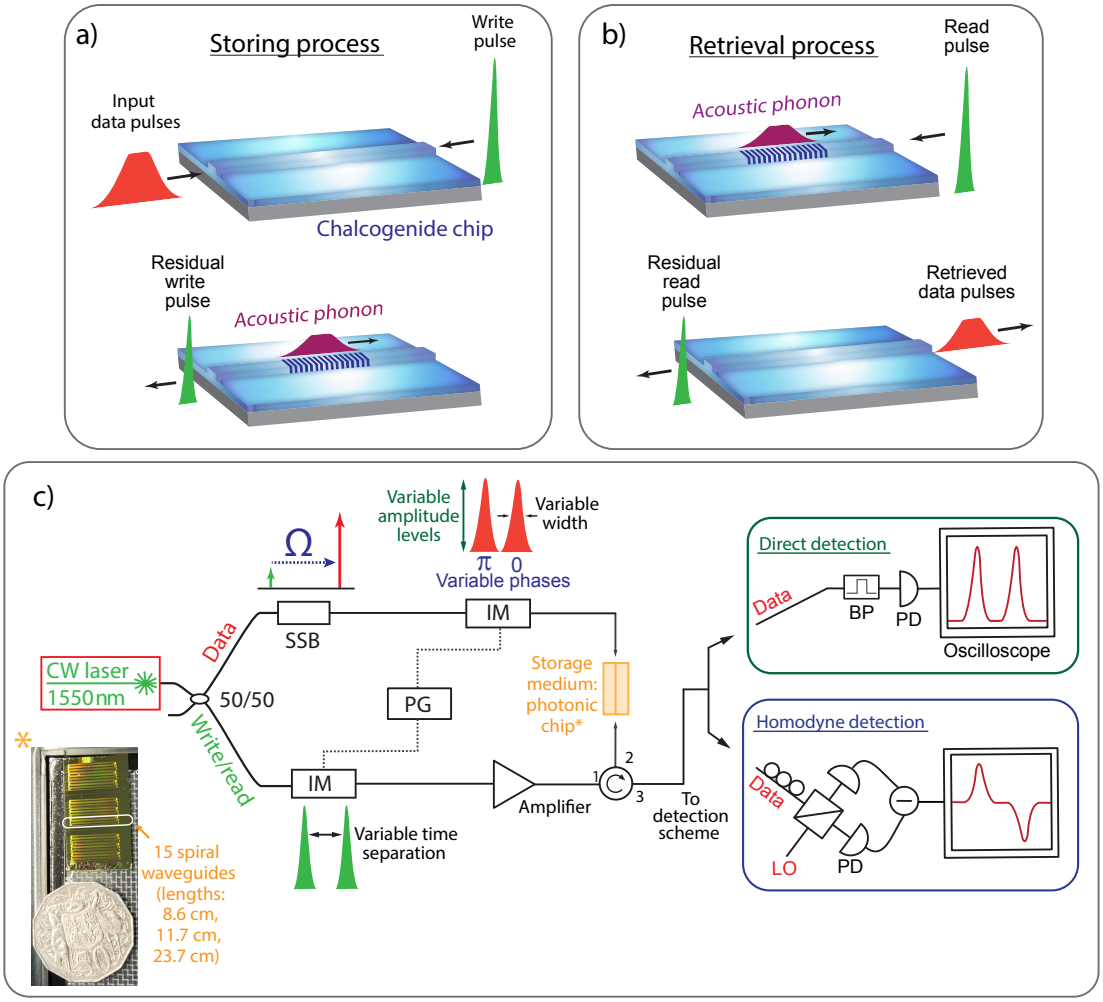

Fig. 7.11 **Basic principle and setup of the photonic-phononic memory** a) An optical data pulse is depleted by a strong counter-propagating write pulse, storing the data pulse as an acoustic phonon. b) In the retrieval process a read pulse depletes the acoustic wave, converting the data pulse back into the optical domain. c) A basic schematic of the experimental setup. The inset shows a chalcogenide chip next to a 50-cent coin. The chip contains more than 100 spiral waveguides with different lengths. Note: This is only a schematic and the actual setup is more advanced and can be found in Supplementary Figure 1 (CW: continuous wave; SSB: single-sideband modulator; IM: intensity modulator; PG: pulse generator; PG: bandpass filter; PD: photo-detector; LO: local oscillator; Ω: Brillouin frequency shift.)

spiral waveguides are grouped in quintets with a footprint per group of 20×0.7 mm. Longer waveguides are available by repeating the same spirals on one chip during the fabrication, leading to waveguides with up to 46 cm length. For details on the fabrication methods of the chip we refer to reference[274].

Lensed fibre-tips are used to couple light in and out of the waveguides. The chalcogenide

glass is sandwiched between the silica substrate and the silica over-cladding. This not only provides guidance of the optical mode due to a contrast in the refractive index but provides also an acoustic impedance mismatch between the soft chalcogenide glass (v_{sound}=2500 m/s) and the stiff silica (v_{sound}=5996 m/s). Both the optical and the acoustic waves are guided in the chalcogenide glass, which provides a large opto-acoustic overlap. Ultra-high Brillouin gain of up to 50 dB amplification of a small continuous wave (CW) seed for a moderate CW pump power of 300 mW was achieved.

Tunability of the storage time

The experimental realizations of an all-integrated multi-wavelength coherent photonic-phononic buffer is shown in figures 7.12, 7.13 and 7.14. Figure 7.12 a) shows the depletion of the optical data pulse with increasing counter-propagating write pulse power (storing process). For this experiment the storage medium is a 46 cm long spiral waveguide. Due to the ultra strong Brillouin gain in chalcogenide waveguides, the depletion reaches over 90% with 20-fold lower write pulse peak power than in highly nonlinear fibre approaches [344] for similar pulse conditions. The peak power levels of the interacting optical pulses presented in this article vary from 10 mW to 50 mW for the data pulses and 3 W to 10 W for the write and read pulses depending on the overall gain of the individual waveguides.

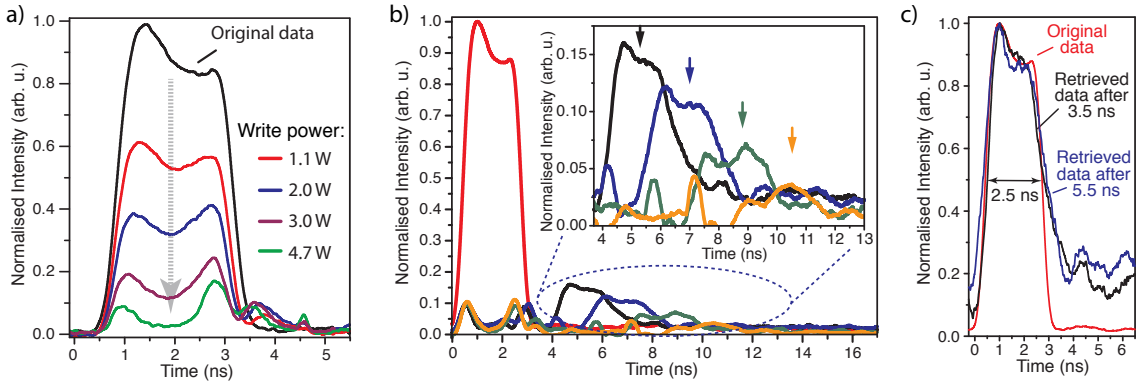

Fig. 7.12 **Store and retrieval process with tunable storage time** a) Storing process: The optical data pulse is depleted by the counter-propagating write pulse, transferring the carried information to the acoustic phonon. Depletion of more than 90% can be achieved. b) Retrieved data pulses after different storage times. The inset shows a zoomed-in version of the retrieved data pulses. c) Original data pulse super-imposed with the retrieved data pulses after 3.5 ns and 5.5 ns respectively; the details of the original shape can be distinguished in the retrieved data pulses.

The storage and subsequent retrieval of the optical data pulses are demonstrated in figure 7.12 b). The storage time can be continuously adjusted by simply controlling the time difference between the read and the write pulses. A readout efficiency of 15% to 32% after 3.5 ns was achieved (see also Supplementary Figure 7.17). The inset of figure 7.12 b) shows a zoomed-in version of four examples of retrieved data pulses after different storage times. From the exponential decrease of the retrieval efficiency an acoustic decay time of 10.5 ns is measured using an exponential fit and is confirmed by a pump-probe measurement of the Brillouin gain linewidth (see supplementary figure 7.16).
In order to study the retrieval of the pulse shape, we superimpose the normalized original data pulse with two normalized retrieved data pulses, displayed in figure 7.12 c). The shape of the optical data pulse is maintained during the storage process indicating that the bandwidth of the photonic-phononic memory is large enough to resolve even small features, such as the peak at the beginning of the optical data pulse. The intrinsic Brillouin linewidth is only in the range of tens of MHz, however due to the strong opto-acoustic coupling in the photonic-phononic waveguides the Brillouin response can be broadened to several GHz [361].

Phase coherence and multiple amplitude storage

We showed in the previous section that we can store nanosecond pulses in a waveguide with continuous tunable storage time while maintaining the pulse shape. In this section we show that we can extend the operational bandwidth of our memory much further, allowing the storage of sub-ns pulses with different amplitude levels. Furthermore we show that the transfer process of photon to phonon back to photon is fully coherent, enabling the storage of different phase states. These demonstrations show a significant increase in the capacity of the memory.
The retrieval of the amplitude and phase information of two short optical pulses with 500 ps pulse width after 3.5 ns is shown in figure 7.13 a) and c). For the storage of these short pulses we used 24 cm long waveguides, hence a better signal-to-noise ratio (due to lower overall propagation loss) is achieved in comparison to the measurements presented in figure 7.12. The pulse width corresponds to a bandwidth of more than 1.5 GHz, almost 2-orders of magnitude wider than the intrinsic Brillouin linewidth. This implies a very high local Brillouin gain in the pulse overlap region as the Brillouin gain is spread out over a wide frequency range.
We encoded 6 different amplitude levels in pulse 1, while maintaining the amplitude level of a second data pulse constant as a reference. A comparison of the original and retrieved pulse 1 (inset) shows that we can easily distinguish 6 different amplitude levels; this can be enhanced

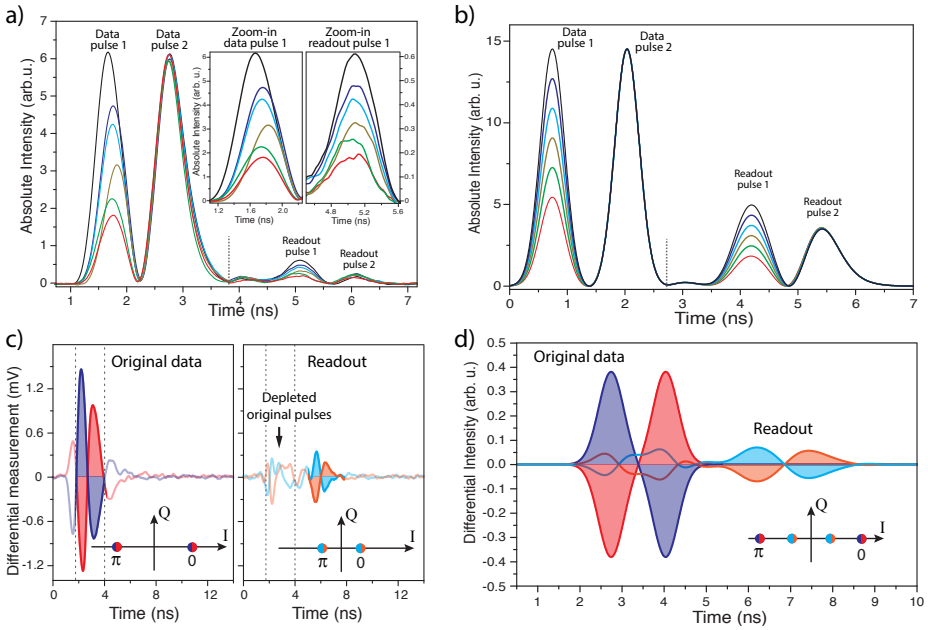

Fig. 7.13 **Amplitude and phase encoded signals** a) Six different amplitude levels of a 500 ps optical pulse can be stored and retrieved after a storage time of 3.5 ns via direct detection. The amplitude of pulse 2 remains constant for the original and retrieved data pulse. The read-out efficiency of pulse 2 is lower due to practical limitations in the experiment (power limitation). b) Simulation data of the amplitude response of the system. c) Two phase levels of two 500 ps optical pulses, either 0 and π or π and 0 are retrieved via homodyne detection after a storage time of 3.5 ns. The lower inset shows the two phases in phase space. d) Simulated phase response of the system.

with a more sensitive detection system. The amplitude of the second retrieved data pulse remains constant as does its original amplitude. We simulate our system using coupled-mode equations [189, 362] and see great agreement with our measurements, presented in figure 7.13 b) (more details on the simulation methods can be found in the Supplementary Note 4). Further to multiple amplitude levels, we can also store and retrieve different optical phases to show the coherence of the state transfer between travelling acoustic and optical waves. To distinguish the phase we replace the direct detection scheme (single photodiode) with an interferometric homodyne detection scheme. Here, the phase encoded signal interferes with a local oscillator and is detected by a balanced detector measuring the difference signal of two equal photodiodes.

Two pulses are encoded with two different phases, either 0 and π (blue) or π and 0 (red), respectively figure 7.13 c). After being stored for 3.5 ns, these same values can be read out (light blue and orange) and are clearly distinguishable. For a better understanding, the states in the phase space (I - Q diagram) are related to the optical pulses. For phase 0, the local

oscillator and the data pulses interfere constructively, resulting in a positive value, for π they interfere destructively which results in a negative pulse on the balanced detector. The phase retrieval is possible due to the coherence of the Brillouin process and proves its potential as a coherent buffer. Note, that this feature can be implemented for any phase in the entire phase space and not only for 0 and π. Here, too, as for the amplitude measurements, we simulate our system and see excellent agreement between the measurements and the simulations (figure 7.13 d).

Multi-wavelength operation

Here, we demonstrate the multi-wavelength capabilities of our memory. On the one hand the memory operation must work at several different wavelengths, while on the other hand the cross-talk between wavelength channels should be minimal. Our Brillouin-based memory works at all wavelengths where the waveguide is transparent, in contrast to resonator-based approaches where one is bound to the particular resonance frequencies.
This transparency window reaches, in the case of chalcogenide, from the visible all the way to the deep infrared. To demonstrate the wavelength multiplexing capacity, we adjusted the operation laser wavelength to 3 different values in the tuning range of our laser. It can be seen from figure 7.14 a) that the same efficiency is achieved for all wavelengths. The pulse shape for the 1552.9 nm measurement is slightly distorted which can be assigned to the limitations in our setup (power limitations and effects of the nonlinear loop (see Supplementary Note 1)) and is not of a fundamental nature.

Every pair of frequencies (data frequency and read/write frequency) excites an acoustic wave at a specific frequency, which can be most easily seen in the equation for the Brillouin frequency shift $\Omega = 2V_A n_{eff}/\lambda$ (Ω Brillouin frequency shift, V_A longitudinal acoustic velocity, n_{eff} effective refractive index and λ laser wavelength). The respective Brillouin shifts Ω are indicated in figure 7.14 a).
The second important point concerns the cross-talk between different wavelength channels: Here, the unique phase matching conditions between travelling acoustic and optical waves inhibits mixing of different frequency channels (as illustrated in figure 7.14 b), e) and h)). The storage and read-out process is strictly bound to specific phase matching conditions, such that the process is operational at different wavelengths at the same time.
To prove the point that there is no cross-talk between different channels we couple two data pulses, separated by only 100 GHz, simultaneously into the waveguide and measure the waveguide output using a dual channel oscilloscope (figure 7.14 c) and d)). When adding

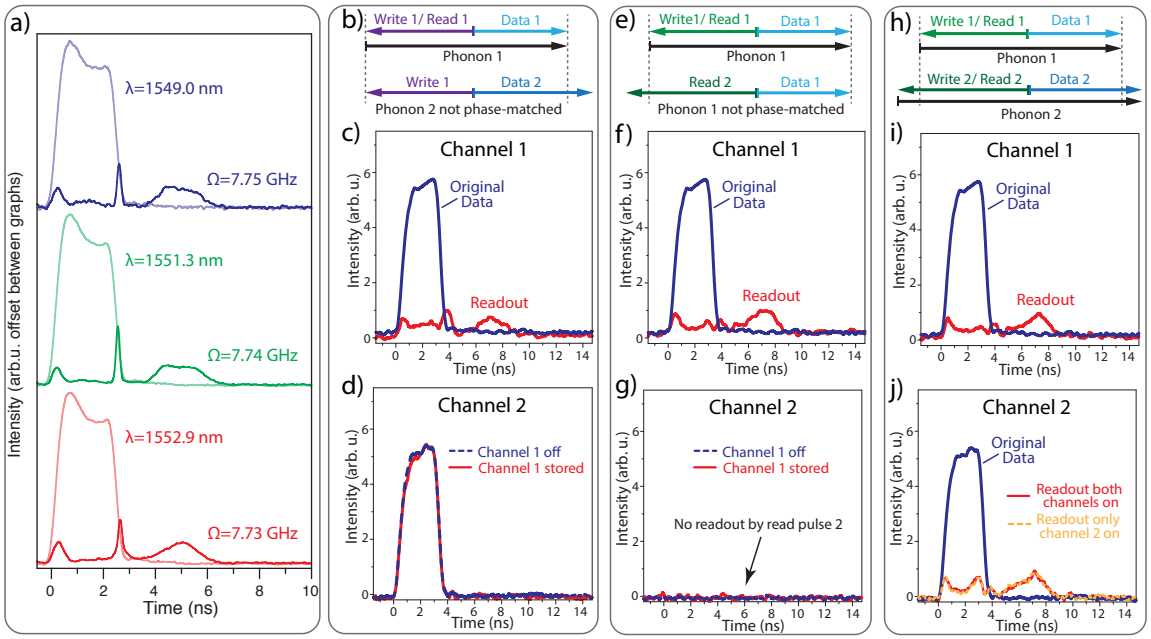

Fig. 7.14 **Multi wavelength operation** a) Multi wavelength operation of the photonic-phononic memory for three different laser wavelengths. The efficiency of the memory remains the same. b) Phase matching condition for two data pulses and one write pulse phase-matched to data pulse 1 (corresponds to measurement c) and d)). The second data pulse is not phase-matched and therefore not affected by the write pulse. c) Storage and retrieval of data pulse channel 1 while a second data pulse (d) in a separate channel (100 GHz away from channel 1) is unaffected. e) Phase matching condition for two separate read pulses with a data pulse and a phonon (corresponds to measurement f) and g)). One can see that the second read pulse cannot readout the phonon. f) Shows the writing and retrieving of a data pulse in channel 1 while at the same time no readout pulse can be seen in channel 2 (g). h) Phase matching condition for two channels operating at two different wavelengths. i) Storage and retrieval of data in channel 1 while simultaneously storing and retrieving data in channel 2 (j). Note: The difference in the noise floor between channel 1 and channel 2 is caused by the different noise properties of the two different photodiodes.

write and read pulses phase-matched to the data pulses in channel 1 only the data pulse in this channel gets stored and retrieved (figure 7.14 c)) while there is no effect observable in channel 2 (figure 7.14 d)). This result shows that one can operate the memory on individual data streams, separated by a standard 100 GHz guard-band, without adding any detrimental distortions on the other channel.

We furthermore experimentally show that a non-phase-matched read pulse cannot retrieve information stored in a different frequency channel (figure 7.14 f) and g)). To demonstrate this, we store and retrieve an optical data pulse in channel 1 (figure 7.14 f), while simultaneously a second read pulse, separated by 100 GHz from the read pulse in channel 1, does not readout the stored data pulse, see figure 7.14 g). This is a major difference to light storage schemes based on opto-mechanical resonator scheme where light interacts with standing

acoustic waves or couples to transverse acoustic modes, as in these cases there is no or only a minimum momentum transfer. Therefore many different optical modes get modulated by the presence of the acoustic mode, hence these schemes are well-suited for wavelength conversion [357].
Finally, we show that there is no cross-talk between the two wavelength channels separated by 100 GHz even when optical data pulses are stored and retrieved simultaneously in the two channels (figure 7.14 i) and j)). For comparison figure 7.14 j) shows also the stored and retrieved data pulse with the second channel turned off (orange dashed line).

Discussion

In this article we have demonstrated a coherent photonic memory based on optically actuated travelling acoustic phonons in a planar waveguide. Our memory relies on a state transfer from photons to slowly propagating phonons and can therefore be seen as a completely different approach compared to schemes which rely on a reduced group velocity of light pulses such as coupled optical resonators [363–365], photonic crystal cavities [366, 204, 203] or slow-light schemes [181, 204, 180, 367]. By transferring the optical pulse to an acoustic wave, our optical buffer allows to circumvent detrimental optical dispersion effects [338, 368] and allows for relatively long delay times of many pulse widths. The delay time can potentially be increased even further using a cascaded process [369] or by further engineering the dissipation rate of the travelling acoustic phonon.
The photonic-phononic memory is fully controlled by the spatial-temporal overlap of the data, write and read optical pulses in a simple planar photonic circuit. Therefore the buffer is not an additional element of the circuit, but the photonic waveguide/link itself can be used as the buffering element bringing additional functionality to optical interconnects for next generation microelectronic networks [370–373].
Storing and retrieving the full coherent information carried by the light signal enables the processing of multiple amplitude and phase levels, which is essential for contemporary communications schemes and greatly increases the number of bits that can be stored. The ultrahigh Brillouin gain in chalcogenide glass allows for the encoding of signals down to 500 ps pulse width. Even shorter pulses can be realized by further reducing waveguide losses and increasing the opto-acoustic coupling by tailoring acoustic properties.
A very important feature of the demonstrated buffer is the operation at separate optical wavelengths without cross-talk. In particular the frequency preserving property due to the stringent phase-matching condition between travelling acoustic and optical waves is essential for multi-channel operation in order to store and retrieve information at different frequency

channels unambiguously. In communication networks and computing architectures, this versatility plus the continuous tunability of the storage time of up to several nanoseconds enables precise and dynamic synchronization of optical data streams between several high-speed parallel processes.

Methods

Experimental setup for light storage

A narrow-linewidth distributed feedback (DFB) laser at 1550 nm is divided into two arms - data and write and read arm - where the data pulse is frequency up-shifted by the Brillouin frequency shift Ω via a single-sideband modulator. The pulses are imprinted by two intensity modulators connected to a short-pulse generator. The write and read pulses are amplified by an erbium doped fibre amplifier (EDFA). The amplified write and read pulses pass through a nonlinear fibre loop.
The loop has two effects: firstly, it allows only the pulses to be transmitted and efficiently suppresses any noise or coherent background present from the laser or amplifier, respectively. Secondly, it improves the pulse shape by smoothing the edges of the pulses. After the loop a second EDFA amplifies the pulses again to reach the necessary peak power of several Watts. Bandpass filters (bandwidth 0.5 nm) are used in both arms to minimize the white noise from the EDFAs. Both paths lead to opposite sides of the photonic chip. The original and retrieved data pulses are observed by a 12 GHz photodiode connected to the oscilloscope. Before the photodiode a tunable narrowband filter is used to assure that only the data pulses reach the photodetector.

Detection schemes

Two different detection schemes are used to detect the transmitted and retrieved data pulses: direct detection with a single photodiode is used for the amplitude retrieval whereas a homodyne detection scheme is used for the phase measurements. For the direct detection scheme a 12 GHz photodiode connected to the oscilloscope is used. For the homodyne detection scheme a local oscillator (continuous wave) at the wavelength of the data pulses interferes at a 50 / 50 coupler with the original and retrieved data pulses. The beat signal is sent to a polarization beam splitter both output signals of which are connected to a balanced photodetector. The polarization of the local oscillator and the data pulses are controlled such that the difference signal of both photodiodes of the balanced photodetector is maximized in order to distinguish the two phases, shifted by π. In both detection schemes a tunable narrow-band filter ($\approx$ 4 GHz) is used to assure that only the data pulses reach the photodetector.

Supplementary

Supplementary Note 1: Detailed experimental setup

The experimental setup is shown in figure 7.15. A continuous wave (CW) narrow-linewidth distributed feedback (DFB) laser at 1550 nm is divided into a data and write-and-read arm by a 50 / 50 fibre coupler. The data pulses are frequency up-shifted by the Brillouin frequency shift $\Omega = 7.7$ GHz via a single-sideband modulator. The CW laser signal is carved into pulses by two intensity modulators connected to a short-pulse generator, allowing the generation of pulses with different amplitude levels and phase states. The pulses are amplified using erbium-doped fibre amplifiers (EDFA) and subsequently filtered by narrow bandwidth (0.5 nm) bandpass filters to reduce the effect of broadband white noise introduced by the amplification step. Additionally to the passive bandpass filter a nonlinear fibre loop is implemented in the write-and-read arm. The loop consists of 1 km standard single-mode fibre, a polarization controller and a 50 / 50 coupler to introduce some asymmetry in the two paths. This fibre loop is used for two reasons: firstly it allows only the pulses to be transmitted and efficiently suppresses any noise or coherent background present from the laser or amplifier respectively. Secondly, it improves the pulse shape by smoothing the edges of the pulses. After the loop a second EDFA amplifies the pulses again to reach the necessary peak power of several watts. Both paths lead to opposite sides of the photonic chip and are coupled to the waveguide using lensed fibres.

For the multi-wavelength measurement a second laser, 100 GHz apart from the first laser, is used and coupled into the data or write-and-read arm, respectively. The output from the chip (circulator port 3 in figure 7.15) is split with a 50 / 50 fibre coupler and sent to two

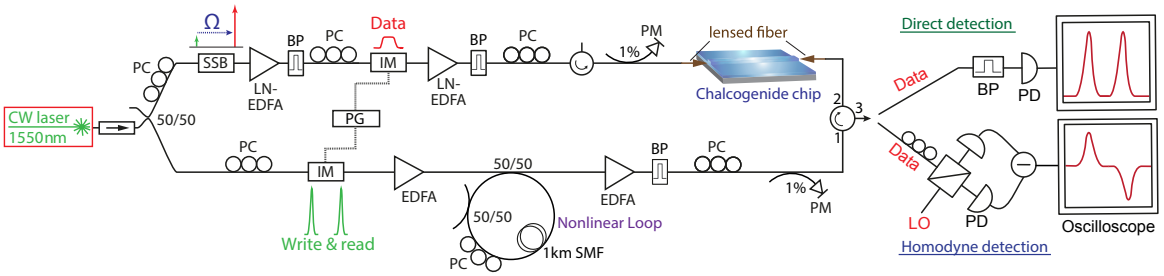

Fig. 7.15 **Experimental setup** CW laser: continuous wave laser; PC: polarization controller; SSB: single sideband modulator; EDFA: erbium doped fibre amplifier; LN-EDFA: low-noise EDFA; BP: bandpass filter; SMF: standard single-mode fibre; PM: power meter; LO: local oscillator; PD: photodetector

narrowband filters to separate the two wavelength channels. Each filtered channel is then detected using two 12 GHz photodiodes connected to a dual channel oscilloscope.

Supplementary Note 2: Acoustic decay time

We analyzed the storage time of the phonon memory and compared it with a standard pump probe measurement of the Brillouin linewidth. Figure 7.16 a) shows different readout pulses for different storage times up to 10.5 ns. For increasing storage times the readout efficiency decreases due to the decaying amplitude of the acoustic wave. The area of the retrieved pulses is integrated to determine the acoustic decay time (figure 7.16 b). The exponential decrease of the pulse areas are plotted in figure 7.16 c) and an exponential fit $\exp(-2t/\tau_A)$ reveals an acoustic decay time of 10.2 ns.

We confirm the acoustic decay time by measuring the linewidth of the Brillouin gain response (figure 7.16 c). A modified version of the setup in figure 7.15 is used to execute the CW pump probe measurements. The intensity modulators were removed and the single-sideband (SSB) modulator is frequency swept by the RF output of a vector network analyzer (VNA) to generate a seed signal. The transmitted seed signal is detected by a photodiode connected to

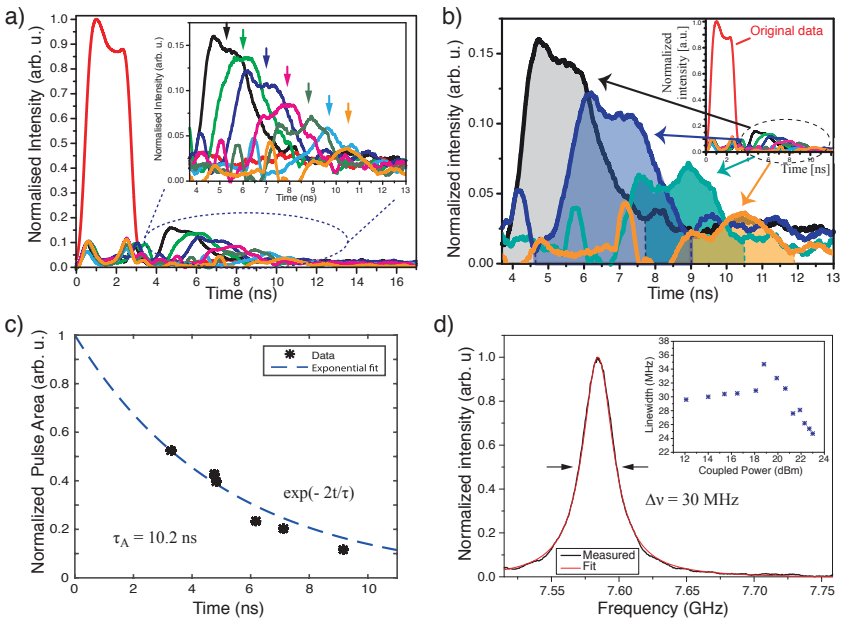

Fig. 7.16 **Storage time and acoustic decay time** a) Measurements of different storage times. b) Four retrieved data pulses with shaded pulse area. c) Pulse area with exponential fit reveals acoustic decay time of 10.2 ns. d) Brillouin linewidth measured with a CW pump-probe setup showing 30 MHz linewidth. The inset shows the linewidth for different pump powers.

the VNA and the Brillouin response for different pump powers is measured.
The Brillouin gain linewidth ν_B relates to the acoustic decay time τ_A as $\tau_A = 1/\pi\Delta\nu_B$. The fit in figure 7.16 c) shows a linewidth of 30 MHz for 21 dBm pump power, which agrees perfectly with the 10.2 ns decay time measured in the storage experiment. As expected the linewidth of the gain peak decreases above the Brillouin threshold (inset figure 7.16 d).
The great agreement of the two measurement techniques not only confirms the consistency of the light storage measurements, but also suggests itself for using the storage technique to locally access material and structure specific acoustic decay times. Whereas CW based pump probe schemes only provide an average of the acoustic decay time over the whole length of the waveguide, the pulsed measurement determines the acoustic decay time at the point of the waveguide where the pulses overlap. The overlap can be scanned along the waveguide providing spatial information about the waveguide.

Supplementary Note 3: Maximum amplitude readout

The readout efficiency could be increased to 32% after 3.5 ns storage time as shown in figure 7.17. It is known from numerical studies that the amplitude of the retrieved pulses can be enhanced by using chirped pulses [189]. The 32% readout depicted in figure 7.17 is achieved by increasing the input power into the nonlinear loop (see setup figure 7.15), deliberately chirping the pulses to achieve the highest amplitude read-out efficiency.
Achieving record readout amplitude efficiencies comes with distortions in the pulse shape. However, there are applications, where the overall readout efficiency is more important than the pulse shape, such as simple on-off keying schemes. In the same way one can increase the maximum retrieval time of the buffer by increasing the efficiency and therefore lifting the amplitude of the retrieved pulse above the noise floor. Higher input power increases the nonlinear process known as self phase modulation, chirping the pulses [108]. The nonlinear loop in the setup therefore not only reduces the noise, but also allows for a more efficient readout amplitude through compression of the retrieved pulse. However the pulse shape is not maintained in this case.

Besides using chirped pulses to improve the maximum retrieval amplitude, it was also shown theoretically that small amounts of chirp help to more efficiently excite the acoustic wave [362]. This can be understood by drawing an analogy to the McCall and Hahn area theorem for atomic two-level system [374]. Analogues to the π pulse in atomic resonances, a normalized pulse area of the write pulses can be defined and is given by [362] $\Theta = \sqrt{g_B c/8A_{\text{eff}}\tau_B n} \times \int A(t)dt$, with the Brillouin gain coefficient g_B, the speed of light c,

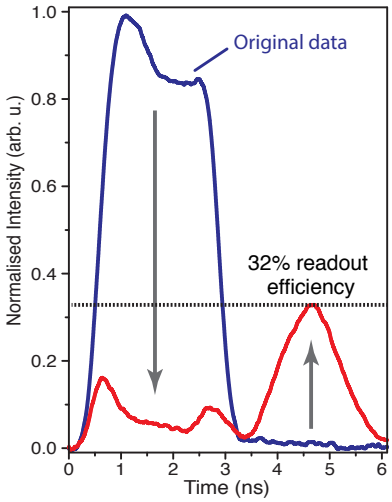

Fig. 7.17 **Maximising the amplitude retrieval efficiency** A 32% retrieval efficiency of the pulse amplitude after a storage time of 3.5 ns was achieved

the effective mode area A_{eff}, the acoustic decay time τ_{B}, the refractive index n and the time integral over the pulse envelope $A(t)$.
The maximum efficiency for exciting the acoustic wave is achieved when $\Theta = (m+1/2)\pi$ with m being an integer number. However the data pulse cannot be transferred to the acoustic wave if the pulse area is an integer multiple of π. If the pulse area is a multiple of π the first half of the pulse will write the acoustic wave, while the second half retrieves it again. However, for a linear chirped pulse the beginning of the pulse has a different frequency as the end of the pulse. Therefore, only a certain part of the pulse resonantly excites the acoustic wave and importantly does not de-excite the acoustic wave.

Supplementary Note 4: Simulation method

To simulate the phase and amplitude response of our system we solved standard coupled mode equations as presented in [189] using an implicit fourth order Runge-Kutta method [278]. The slowly-varying envelope coupled mode equations for a forward travelling pump wave A_{P}, a counterpropagating Stokes wave A_{S} and an acoustic wave Q can be written in the following form [189]:

$$\frac{\partial A_{\text{P}}}{\partial z} + \frac{n}{c}\frac{\partial A_{\text{P}}}{\partial t} = -\frac{g_0}{2A_{\text{eff}}} Q A_{\text{S}} - \frac{1}{2}\alpha A_{\text{P}} \tag{7.1}$$

$$-\frac{\partial A_{\text{S}}}{\partial z} + \frac{n}{c}\frac{\partial A_{\text{S}}}{\partial t} = \frac{g_0}{2A_{\text{eff}}} Q^* A_{\text{P}} - \frac{1}{2}\alpha A_{\text{S}} \tag{7.2}$$

$$2\tau_B \frac{\partial Q}{\partial t} + Q = A_P A_S^* \tag{7.3}$$

The slowly varying envelopes A_P, A_S are normalized such that $|A_{P/S}|^2$ is the power in watts, Q is the amplitude of the acoustic wave, n is the refractive index, c the speed of light, g_0 the Brillouin gain coefficient, A_{eff} the effective mode area, τ_B the acoustic lifetime and α the waveguide loss parameter.
The envelopes of the input data, write-and-read pulses are approximated to have Gaussian form [362]:

$$A_{P/S} = A_0 \exp(-\frac{1+iC}{2}\frac{t^2}{\tau^2}) \tag{7.4}$$

with the parameter C giving the chirp rate in GHz / ns following the definition of [362] and τ being the FWHM. The parameters used for the amplitude simulations (figure 7.12 b)) are as follows: $n = 2.4$, $g_0 = 0.715 \cdot 10^{-9}\mathrm{m/W}$, $A_{eff} = 1.5 \cdot 10^{-15}\mathrm{m}^2$, $\tau_B = 10.5\,\mathrm{ns}$, $\alpha = 0.2\,\mathrm{dB/cm}$. The FWHM of the data pulses is 500 ps and the peak power is varying in equidistant steps from 15 mW to 40 mW. The FWHM of the data pulses was 1 ns, the peak power 3.5 W and $C = 0.88$ GHz / ns. The temporal separation of the write and the read pulse was 3.5 ns. The parameters used for the phase simulations (figure 7.12 d)) are the same as for the amplitude simulations with 40 mW of data power and two different phases 0 and π.

7.3 Outlook

In this section, further measurements and concepts of the photonic phononic memory are presented. The presented results are based on the following postdeadline and conference paper [375–378] and show further advanced signal processing schemes and capabilities of the BBM.

A distributed optical memory - cascaded light storage

In this section, we introduce the idea of a *distributed* optical memory. It can be seen in analogy to distributed computing schemes in standard micro-electronic computer chips that rely on a decentralized memory. To the best of our knowledge, this is the first time such a memory concept is proposed in an optical link. We show that optical information can be stored at every spatial position in the circuit and multiple conversions from the optical to the acoustic domain and back are possible. Importantly the multiple storage processes are achieved solely by tailoring the external write and read pulses. In a complex photonic circuit, it allows controlling the flow of optical information between different optical components and elements, where it can undergo additional signal processing operations. This advanced functionality is possible as the BBM does not rely on a localized memory unit, such as, e.g., a structural resonance at a fixed position, but the storage is achieved in the photonic link itself. We show that without any additional intervention the storing and retrieving process can be cascaded in the waveguide and hence only one control laser, external or on-chip, can store data pulses multiple times in a photonic circuit. Therefore not every "buffering step" requires its own laser source (a great advantage given that on-chip lasers are still a challenging task). The basic principle of the proof-of-principle experiment of a distributed optical memory is shown in figure 7.18. A sequence of write and read pulses are counter-propagating the

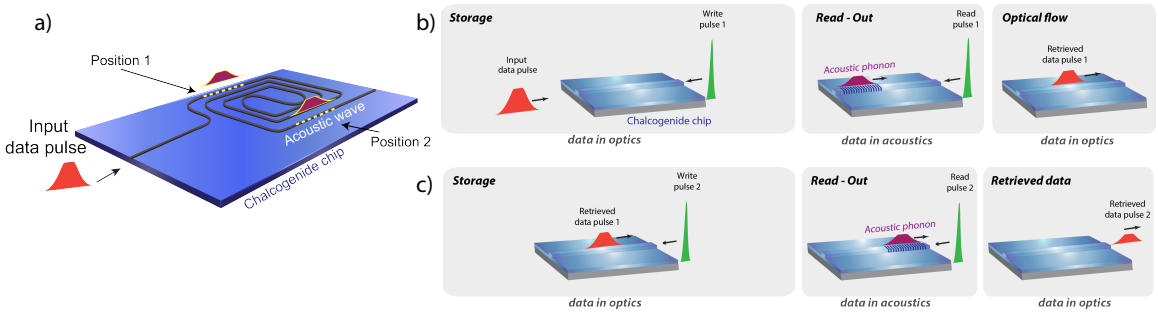

Fig. 7.18 a) Basic scheme of a distributed photonic memory where information can be stored at multiple positions in an integrated circuit. b) Basic scheme of two serial storage operations in a photonic circuit.

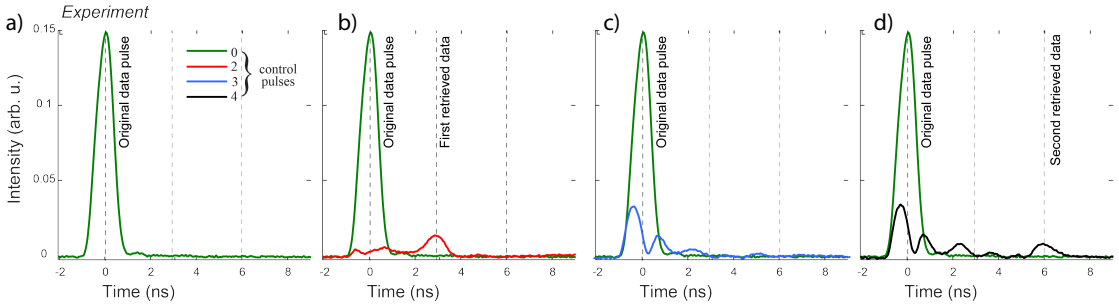

Fig. 7.19 Experimental results of a multi-storage operation in a waveguide. a) Transmitted data pulse with no counter-propagating write/ read pulses. b) Storage and retrieval operation in the waveguide close to the front facet of the waveguide. c) A second write pulse depletes the stored and retrieved optical data pulse for a second time. d) A second read pulse retrieves the optical data pulse after it was stored for the second time.

optical data pulses, transferring the optical information to acoustic waves and back multiple times in a photonic waveguide.

Figure 7.19 shows the experimental results of a double storage process. The data and the write pulses are synchronized in a way that both spatially overlap at the beginning of the waveguide. After the first storage and retrieval process, a third optical pulse is sent into the waveguide. This third optical pulse acts as a second write pulse and depletes the - just retrieved - optical data pulse again, writing now for a second time an acoustic wave. This acoustic wave is read out by a fourth optical pulse, which functions as a second read pulse. Hence, we experimentally demonstrate that optical information can be stored multiple times in the BBM via multiple tailored optical write and read pulses, which proves the great flexibility of the BBM concept.

Non-reciprocal light storage

It is known that SBS is a non-reciprocal effect [379, 95, 96]. Non-reciprocal effects are of great importance from a technological point of view, as they enable the design of devices that allow propagation in one direction but not the other. Hence it could enable non-magnetic isolators that can be readily integrated into photonic circuits. Besides the technological importance non-reciprocal behavior is also an intriguing concept from a fundamental physics point of view; The idea that a light wave can propagate in one direction but not the other should stun the imagination of every physicist. It was also recently shown theoretically that non-reciprocity allows overcoming restrictions such as the time-bandwidth product, that appeared so far to be of fundamental nature [380].

Here we show that the BBM allows for non-reciprocal light storage. The operation principle

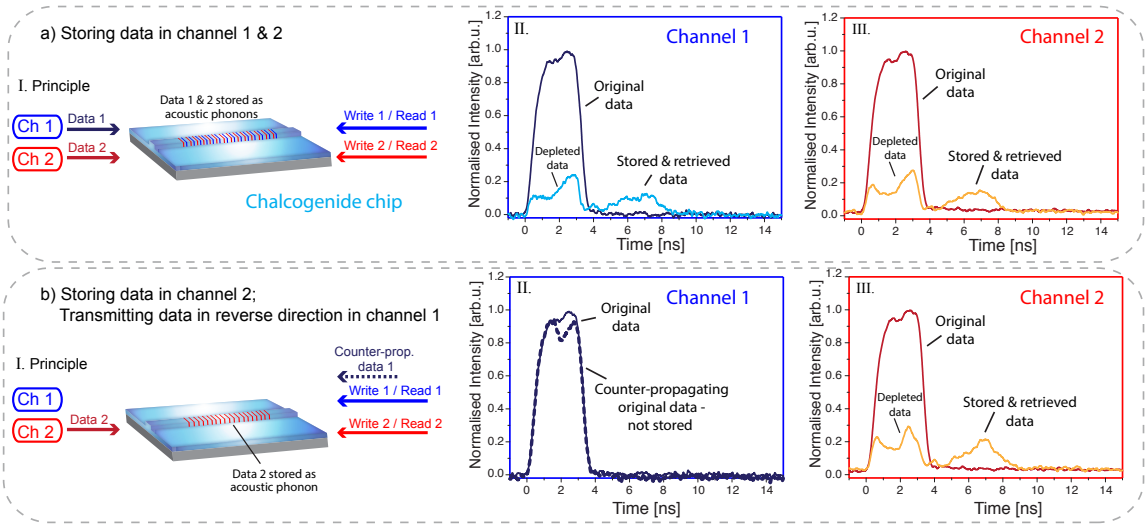

Fig. 7.20 a) Simultaneous storage of data pulses in wavelength channel one and two and subsequent retrieval after 3.5 ns [376]. b) A reversed data pulse in channel one is transmitted without being affected by write and read pulses in channel one. Furthermore, data pulses simultaneously stored in wavelength channel two do not affect the non-reciprocal behavior in channel one [376].

and experimental results are shown in figure 7.20 a) and b). Light pulses are simultaneously stored and retrieved in two frequency channels (figure 7.20 a)). In figure 7.20 b) the propagation direction of one of the data pulses is reversed (channel 1). While the optical data pulses in the second channel are still delayed in the BBM, the counter-propagating data pulses in channel one are not affected by the BBM and are transmitted.

The non-reciprocal storage operation enables advanced signal processing operations, such as the discrimination of forward and backward traveling data streams that have the same wavelength and hence cannot be separated by a spectral filter. It also shows that back-reflections of data pulses in a pulse train do no deteriorate the performance of the memory as they are not stored.

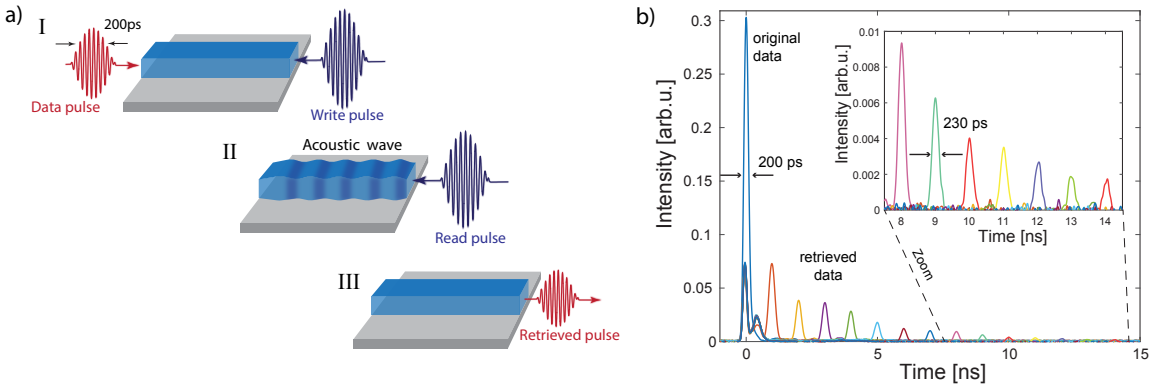

Fig. 7.21 a) Principle of storing short pulses on a chip as acoustic waves [377]. b) Storage and retrieval of 200 ps pulses for up to 14 ns. The inset shows a zoom-in from 8 - 14 ns [377].

Picosecond pulses and large fractional delay

In this section measurements of the storage and retrieval of pulses as short as 200 ps are shown (see figure 7.21). Retrieved data pulses can be detected for a storage time as large as 14 ns and hence the fractional delay achieved in the BBM is 70 pulse widths [377].

The FWHM of the retrieved pulses is shown in figure 7.22 a) and compared to the FWHM of the input data pulses (red dotted line). We see that even for large fractional delays only a slightly increased FWHM is observed. The reason for the increased width is still part of further investigations. Furthermore, short pulses with different amplitude levels are stored and retrieved (see figure 7.22 b) and the linear relationship between the input amplitude and the retrieved pulse amplitude is shown in figure 7.22.

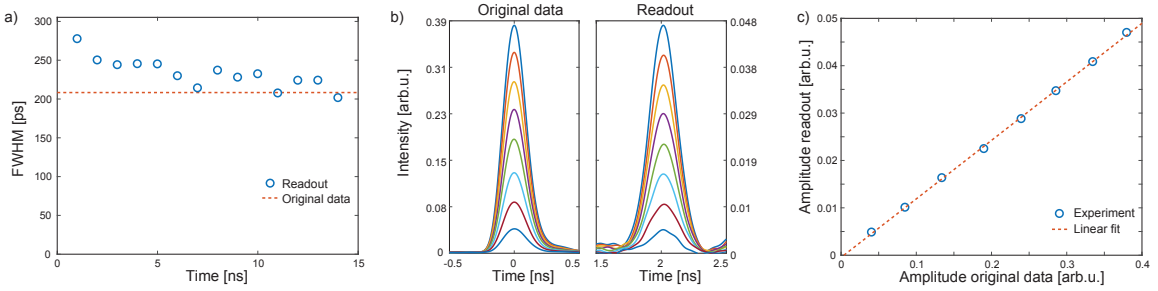

Fig. 7.22 a) FWHM of the retrieved data pulses. The red dotted line indicates the FWHM of the input pulses [377]. b) Storage and retrieval of 8 different amplitude levels [377]. c) Linear dependence of the input amplitude and retrieved amplitude [377].

Replenishing of the acoustic phonon

We have seen in the last chapter that the bandwidth of the BBM can be greatly extended, enabling a very large fractional delay of over 70 pulse widths. This impressive result was enabled by the ultra-high gain of chalcogenide waveguides that allowed to broaden the SBS resonance to exceed several GHz, almost reaching a technically limited bandwidth of the Brillouin frequency shift. If the bandwidth of the pulses exceeds this bandwidth the data and write read pulses start to overlap spectrally. However, materials with much higher Brillouin frequency shift might relax this constraint.
Besides the bandwidth, the overall fractional delay is limited by the lifetime of the acoustic wave. A way to decrease the decay rate of the acoustic wave hence can lead to even further improvements. Here we show that operating the BBM in the inverse frequency regime, will lead to a situation where additional read pulses not deplete the acoustic wave but replenish it. The basic principle and the experimental and theoretical results are shown in figure 7.23.

In the inverse frequency regime, the write and read pulses are up-shifted in frequency relative to the data pulses by the Brillouin frequency shift. When the pulses interact in the waveguide they still are creating an acoustic wave, however, the data pulse will not be depleted but the write pulse (however due to the large power difference in the pulses the relative power depletion of the write pulse is only minimal). Excitingly if the read pulse interacts with the just written acoustic wave, it will recreate a data pulse from that acoustic

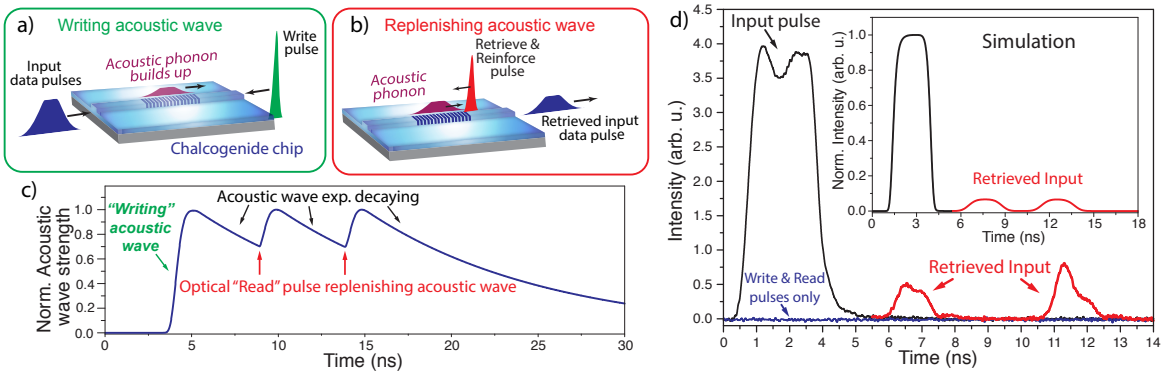

Fig. 7.23 a) Two optical pulses resonantly writing the acoustic wave inside the waveguide. b) The acoustic phonon interacts with an optical retrieve pulse. This not only creates a copy of the initial data pulse but also reinforces the acoustic wave. c) Simulation results of the strength of the acoustic wave. The acoustic wave is exponentially decaying; however, the retrieval pulses replenish the acoustic wave to its original strength. d) Measurement shows the original data pulse (black) and the delayed retrieved pulses (red). The inset shows numerical simulations confirming our measurements.

wave, but as the read pulse is located at the larger frequency, it will not deplete the acoustic wave in this process but rather reinforces. The recreated data pulse is at the lower frequency; hence when a read photon recreates a data photon, it loses energy which re-excites the acoustic wave. This is shown in first proof-of-principle experiments (figure 7.23).

Concluding remarks

The great potential of storing light pulses in traveling acoustic waves on a chip was demonstrated. Showing all the required ingredients to store telecommunication signals were shown, hence storing the later on a chip would be the next logical step. Showing that the BBM can be used to store an actual bit stream of data on a chip would be a great technological step forward. Furthermore, it would allow to study bit error rates and quantify the influence of noise added in the storing process. The signal-to-noise ratio is of great importance not only for any practical application but also for potential further extension to the regime of few photons. We see from the measurements presented in this chapter that the visibility of the retrieved data pulses is reduced compared to the original data pulses. How much additional noise is added to the pulses in the transfer photon-phonon-photon is yet to be determined.
Besides further engineering the technical implementations, a lot of fundamental science questions need to be answered. What are, e.g., the limitations concerning fractional delay for this memory technique? A better understanding of the dissipation of the acoustic wave would help to increase storage times even further. Another exciting path for the BBM is to explore different material platforms that can provide longer acoustic lifetime (e.g. As_2Se_3 has about three times the acoustic lifetime of As_2S_3 [260]) or materials with a much larger Brillouin frequency shift (e.g., diamond has a Brillouin frequency shift of around 72 GHz [381]). The larger Brillouin frequency shift allows to further broaden the data spectrum without spectrally overlapping with the read and write pulses. Also engineering dissipation and leakage of the phonon might enable longer storage times in the future [382–384].

Chapter 8

Summary and Outlook

This final chapter summarizes the results presented in this work but is also given an outlook on future directions of SBS research. This outlook reflects a personal opinion and at this point cannot be anything but speculative. As chapter 5 to 7 all included already an outlook and proposed future directions for the individual projects, the outlook here is more concerned with SBS research as a whole and future directions within the field.

Summary

In this thesis, SBS on a chip has been induced, manipulated and controlled in different ways. In chapter 5 a method was established that can be used to either enhance or inhibit SBS on a chip. This has been achieved by inscribing a Hill grating into a waveguide on a chip with precisely controlled spectral features. The edges of these grating structures were shown to enhance SBS in the waveguide. This demonstration follows a line of enhanced nonlinearities using band-edge effects, however, marks the first application of the technique in the context of SBS.

Furthermore, it allowed for the first time to generate a cascade of more than two Stokes waves in backward SBS on a chip. A cascade of up to 15 spectral lines could be generated using this enhancement method. It was shown that these frequency comb lines are all equally spaced and the phases are locked. Hence it marks the first Brillouin based pulsed laser source generated on a chip.

We also showed that the on-chip photonic bandgap structure can be utilized to suppress SBS fundamentally. Here for the first time, the bandgap is used to suppress a stimulated scattering process. We demonstrate that there is no Stokes wave building up in the waveguide when tuned inside the bandgap. Whereas previous studies mainly focused on inhibiting sponta-

neous emission, we show experimentally that the concept of inhibition extends to nonlinear optical effects. This is an important finding as it provides a tool to suppress nonlinearities in photonic circuits selectively.

Whereas in chapter 5 SBS was investigated in low-Q optical waveguide cavities with optical feedback, in chapter 6 SBS in a microwave cavity was investigated. The nature of this cavity was half electrical and half optical forming a feedback circuit for RF waves. It was shown that SBS can be harnessed in this configuration to generate widely tunable RF signals that have low phase-noise. Continuous tunability up to 40 GHz was shown, and the phase-noise of the generated RF signal was studied.

In chapter 7 an on-chip Brillouin-based memory was introduced, which we termed BBM. The memory is based on a coherent transfer of optical waves to acoustic waves. We showed for the first time that this memory technique is able to store phase and amplitude information. Furthermore, multi-frequency operation was investigated. We demonstrated experimentally that due to the unique phase-matching condition between optical and traveling acoustic waves there is no observable cross-talk between information stored in separate wavelength channel, even when stored simultaneously. In the outlook of chapter 7 we alluded to further features of the BBM technique. We demonstrated cascaded as well as non-reciprocal light storage. We also showed that the bandwidth of the stored data greatly exceeds the intrinsic Brillouin linewidth.

Outlook

Harnessing SBS in micro-structured or chip integrated waveguides is still a very young and fast-growing research field. In particular, the ability to design photonic-phononic waveguides made SBS one of the strongest and most tailorable nonlinear interactions. This opens up many opportunities for future research endeavors - on the one hand, there are still many open fundamental physics questions that want to be studied, on the other hand, there are already many demonstrations of applications, which need further engineering to make them "real world" solutions. Here an overview of these directions is given, starting from challenges in applied SBS research, segueing to the more fundamental scientific questions.
A better understanding of the noise properties of on-chip SBS would provide critical knowledge for the development of further applications and devices. Is there an advantage of having ultra-high gain in a small length scale compared to long lengths of optical fiber? Over the short length scales of the waveguides geometric and temperature gradients can be kept to a

minimum, and hence chip-scale waveguides should be beneficial regarding noise. But there is also the fundamental question of the noise contribution in general in this ultra-high gain configuration, considering the much lower threshold power, large stimulated amplification of more than 50 dB, the influence of spontaneous Brillouin noise in this configuration, and other aspects.
An improved understanding of the on-chip Brillouin noise is not only crucial for further optimization of the Brillouin OEO presented in this thesis, but essential to all chip-based SBS applications. This better understanding will allow optimizing the performance of, e.g., SBS-based microwave filter, and phase shifter. At this stage optimizing the performance of previously demonstrated SBS based applications, particularly in microwave photonics, will be one of the big frontiers in applied on-chip SBS research.

On the SBS application side, it was shown in this thesis that on-chip SBS is not only able to generate stable optical laser sources, but also stable microwave signals in planar circuits. Hence it extends the on-chip SBS microwave photonics toolbox from signal processing, such as filtering and phase-shifting, to microwave sources. The availability of a stable RF source in a planar circuit opens many possibilities as now the source can be combined with other on-chip functionalities in one circuit on a chip. Many microwave processing schemes, for example, rely on local oscillators that can be provided by the SBS microwave source directly on the chip.

The body of work presented around Brillouin based light storage shows the great potential of this technique. Demonstrating functionalities and performance that greatly exceeds what has initially thought this concept is capable of. We showed all the functionalities required to be compatible with modern telecommunication schemes. Hence we now can imagine telecommunication system engineers to apply this technique in their system and further investigate the performance regarding telecommunication benchmarks, such as, e.g., bit-error-rates.
The here presented experimental demonstration also opens new possibilities in the field of integrated photonics, in particular for research on optical interconnects. Here new architectures might arise, where optical waveguides between processors do not only functions as a connection but also as a memory element.

Another exciting path of on-chip SBS research is the search for new material platforms. On the one hand, there is a drive to develop existing platforms further to achieve maximum performance. On the other hand, there is the search for new material platforms suitable for SBS. Chalcogenide glass is today certainly the most mature platform for applications

based on backward SBS. Most demonstrations are based on Arsenic trisulfide (As_2S_3) but there are many other chalcogenide glass compositions that might be promising for future integrated SBS circuits [385]. The acoustic lifetime in chalcogenide fiber made out of As_2Se_3 is about three times higher compared to the As_2S_3 waveguides studied in this thesis [260]. Furthermore, it is known that Te based glasses show only minimal photo-sensitivity and offer the potential of low-loss waveguides [386]. Other chalcogenides incorporate Ge and SBS was observed in microstructured fiber made out of such a glass [387]. The reported Brillouin gain was below the gains achieved in As_2S_3. However, the higher softening temperature in this chalcogenide composition might be beneficial in the fabrication process and lead to better power handling of the waveguides, which might compensate for the slightly lower Brillouin gain.

From a technological point of view Silicon is still one of the most interesting platforms due to the CMOS industry. Many demonstrations of forward Brillouin scattering could be shown in this platform; however, backward SBS is still elusive in silicon. Ways to implement backward SBS in silicon by e.g. cleverly designed waveguides [105] or resonators [388–390] would hence further propel the field. Other techniques explored ways to break the symmetry between the sidebands in forward Brillouin scattering to achieve exponential gain in this configuration [103].

Besides silicon, there are many other semiconductors, which are promising platforms for SBS. It was shown that GaAs shows strong photo-elastic and piezo-electric effects [391, 354, 392] and high frequency surface acoustic waves could have been recently demonstrated in ALN [355]. If these platforms also show large Brillouin gains is worth to be investigated in the future.

Diamond is another very promising material platform for SBS due to its unique optical and mechanical properties [393–396]. For optomechanical applications, the low dissipation rate allows for high mechanical Q-factors [394–396]. Combining these high mechanical Q-factors with vacancy centers in the diamond matrix has great potential for quantum applications and quantum networks [397, 398].

Recently, the first observation of SBS in a diamond Raman laser cavity was observed [381]. The observed Stokes shift is 72 GHz in this demonstration, and hence is much larger compared to most materials studied for SBS. The larger BFS might be beneficial for many applications as it makes it easier to prevent any overlap between the pump and the Stokes wave or remove detrimental pump back-reflections. In the context of the BBM the large frequency shift would not only have these aforementioned advantages in the experimental implementation but would also allow to further broaden the bandwidth of the data pulses

without risking any spectral overlap with the write and read pulses.

The work presented in this thesis provides a better understanding of SBS on-chip - on a fundamental level as well as in the context of potential applications and signal processing capabilities. It showed how the interaction can be tailored in waveguides, that goes beyond the intrinsic electrostrictive and photo-elastic properties of the waveguide materials and geometry by including the optical DOS in the description. Tailoring the DOS allows tailoring and controlling the nonlinear interactions and is opening the door for many future applications. Furthermore, our demonstration of inhibiting selectively optical nonlinearities has far-reaching opportunities for integrated nonlinear circuits. Also extending the concept to the quantum regime offers many opportunities for quantum light sources and quantum circuits.

On the fundamental side we see a trend emerging over the last years that alludes to a convergence of SBS research and optomechanics. Both research fields did not overlap much in the past but the ability to implement and tailor SBS on a chip came with the realization that there is an overlap between both field. Several theory papers dealt with that convergence [102, 399]. It is predicted that most phenomena showed in cavity optomechanics can also be implemented in a Brillouin configuration. The traveling acoustic wave nature might open new opportunities and possibilities in the context of optomechanical systems. The stringent phase-matching condition allows only certain waves to couple. The frequency is usually much higher than in optomechanical systems, which leads to a lower occupation of the phonon bath and hence the effect of thermal noise might be reduced. However, the effect of thermal noise does not only depend on the thermal occupation of the phonon bath but also depends on the Q-factor. The higher frequency comes with a much shorter lifetime, which would be one challenge to address. Backward SBS systems can be, furthermore, driven with a lot of power before any cascading effects happen.
The first experimental investigation showing the convergence of Brillouin scattering and optomechanics were shown recently [400]. Brillouin scattering in a crystalline phononic resonator at low temperatures has been demonstrated. At these low temperatures, the phonon lifetime is much longer, and the coherence length of the phonon exceeds the length of the crystals investigated. Hence, the Brillouin spectrum shows discrete lines, consistent with the observation of Brillouin scattering in waveguides thinner than the coherence length of the phonon [69].
Low temperature SBS offers many new opportunities to investigate fundamental properties of SBS. The lower phonon occupation numbers at these temperatures will greatly reduce the noise contribution. Experiments with low photon numbers might be possible and Brillouin

experiments in the quantum regime might be at reach. Furthermore is the phonon lifetimes much larger. Temperature-dependent studies might help to understand the phonon dissipation further.

It was shown theoretically that it is possible to reach the so-called strong coupling regime in a Brillouin configuration [401]. The strong coupling regime was investigated in optomechanical cavity systems previously [54, 62]. These results drew a lot of attention as the strong coupling regime allows a parametric conversion between different oscillating modes. Instead of describing a system with different independent modes, in the strong coupling regime the system is described using joint eigenmodes. The consequence is an anti-crossing in the dispersion relation and the occurrence of Rabi oscillation. On a quantum level, this behavior can be described as a coherent superposition of the two coupled modes.
Reaching this regime in a Brillouin configuration would allow many interesting applications. In the context of the BBM presented in this thesis, it might enable parametric conversion between the photon and phonons greatly boosting the efficiency of the memory but potentially also allowing efficient storage at the single photon level.
The findings presented here do open new possibilities for system engineers but also spark interest for further fundamental research. We showed that the BBM can be used to store and retrieve the amplitude, phase, and frequency of an optical pulse. Hence it should be possible to coherently store a quantum state of light using the BBM. Quantum memories are one of the big challenges for quantum networks. Operating the BBM at cryogenic temperatures might allow operating at a single photon level. Operating the BBM at these low temperature would furthermore have the advantage of longer phonon lifetimes and hence would allow for much longer storage times.

Understanding the cause for the phonon lifetime, the phononic loss mechanism and dissipation of the acoustic wave in waveguides is an interesting fundamental question. Being able to control, tailor and potentially increase the lifetime would have far-reaching consequences for many SBS based applications. The BBM can help to form a better understanding of the decay mechanisms, giving direct access to the phonon lifetime. Using even shorter pulses could give insights into the temporal behavior of the decay mechanisms. Furthermore, does it allow to locally study the acoustic decay in waveguides, and gives insights into the waveguide environment on the decay mechanisms. Common techniques used to determine the acoustic lifetime are based on measuring the spectral width of the Brillouin gain linewidth using CW pump-probe techniques. The acoustic lifetime is then inferred from the width of the measured

peak. This technique, however, cannot provide detailed temporal and spatial information of the decay processes.

References

[1] L. Brillouin, "Diffusion de la lumière et des rayons X par un corps transparent homogène," Annales de Physique **9**, 88–122 (1922).

[2] L. Mandelstam, "Light scattering by inhomogeneous media," Zh. Russ. Fiz-Khim **58** (1926).

[3] T. H. Maiman, "Stimulated Optical Radiation in Ruby," Nature **187**, 493–494 (1960).

[4] C. V. Raman and K. S. Krishnan, "The Optical Analogue of the Compton Effect," Nature **121**, 711–711 (1928).

[5] C. V. Raman and K. S. Krishnan, "The Negative Absorption of Radiation," Nature **122**, 12–13 (1928).

[6] C. V. Raman, "A Change of Wave-length in Light Scattering," Nature **121**, 619–619 (1928).

[7] E. Gross, "Change of Wave-length of Light due to Elastic Heat Waves at Scattering in Liquids." Nature **126**, 201–202 (1930).

[8] P. Debye and F. W. Sears, "On the Scattering of Light by Supersonic Waves," Proceedings of the National Academy of Sciences **18**, 409–414 (1932).

[9] C. V. Raman and N. S. N. Nathe, "The diffraction of light by high frequency sound waves: Part I," Proc. Indian Acad. Sci. - Sect. A **2**, 406–412 (1935).

[10] E. L. Feinberg, "Igor' Evgen'evich Tamm," Physics-Uspekhi **38**, 773–789 (1995).

[11] C. V. Raman and C. S. Venkateswaran, "Optical Observation of the Debye Heat Waves in Crystals," Nature **142**, 250–250 (1938).

[12] R. S. Krishnan, "Elastic constant of crystals from light scattering measurements," Proceedings of the Indian Academy of Sciences - Section A **41**, 91–97 (1954).

[13] P. A. Franken, A. E. Hill, C. W. Peters, and G. Weinreich, "Generation of optical harmonics," Physical Review Letters **7**, 118–119 (1961).

[14] R. Chiao, C. Townes, and B. Stoicheff, "Stimulated Brillouin Scattering and Coherent Generation of Intense Hypersonic Waves," Physical Review Letters **12**, 592–595 (1964).

[15] E. Garmire and C. H. Townes, "Stimulated Brillouin Scattering in Liquids1," Applied Physics Letters **5**, 84 (1964).

[16] R. Brewer and K. Rieckhoff, "Stimulated Brillouin Scattering in Liquids," Physical Review Letters **13**, 334–336 (1964).

[17] R. Y. Chiao and B. P. Stoicheff, "Brillouin Scattering in Liquids Excited by the He-Ne Maser," Journal of the Optical Society of America **54**, 1286 (1964).

[18] E. E. Hagenlocker and W. G. Rado, "Stimulated Brillouin and Raman Scattering in Gases," Applied Physics Letters **7**, 236 (1965).

[19] N. M. Kroll, "Excitation of hypersonic vibrations by means of photoelastic coupling of high-intensity light waves to elastic waves," Journal of Applied Physics **36**, 34–43 (1965).

[20] C. L. Tang, "Saturation and spectral characteristics of the Stokes emission in the stimulated Brillouin process," Journal of Applied Physics **37**, 2945–2955 (1966).

[21] D. Pohl, M. Maier, and W. Kaiser, "Phonon lifetimes measured in amplifiers for Brillouin radiation," Physical Review Letters **20**, 366–368 (1968).

[22] K. Kao and G. Hockham, "Dielectric-fibre surface waveguides for optical frequencies," Proceedings of the Institution of Electrical Engineers **113**, 1151 (1966).

[23] E. Ippen and R. Stolen, "Stimulated Brillouin scattering in optical fibers," Applied Physics Letters **21**, 539 (1972).

[24] D. A. Fishman and J. A. Nagel, "Degradations due to stimulated Brillouin scattering in multigigabit intensity-modulated fiber-optic systems," Journal of Lightwave Technology **11**, 1721–1728 (1993).

[25] K. Shiraki, M. Ohashi, and M. Tateda, "Suppression of stimulated Brillouin scattering in a fibre by changing the core radius," Electronics Letters **31**, 668 (1995).

[26] K. Shiraki, M. Ohashi, and M. Tateda, "Performance of strain-free stimulated brillouin scattering suppression fiber," Journal of Lightwave Technology **14**, 549–554 (1996).

[27] N. A. Brilliant, "Stimulated Brillouin scattering in a dual-clad fiber amplifier," Journal of the Optical Society of America B **19**, 2551–2557 (2002).

[28] A. F. El-Sherif and T. A. King, "High-peak-power operation of a Q-switched Tm3+-doped silica fiber laser operating near 2 microm." Optics Letters **28**, 22–24 (2003).

[29] H. Lee and G. Agrawal, "Suppression of stimulated Brillouin scattering in optical fibers using fiber Bragg gratings." Optics Express **11**, 3467–3472 (2003).

[30] J. M. Chavez Boggio, J. D. Marconi, and H. L. Fragnito, "Experimental and numerical investigation of the SBS-threshold increase in an optical fiber by applying strain distributions," Journal of Lightwave Technology **23**, 3808–3814 (2005).

[31] V. I. Kovalev and R. G. Harrison, "Suppression of stimulated Brillouin scattering in high-power single-frequency fiber amplifiers." Optics Letters **31**, 161–163 (2006).

[32] A. Liu, "Suppressing stimulated Brillouin scattering in fiber amplifiers using nonuniform fiber and temperature gradient." Optics express **15**, 977–984 (2007).

[33] M. Merklein, I. V. Kabakova, T. F. S. Büttner, D.-Y. Choi, B. Luther-Davies, S. J. Madden, and B. J. Eggleton, "Enhancing and inhibiting stimulated Brillouin scattering in photonic integrated circuits," Nature Communications **6**, 6396 (2015).

[34] O. Florez, P. F. Jarschel, Y. A. V. Espinel, C. M. B. Cordeiro, T. P. Mayer Alegre, G. S. Wiederhecker, and P. Dainese, "Brillouin scattering self-cancellation," Nature Communications **7**, 11759 (2016).

[35] K. O. Hill, B. S. Kawasaki, and D. C. Johnson, "cw Brillouin laser," Applied Physics Letters **28**, 608 (1976).

[36] K. O. Hill, D. C. Johnson, and B. S. Kawasaki, "CW generation of multiple Stokes and anti-Stokes Brillouin-shifted frequencies," Applied Physics Letters **29**, 185–187 (1976).

[37] F. A. Korolev, O. M. Vokhnik, and V. I. Odintsov, "Mode locking and ultrashort light pulses in SMBS in an optical resonator," Journal of Experimental and Theoretical Physics Letters **18**, 32–33 (1973).

[38] B. S. Kawasaki, D. C. Johnson, Y. Fujii, and K. O. Hill, "Bandwidth-limited operation of a mode-locked Brillouin parametric oscillator," Applied Physics Letters **32**, 429–431 (1978).

[39] V. N. Lugovoi, "Theory of Mode Locking at Coherent Brillouin Interaction," IEEE Journal of Quantum Electronics **19**, 764–769 (1983).

[40] L. F. Stokes, M. Chodorow, and H. J. Shaw, "All-fiber stimulated Brillouin ring laser with submilliwatt pump threshold." Optics Letters **7**, 509–511 (1982).

[41] R. M. Shelby, M. D. Levenson, and P. W. Bayer, "Guided acoustic-wave Brillouin scattering," Physical Review B **31**, 5244–5252 (1985).

[42] J. C. Knight, T. A. Birks, P. S. J. Russell, and D. Atkin, "All-silica signal-mode optical fiber with photonic crystal cladding," Optics Letters **21**, 1547–1549 (1996).

[43] P. S. J. Russell, "Photonic crystal fibers." Science **299**, 358–362 (2003).

[44] P. Dainese, P. S. J. Russell, G. S. Wiederhecker, N. Joly, H. L. Fragnito, V. Laude, and A. Khelif, "Raman-like light scattering from acoustic phonons in photonic crystal fiber." Optics Express **14**, 4141–4150 (2006).

[45] D. Elser, U. L. Andersen, A. Korn, O. Glöckl, S. Lorenz, C. Marquardt, and G. Leuchs, "Reduction of guided acoustic wave brillouin scattering in photonic crystal fibers," Physical Review Letters **97**, 1–4 (2006).

[46] J.-C. Beugnot, T. Sylvestre, H. Maillotte, G. Mélin, and V. Laude, "Guided acoustic wave Brillouin scattering in photonic crystal fibers," Optics Letters **32**, 17 (2007).

[47] D. Elser, C. Wittmann, U. L. Andersen, O. Glöckl, S. Lorenz, C. Marquardt, and G. Leuchs, "Guided acoustic wave Brillouin scattering in photonic crystal fibers," Journal of Physics: Conference Series **92**, 012108 (2007).

[48] B. Stiller, M. Delqué, J.-C. Beugnot, M. W. Lee, G. Mélin, H. Maillotte, V. Laude, and T. Sylvestre, "Frequency-selective excitation of guided acoustic modes in a photonic crystal fiber," Optics Express **19**, 7689 (2011).

[49] V. Laude and J. C. Beugnot, "Generation of phonons from electrostriction in small-core optical waveguides," AIP Advances **3** (2013).

[50] P. Dainese, P. S. J. Russell, N. Joly, J. C. Knight, G. S. Wiederhecker, H. L. Fragnito, V. Laude, and A. Khelif, "Stimulated Brillouin scattering from multi-GHz-guided acoustic phonons in nanostructured photonic crystal fibres," (2006).

[51] J. C. Beugnot, T. Sylvestre, D. Alasia, H. Maillotte, V. Laude, A. Monteville, L. Provino, N. Traynor, S. F. Mafang, and L. Thévenaz, "Complete experimental characterization of stimulated Brillouin scattering in photonic crystal fiber," Optics Express **15**, 15517 (2007).

[52] B. Stiller, S. M. Foaleng, J.-C. Beugnot, M. W. Lee, M. Delqué, G. Bouwmans, A. Kudlinski, L. Thévenaz, H. Maillotte, and T. Sylvestre, "Photonic crystal fiber mapping using Brillouin echoes distributed sensing." Optics Express **18**, 20136–20142 (2010).

[53] T. J. Kippenberg and K. J. Vahala, "Cavity optomechanics: back-action at the mesoscale." Science **321**, 1172–6 (2008).

[54] S. Gröblacher, K. Hammerer, M. R. Vanner, and M. Aspelmeyer, "Observation of strong coupling between a micromechanical resonator and an optical cavity field." Nature **460**, 724–727 (2009).

[55] G. S. Wiederhecker, L. Chen, A. Gondarenko, and M. Lipson, "Controlling photonic structures using optical forces." Nature **462**, 633–636 (2009).

[56] S. Weis, R. Riviere, S. Deleglise, E. Gavartin, O. Arcizet, A. Schliesser, and T. J. Kippenberg, "Optomechanically Induced Transparency," Science **330**, 1520–1523 (2010).

[57] J. Chan, T. P. M. Alegre, A. H. Safavi-Naeini, J. T. Hill, A. Krause, S. Gröblacher, M. Aspelmeyer, and O. Painter, "Laser cooling of a nanomechanical oscillator into its quantum ground state." Nature **478**, 89–92 (2011).

[58] J. D. Teufel, D. Li, M. S. Allman, K. Cicak, a. J. Sirois, J. D. Whittaker, and R. W. Simmonds, "Circuit cavity electromechanics in the strong-coupling regime," Nature **471**, 204–208 (2011).

[59] A. H. Safavi-Naeini, T. P. Mayer Alegre, J. Chan, M. Eichenfield, M. Winger, Q. Lin, J. T. Hill, D. E. Chang, and O. Painter, "Electromagnetically induced transparency and slow light with optomechanics." Nature **472**, 69–73 (2011).

[60] D. W. C. Brooks, T. Botter, S. Schreppler, T. P. Purdy, N. Brahms, and D. M. Stamper-Kurn, "Non-classical light generated by quantum-noise-driven cavity optomechanics," Nature **488**, 476–480 (2012).

[61] A. H. Safavi-Naeini, J. Chan, J. T. Hill, T. P. M. Alegre, A. Krause, and O. Painter, "Observation of quantum motion of a nanomechanical resonator," Physical Review Letters **108**, 1–5 (2012).

[62] E. Verhagen, S. Deléglise, S. Weis, a. Schliesser, and T. J. Kippenberg, "Quantum-coherent coupling of a mechanical oscillator to an optical cavity mode." Nature **482**, 63–7 (2012).

[63] C. Dong, V. Fiore, M. C. Kuzyk, and H. Wang, "Optomechanical Dark Mode," Science **338**, 1609–1613 (2012).

[64] T. A. Palomaki, J. W. Harlow, J. D. Teufel, R. W. Simmonds, and K. W. Lehnert, "Coherent state transfer between itinerant microwave fields and a mechanical oscillator." Nature **495**, 210–4 (2013).

[65] R. Riedinger, S. Hong, R. A. Norte, J. A. Slater, J. Shang, A. G. Krause, V. Anant, M. Aspelmeyer, and S. Gröblacher, "Non-classical correlations between single photons and phonons from a mechanical oscillator," Nature **530**, 313–316 (2016).

[66] Y. Chu, P. Kharel, W. H. Renninger, L. D. Burkhart, L. Frunzio, P. T. Rakich, and R. J. Schoelkopf, "Quantum acoustics with superconducting qubits," Science **358**, 199–202 (2017).

[67] P. T. Rakich, C. Reinke, R. Camacho, P. Davids, and Z. Wang, "Giant enhancement of stimulated Brillouin scattering in the subwavelength limit," Physical Review X **2**, 1–15 (2012).

[68] R. Van Laer, "Light-Sound Interaction in Nanoscale Silicon Waveguides," Ph.D. thesis (2016).

[69] J. R. Sandercock, "Structure in the Brillouin Spectra of Thin Films," Physical Review Letters **29**, 1735–1738 (1972).

[70] N. Rowell, V. C. Y. So, and G. I. Stegeman, "Brillouin scattering in a thin-film waveguide," Applied Physics Letters **32**, 154–155 (1978).

[71] N. L. Rowell, P. J. Thomas, H. M. Van Driel, and G. I. Stegeman, "Brillouin spectrum of single-mode optical fibers," Applied Physics Letters **34**, 139–141 (1979).

[72] N. L. Rowell and G. I. Stegeman, "Brillouin scattering from surface phonons in thin films," Physical Review Letters **41**, 970–973 (1978).

[73] R. Loudon, "Theory of Surface-Ripple Brillouin Scattering by Solids," Physical Review Letters **40**, 581–583 (1978).

[74] R. Normandin, V. C.-Y. So, N. Rowell, and G. I. Stegeman, "Scattering of guided optical beams by surface acoustic waves in thin films," Journal of the Optical Society of America **69**, 1153 (1979).

[75] R. Pant, C. G. Poulton, D.-Y. Choi, H. Mcfarlane, S. Hile, E. Li, L. Thevenaz, B. Luther-Davies, S. J. Madden, and B. J. Eggleton, "On-chip stimulated Brillouin scattering," Optics Express **19**, 8285–8290 (2011).

[76] S. Levy, V. Lyubin, M. Klebanov, J. Scheuer, and A. Zadok, "Stimulated Brillouin scattering amplification in centimeter-long directly written chalcogenide waveguides." Optics Letters **37**, 5112–4 (2012).

[77] R. Pant, A. Byrnes, C. G. Poulton, E. Li, D.-Y. Choi, S. Madden, B. Luther-Davies, and B. J. Eggleton, "Photonic-chip-based tunable slow and fast light via stimulated Brillouin scattering," Optics Letters **37**, 969 (2012).

[78] A. Byrnes, R. Pant, E. Li, D.-Y. Choi, C. G. Poulton, S. Fan, S. Madden, B. Luther-Davies, and B. J. Eggleton, "Photonic chip based tunable and reconfigurable narrowband microwave photonic filter using stimulated Brillouin scattering," Optics Express **20**, 18836 (2012).

[79] R. Pant, E. Li, C. G. Poulton, D.-Y. Choi, S. Madden, B. Luther-Davies, and B. J. Eggleton, "Observation of Brillouin dynamic grating in a photonic chip." Optics Letters **38**, 305–7 (2013).

[80] I. V. Kabakova, R. Pant, D.-Y. Choi, S. Debbarma, B. Luther-Davies, S. J. Madden, and B. J. Eggleton, "Narrow linewidth Brillouin laser based on chalcogenide photonic chip." Optics Letters **38**, 3208–11 (2013).

[81] M. Merklein, A. Casas-Bedoya, D. Marpaung, T. F. S. Buttner, M. Pagani, B. Morrison, I. V. Kabakova, and B. J. Eggleton, "Stimulated Brillouin Scattering in Photonic Integrated Circuits: Novel Applications and Devices," IEEE Journal of Selected Topics in Quantum Electronics **22**, 336–346 (2016).

[82] D. Marpaung, B. Morrison, M. Pagani, R. Pant, D.-Y. Choi, B. Luther-Davies, S. J. Madden, and B. J. Eggleton, "Low-power, chip-based stimulated Brillouin scattering microwave photonic filter with ultrahigh selectivity," Optica **2**, 76 (2015).

[83] I. S. Grudinin, A. B. Matsko, and L. Maleki, "Brillouin Lasing with a CaF2 Whispering Gallery Mode Resonator," Physical Review Letters **102**, 043902 (2009).

[84] M. Tomes and T. Carmon, "Photonic Micro-Electromechanical Systems Vibrating at X-band (11-GHz) Rates," Physical Review Letters **102**, 113601 (2009).

[85] H. Lee, T. Chen, J. Li, K. Y. Yang, S. Jeon, O. Painter, and K. J. Vahala, "Chemically etched ultrahigh-Q wedge-resonator on a silicon chip," Nature Photonics **6**, 369–373 (2012).

[86] M. Aspelmeyer, T. J. Kippenberg, and F. Marquardt, *Cavity Optomechanics* (Springer Berlin Heidelberg, Berlin, Heidelberg, 2014).

[87] O. Ristow, M. Merklein, M. Grossmann, M. Hettich, M. Schubert, A. Bruchhausen, J. Grebing, A. Erbe, D. Mounier, V. Gusev, E. Scheer, T. Dekorsy, and E. C. S. Barretto, "Ultrafast spectroscopy of super high frequency mechanical modes of doubly clamped beams," Applied Physics Letters **103**, 1–5 (2013).

[88] J. Li, H. Lee, T. Chen, and K. Vahala, "Characterization of a high coherence, Brillouin microcavity laser on silicon," Optics Express **20**, 369–373 (2012).

[89] W. Loh, A. Green, F. Baynes, D. Cole, F. Quinlan, H. Lee, K. J. Vahala, S. Papp, and S. Diddams, "Dual-microcavity narrow-linewidth Brillouin laser," Optica **2**, 13 (2015).

[90] J. Li, H. Lee, and K. J. Vahala, "Microwave synthesizer using an on-chip Brillouin oscillator." Nature Communications **4**, 2097 (2013).

[91] J. Li, X. Yi, H. Lee, S. A. Diddams, and K. J. Vahala, "Electro-optical frequency division and stable microwave synthesis," Science **345**, 309–313 (2014).

[92] J. Li, M.-G. Suh, and K. Vahala, "Microresonator Brillouin gyroscope," Optica **4**, 346 (2017).

[93] J. Zehnpfennig, G. Bahl, M. Tomes, and T. Carmon, "Surface optomechanics: Calculating optically excited acoustical whispering gallery modes in microspheres," **19**, 10 (2011).

[94] G. Bahl, M. Tomes, F. Marquardt, and T. Carmon, "Observation of spontaneous Brillouin cooling," Nature Physics **8**, 203–207 (2012).

[95] J. Kim, M. C. Kuzyk, K. Han, H. Wang, and G. Bahl, "Non-reciprocal Brillouin scattering induced transparency," Nature Physics **11**, 275–280 (2015).

[96] C.-H. Dong, Z. Shen, C.-L. Zou, Y.-L. Zhang, W. Fu, and G.-C. Guo, "Brillouin-scattering-induced transparency and non-reciprocal light storage," Nature Communications **6** (2015).

[97] H. Shin, W. Qiu, R. Jarecki, J. A. Cox, R. H. Olsson, A. Starbuck, Z. Wang, and P. T. Rakich, "Tailorable stimulated Brillouin scattering in nanoscale silicon waveguides." Nature Communications **4**, 1944 (2013).

[98] R. Van Laer, B. Kuyken, D. Van Thourhout, and R. Baets, "Interaction between light and highly confined hypersound in a silicon photonic nanowire," Nature Photonics **9**, 199–203 (2015).

[99] H. Shin, J. A. Cox, R. Jarecki, A. Starbuck, Z. Wang, and P. T. Rakich, "Control of coherent information via on-chip photonic-phononic emitter-receivers." Nature Communications **6**, 6427 (2015).

[100] R. V. Laer, A. Bazin, B. Kuyken, R. Baets, and D. V. Thourhout, "Net on-chip Brillouin gain based on suspended silicon nanowires," New Journal of Physics **17** (2015).

[101] E. A. Kittlaus, H. Shin, and P. T. Rakich, "Large Brillouin amplification in silicon," Nature Photonics **10**, 463–467 (2016).

[102] R. Van Laer, R. Baets, and D. Van Thourhout, "Unifying Brillouin scattering and cavity optomechanics," Physical Review A **93**, 053828 (2016).

[103] E. A. Kittlaus, N. T. Otterstrom, and P. T. Rakich, "On-chip inter-modal Brillouin scattering," Nature Communications **8**, 15819 (2017).

[104] C. Wolff, P. Gutsche, M. J. Steel, B. J. Eggleton, and C. G. Poulton, "Impact of nonlinear loss on stimulated Brillouin scattering," Journal of the Optical Society of America B **32**, 1968 (2015).

[105] C. J. Sarabalis, J. T. Hill, and A. H. Safavi-Naeini, "Guided acoustic and optical waves in silicon-on-insulator for Brillouin scattering and optomechanics," APL Photonics **1**, 071301 (2016).

[106] B. J. Eggleton, C. G. Poulton, and R. Pant, "Inducing and harnessing stimulated Brillouin scattering in photonic integrated circuits," Advances in Optics and Photonics **5**, 536–587 (2013).

[107] A. Kobyakov, M. Sauer, and D. Chowdhury, "Stimulated Brillouin scattering in optical fibers," Advances in Optics and Photonics **2**, 1–59 (2010).

[108] R. W. Boyd, *Nonlinear Optics* (Acad. Press, 2003).

[109] C. G. Poulton, R. Pant, and B. J. Eggleton, "Acoustic confinement and stimulated Brillouin scattering in integrated optical waveguides," Journal of the Optical Society of America B **30**, 2657–2664 (2013).

[110] M. Pagani, D. Marpaung, and B. J. Eggleton, "Ultra-wideband microwave photonic phase shifter with configurable amplitude response." Optics Letters **39**, 5854–7 (2014).

[111] M. Pagani, D. Marpaung, D.-Y. Choi, S. J. Madden, B. Luther-Davies, and B. Eggleton, "Tunable wideband microwave photonic phase shifter using on-chip stimulated Brillouin scattering," Optics Express **22**, 28810–28818 (2014).

[112] A. Loayssa and F. J. Lahoz, "Broad-band RF photonic phase shifter based on stimulated brillouin scattering and single-sideband modulation," IEEE Photonics Technology Letters **18**, 208–210 (2006).

[113] C. Wolff, B. Stiller, B. J. Eggleton, M. J. Steel, and C. G. Poulton, "Cascaded forward Brillouin scattering to all Stokes orders," pp. 1–16 (2016).

[114] A. Debut, S. Randoux, and J. Zemmouri, "Linewidth narrowing in Brillouin lasers: Theoretical analysis," Physical Review A **62**, 023803 (2000).

[115] K. H. Tow, Y. Léguillon, S. Fresnel, P. Besnard, L. Brilland, D. Méchin, D. Trégoat, J. Troles, and P. Toupin, "Linewidth-narrowing and intensity noise reduction of the 2nd order Stokes component of a low threshold Brillouin laser made of Ge10As22Se68 chalcogenide fiber." Optics Express **20**, B104–9 (2012).

[116] S. P. Smith, F. Zarinetchi, and S. Ezekiel, "Narrow-linewidth stimulated Brillouin fiber laser and applications." Optics Letters **16**, 393–5 (1991).

[117] K. S. Abedin, "Single-frequency Brillouin lasing using single-mode As2Se3 chalcogenide fiber." Optics Express **14**, 4037–42 (2006).

[118] K. Hu, I. V. Kabakova, T. F. S. Büttner, S. Lefrancois, D. D. Hudson, S. He, and B. J. Eggleton, "Low-threshold Brillouin laser at 2 μm based on suspended-core chalcogenide fiber," Optics Letters **39**, 4651 (2014).

[119] I. V. Kabakova, R. Pant, H. G. Winful, and B. J. Eggleton, "Chalcogenide Brillouin lasers," Journal of Nonlinear Optical Physics & Materials **23**, 1450001 (2014).

[120] J. Li, H. Lee, and K. J. Vahala, "Low-noise Brillouin laser on a chip at 1064 nm." Optics Letters **39**, 287–90 (2014).

[121] W. Loh, S. B. Papp, and S. A. Diddams, "Noise and dynamics of stimulated-Brillouin-scattering microresonator lasers," Physical Review A **91**, 053843 (2015).

[122] B. Morrison, A. Casas-Bedoya, G. Ren, K. Vu, Y. Liu, A. Zarifi, T. G. Nguyen, D.-Y. Choi, D. Marpaung, S. J. Madden, A. Mitchell, and B. J. Eggleton, "Compact Brillouin devices through hybrid integration on silicon," Optica **4**, 847 (2017).

[123] N. T. Otterstrom, R. O. Behunin, E. A. Kittlaus, Z. Wang, and P. T. Rakich, "A silicon Brillouin laser," arXiv:1705.05813 (2017).

[124] I. S. Grudinin, H. Lee, O. Painter, and K. J. Vahala, "Phonon laser action in a tunable two-level system," Physical Review Letters **104**, 2–5 (2010).

[125] K. S. Abedin, P. S. Westbrook, J. W. Nicholson, J. Porque, T. Kremp, and X. Liu, "Single-frequency Brillouin distributed feedback fiber laser." Optics Letters **37**, 605–7 (2012).

[126] S. Loranger, V. Lambin-Iezzi, M. Wahbeh, and R. Kashyap, "Stimulated Brillouin scattering in ultra-long distributed feedback Bragg gratings in standard optical fiber," Optics Letters **41**, 1797 (2016).

[127] D. Xiang, P. Lu, Y. Xu, L. Chen, and X. Bao, "Random Brillouin fiber laser for tunable ultra-narrow linewidth microwave generation," Optics Letters **41**, 4839 (2016).

[128] S. Gao, L. Zhang, Y. Xu, P. Lu, L. Chen, and X. Bao, "Tapered fiber based Brillouin random fiber laser and its application for linewidth measurement," Optics Express **24**, 28353 (2016).

[129] M. Pang, X. Bao, L. Chen, Z. Qin, Y. Lu, and P. Lu, "Frequency stabilized coherent Brillouin random fiber laser: theory and experiments." Optics Express **21**, 27155–68 (2013).

[130] H. G. Winful, I. V. Kabakova, and B. J. Eggleton, "Model for distributed feedback Brillouin lasers." Optics Express **21**, 16191–16199 (2013).

[131] B. Redding, M. A. Choma, and H. Cao, "Speckle-free laser imaging using random laser illumination," Nature Photonics **6**, 355–359 (2012).

[132] T. F. S. Büttner, I. V. Kabakova, D. D. Hudson, R. Pant, C. G. Poulton, A. C. Judge, and B. J. Eggleton, "Phase-locking and Pulse Generation in Multi-Frequency Brillouin Oscillator via Four Wave Mixing." Scientific Reports **4**, 5032 (2014).

[133] T. F. S. Büttner, M. Merklein, I. V. Kabakova, D. D. Hudson, D.-Y. Choi, B. Luther-Davies, S. J. Madden, and B. J. Eggleton, "Phase-locked, chip-based, cascaded stimulated Brillouin scattering," Optica **1**, 311 (2014).

[134] D. Braje, L. Hollberg, and S. Diddams, "Brillouin-Enhanced Hyperparametric Generation of an Optical Frequency Comb in a Monolithic Highly Nonlinear Fiber Cavity Pumped by a cw Laser," Physical Review Letters **102**, 193902 (2009).

[135] F. Ferdous, H. Miao, D. E. Leaird, K. Srinivasan, J. Wang, L. Chen, L. T. Varghese, and A. M. Weiner, "Spectral line-by-line pulse shaping of on-chip microresonator frequency combs," Nature Photonics **5**, 770–776 (2011).

[136] S. A. Diddams, L. Hollberg, and V. Mbele, "Molecular fingerprinting with the resolved modes of a femtosecond laser frequency comb." Nature **445**, 627–630 (2007).

[137] J. Pfeifle, V. Brasch, M. Lauermann, Y. Yu, D. Wegner, T. Herr, K. Hartinger, P. Schindler, J. Li, D. Hillerkuss, R. Schmogrow, C. Weimann, R. Holzwarth, W. Freude, J. Leuthold, T. J. Kippenberg, and C. Koos, "Coherent terabit communications with microresonator Kerr frequency combs," Nature Photonics **8**, 375–380 (2014).

[138] R. Pant, E. Li, D.-Y. Choi, C. G. Poulton, S. J. Madden, B. Luther-Davies, and B. J. Eggleton, "Cavity enhanced stimulated Brillouin scattering in an optical chip for multiorder Stokes generation," Optics Letters **36**, 3687–3689 (2011).

[139] M. S. Kang, N. Y. Joly, and P. S. J. Russell, "Passive mode-locking of fiber ring laser at the 337th harmonic using gigahertz acoustic core resonances." Optics Letters **38**, 561–3 (2013).

[140] B. Stiller and T. Sylvestre, "Observation of acoustically induced modulation instability in a Brillouin photonic crystal fiber laser." Optics Letters **38**, 1570–2 (2013).

[141] A. Butsch, J. R. Koehler, R. E. Noskov, and P. S. Russell, "CW-pumped single-pass frequency comb generation by resonant optomechanical nonlinearity in dual-nanoweb fiber," Optica **1**, 158 (2014).

[142] D. Culverhouse, K. Kalli, and D. Jackson, "Stimulated Brillouin scattering ring resonator laser for SBS gain studies and microwave generation," Electronics Letters **27**, 2033 (1991).

[143] S. Preußler, N. Wenzel, R.-P. Braun, N. Owschimikow, C. Vogel, A. Deninger, A. Zadok, U. Woggon, and T. Schneider, "Generation of ultra-narrow, stable and tunable millimeter- and terahertz- waves with very low phase noise." Optics Express **21**, 23950–62 (2013).

[144] X. Yao, "Brillouin selective sideband amplification of microwave photonic signals," IEEE Photonics Technology Letters **10**, 138–140 (1998).

[145] M. Merklein, B. Stiller, I. V. Kabakova, U. S. Mutugala, K. Vu, S. J. Madden, B. J. Eggleton, and R. Slavík, "Widely tunable, low phase noise microwave source based on a photonic chip," Optics Letters **41**, 4633 (2016).

[146] B. Morrison, D. Marpaung, R. Pant, E. Li, D. Y. Choi, S. Madden, B. Luther-Davies, and B. J. Eggleton, "Tunable microwave photonic notch filter using on-chip stimulated Brillouin scattering," Optics Communications **313**, 85–89 (2014).

[147] A. Casas-Bedoya, B. Morrison, M. Pagani, D. Marpaung, and B. J. Eggleton, "Tunable narrowband microwave photonic filter created by stimulated Brillouin scattering from a silicon nanowire," Optics Letters **40**, 4154 (2015).

[148] A. Choudhary, I. Aryanfar, S. Shahnia, B. Morrison, K. Vu, S. Madden, B. Luther-Davies, D. Marpaung, and B. J. Eggleton, "Tailoring of the Brillouin gain for on-chip widely tunable and reconfigurable broadband microwave photonic filters," Optics Letters **41**, 436–439 (2016).

[149] A. Choudhary, B. Morrison, I. Aryanfar, S. Shahnia, M. Pagani, Y. Liu, K. Vu, S. Madden, D. Marpaung, and B. J. Eggleton, "Advanced Integrated Microwave Signal Processing With Giant On-Chip Brillouin Gain," Journal of Lightwave Technology **35**, 846–854 (2017).

[150] M. Pu, L. Liu, W. Xue, Y. Ding, H. Ou, K. Yvind, and J. M. Hvam, "Widely tunable microwave phase shifter based on silicon-on-insulator dual-microring resonator." Optics Express **18**, 6172–6182 (2010).

[151] M. Burla, D. Marpaung, L. Zhuang, C. Roeloffzen, M. R. Khan, A. Leinse, M. Hoekman, and R. Heideman, "On-chip CMOS compatible reconfigurable optical delay line with separate carrier tuning for microwave photonic signal processing," Optics Express **19**, 21475 (2011).

[152] M. Burla, L. R. Cortés, M. Li, X. Wang, L. Chrostowski, and J. Azaña, "Integrated waveguide Bragg gratings for microwave photonics signal processing." Optics Express **21**, 25120–47 (2013).

[153] I. Aryanfar, D. Marpaung, A. Choudhary, Y. Liu, K. Vu, D.-Y. Choi, P. Ma, S. Madden, and B. J. Eggleton, "Chip-based Brillouin radio frequency photonic phase shifter and wideband time delay," Optics Letters **42**, 1313 (2017).

[154] K. Shimizu, T. Horiguchi, Y. Koyamada, and T. Kurashima, "Coherent Self-Heterodyne Brillouin OTDR for Measurement of Brillouin Frequency Shift Distribution in Optical Fibers," Journal of Lightwave Technology **12**, 730–736 (1994).

[155] T. Kurashima, M. Tateda, T. Horiguchi, and Y. Koyamada, "Performance improvement of a combined OTDR for distributed strain and loss measurement by randomizing the reference light polarization state," IEEE Photonics Technology Letters **9**, 360–362 (1997).

[156] T. Horiguchi and M. Tateda, "Optical-fiber-attenuation investigation using stimulated Brillouin scattering between a pulse and a continuous wave," Optics Letters **14**, 408 (1989).

[157] D. Culverhouse, F. Farahi, C. Pannell, and D. Jackson, "Potential of stimulated Brillouin scattering as sensing mechanism for distributed temperature sensors," Electronics Letters **25**, 913 (1989).

[158] M. Niklès, L. Thévenaz, and P. A. Robert, "Simple distributed fiber sensor based on Brillouin gain spectrum analysis," Optics Letters **21**, 758 (1996).

[159] X. Bao, D. J. Webb, and D. A. Jackson, "22-km distributed temperature sensor using Brillouin gain in an optical fiber," Optics Letters **18**, 552 (1993).

[160] X. Bao, D. J. Webb, and D. A. Jackson, "32-km distributed temperature sensor based on Brillouin loss in an optical fiber," Optics Letters **18**, 1561 (1993).

[161] X. Bao, A. Brown, M. DeMerchant, and J. Smith, "Characterization of the Brillouin-loss spectrum of single-mode fibers by use of very short (<10-ns) pulses," Optics Letters **24**, 510 (1999).

[162] L. Zou, X. Bao, Y. Wan, and L. Chen, "Coherent probe-pump-based Brillouin sensor for centimeter-crack detection." Optics Letters **30**, 370–372 (2005).

[163] A. W. Brown, B. G. Colpitts, and K. Brown, "Dark-pulse Brillouin optical time-domain sensor with 20-mm spatial resolution," Journal of Lightwave Technology **25**, 381–386 (2007).

[164] S. M. Foaleng, M. Tur, J.-C. Beugnot, and L. Thevenaz, "High Spatial and Spectral Resolution Long-Range Sensing Using Brillouin Echoes," Journal of Lightwave Technology **28**, 2993–3003 (2010).

[165] M. W. Lee, B. Stiller, J. Hauden, H. Maillotte, C. Roch, L. Thévenaz, and T. Sylvestre, "Differential phase-shift-keying technique-based brillouin echo-distributed sensing," IEEE Photonics Technology Letters **24**, 79–81 (2012).

[166] K. Y. Song, W. Zou, Z. He, and K. Hotate, "All-optical dynamic grating generation based on Brillouin scattering in polarization-maintaining fiber," Optics Letters **33**, 926 (2008).

[167] K. Y. Song, W. Zou, Z. He, and K. Hotate, "Optical time-domain measurement of Brillouin dynamic grating spectrum in a polarization-maintaining fiber." Optics Letters **34**, 1381–3 (2009).

[168] Kwang Yong Song, Sanghoon Chin, N. Primerov, and L. Thevenaz, "Time-Domain Distributed Fiber Sensor With 1 cm Spatial Resolution Based on Brillouin Dynamic Grating," Journal of Lightwave Technology **28**, 2062–2067 (2010).

[169] D. Garus, K. Krebber, F. Schliep, and T. Gogolla, "Distributed sensing technique based on Brillouin optical-fiber frequency-domain analysis." Optics Letters **21**, 1402–1404 (1996).

[170] D. Garus, T. Gogolla, K. Krebber, and F. Schliep, "Brillouin optical-fiber frequency-domain analysis for distributed temperature and strain measurements," Journal of Lightwave Technology **15**, 654–662 (1997).

[171] K. Hotate and T. Hasegawa, "Measurement of Brillouin Gain Spectrum Distribution along an Optical Fiber Using a Correlation-Based Technique – Proposal, Experiment and Simulation," IEICE Trans. Electronics **E83-C**, 405–412 (2000).

[172] K. Hotate and M. Tanaka, "Distributed fiber brillouin strain sensing with 1-cm spatial resolution by correlation-based continuous-wave technique," IEEE Photonics Technology Letters **14**, 179–181 (2002).

[173] R. Cohen, Y. London, Y. Antman, and A. Zadok, "Brillouin optical correlation domain analysis with 4 millimeter resolution based on amplified spontaneous emission." Optics Express **22**, 12070–8 (2014).

[174] K. Hotate, R. Watanabe, Z. He, and M. Kishi, "Measurement of Brillouin frequency shift distribution in PLC by Brillouin Optical Correlation Domain Analysis," **8421**, 10–13 (2012).

[175] A. Zarifi, B. Stiller, M. Merklein, N. Li, K. Vu, D.-Y. Choi, P. Ma, S. J. Madden, and B. J. Eggleton, "Highly localized distributed Brillouin scattering response in a photonic integrated circuit," APL Photonics **3**, 036101 (2018).

[176] O. Terra, G. Grosche, and H. Schnatz, "Brillouin amplification in phase coherent transfer of optical frequencies over 480 km fiber," Optics Express **18**, 16102–16111 (2010).

[177] M. Junker, M. J. Ammann, A. T. Schwarzbacher, J. Klinger, K. U. Lauterbach, and T. Schneider, "A comparative test of brillouin amplification and erbium-doped fiber amplification for the generation of millimeter waves with low phase noise properties," IEEE Transactions on Microwave Theory and Techniques **54**, 1576–1580 (2006).

[178] M. Pelusi, A. Choudhary, T. Inoue, D. Marpaung, B. J. Eggleton, K. Solis-Trapala, H. N. Tan, and S. Namiki, "Low noise frequency comb carriers for 64-QAM via a Brillouin comb amplifier," Optics Express **25**, 17847 (2017).

[179] K. Y. Song, M. G. Herráez, and L. Thévenaz, "Long optically controlled delays in optical fibers." Optics Letters **30**, 1782–1784 (2005).

[180] Y. Okawachi, M. Bigelow, J. Sharping, Z. Zhu, A. Schweinsberg, D. Gauthier, R. Boyd, and A. Gaeta, "Tunable All-Optical Delays via Brillouin Slow Light in an Optical Fiber," Physical Review Letters **94**, 153902 (2005).

[181] L. Thévenaz, "Slow and fast light in optical fibres," Nature Photonics **2**, 474–481 (2008).

[182] R. G. Smith, "Optical Power Handling Capacity of Low Loss Optical Fibers as Determined by Stimulated Raman and Brillouin Scattering," Applied Optics **11**, 2489–2494 (1972).

[183] B. E. A. Saleh and M. C. Teich, *Fundamentals of Photonics*, Wiley Series in Pure and Applied Optics (John Wiley & Sons, Inc., New York, USA, 1991).

[184] G. G. P. Agrawal, *Nonlinear fiber optics* (Academic Press, 2001), 3rd ed.

[185] J.-C. Beugnot, S. Lebrun, G. Pauliat, H. Maillotte, V. Laude, and T. Sylvestre, "Brillouin light scattering from surface acoustic waves in a subwavelength-diameter optical fibre." Nature Communications **5**, 5242 (2014).

[186] B. A. Auld, *Acoustic fields and waves in solids*, vol. 1 (John Wiley & Sons, Inc., 1973).

[187] L. D. Landau and E. M. Lifshitz, *Theory of Elasticity* (Butterworth-Heinemann, 1986), 3rd ed.

[188] M. Merklein, "Femtosekunden Spektroskopie akustischer Anregung von Nanostrukturen," Diplom thesis, University of Konstanz (2012).

[189] H. Winful, "Chirped Brillouin dynamic gratings for storing and compressing light," Optics Express **21**, 10039–10047 (2013).

[190] P. T. Rakich, P. Davids, and Z. Wang, "Tailoring optical forces in waveguides through radiation pressure and electrostrictive forces," Optics Express **18**, 14439 (2010).

[191] C. Wolff, M. J. Steel, B. J. Eggleton, and C. G. Poulton, "Stimulated Brillouin scattering in integrated photonic waveguides: Forces, scattering mechanisms, and coupled-mode analysis," Physical Review A **92**, 013836 (2015).

[192] C. Wolff, M. J. Steel, B. J. Eggleton, and C. G. Poulton, "arxiv Stimulated Brillouin Scattering in integrated photonic waveguides: forces, scattering mechanisms and coupled mode analysis," arXiv:1407.3521 pp. 1–17 (2014).

[193] K. O. Hill, Y. Fujii, D. C. Johnson, and B. S. Kawasaki, "Photosensitivity in optical fiber waveguides: Application to reflection filter fabrication," Applied Physics Letters **32**, 647–649 (1978).

[194] R. Kashyap, "Fiber Bragg Gratings," in "Fiber Bragg Gratings," (Elsevier, 2010), 2nd ed.

[195] T. Erdogan, "Fiber grating spectra," Journal of Lightwave Technology **15**, 1277–1294 (1997).

[196] G. Lenz, B. Eggleton, C. Madsen, and R. Slusher, "Optical delay lines based on optical filters," IEEE Journal of Quantum Electronics **37**, 525–532 (2001).

[197] B. J. Eggleton, A. Ahuja, P. S. Westbrook, J. A. Rogers, P. Kuo, T. N. Nielsen, and B. Mikkelsen, "Integrated tunable fiber gratings for dispersion management in high-bit rate systems," Journal of Lightwave Technology **18**, 1418–1432 (2000).

[198] I. V. Kabakova, C. M. de Sterke, and B. J. Eggleton, "Bistable switching and reshaping of optical pulses in a Bragg grating cavity," Journal of the Optical Society of America B **27**, 2648–2653 (2010).

[199] B. Eggleton, R. Slusher, C. de Sterke, P. Krug, and J. Sipe, "Bragg Grating Solitons," Physical Review Letters **76**, 1627–1630 (1996).

[200] G. Meltz, W. W. Morey, and W. H. Glenn, "Formation of Bragg gratings in optical fibers by a transverse holographic method," Optics Letters **14**, 823 (1989).

[201] K. O. Hill, B. Malo, F. Bilodeau, D. C. Johnson, and J. Albert, "Bragg gratings fabricated in monomode photosensitive optical fiber by UV exposure through a phase mask," Applied Physics Letters **62**, 1035–1037 (1993).

[202] C. de Sterke, N. Broderick, B. J. Eggleton, and M. Steel, "Nonlinear Optics in Fiber Gratings," Optical Fiber Technology **2**, 253–268 (1996).

[203] T. F. Krauss, "Slow light in photonic crystal waveguides," Journal of Physics D: Applied Physics **40**, 2666–2670 (2007).

[204] T. Baba, "Slow light in photonic crystals," Nature Photonics **2**, 465–473 (2008).

[205] L. V. Hau, S. E. Harris, Z. Dutton, and C. H. Behroozi, "Light speed reduction to 17 metres per second in an ultracold atomic gas," Nature **397**, 594–598 (1999).

[206] R. M. Camacho, M. V. Pack, J. C. Howell, A. Schweinsberg, and R. W. Boyd, "Wide-bandwidth, tunable, multiple-pulse-width optical delays using slow light in cesium vapor," Physical Review Letters **98**, 2–5 (2007).

[207] A. Yariv, Y. Xu, R. K. Lee, and A. Scherer, "Coupled resonator optical waveguide: A proposal and analysis," Optics Letters **vol**, 24pp711–713 (1999).

[208] K. Y. Song, M. Herráez, and L. Thévenaz, "Observation of pulse delaying and advancement in optical fibers using stimulated Brillouin scattering." Optics Express **13**, 82–88 (2005).

[209] C. Monat, M. de Sterke, and B. J. Eggleton, "Slow light enhanced nonlinear optics in periodic structures," Journal of Optics **12**, 104003 (2010).

[210] B. Corcoran, C. Monat, C. Grillet, D. J. Moss, B. J. Eggleton, T. P. White, L. O'Faolain, and T. F. Krauss, "Green light emission in silicon through slow-light enhanced third-harmonic generation in photonic-crystal waveguides," Nature Photonics **3**, 206–210 (2009).

[211] R. W. Boyd, "Material slow light and structural slow light: similarities and differences for nonlinear optics," Journal of the Optical Society of America B **29**, 2644 (2012).

[212] J. Khurgin and R. Tucker, *Slow light: Science and applications* (CRC Press, 2008).

[213] J. B. Khurgin, "Slow light in various media: a tutorial," Advances in Optics and Photonics **2**, 287–318 (2010).

[214] H. G. Winful, "The Meaning of Group Delay in Barrier Tunneling: A Reexamination of Superluminal Group Velocities," in "Slow and Fast Light," , vol. 8 (OSA, Washington, D.C., 2006), vol. 8, p. TuD1.

[215] Y. A. Vlasov, M. O'Boyle, H. F. Hamann, and S. J. McNab, "Active control of slow light on a chip with photonic crystal waveguides." Nature **438**, 65–69 (2005).

[216] C. Monat, M. Ebnali-Heidari, C. Grillet, B. Corcoran, B. J. Eggleton, T. P. White, L. O'Faolain, J. Li, and T. F. Krauss, "Four-wave mixing in slow light engineered silicon photonic crystal waveguides." Optics Express **18**, 22915–22927 (2010).

[217] L. O'Faolain, S. A. Schulz, D. M. Beggs, T. P. White, M. Spasenović, L. Kuipers, F. Morichetti, A. Melloni, S. Mazoyer, J. P. Hugonin, P. Lalanne, and T. F. Krauss, "Loss engineered slow light waveguides," Optics Express **18**, 27627–27638 (2010).

[218] S. Hughes, L. Ramunno, J. F. Young, and J. E. Sipe, "Extrinsic optical scattering loss in photonic crystal waveguides: Role of fabrication disorder and photon group velocity," Physical Review Letters **94**, 1–4 (2005).

[219] N. Bhat and J. Sipe, "Optical pulse propagation in nonlinear photonic crystals," Physical Review E **64**, 056604 (2001).

[220] C. Martijn De Sterke and J. E. Sipe, "Coupled modes and the nonlinear Schrödinger equation," Physical Review A **42**, 550–555 (1990).

[221] M. Santagiustina, C. G. SOMEDA, G. Vadala', S. Combrie', and A. De Rossi, "Theory of Slow Light Enhanced Four-Wave Mixing in Photonic Crystal Waveguides," Optics Express **18**, 21024 (2010).

[222] J. Li, L. O'Faolain, I. H. Rey, and T. F. Krauss, "Four-wave mixing in photonic crystal waveguides: slow light enhancement and limitations." Optics Express **19**, 4458–63 (2011).

[223] E. M. Purcell, "Spontaneous emission probabilities at radio frequencies," Physical Review **69** (1946).

[224] D. Kleppner, "Inhibited spontaneous emission," Physical Review Letters **47**, 233–236 (1981).

[225] E. Yablonovitch, "Inhibited Spontaneous Emission in Solid-State Physics and Electronics," Physical Review Letters **58**, 2059–2062 (1987).

[226] S. John, "Strong localization of photons in certain disordered dielectric superlattices," Physical Review Letters **58**, 2486–2489 (1987).

[227] E. Yablonovitch, T. J. Gmitter, and R. Bhat, "Inhibited and enhanced spontaneous emission from optically thin AlGaAs/GaAs Double Heterostructures," Physical Review Letters **61**, 2546–2549 (1988).

[228] E. Yablonovitch and T. J. Gmitter, "Photonic band structure: The face-centered-cubic case," Physical Review Letters **63**, 1950–1953 (1989).

[229] J. Martorell and N. M. Lawandy, "Observation of inhibited spontaneous emission in a periodic dielectric structure," Physical Review Letters **65**, 1877–1880 (1990).

[230] P. Lodahl, A. Floris van Driel, I. S. Nikolaev, A. Irman, K. Overgaag, D. Vanmaekelbergh, and W. L. Vos, "Controlling the dynamics of spontaneous emission from quantum dots by photonic crystals," Nature **430**, 654–657 (2004).

[231] M. Fujita, S. Takahashi, Y. Tanaka, T. Asano, and S. Noda, "Simultaneous inhibition and redistribution of spontaneous light emission in photonic crystals." Science **308**, 1296–1298 (2005).

[232] S. Noda, M. Fujita, and T. Asano, "Spontaneous-emission control by photonic crystals and nanocavities," Nature Photonics **1**, 449–458 (2007).

[233] M. D. Leistikow, A. P. Mosk, E. Yeganegi, S. R. Huisman, A. Lagendijk, and W. L. Vos, "Inhibited spontaneous emission of quantum dots observed in a 3D photonic band gap," Physical Review Letters **107**, 1–5 (2011).

[234] D. Gomila, R. Zambrini, and G.-L. Oppo, "Photonic Band-Gap Inhibition of Modulational Instabilities," Physical Review Letters **92**, 253904 (2004).

[235] D. Gomila and G.-L. Oppo, "Coupled-mode theory for photonic band-gap inhibition of spatial instabilities," Physical Review E **72**, 016614 (2005).

[236] N. Marsal, D. Wolfersberger, M. Sciamanna, G. Montemezzani, and D. N. Neshev, "Experimental control of pattern formation by photonic lattices," Optics Letters **33**, 2509 (2008).

[237] N. Marsal, D. Wolfersberger, M. Sciamanna, G. Montemezzani, and D. N. Neshev, "All-optical control of nonlinear pattern modes by periodic photonic structures," IEEE Journal of Quantum Electronics **45**, 1380–1387 (2009).

[238] N. Borrelli, *Photosensitive Glass and Glass-Ceramics* (CRC Press, Taylor & Francis Group, 2016).

[239] D.-Y. Choi, S. Madden, A. Rode, R. Wang, B. Luther-Davies, N. J. Baker, and B. J. Eggleton, "Integrated shadow mask for sampled Bragg gratings in chalcogenide (As(2)S(3)) planar waveguides." Optics Express **15**, 7708–12 (2007).

[240] N. J. Baker, H. W. Lee, I. C. Littler, C. M. de Sterke, B. J. Eggleton, D.-Y. Choi, S. Madden, and B. Luther-Davies, "Sampled Bragg gratings in chalcogenide (As2S3) rib-waveguides." Optics Express **14**, 9451–9459 (2006).

[241] T. F. S. Büttner, I. V. Kabakova, D. D. Hudson, R. Pant, E. Li, and B. J. Eggleton, "Multi-wavelength gratings formed via cascaded stimulated Brillouin scattering." Optics Express **20**, 26434–26440 (2012).

[242] M. A. Popescu, *Non-Crystalline Chalcogenides*, vol. 8 of *Solid-State Science and Technology Library* (Kluwer Academic Publishers, Dordrecht, 2002).

[243] A. Apling, A. Leadbetter, and A. Wright, "A comparison of the structures of vapour-deposited and bulk arsenic sulphide glasses," Journal of Non-Crystalline Solids **23**, 369–384 (1977).

[244] N. Hô, J. M. Laniel, R. Vallée, and A. Villeneuve, "Photosensitivity of As2S3 chalcogenide thin films at 1.5 microm." Optics Letters **28**, 965–967 (2003).

[245] J. Hu, M. Torregiani, F. Morichetti, N. Carlie, A. Agarwal, K. Richardson, L. C. Kimerling, and A. Melloni, "Resonant cavity-enhanced photosensitivity in As2S3 chalcogenide glass at 1550 nm telecommunication wavelength." Optics Letters **35**, 874–876 (2010).

[246] T. F. Krauss, "Why do we need slow light?" Nature Photonics **2**, 448–450 (2008).

[247] M. Soljacić and J. D. Joannopoulos, "Enhancement of nonlinear effects using photonic crystals." Nature materials **3**, 211–219 (2004).

[248] Y. Hamachi, S. Kubo, and T. Baba, "Slow light with low dispersion and nonlinear enhancement in a lattice-shifted photonic crystal waveguide." Optics Letters **34**, 1072–1074 (2009).

[249] K. Inoue, H. Oda, N. Ikeda, and K. Asakawa, "Enhanced third-order nonlinear effects in slow-light photonic-crystal slab waveguides of line-defect." Optics Express **17**, 7206–7216 (2009).

[250] J. T. Mok, C. M. de Sterke, I. C. M. Littler, and B. J. Eggleton, "Dispersionless slow light using gap solitons," Nature Physics **2**, 775–780 (2006).

[251] J. P. Dowling, M. Scalora, M. J. Bloemer, and C. M. Bowden, "The photonic band edge laser: A new approach to gain enhancement," Journal of Applied Physics **75**, 1896–1899 (1994).

[252] R. Slavík, F. Parmigiani, J. Kakande, C. Lundström, M. Sjödin, P. A. Andrekson, R. Weerasuriya, S. Sygletos, A. D. Ellis, L. Grüner-Nielsen, D. Jakobsen, S. Herstrøm, R. Phelan, J. O'Gorman, A. Bogris, D. Syvridis, S. Dasgupta, P. Petropoulos, and D. J. Richardson, "All-optical phase and amplitude regenerator for next-generation telecommunications systems," Nature Photonics **4**, 690–695 (2010).

[253] Y. Zhang, J. Schröder, C. Husko, S. Lefrancois, D.-Y. Choi, S. Madden, B. Luther-Davies, and B. J. Eggleton, "Pump-degenerate phase-sensitive amplification in chalcogenide waveguides," Journal of the Optical Society of America B **31**, 780–787 (2014).

[254] Y. Zhang, C. Husko, J. Schröder, S. Lefrancois, I. H. Rey, T. F. Krauss, and B. J. Eggleton, "Phase-sensitive amplification in silicon photonic crystal waveguides." Optics Letters **39**, 363–366 (2014).

[255] J. Leuthold, C. Koos, and W. Freude, "Nonlinear silicon photonics," Nature Photonics **4**, 535–544 (2010).

[256] M. A. Foster, A. C. Turner, J. E. Sharping, B. S. Schmidt, M. Lipson, and A. L. Gaeta, "Broad-band optical parametric gain on a silicon photonic chip." Nature **441**, 960–963 (2006).

[257] K. Ogusu, "Effect of stimulated Brillouin scattering on nonlinear pulse propagation in fiber Bragg gratings," Journal of the Optical Society of America B **17**, 769–774 (2000).

[258] M. Lee, R. Pant, and M. A. Neifeld, "Improved slow-light delay performance of a broadband stimulated Brillouin scattering system using fiber Bragg gratings." Applied Optics **47**, 6404–6415 (2008).

[259] B. J. Eggleton, "Chalcogenide photonics: fabrication, devices and applications Introduction," Optics Express **18**, 26632 (2010).

[260] K. S. Abedin, "Observation of strong stimulated Brillouin scattering in single-mode As2Se3 chalcogenide fiber." Optics Express **13**, 10266–10271 (2005).

[261] A. Asatryan, S. Fabre, K. Busch, R. McPhedran, L. Botten, M. de Sterke, and N. a. Nicorovici, "Two-dimensional local density of states in two-dimensional photonic crystals." Optics Express **8**, 191–196 (2001).

[262] R. McPhedran, L. Botten, J. McOrist, a. Asatryan, C. de Sterke, and N. Nicorovici, "Density of states functions for photonic crystals," Physical Review E **69**, 016609 (2004).

[263] K. Sakoda, *Optical Properties of Photonic Crystals*, Springer Series in Optical Sciences (Springer, 2005).

[264] K. Kuroda, T. Sawada, T. Kuroda, K. Watanabe, and K. Sakoda, "Doubly enhanced spontaneous emission due to increased photon density of states at photonic band edge frequencies." Optics Express **17**, 13168–13177 (2009).

[265] K. Kuroda, T. Sawada, T. Kuroda, K. Watanabe, and K. Sakoda, "Enhanced spontaneous emission observed at one-dimensional photonic band edges," Journal of the Optical Society of America B **27**, 45–50 (2009).

[266] P. a. M. Dirac, "The Quantum Theory of the Emission and Absorption of Radiation," Proceedings of the Royal Society A: Mathematical, Physical and Engineering Sciences **114**, 243–265 (1927).

[267] H. S. Kim, S.-H. Kim, D.-K. Ko, G. Lim, B. H. Cha, and J. Lee, "Threshold reduction of stimulated Brillouin scattering by the enhanced Stokes noise initiation," Applied Physics Letters **74**, 1358–1360 (1999).

[268] Y. Zhu, Q. Lu, S. Guo, X. Xu, and X. Cheng, "Threshold reduction of stimulated Brillouin scattering by Stokes seeds via acousto-optic effect," Optics Communications **281**, 4523–4525 (2008).

[269] M. Karow, J. Neumann, D. Kracht, and P. Weßels, "Impact of amplified spontaneous emission on Brillouin scattering of a single-frequency signal." Optics Express **20**, 10572–82 (2012).

[270] M. Pelusi, F. Luan, T. D. Vo, M. R. E. Lamont, S. J. Madden, D. A. Bulla, D.-Y. Choi, B. Luther-Davies, and B. J. Eggleton, "Photonic-chip-based radio-frequency spectrum analyser with terahertz bandwidth," Nature Photonics **3**, 139–143 (2009).

[271] R. Salem, M. A. Foster, A. C. Turner, D. F. Geraghty, M. Lipson, and A. L. Gaeta, "Signal regeneration using low-power four-wave mixing on silicon chip," Nature Photonics **2**, 35–38 (2007).

[272] P. Del'Haye, A. Schliesser, O. Arcizet, T. Wilken, R. Holzwarth, and T. J. Kippenberg, "Optical frequency comb generation from a monolithic microresonator." Nature **450**, 1214–1217 (2007).

[273] S. Loranger, V. L. Iezzi, and R. Kashyap, "Demonstration of an ultra-high frequency picosecond pulse generator using an SBS frequency comb and self phase-locking." Optics Express **20**, 19455–19462 (2012).

[274] S. J. Madden, D.-Y. Choi, D. a. Bulla, a. V. Rode, B. Luther-Davies, V. G. Ta'eed, M. D. Pelusi, and B. J. Eggleton, "Long, low loss etched As(2)S(3) chalcogenide waveguides for all-optical signal regeneration." Optics Express **15**, 14414–14421 (2007).

[275] D.-Y. Choi, A. Wade, S. Madden, R. Wang, D. Bulla, and B. Luther-Davies, "Photo-induced and Thermal Annealing of Chalcogenide Films for Waveguide Fabrication," Physics Procedia **48**, 196–205 (2013).

[276] D. Y. Choi, S. Madden, D. A. Bulla, R. Wang, A. Rode, and B. Luther-Davies, "Submicrometer-thick low-loss As2S3 planar waveguides for nonlinear optical devices." IEEE Photonics Technology Letters **22**, 495–497 (2010).

[277] X. Gai, D.-Y. Choi, S. Madden, Z. Yang, R. Wang, and B. Luther-Davies, "Supercontinuum generation in the mid-infrared from a dispersion-engineered As2S3 glass rib waveguide," Optics Letters **37**, 3870–3872 (2012).

[278] C. M. D. Sterke, K. R. Jackson, and B. D. Robert, "Nonlinear coupled-mode equations on a finite interval: a numerical procedure," Journal of the Optical Society of America B **8**, 403–412 (1991).

[279] A. Bartels, D. Heinecke, and S. A. Diddams, "10-GHz Self-Referenced Optical Frequency Comb," Science **326**, 681–681 (2009).

[280] L. G. Helt, A. M. Brańczyk, M. Liscidini, and M. J. Steel, "Parasitic Photon-Pair Suppression via Photonic Stop-Band Engineering," Physical Review Letters **118**, 1–5 (2017).

[281] P. G. Kwiat, K. Mattle, H. Weinfurter, A. Zeilinger, A. V. Sergienko, and Y. Shih, "New high-intensity source of polarization-entangled photon pairs," Physical Review Letters **75**, 4337–4341 (1995).

[282] M. Collins, C. Xiong, I. Rey, T. Vo, J. He, S. Shahnia, C. Reardon, T. Krauss, M. Steel, A. Clark, and B. Eggleton, "Integrated spatial multiplexing of heralded single-photon sources," Nature Communications **4**, 1–7 (2013).

[283] Y.-C. Chen and G. Bahl, "Raman cooling of solids through photonic density of states engineering," Optica **2**, 893 (2015).

[284] S. Kim and G. Bahl, "Role of optical density of states in Brillouin optomechanical cooling," Optics Express **25**, 776 (2017).

[285] Y.-C. Chen, S. Kim, and G. Bahl, "Brillouin cooling in a linear waveguide," New Journal of Physics **18**, 115004 (2016).

[286] S. K. Turitsyn, S. A. Babin, A. E. El-Taher, P. Harper, D. V. Churkin, S. I. Kablukov, J. D. Ania-Castañón, V. Karalekas, and E. V. Podivilov, "Random distributed feedback fibre laser," Nature Photonics **542**, 133–193 (2010).

[287] M. Gagné and R. Kashyap, "Demonstration of a 3 mW threshold Er-doped random fiber laser based on a unique fiber Bragg grating." Optics Express **17**, 19067–19074 (2009).

[288] D. V. Churkin, A. E. El-Taher, I. D. Vatnik, J. D. Ania-Castañón, P. Harper, E. V. Podivilov, S. a. Babin, and S. K. Turitsyn, "Experimental and theoretical study of longitudinal power distribution in a random DFB fiber laser." Optics Express **20**, 11178–88 (2012).

[289] D. S. Wiersma and S. Cavalieri, "Light emissionA temperature-tunable random laser," Nature **414**, 708–709 (2001).

[290] X. S. Yao and L. Maleki, "Optoelectronic microwave oscillator," **13**, 1725–1735 (1996).

[291] X. S. Yao and L. Maleki, "Multiloop optoelectronic oscillator," IEEE Journal of Quantum Electronics **36**, 79–84 (2000).

[292] T. Zhang, J. Xiong, P. Wang, J. Zheng, F. Zhang, T. Pu, and X. Chen, "Tunable optoelectronic oscillator using FWM dynamics of an optical-injected DFB Laser," IEEE Photonics Technology Letters **27**, 1313–1316 (2015).

[293] X. S. Yao, "Phase-to-amplitude modulation conversion using Brillouin selective sideband amplification," IEEE Photonics Technology Letters **10**, 264–266 (1998).

[294] Huanfa Peng, Cheng Zhang, Xiaopeng Xie, Tao Sun, Peng Guo, Xiaoqi Zhu, Lixin Zhu, Weiwei Hu, and Zhangyuan Chen, "Tunable DC-60 GHz RF Generation Utilizing a Dual-Loop Optoelectronic Oscillator Based on Stimulated Brillouin Scattering," Journal of Lightwave Technology **33**, 2707–2715 (2015).

[295] E. Rubiola, *Phase Noise and Frequency Stability in Oscillators* (Cambridge University Press, Cambridge, 2008).

[296] S. Romisch, J. Kitching, E. Ferre-Pikal, L. Hollberg, and F. Walls, "Performance evaluation of an optoelectronic oscillator," IEEE Transactions on Ultrasonics, Ferroelectrics and Frequency Control **47**, 1159–1165 (2000).

[297] R. Navid, C. Jungemann, T. H. Lee, and R. W. Dutton, "Close-in phase noise in integrated oscillators," in "Spie," L. B. White, ed. (2004), p. 27.

[298] S. Jahanbakht, "Noise spectrum characterization of optoelectronic oscillators in the presence of laser frequency noise," Applied Optics **55**, 1854 (2016).

[299] D. Marpaung, C. Roeloffzen, R. Heideman, A. Leinse, S. Sales, and J. Capmany, "Integrated microwave photonics," Laser & Photonics Reviews **7**, 506–538 (2013).

[300] X. S. Yao and L. Maleki, "Optoelectronic microwave oscillator," Journal of the Optical Society of America B **13**, 1725 (1996).

[301] L. Maleki, "The optoelectronic oscillator," Nature Photonics **5**, 728–730 (2011).

[302] X. S. Yao, "High-quality microwave signal generation by use of Brillouin scattering in optical fibers." Optics letters **22**, 1329–1331 (1997).

[303] J. Yu, X. Yao, and L. Maleki, "Compact optoelectronic oscillator with ultra-low phase noise performance," Electronics Letters **35**, 1554 (1999).

[304] S. Liao, N.-N. Feng, D. Feng, P. Dong, R. Shafiiha, C.-C. Kung, H. Liang, W. Qian, Y. Liu, J. Fong, J. E. Cunningham, Y. Luo, and M. Asghari, "36 GHz submicron silicon waveguide germanium photodetector." Optics Express **19**, 10967–10972 (2011).

[305] N.-N. Feng, P. Dong, D. Zheng, S. Liao, H. Liang, R. Shafiiha, D. Feng, G. Li, J. E. Cunningham, A. V. Krishnamoorthy, and M. Asghari, "Vertical p-i-n germanium photodetector with high external responsivity integrated with large core Si waveguides." Optics Express **18**, 96–101 (2010).

[306] C. T. Phare, Y.-H. Daniel Lee, J. Cardenas, and M. Lipson, "Graphene electro-optic modulator with 30 GHz bandwidth," Nature Photonics **9**, 511–514 (2015).

[307] C. Haffner, W. Heni, Y. Fedoryshyn, J. Niegemann, a. Melikyan, D. L. Elder, B. Baeuerle, Y. Salamin, a. Josten, U. Koch, C. Hoessbacher, F. Ducry, L. Juchli, a. Emboras, D. Hillerkuss, M. Kohl, L. R. Dalton, C. Hafner, and J. Leuthold, "All-plasmonic Mach–Zehnder modulator enabling optical high-speed communication at the microscale," Nature Photonics **9**, 525–528 (2015).

[308] G. T. Reed, G. Mashanovich, F. Y. Gardes, and D. J. Thomson, "Silicon optical modulators," Nature Photonics **4**, 518–526 (2010).

[309] L. Alloatti, R. Palmer, S. Diebold, K. P. Pahl, B. Chen, R. Dinu, M. Fournier, J.-M. Fedeli, T. Zwick, W. Freude, C. Koos, and J. Leuthold, "100 GHz silicon-organic hybrid modulator," Light: Science & Applications **3**, e173 (2014).

[310] L. Liu, J. Dong, D. Gao, A. Zheng, and X. Zhang, "On-chip passive three-port circuit of all-optical ordered-route transmission," Scientific Reports **5**, 10190 (2015).

[311] N. Lindenmann, G. Balthasar, D. Hillerkuss, R. Schmogrow, M. Jordan, J. Leuthold, W. Freude, and C. Koos, "Photonic wire bonding: a novel concept for chip-scale interconnects." Optics Express **20**, 17667–77 (2012).

[312] S. Madden, Z. Jin, D. Choi, S. Debbarma, D. Bulla, and B. Luther-Davies, "Low loss coupling to sub-micron thick rib and nanowire waveguides by vertical tapering." Optics Express **21**, 3582–94 (2013).

[313] F. Xia, T. Mueller, Y.-m. Lin, A. Valdes-Garcia, and P. Avouris, "Ultrafast graphene photodetector," Nature Nanotechnology **4**, 839–843 (2009).

[314] A. David and M. Horowitz, "Low-frequency transmitted intensity noise induced by stimulated Brillouin scattering in optical fibers." Optics Express **19**, 11792–803 (2011).

[315] M. F. Ferreira, J. F. Rocha, and J. L. Pinto, "Analysis of the gain and noise characteristics of fibre Brillouin amplifiers," Optical and Quantum Electronics **26**, 35–44 (1994).

[316] D. Jalas, A. Petrov, M. Eich, W. Freude, S. Fan, Z. Yu, R. Baets, M. Popović, A. Melloni, J. D. Joannopoulos, M. Vanwolleghem, C. R. Doerr, and H. Renner, "What is — and what is not — an optical isolator," Nature Photonics **7**, 579–582 (2013).

[317] D. Huang, P. Pintus, C. Zhang, Y. Shoji, T. Mizumoto, and J. E. Bowers, "Reconfigurable integrated optical circulator," in "Conference on Lasers and Electro-Optics," (OSA, Washington, D.C., 2016), p. SM3E.1.

[318] M. Cherchi, S. Ylinen, M. Harjanne, M. Kapulainen, T. Vehmas, T. Aalto, G. T. Kanellos, D. Fitsios, and N. Pleros, "Fabrication-tolerant optical filters for dense integration on a micron-scale SOI platform," in "Proc. SPIE 8990, Silicon Photonics IX," J. Kubby and G. T. Reed, eds. (2014), p. 89900F.

[319] T. Ye, Y. Fu, L. Qiao, and T. Chu, "Low-crosstalk Si arrayed waveguide grating with parabolic tapers," Optics Express **22**, 31899 (2014).

[320] H. Peng, Y. Xu, X. Peng, X. Zhu, R. Guo, F. Chen, H. Du, Y. Chen, C. Zhang, L. Zhu, W. Hu, and Z. Chen, "Wideband tunable optoelectronic oscillator based on the deamplification of stimulated Brillouin scattering," Optics Express **25**, 10287 (2017).

[321] H. Lee, T. Chen, J. Li, O. Painter, and K. J. Vahala, "Ultra-low-loss optical delay line on a silicon chip." Nature Communications **3**, 867 (2012).

[322] S. Preussler and T. Schneider, "Stimulated Brillouin scattering gain bandwidth reduction and applications in microwave photonics and optical signal processing," Optical Engineering **55**, 031110 (2015).

[323] A. Choudhary, Y. Liu, B. Morrison, K. Vu, D.-Y. Choi, P. Ma, S. Madden, D. Marpaung, and B. J. Eggleton, "High-resolution, on-chip RF photonic signal processor using Brillouin gain shaping and RF interference," Scientific Reports **7**, 5932 (2017).

[324] M. Merklein, B. Stiller, K. Vu, S. J. Madden, and B. J. Eggleton, "A chip-integrated coherent photonic-phononic memory," Nature Communications **8**, 574 (2017).

[325] Q. Xu, P. Dong, and M. Lipson, "Breaking the delay-bandwidth limit in a photonic structure," Nature Physics **3**, 406–410 (2007).

[326] A. Zadok, A. Eyal, and M. Tur, "Stimulated Brillouin scattering slow light in optical fibers," Applied Optics **50**, E38 (2011).

[327] M. González Herráez, K. Y. Song, and L. Thévenaz, "Arbitrary-bandwidth Brillouin slow light in optical fibers." Optics Express **14**, 1395–400 (2006).

[328] A. Zadok, A. Eyal, and M. Tur, "Extended delay of broadband signals in stimulated Brillouin scattering slow light using synthesized pump chirp." Optics Express **14**, 8498–8505 (2006).

[329] T. Schneider, M. Junker, and K.-U. Lauterbach, "Potential ultra wide slow-light bandwidth enhancement." Optics Express **14**, 11082–7 (2006).

[330] Z. Zhu, A. M. C. Dawes, D. J. Gauthier, L. Zhang, and A. E. Willner, "Broadband SBS Slow Light in an Optical Fiber," Journal of Lightwave Technology **25**, 201–206 (2007).

[331] L. Yi, Y. Jaouen, W. Hu, Y. Su, and S. Bigo, "Improved slow-light performance of 10 Gb/s NRZ, PSBT and DPSK signals in fiber broadband SBS." Optics Express **15**, 16972–9 (2007).

[332] T. Schneider, M. Junker, and K.-U. Lauterbach, "Time Delay Enhancement in Stimulated-Brillouin-Scattering-Based Slow-Light Systems," Optics Letters **32**, 220–222 (2007).

[333] R. Pant, M. D. Stenner, M. A. Neifeld, and D. J. Gauthier, "Optimal pump profile designs for broadband SBS slow-light systems." Optics Express **16**, 2764–2777 (2008).

[334] T. Schneider, M. Junker, K. Lauterbach, and R. Henker, "Distortion reduction in cascaded slow light delays," Electronics Letters **42**, 1110 (2006).

[335] K. Y. Song, M. González Herráez, and L. Thévenaz, "Gain-assisted pulse advancement using single and double Brillouin gain peaks in optical fibers." Optics Express **13**, 9758–65 (2005).

[336] A. Minardo, R. Bernini, and L. Zeni, "Low distortion Brillouin slow light in optical fibers using AM modulation," Optics Express **14**, 5866–5876 (2006).

[337] Z. Shi, R. Pant, Z. Zhu, M. D. Stenner, M. A. Neifeld, D. J. Gauthier, and R. W. Boyd, "Design of a tunable time-delay element using multiple gain lines for increased fractional delay with high data fidelity." Optics Letters **32**, 1986–1988 (2007).

[338] J. B. Khurgin, "Performance Limits on Delay Lines Based on Optical Amplifiers," Optics Letters **31**, 948–950 (2006).

[339] S. Preussler, K. Jamshidi, A. Wiatrek, R. Henker, C.-a. Bunge, and T. Schneider, "Quasi-Light-Storage based on time-frequency coherence." Optics Express **17**, 15790–15798 (2009).

[340] T. Schneider, K. Jamshidi, and S. Preubler, "Quasi-light storage: A method for the tunable storage of optical packets with a potential delay-bandwidth product of several thousand bits," Journal of Lightwave Technology **28**, 2586–2592 (2010).

[341] S. Preussler, A. Wiatrek, K. Jamshidi, and T. Schneider, "Quasi-light-storage enhancement by reducing the Brillouin gain bandwidth." Applied Optics **50**, 4252–4256 (2011).

[342] K. Jamshidi, S. Preuler, A. Wiatrek, and T. Schneider, "A review to the all-optical quasi-light storage," IEEE Journal on Selected Topics in Quantum Electronics **18**, 884–890 (2012).

[343] S. Preussler, A. Wiatrek, K. Jamshidi, and T. Schneider, "Brillouin scattering gain bandwidth reduction down to 3.4MHz." Optics Express **19**, 8565–8570 (2011).

[344] Z. Zhu, D. J. Gauthier, and R. W. Boyd, "Stored light in an optical fiber via stimulated Brillouin scattering." Science **318**, 1748–50 (2007).

[345] V. Fiore, Y. Yang, M. C. Kuzyk, R. Barbour, L. Tian, and H. Wang, "Storing optical information as a mechanical excitation in a silica optomechanical resonator," Physical Review Letters **107**, 1–5 (2011).

[346] V. Fiore, C. Dong, M. C. Kuzyk, and H. Wang, "Optomechanical light storage in a silica microresonator," Physical Review A **87**, 023812 (2013).

[347] J. T. Hill, A. H. Safavi-Naeini, J. Chan, and O. Painter, "Coherent optical wavelength conversion via cavity optomechanics." Nature Communications **3**, 1196 (2012).

[348] Z. Shen, Y.-L. Zhang, Y. Chen, C.-L. Zou, Y.-F. Xiao, X.-B. Zou, F.-W. Sun, G.-C. Guo, and C.-H. Dong, "Experimental realization of optomechanically induced non-reciprocity," Nature Photonics **10**, 657–661 (2016).

[349] M. Eichenfield, J. Chan, R. M. Camacho, K. J. Vahala, and O. Painter, "Optomechanical crystals." Nature **462**, 78–82 (2009).

[350] A. H. Safavi-Naeini, T. P. M. Alegre, M. Winger, and O. Painter, "Optomechanics in an ultrahigh- Q two-dimensional photonic crystal cavity," Applied Physics Letters **97**, 97–99 (2010).

[351] A. H. Safavi-Naeini and O. Painter, "Proposal for an optomechanical traveling wave phonon-photon translator," New Journal of Physics **13** (2011).

[352] K. Fang, M. H. Matheny, X. Luan, and O. Painter, "Optical transduction and routing of microwave phonons in cavity-optomechanical circuits," Nature Photonics **10**, 489–496 (2016).

[353] C. Galland, N. Sangouard, N. Piro, N. Gisin, and T. J. Kippenberg, "Heralded single-phonon preparation, storage, and readout in cavity optomechanics," Physical Review Letters **112**, 1–6 (2014).

[354] K. C. Balram, M. I. Davanço, J. D. Song, and K. Srinivasan, "Coherent coupling between radiofrequency, optical and acoustic waves in piezo-optomechanical circuits," Nature Photonics **10**, 346–352 (2016).

[355] H. Li, S. A. Tadesse, Q. Liu, and M. Li, "Nanophotonic cavity optomechanics with propagating acoustic waves at frequencies up to 12 GHz," Optica **2**, 826 (2015).

[356] D. E. Chang, A. H. Safavi-Naeini, M. Hafezi, and O. Painter, "Slowing and stopping light using an optomechanical crystal array," New Journal of Physics **13**, 023003 (2011).

[357] L. Fan, C.-L. Zou, M. Poot, R. Cheng, X. Guo, X. Han, and H. X. Tang, "Noise-free quantum optical frequency shifting driven by mechanics," (2016).

[358] M. Cai, O. Painter, and K. J. Vahala, "Observation of Critical Coupling in a Fiber Taper to a Silica-Microsphere Whispering-Gallery Mode System," Physical Review Letters **85**, 74–77 (2000).

[359] K. J. Vahala, "Optical microcavities." Nature **424**, 839–46 (2003).

[360] M. Santagiustina, S. Chin, N. Primerov, L. Ursini, and L. Thévenaz, "All-optical signal processing using dynamic Brillouin gratings." Scientific Reports **3** (2013).

[361] Y. Zhu, M. Lee, M. A. Neifeld, and D. J. Gauthier, "High-fidelity, broadband stimulated-Brillouin-scattering-based slow light using fast noise modulation," Optics Express **19**, 687 (2011).

[362] M. Dong and H. G. Winful, "Area dependence of chirped-pulse stimulated Brillouin scattering: implications for stored light and dynamic gratings," Journal of the Optical Society of America B **32**, 2514 (2015).

[363] B. G. Lee, B. a. Small, K. Bergman, Q. Xu, and M. Lipson, "Transmission of high-data-rate optical signals through a micrometer-scale silicon ring resonator," Optics Letters **31**, 2701 (2006).

[364] J. Cardenas, M. A. Foster, N. Sherwood-Droz, C. B. Poitras, H. L. R. Lira, B. Zhang, A. L. Gaeta, J. B. Khurgin, P. Morton, and M. Lipson, "Wide-bandwidth continuously tunable optical delay line using silicon microring resonators." Optics Express **18**, 26525–34 (2010).

[365] F. Xia, L. Sekaric, and Y. Vlasov, "Ultracompact optical buffers on a silicon chip," Nature Photonics **1**, 65–71 (2007).

[366] E. Kuramochi, K. Nozaki, A. Shinya, K. Takeda, T. Sato, S. Matsuo, H. Taniyama, H. Sumikura, and M. Notomi, "Large-scale integration of wavelength-addressable all-optical memories on a photonic crystal chip," Nature Photonics **8**, 474–481 (2014).

[367] H. Gersen, T. J. Karle, R. J. P. Engelen, W. Bogaerts, J. P. Korterik, N. F. Van Hulst, T. F. Krauss, and L. Kuipers, "Real-space observation of ultraslow light in photonlc crystal waveguides," Physical Review Letters **94**, 3–6 (2005).

[368] J. B. Khurgin, "Optical buffers based on slow light in electromagnetically induced transparent media and coupled resonator structures: comparative analysis," Journal of the Optical Society of America B **22**, 1062 (2005).

[369] L. Fan, K. Y. Fong, M. Poot, and H. X. Tang, "Cascaded optical transparency in multimode-cavity optomechanical systems." Nature Communications **6**, 5850 (2015).

[370] D. Miller, "Optical interconnects to electronic chips." Applied Optics **49**, 70 (2010).

[371] A. Alduino and M. Paniccia, "Interconnects: Wiring electronics with light," Nature Photonics **1**, 153–155 (2007).

[372] B. G. Lee, X. Chen, A. Biberman, X. Liu, I.-W. Hsieh, C.-Y. Chou, J. I. Dadap, F. Xia, W. M. J. Green, L. Sekaric, Y. A. Vlasov, R. M. Osgood, and K. Bergman, "Ultrahigh-Bandwidth Silicon Photonic Nanowire Waveguides for On-Chip Networks," IEEE Photonics Technology Letters **20**, 398–400 (2008).

[373] D. Miller, "Device Requirements for Optical Interconnects to Silicon Chips," Proceedings of the IEEE **97**, 1166–1185 (2009).

[374] S. L. McCall and E. L. Hahn, "Self-Induced Transparency," Physical Review **183**, 457–485 (1969).

[375] B. Stiller, M. Merklein, C. Wolff, K. Vu, S. J. Madden, and B. J. Eggleton, "Cascaded waveguide-based photon-phonon memory," in "CLEO/Europe-EQEC," (2017), pp. CD–7.5.

[376] M. Merklein, B. Stiller, K. Vu, P. Ma, S. J. Madden, and B. J. Eggleton, "On-chip non-reciprocal light storage," in "CLEO/Europe-EQEC," (2017), pp. 2191 PD–2.4.

[377] K. Jaksch, M. Merklein, K. Vu, P. Ma, S. J. Madden, B. J. Eggleton, and B. Stiller, "Brillouin-based Light Storage of 200ps-long Pulses for 70 Pulse Widths," in "Frontiers in Optics 2017," (OSA, Washington, D.C., 2017), p. FTh4A.5.

[378] M. Merklein, B. Stiller, C. Wolff, K. Vu, S. J. Madden, and B. J. Eggleton, "Optically replenishing coherent acoustic phonons in photonic circuits," in "CLEO/Europe-EQEC," (2017), pp. 868/CD–11.5.

[379] C. G. Poulton, R. Pant, A. Byrnes, S. Fan, M. J. Steel, and B. J. Eggleton, "Design for broadband on-chip isolator using stimulated Brillouin scattering in dispersion-engineered chalcogenide waveguides," Optics Express **20**, 21235 (2012).

[380] K. L. Tsakmakidis, L. Shen, S. A. Schulz, X. Zheng, J. Upham, X. Deng, H. Altug, A. F. Vakakis, and R. W. Boyd, "Breaking Lorentz reciprocity to overcome the time-bandwidth limit in physics and engineering," Science **356**, 1260–1264 (2017).

[381] R. J. Williams, J. Nold, M. Strecker, O. Kitzler, A. Mckay, T. Schreiber, and R. P. Mildren, "Efficient Raman frequency conversion of high-power fiber lasers in diamond," Laser & Photonics Reviews **9**, 405–411 (2015).

[382] R. O. Behunin, P. Kharel, W. H. Renninger, and P. T. Rakich, "Engineering dissipation with phononic spectral hole burning," Nature Materials **16**, 315–321 (2016).

[383] R. N. Patel, C. J. Sarabalis, W. Jiang, J. T. Hill, and A. H. Safavi-Naeini, "Engineering Phonon Leakage in Nanomechanical Resonators," Physical Review Applied **8**, 041001 (2017).

[384] G. O. Luiz, F. G. S. Santos, R. S. Benevides, Y. A. V. Espinel, T. P. M. Alegre, and G. S. Wiederhecker, "Efficient anchor loss suppression in coupled near-field optomechanical resonators," arXiv:1701.03321 (2017).

[385] G. E. Snopatin, V. S. Shiryaev, V. G. Plotnichenko, E. M. Dianov, and M. F. Churbanov, "High-purity chalcogenide glasses for fiber optics," Inorganic Materials **45**, 1439–1460 (2009).

[386] S. J. Madden and K. T. Vu, "High-Performance Integrated Optics with Tellurite Glasses: Status and Prospects," International Journal of Applied Glass Science **3**, 289–298 (2012).

[387] C. Fortier, J. Fatome, S. Pitois, F. Smektala, G. Millot, J. Troles, F. Desevedavy, P. Houizot, L. Brilland, and N. Traynor, "Experimental investigation of Brillouin and Raman scattering in a 2SG sulfide glass microstructured chalcogenide fiber." Optics express **16**, 9398–9404 (2008).

[388] F. G. S. Santos, Y. A. V. Espinel, G. O. Luiz, R. S. Benevides, G. S. Wiederhecker, and T. P. Mayer Alegre, "Hybrid confinement of optical and mechanical modes in a bullseye optomechanical resonator," Optics Express **25**, 508 (2017).

[389] Y. A. V. Espinel, F. G. S. Santos, G. O. Luiz, T. P. M. Alegre, and G. S. Wiederhecker, "Brillouin Optomechanics in Coupled Silicon Microcavities," Scientific Reports **7**, 43423 (2017).

[390] R. Benevides, F. G. S. Santos, G. O. Luiz, G. S. Wiederhecker, and T. P. M. Alegre, "Ultrahigh-Q optomechanical crystal cavities fabricated in a CMOS foundry," Scientific Reports **7**, 2491 (2017).

[391] K. C. Balram, M. Davanço, J. Y. Lim, J. D. Song, and K. Srinivasan, "Moving boundary and photoelastic coupling in GaAs optomechanical resonators," Optica **1**, 414 (2014).

[392] K. C. Balram, M. I. Davanço, B. R. Ilic, J. H. Kyhm, J. D. Song, and K. Srinivasan, "Acousto-Optic Modulation and Optoacoustic Gating in Piezo-Optomechanical Circuits," Physical Review Applied **7**, 1–9 (2017).

[393] S. Coe and R. Sussmann, "Optical, thermal and mechanical properties of CVD diamond," Diamond and Related Materials **9**, 1726–1729 (2000).

[394] Y. Tao, J. M. Boss, B. a. Moores, and C. L. Degen, "Single-crystal diamond nanomechanical resonators with quality factors exceeding one million." Nature Communications **5**, 3638 (2014).

[395] M. Mitchell, B. Khanaliloo, D. P. Lake, T. Masuda, J. P. Hadden, and P. E. Barclay, "Single-crystal diamond low-dissipation cavity optomechanics," Optica **3**, 963 (2016).

[396] M. J. Burek, J. D. Cohen, S. M. Meenehan, N. El-Sawah, C. Chia, T. Ruelle, S. Meesala, J. Rochman, H. A. Atikian, M. Markham, D. J. Twitchen, M. D. Lukin, O. Painter, and M. Lončar, "Diamond optomechanical crystals," Optica **3**, 1404 (2016).

[397] D. A. Golter, T. Oo, M. Amezcua, K. A. Stewart, and H. Wang, "Optomechanical Quantum Control of a Nitrogen-Vacancy Center in Diamond," Physical Review Letters **116**, 1–6 (2016).

[398] A. Sipahigil, R. E. Evans, D. D. Sukachev, M. J. Burek, J. Borregaard, M. K. Bhaskar, C. T. Nguyen, J. L. Pacheco, H. A. Atikian, C. Meuwly, R. M. Camacho, F. Jelezko, E. Bielejec, H. Park, M. Lon ar, and M. D. Lukin, "An integrated diamond nanophotonics platform for quantum optical networks," Science **6875** (2016).

[399] P. Rakich and F. Marquardt, "Quantum Theory of Continuum Optomechanics," arXiv:1610.03012 pp. 1–12 (2016).

[400] W. H. Renninger, P. Kharel, R. O. Behunin, and P. T. Rakich, "Bulk crystalline optomechanics," arXiv:1703.08231 (2017).

[401] K. P. Huy, J.-C. Beugnot, J.-C. Tchahame, and T. Sylvestre, "Strong coupling between phonons and optical beating in backward Brillouin scattering," Physical Review A **94**, 043847 (2016).